Stony Brook University

OFFICIAL COPY

The official electronic file of this thesis or dissertation is maintained by the University Libraries on behalf of The Graduate School at Stony Brook University.

© All Rights Reserved by Author.

Synchrotron X-ray Scattering Characterization of Soft Materials: Rubber and Plastics

A Dissertation Presented

by

Justin Che

to

The Graduate School

in Partial Fulfillment of the

Requirements

for the Degree of

Doctor of Philosophy

in

Chemistry

Stony Brook University

December 2013

Stony Brook University

The Graduate School

Justin Che

We, the dissertation committee for the above candidate for the

Doctor of Philosophy degree,

hereby recommend acceptance of this dissertation.

Professor Benjamin S. Hsiao – Dissertation Advisor
Vice President for Research, Department of Chemistry

Professor Benjamin Chu – Dissertation Co-Advisor
Distinguished Professor, Department of Chemistry

Professor Robert B. Grubbs - Chairperson of Defense
Associate Professor, Department of Chemistry

Professor Tadanori Koga – Third Member of Academic Committee
Associate Professor, Department of Chemistry and Materials Science and Engineering

Dr. Lin Yang – Outside Member
Physicist, Photon Sciences Directorate, Brookhaven National Laboratory

This dissertation is accepted by the Graduate School

Charles Taber
Dean of the Graduate School

Abstract of the Dissertation

Synchrotron X-ray Scattering Characterization of Soft Materials: Rubber and Plastics

by

Justin Che

Doctor of Philosophy

in

Chemistry

Stony Brook University

2013

Synchrotron X-ray scattering and diffraction techniques have been widely used to study the structure and property relationships of materials. It is important to first identify the driving physics and basic understanding of the structure change during mechanical usage before leading to material design for potential applications. In this thesis, the combined wide-angle X-ray diffraction (WAXD) and small-angle X-ray scattering (SAXS) techniques have been used to analyze in-situ structure formation over a large range of length scale from 1 nm to 100 nm during mechanical deformation. In specific, the in-situ structural development and morphological changes in polymer plastics and rubber during tensile deformation were studied.

The chosen systems included the lamellar structural changes of uniaxially oriented semi-crystalline polyethylene (PE) fibers using in-situ WAXD and SAXS techniques. The deformation mechanism in PE was found to be driven by an initial structural rearrangement of the lamellar stacks, followed by crystallographic slippage and strain-hardening. The experimental deformation results were qualitatively compared with atomistic simulations of tensile deformation to provide further insights into the interlamellar regions and its overall effect on PE deformation. Various temperatures, strain rates, and modes of deformation were explored.

In natural rubber (NR), the behavior of strain-induced crystallization (SIC) was found to be primarily responsible for its outstanding mechanical properties, such as high tensile strength, tear strength, cut resistance, and durability. The underlying mechanism could be attributed to the pseudo-network and the non-rubber components-polymer interactions in NR. In other words, the inhomogeneity of cross-linked topology in NR leads to a microfibrillar structure composed of crystalline segments between the cross-links during stretching. A novel two-dimensional WAXD simulation method was developed to analyze the SIC of un-vulcanized NR, vulcanized NR, and synthetic polyisoprene rubber (IR). Crystallite properties, such as size, volume, orientation, crystal fractions, and crystal disordering, were obtained and compared at various temperatures from -50 to 50˚C. The effects of temperature on the mechanical properties and the SIC process are discussed.

This thesis is dedicated to my family and friends
for their continuous love and endless support.

Table of Contents

Page

List of Figures xi
List of Tables xix
List of Abbreviations xx
Acknowledgements xxiii
List of Publications xxv
List of Presentation xxvii

Chapter 1 Introduction

1.1 Introduction to Natural Rubber 1
  1.1.1 Structure of Natural Rubber 2
  1.1.2 Natural Rubber Latex 3
  1.1.3 Comparison Between Natural Rubber and Synthetic Polyisoprene Rubber 4
  1.1.4 Natural Rubber Derivatives 6
  1.1.5 Effect of Natural Rubber Derivatives on its Mechanical Properties 8
  1.1.6 Rubber Vulcanization 9
  1.1.7 Strain-Induced Crystallization 10
1.2 Introduction to Polyethylene 13
  1.2.1 Semi-Crystalline Structure of Polyethylene 13
  1.2.2 Different Density Systems of Polyethylene 14
  1.2.3 Deformation Mechanism in Polyethylene 15
1.3 Chapter Contents 17
1.4 References 18

Chapter 2 Chain Dynamics and Strain-Induced Crystallization of Pre- and Post-Vulcanized Natural Rubber Latex Using Proton Multiple Quantum NMR and Uniaxial Deformation by *In-Situ* Synchrotron X-Ray Diffraction

2.1 Introduction 20
2.2 Experimental Methods 22
  2.2.1 Rubber Latex Samples 22
  2.2.2 Time-Domain NMR Measurements 24
    2.2.2.1 Saturation Recovery Experiments 24
    2.2.2.2 ^{1}H DQ-NMR Experiments 25
  2.2.3 Synchrotron X-ray and Tensile Measurements 28
2.3 Results 29
  2.3.1 ^{1}H DQ Solid-State NMR 29
    2.3.1.1 Pre-vulcanization Kinetics 29
    2.3.1.2 Rubber Network Structure 31
  2.3.2 Stress-Strain Relations 39
  2.3.3 WAXD Results 43
2.4 Discussion 48
2.5 Conclusion 51
2.6 References 53

Chapter 3 Entanglements and Networks of Strain-Induced Crystallization in Natural Rubber at Various Temperatures

3.1 Introduction 55
3.2 Experimental Methods 59
  3.2.1 Sample Preparation 59
  3.2.2 Sample Characterization 59
3.3 Results and Discussion 60
  3.3.1 Un-vulcanized State 60
  3.3.2 Vulcanized State 62
  3.3.3 Theory of Rubber Elasticity: Stress-Temperature Relation 65
  3.3.4 Proposed Model on the Stress-Strain Relation 66
3.4 Conclusion 68
3.5 References 68

Chapter 4 Crystal and Crystallites Structure of Natural Rubber and Synthetic *cis*-1,4-Polyisoprene by a New Two Dimensional Wide Angle X-ray Diffraction Simulation Method: Strain-Induced Crystallization

4.1 Introduction 70
4.2 Experimental Methods 73
    4.2.1 2D WAXD Pattern Simulation 73
    4.2.2 Materials and Sample Preparation 76
    4.2.3 Time-Resolved WAXD Measurements and Tensile Deformation 76
4.3 Results and Discussion 77
    4.3.1 Crystalline Fraction 86
    4.3.2 Crystallite Size 86
    4.3.3 Crystallite Orientation 88
    4.3.4 Displacement Disorder in Crystal 89
    4.3.5 Proposed SIC Model 90
4.4 Conclusion 91
4.5 References 92

Chapter 5 Crystal and Crystallites Structure of Natural Rubber and Peroxide Vulcanized Natural Rubber by a Two Dimensional Wide Angle X-ray Diffraction Simulation Method: Strain-Induced Crystallization Versus Temperature-Induced Crystallization

5.1 Introduction 94
5.2 Experimental Methods 96
    5.2.1 Materials and Sample Preparation 96
    5.2.2 Time-Resolved WAXD Measurements and Tensile Deformation 97
    5.2.3 WAXD Data Analysis 98
    5.2.4 SAXS Data Analysis 100

5.3 Results and Discussion 101
  5.3.1 WAXD Results 101
    5.3.1.1 Crystallite Size and Crystalline Fraction 105
    5.3.1.2 Crystallite Orientation and Displacement Disorder in Crystal 108
  5.3.2 SAXS Results 110
  5.3.3 Proposed Models 115
5.4 Conclusion 117
5.5 References 117

Chapter 6 Plastic Deformation of Semi-crystalline Polyethylene by X-ray Scattering: Comparison with Atomistic Simulations

6.1 Introduction 120
6.2 Experimental Methods 122
  6.2.1 Sample Preparation 122
  6.2.2 X-ray Scattering 122
  6.2.3 Scattering Data Analysis 123
  6.2.4 Simulation Model and Methods 126
6.3 Results and Discussion 128
  6.3.1 X-ray Results During Deformation 128
  6.3.2 Comparison Between Simulation and Experiment 135
6.4 Conclusion 144
6.5 References 144

Chapter 7 Morphological Effects on Swelling in Semi-Crystalline Polyethylene

7.1 Introduction 146
7.2 Experimental Methods 147
  7.2.1 Materials and Sample Preparation 147
  7.2.2 Differential Scanning Calorimetry 148
  7.2.3 X-ray Scattering 148

7.2.4 SAXS Stacking Model Fitting 149
7.2.5 2D Correlation Analysis 150
7.3 Results and Discussion 152
7.3.1 DSC and WAXD 152
7.3.2 Diffusion Coefficient 154
7.3.3 SAXS Stacking Model 155
7.3.4 2D Correlation Analysis 156
7.4 Conclusion 159
7.5 References 159

Chapter 8 – Conclusion 161
8.1 Future Work 164
8.2 References 166

Bibliography 167

List of Figures

Figure 1.1 Emerging applications for elastomers to 2017.

Figure 1.2 Chemical structure of natural rubber: *cis*-1,4-polyisoprene.

Figure 1.3 Proposed structures of a linear rubber chain and the naturally occurring network in NR.

Figure 1.4 Structure and composition of natural rubber latex particles.

Figure 1.5 Molecular weight distribution of NR and IR determined from gel permeation chromatography.

Figure 1.6 Removal of non-rubber components in NR.

Figure 1.7 Centrifugation of NR latex.

Figure 1.8 Stress-strain relationships during stretching and relaxation of NR, DPNR, TENR, and IR.

Figure 1.9 (a) Sulfur and (b) peroxide vulcanization of rubber chains.

Figure 1.10 Strain-induced crystallization in a uniaxial deformed NR sample.

Figure 1.11 WAXD patterns obtained at 25 ˚C for un-vulcanized NR, DPNR, TENR, and IR at strain 0 and strain 6.

Figure 1.12 Strain-induced crystallization contents obtained at 25 ˚C for un-vulcanized NR, DPNR, TENR, and IR.

Figure 1.13 Structure of polyethylene: spherulite, lamellae, amorphous and crystalline regions.

Figure 1.14 Orthorhombic crystal structure of polyethylene.

Figure 1.15 Linear, branched, and cross-linked arrangements in a polymer.

Figure 1.16 Typical stress-strain curve of a thermoplastic, semi-crystalline polymer.

Figure 1.17 Proposed deformation mechanism in PE.

Figure 2.1 (A) Saturation recovery curve for NR latex state sample. Double exponential fits, where $M_z(t)$ is the longitudinal magnetization at the experiment time t and A represents the fraction of sample with solid-like behavior, were used to analyze the curves. (B) Identification and subtraction of non-coupled fraction tails in a latex sample after and before drying. In the latex samples, the non-coupled fraction is

mainly composed by water (i.e. the small fraction of water that was magnetized caused by the short r.d. used in the experiments) and non-elastic network defects, whereas in dry samples, the slowly relaxed tails are mainly related with network defects.

Figure 2.2 Relative intensity at the selected DQ evolution time of 2.2 ms as a function of pre-vulcanization time for various concentrations of DPTT. The 1.2 phr peroxide vulcanized sample is also shown. The optimum vulcanization time (t_{90}) is shown in parenthesis for each sample.

Figure 2.3 Percentage of non-coupled network defects in each state for the studied samples.

Figure 2.4 (A) Cross-linking density (ν) of various concentrations of DPTT and peroxide in the three different states: pre-vulcanization in latex state, drying and film formation, and post-vulcanization in film state. (B) Efficiency of pre- and post-vulcanization reactions for DPTT and peroxide as the relationship of cross-link density (measured by NMR) and the concentration of vulcanizing agent. Numbers in brackets represent the slope of the linear fit for DPTT vulcanization processes.

Figure 2.5 Variation of the relative width of the distribution of cross-link density (σ) to the average value (D_{res}) for all three different states. A Gaussian distribution of cross-link density was assumed.

Figure 2.6 Actual spatial cross-link distribution for pre-vulcanized samples in latex state (A) and dried films (B) according to the regularization analysis of NMR data.

Figure 2.7 Effect of washing the excess of curing agent on the cross-linking density (A) and relative width of spatial cross-links distribution (B) in the three different states: pre-vulcanization in latex state, drying and film formation, and post-vulcanization in film state.

Figure 2.8 Stress-strain relationships during stretching and relaxation of Latex and Latex with post-heat treatment at 130 °C.

Figure 2.9 Comparison of the stress-strain relations of pre- and post-vulcanized latex with various concentrations of DPTT.

Figure 2.10 Comparison of the stress-strain relations of pre- and post-vulcanized latex with various concentrations of peroxide.

Figure 2.11 Selected two-dimensional WAXD patterns of latex, latex with post-heat treatment at 130 ˚C, pre- and post-vulcanized latex with 2.25 phr of DPTT (labeled as DPTT 1.5 and 1.5 PostV respectively), and pre-vulcanized latex with 1.8 phr of peroxide (labeled as Per 1.8 and Per 1.8 PostV respectively) during stretching.

Figure 2.12 Integrated intensities of the two-dimensional WAXD patterns for latex, latex with post-heat treatment, pre- and post-vulcanized latex with 2.25 phr of DPTT, pre- and post-vulcanized latex with 1.8 phr of peroxide at strains 2 (a) and 6 (b).

Figure 2.13 Crystallinity fraction with respect to strain for (a) latex and latex with post-heat treatment, comparison of crystallinity fraction between pre- and post-vulcanization with (b) DPTT and (c) peroxide.

Figure 2.14 A schematic model of the 3 different states for vulcanized latex: pre-vulcanization in latex state, drying and film formation, and post-vulcanization in film state.

Figure 3.1 Stress strain relations of un-vulcanized NR at temperatures from -50 to 75 ˚C. The WAXD images at each temperature were obtained at the largest strain before breaking. The vertical arrows show the onset strains of SIC at the temperatures.

Figure 3.2. A schematic model of un-vulcanized NR prior to deformation (left) and after deformation (right). Entanglements (blue circles), pseudo end-linking networks (green squares), and SIC (gray squares) are shown.

Figure 3.3 Stress strain relations of peroxide vulcanized NR (PVNR) at temperatures from -50 to 75 °C. The WAXD images at each temperature were obtained at the largest strain before breaking. The vertical arrows show the onset strains of SIC at the temperatures.

Figure 3.4 Stress-temperature relations of PVNR at strain 1.0 (●), 3.0 (▲), 5.0 (■).

Figure 3.5 A schematic model of peroxide vulcanized NR (PVNR) prior to deformation (left) and after deformation (right). Entanglements (blue circles), pseudo end-linking networks (green squares), chemical bond networks (red circles), and SIC (gray squares) are shown.

Figure 3.6 A hypothetical model on the stress-strain relation.

Figure 4.1 Geometric relationship between the scattering vector s and the primary axes of the fiber $J(s, \varphi)$ and individual structural unit $I(s,\varphi_{hkl})$.

Figure 4.2 Observed WAXD images, with Fraser correction, at strain 6.0 for un-vulcanized NR and IR at -50˚C.

Figure 4.3. The scattering peak positions and relative intensities in one dimensional profile of Takahashi-Immirzi's data (Δ), Rajkumar's data(▼) and our observed profile of NR and IR.

Figure 4.4 One-dimensional integrated intensities of NR at -50˚C at various strains. From strains 0.0 to 3.0, the amorphous halo is observed. From strains 4.0 to 6.0, both the crystal peaks and amorphous halo are observed.

Figure 4.5 Orthorhombic unit cell of *cis*-1,4-polyisoprene with $P2_12_12_1$ symmetry. The unit cell dimensions are a = 13.048 Å, b = 9.391 Å, and c = 8.551 Å. These carbon atom coordinates are modified Rajkumar's coordinates.

Figure 4.6 Two-dimensional observed and simulated WAXD patterns at strain 6.0 for NR and IR at -50˚C. The top and bottom portions of the images represent the observed and simulated WAXD pattern, respectively.

Figure 4.7 (a) One-dimensional integrated intensity profile of the observed (solid line) and simulated (long dashed line) WAXD pattern at strain 6.0 for NR and IR at -50˚C. The separated simulated peaks are shown in small dash lines. (b) One-dimensional standardized residual plots calculated from the difference between the simulation and observed intensities in (a).

Figure 4.8 Crystalline fraction as a function of strain for NR and IR at -50˚C. The onset strains of SIC in NR and IR are 1.61 and 3.97, respectively.

Figure 4.9 Crystallite sizes of the (*200*), (*120*) and (002) diffraction peaks as a function of strain for NR and IR at -50˚C

Figure 4.10 P_2 orientation of the crystallites as a function of strain for NR and IR at -50˚C.

Figure 4.11 Debye-Waller factor, B, as a function of strain for NR and IR at -50˚C.

Figure 4.12 A model of the average crystallite size for the SIC of un-vulcanized NR at -50˚C.

Figure 5.1 Two-dimensional observed and simulated WAXD patterns of the SIC of (a) NR and (b) PVNR at various strains and temperatures (-50, -25, 0, 25, 50 ˚C), and (c) the TIC of NR and PVNR. The patterns shown for SIC are those that are obtained at the maximum strain during deformation before breaking. The top and bottom portions of all the images represent the experimentally observed and simulated WAXD pattern, respectively.

Figure 5.2 One-dimensional (1D) integrated intensity profile of the experimental (solid line) and simulated (long dashed line) WAXD patterns from Figure 5.1 for the SIC of (a) NR and (b) PVNR at various strains and temperatures, and (c) the TIC of NR and PVNR. The separated simulated peaks are shown in small dash lines. The standardized residual plots are calculated from the difference between the simulation and observed intensities.

Figure 5.3 The crystallite sizes for the (*200*), (*120*), and (*002*) diffraction peaks as a function of temperature for the SIC (left) and TIC (right) of NR and PVNR. For the SIC samples, the data shown are obtained at the maximum strain during deformation before breaking as indicated in Figure 5.1. For NR, all data points shown are at strain 6. For PVNR, the data shown are at strain 4 for -50 ˚C and strain 5 for all the other temperatures.

Figure 5.4 P_2 orientation of the crystallites as a function of temperature for the SIC of NR and PVNR. For NR, all data points shown are at strain 6. For PVNR, the data shown are at strain 4 for -50 ˚C and strain 5 for all the other temperatures.

Figure 5.5 The displacement disorder factor, *B*, as a function of temperature for the SIC (left) and TIC (right) of NR and PVNR. For the SIC of NR, all data points shown are at strain 6. For the SIC of PVNR, the data shown are at strain 4 for -50 ˚C and strain 5 for all the other temperatures.

Figure 5.6 Two-dimensional SAXS patterns of the SIC at various strains and temperatures (-50, -25, 0, 25, 50 ˚C), and the TIC of NR and PVNR. A scale bar for the SAXS patterns are shown as the red line in the top left at NR strain 0 at -50 ˚C. The scale bar represents 0.05 nm^{-1}.

Figure 5.7 The corresponding one-dimensional SAXS integrated intensity profiles of the experimental SAXS patterns from Figure 5.6 for the SIC at (a) strain 0 and (b) strain 6, and (c) TIC of NR and PVNR.

Figure 5.8 (a) Two-phase stacking model fittings (shown in red) applied to the raw integrated SAXS intensities for the SIC of NR at -25 ˚C (black) and 0 ˚C (blue) at strain 6. (b) Summary of parameters obtained from the fitting in (a), including crystalline layer thickness (<T>), amorphous layer thickness (<t>), long-period spacing (L), and crystallinity fraction determined from SAXS (X_{cs}).

Figure 5.9 A schematic representation of the SIC at strain 6 at various temperatures and the TIC of NR. The crystallites circled in red are enlarged and shown in the center of the figure. The average number of unit cells in the *a*, *b*, and *c* direction (denoted as *a* x *b* x *c*) and the number of chains per crystallite are also shown.

Figure 6.1 An example of the two-phase stacking model fitting to the experimental integrated raw SAXS intensity.

Figure 6.2 Reproduced from Reference 16. (a) Amorphous topology (red) generated from Interphase Monte Carlo algorithm. (b) Semicrystalline model simulation cell with crystalline beads added at chain ends to give realistic degree of crystallinity, average molecular weight and polydispersity in the model polyethylene system. (c) Visualization of the repeated stacked lamellae resulting from periodic boundary conditions in the Monte Carlo and molecular dynamics simulations.

Figure 6.3 Stress-strain curves for (a) 25°C experiment, (b) 100°C experiment, (c) simulation with constant lateral sides, and (d) simulation with constant volume. The simulations in (c) exhibit similar features (yield, plastic deformation, and strain hardening) as the 25°C experiment, but they tend to occur at lower strains and are more pronounced. Similarly, the slow simulation in (d) shows yield, melting, and strain hardening features also seen in the 100°C experiment, and the simulated features tend to be more pronounced and occur at lower strains.

Figure 6.4 2D WAXD patterns for the deformation at (a) 25˚C and (b) 100˚C. 2D SAXS patterns for the deformation at (c) 25˚C and (d) 100˚C. Scale bars for the WAXD and SAXS patterns are shown as the red line in (a) and (c) at strain 0. The scale bars for WAXD and SAXS represents 2.35 nm^{-1} and 0.05 nm^{-1} respectively.

Figure 6.5 1D integrated WAXD intensities for the deformation at (a) 25˚C and (b) 100˚C. 1D integrated SAXS intensities for the deformation at (c) 25˚C and (d) 100˚C.

Figure 6.6 Unoriented isotropic and oriented anisotropic fractions as a function of strain for the deformation of HDPE at 25˚C and 100˚C.

Figure 6.7 P_2 orientation factor of the polymer crystals with respect to the filament axis as a function of strain for the deformation at 25˚C and 100˚C.

Figure 6.8 Polar azimuthal scans at the peak maximum of the lamellar long period at varying strains for the deformation at 25˚C and 100˚C. The intensities were offset to increase clarity.

Figure 6.9 Long period (L), crystalline layer thickness (<T>), and amorphous layer thickness (<t>) as a function of strain for the deformation of HDPE at 25˚C and 100˚C from (a) the simple calculation method using the experimental WAXD and SAXS results, and (b) the two-phase stacking model fitting.

Figure 6.10 Linear maps between experimental and simulation time and strain. (a) and (c) map the constant volume, slow deformation simulation to the 100°C experiment. (b) and (d) map the fixed lateral sides, fast deformation simulation to the 25°C experiment. Initial points correspond to zero time and strain, final points correspond to time to yield and yield strain for the time and strain maps, respectively.

Figure 6.11 Stress-strain curves for (a) simulation with constant lateral sides (black) and the 25°C experiment (blue), (b) simulation with constant volume and the 100°C experiment (red). The simulation strain is mapped to experimental strain space using the linear maps for time and strain in Figure 6.9 (d) and (c), respectively. The simulations in (a) exhibit similar features (yield, plastic deformation, and strain hardening) as the 25°C experiment, but both post-yield softening and subsequent strain hardening are more pronounced. Similarly, the slow simulation in (b) shows yield, melting, and strain hardening features also seen in the 100°C experiment, and the simulated features tend to be more pronounced and occur at higher (mapped) strains.

Figure 6.12 The change in percent crystallinity in simulations of deformation with (a) constant lateral dimensions and the 25°C experiment, and (b) constant volume simulations and two 100°C experiments. Two experiments were performed at 100°C; one with a higher collection frequency deformed to 1.5 strain (dashed red line) and one with a lower collection frequency deformed to 3.0 strain (solid red line).

Figure 6.13 Evolution of lamellar morphology. (a) Gibbs dividing interfaces between crystalline (shown as the two blue regions on the right side of the figure) and noncrystalline domains (shown as the red region on the right side of the figure) as a function of strain for the constant volume "slow" and "fast" deformation simulations. The red line represents a hypothetical affine deformation, and the equilibrium data is from a simulation with no deformation. (b) Crystal (squares) and amorphous (circles) thickness of the HDPE computed from SAXS and WAXD data collected from two experiments during 100°C uniaxial deformation. As in Figure 6.12, the two experiments employed different collection frequencies to capture the low strain behavior.

Figure 7.1 (a) Percent weight gain and (b) percent weight gain normalized by amorphous fraction by DSC of LLDPE compared with HDPE after soaking in toluene for different periods of time.

Figure 7.2 (a) Crystallinity and (b) peak melting temperature by DSC of LLDPE compared with HDPE after soaking in toluene for different periods of time.

Figure 7.3 Orthorhombic unit cell dimensions by WAXD of LLDPE compared with HDPE after soaking in toluene for different periods of time.

Figure 7.4 Long period, L_p, average crystalline, <T>, and amorphous <t> layer thicknesses calculated by (a) traditional SAXS/WAXS method and (b) fitting to a stacking model.

Figure 7.5 2D synchronous correlation plots of SAXS profiles as a function of soaking time for (a) HDPE and (b) LLDPE. Positive contours are outlined in red and negative contours are filled blue. Average profiles are shown on the side.

Figure 7.6 Autocorrelation intensity along diagonal of 2D synchronous correlation plots of SAXS profiles as a function of soaking time for (a) HDPE and (b) LLDPE.

List of Tables

Table 1.1 Composition of natural rubber (NR) and synthetic polyisoprene rubber (IR).
Table 1.2 Characterization of proteins and phospholipids in un-vulcanized NR, DPNR, and TENR.
Table 1.3 ASTM and industrial polyethylene density-based classification.

Table 2.1 Recipes and Curing Conditions for Rubber Latex Samples Vulcanized with DPTT
Table 2.2 Recipes and Curing Conditions for Rubber Latex Samples Vulcanized with Peroxide
Table 2.3 100% modulus, 300% modulus and tensile strength of un-vulcanized and vulcanized latex samples at various concentrations and post-heat treatment 130 ˚C.

Table 4.1 Observed and calculated WAXD intensities for each specific (*hkl*) planes

Table 5.1 Summary of the average number amount of unit cells per crystallite (*n*) in the *a*-, *b*-, and *c*-direction (denoted as *a* x *b x c*), the volume of the crystallite (V_c), and the crystallite fraction determined from WAXD (X_{cw}) for the SIC (at various temperatures) and the TIC of NR and PVNR. For the SIC samples, the data shown are obtained at the maximum strain during deformation before breaking as indicated in Figure 5.1. For NR, all data shown are at strain 6. For PVNR, the data shown are at strain 4 for -50 ˚C and strain 5 for all the other temperatures.

Table 7.1Total percent increase after soaking in toluene for 24 hours of long period, L_p, average crystalline layer thickness <T> and average amorphous layer thickness <t> obtained by tradition WAXS/SAXS analysis and with Stacking model.

List of Abbreviations

1D	One-Dimensional
2D	Two-Dimensional
ASTM	American Society for Testing and Materials
BNL	Brookhaven National Laboratory
BR	Butadiene Rubber
CCD	Charged Couple Device
DPNR	Deproteinized Natural Rubber
DPTT	Dipentamethylenethiuram Tetrasulfide
DRC	Dry Rubber Content
D_{res}	Residual Dipolar Couplings
DQ	Double-Quantum
DSC	Differential Scanning Calorimetry
EMCC	ExxonMobil Chemical Company
FTIR	Fourier Transform Infrared Spectroscopy
GPC	Gel Permeation Chromatography
HDPE	High-Density Polyethylene
I_{1d}	One-dimensional Intensity
I_{DQ}	Double-Quantum Intensity
I_{nDQ}	Normalized Double-Quantum Intensity
I_{ref}	Reference Decay Intensity
$I_{\Sigma MQ}$	Total Multiple-Quantum Magnetization
IMC	Interphase Monte Carlo
IR	Synthetic Polyisoprene Rubber
L_p	Long-Period
LDPE	Low-Density Polyethylene
LLDPE	Linear Low-Density Polyethylene
M_c	Molecular Weight Between Constraints
MD	Molecular Dynamics

MDPE	Medium-Density Polyethylene
MQ	Multiple-Quantum
MWD	Molecular Weight Distribution
NMR	Nuclear Magnetic Resonance
NR	Natural Rubber
NSLS	National Synchrotron Light Source
P_2	Hermans' Orientation Parameter
PE	Polyethylene
Per	Peroxide
PostV	Post-Vulcanization
phr	parts per hundred rubber
PVNR	Peroxide Vulcanized Natural Rubber
RDC	Residual dipolar Coupling
R_{max}	Maximum Length of chain from end-to-end vector
rpm	Revolution Per Minute
RSS	Ribbed Smoked Sheet
SAXS	Small-Angle X-ray Scattering
SAXS	Small-Angle Neutron Scattering
SBR	Styrene-Butadiene Rubber
SM	Semi-Crystalline Model
SVNR	Sulfur Vulcanized Natural Rubber
SIC	Strain-induced Crystallization
TEM	Transmission Electron Microscopy
TENR	Transesterified Natural Rubber
<T>	Crystalline layer Thickness
<t>	Amorphous Layer Thickness
T_g	Glass Transition Temperature
T_m	Melting Temperature
TIC	Temperature-Induced Crystallization
UHMWPE	Ultra High Molecular Weight Polyethylene

ULLDPE	Ultra Linear-Low Density Polyethylene
WAXD	Wide-Angle X-ray Diffraction
X_{cw}	Crystallinity Fraction from WAXD
X_{cs}	Crystallinity Fraction from SAXS
ZnO	Zinc Oxide

Acknowledgements

This thesis work would not have been possible without the contributions of many different people in their different ways. I would like to extend my appreciation to the following:

Foremost, I would like to express my deepest sincere gratitude to my thesis advisors, Professor Benjamin S. Hsiao and Professor Benjamin Chu, for their continuous help and support throughout my PhD studies. Their wisdom, advice, and guidance have motivated me to complete my PhD studies and also provided me with an invaluable research experience. I would like to especially acknowledge and give my greatest appreciations to Dr. Shigeyuki Toki for his mentorship and guidance, who taught me a tremendous amount of knowledge on rubber theory and characterization. I would like to personally thank the rest of my committee, Professor Robert B. Grubbs, Professor John B. Parise, and Professor Tadanori Koga for their valuable comments and insights. I also want to thank Dr. Lin Yang for serving in my committee as an outside member.

I especially want to acknowledge the help, support, and assistance from Dr. Christian Burger, Dr. Lixia Rong, Dr. Dufei Fang, and Dr. Hongyang Ma. I would like to extend my gratitude to my group members: Yimin Mao, Ran Wang, Yang Liu, Xiaowei Li, Xiao Wang, Tsung-Ming Yeh, Zhe Wang, Rui Yang, and Ying Su. I would like to thank our secretary, Ms. Jane Wainio, for her great assistance in the past few years.

More importantly, this research would not be possible without the financial support from the National Science Foundation and our industrial collaborators: ExxonMobil Company, Goodyear Tire and Rubber Company, Cooper Tire and Rubber Company, and the United States Department of Agriculture (USDA). I would like to Dr. Andy H. Tsou, Dr. C. Rebecca Locker, and Dr. Diana S. Smirnova from ExxonMobil Company. I would like to thank Dr. Frank Feher, Dr. Dan Qu, Dr. Arindam Mazumdar, Dr. Kuo-Chih Hua from Goodyear Tire and Rubber Company. I would like to thank Dr. Howard A. Colvin and Dr. Michael G. Shivers from Cooper Tire and Rubber Company. Finally, I want to thank Dr. Colleen McMahan from USDA.

In addition to our industrial collaborators, I would like to acknowledge our academic collaborators from around the world. I would like to thank Dr. Juan L. Valentin, Dr. Justo Brasero, and Dr. Adun Nimpaiboon from the Institute of Polymer Science and Technology in

Madrid, Spain. I would like to thank Dr. Sureerut Amnuaypornsri and Dr. Jitladda Sakdapipanich from Mahidol University in Bangkok, Thailand. I want to thank Dr. Gregory C. Rutledge and Dr. Sanghun Lee from the Department of Chemical Engineering at Massachusetts Institute of Technology (MIT).

Finally, I would like to thank my family and friends for their endless support. Their motivation inspired me to pursue higher education and complete my PhD studies.

List of Publications

1. Justin Che, *"*Investigating the photophysics of conjugated polymer chemosensors in the solid state", *Volume 301 of Honors theses: Science and mathematics,* State University of New York at Binghamton, Department of Chemistry **(2009)**

2. Sherryllene S. Pinnock; Catherine N. Malele; Justin Che; Wayne E. Jones, Jr. The Role of Intermolecular Interactions in the Solid State Fluorescent Conjugated Polymer Chemosensors. *J. Fluoresc.* **(2011)** *22*, 583-589
   DOI: 10.1007/s10895-011-0993-1

3. Shen Zhao, Dong Su, Justin Che, Bingyin Jiang and Alexander Orlov, " Photocatalytic properties of TiO2 supported on SBA-15 mesoporous materials with large pores and short channels", *Materials Letters* **(2011)** *65, 3354*–3357
   DOI: 10.1016/j.matlet.2011.07.053

4. Masatoshi Tosaka, Shigeyuki Toki, Justin Che, Lixia Rong and Benjamin S. Hsiao, "Development of Internal Fine Structure in Stretched Rubber Vulcanizates", *Journal of Polymer Science: Polymer Physics* **(2011)** *49*, 1157-1162
   DOI: 10.1002/polb.22290

5. Justin Che, Shigeyuki Toki, Juan Valentin, Justo Brasero, Adun Nimpaiboon, Lixia Rong, Benjamin S. Hsiao, "Chain Dynamics and Strain-Induced Crystallization of Pre- and Post-Vulcanized Natural Rubber Latex Using Proton Multiple Quantum NMR and Uniaxial Deformation by *In-Situ* Synchrotron X-Ray Diffraction", *Macromolecules* **(2012)** *45*, 6491-6503
   DOI: 10.1021/ma3006894

6. Justin Che, Christian Burger, Shigeyuki Toki, Lixia Rong, Benjamin S. Hsiao, "Crystal Structures and Crystallite Sizes of Natural Rubber and Synthetic *cis*-1,4-Polyisoprene by a Two-Dimensional Wide Angle X-Ray Diffraction Simulation Method. I. Strain-Induced Crystallization", *Macromolecules,* **(2013)** *46*, 4520-4528
   DOI: 10.1021/ma400420k

7. Justin Che, C. Rebecca Locker, Sanghun Lee, Gregory Rutledge, Benjamin S. Hsiao, Andy H. Tsou, "Plastic Deformation of Semi-Crystalline Polyethylene by X-ray Scattering: Comparison with Atomistic Simulations", *Macromolecules,* **(2013)**, *46*, 5279-5289
   DOI: 10.1021/ma4005007

8. Shigeyuki Toki, Justin Che, Lixia Rong, Benjamin S. Hsiao, Sureerut Amnuaypornsri, Adul Nimpaiboon, Jitladda Sakdapipanich, "Entanglements and Networks in Strain-Induced Crystallization and Stress-Strain Relations in Natural Rubber and Synthetic Polyisoprene at Varied Temperatures", *Macromolecules,* **(2013)***, 46*, 5238-5248

DOI: 10.1021/ma400504k

9. Xiaowei Li, Yimin Mao, Christian Burger, Justin Che, Benjamin S. Hsiao, Rahul R. Kulkarni, Andy H. Tsou, "The Effect of Comonomer Content on Structure and Property Relationship of Propylene-1-Octene Copolymer during Uniaxial Stretching", *Polymer*, **(2013)**, *54*, 4545-4554
   DOI: 10.1016/j.polymer.2013.06.017

10. Yumei Zhang, Huaping Wang, Shenghui Chen, Xiaofeng Wang, Dufei Fang, Christian Burger, Justin Che, Xiaowei Li, Benjamin S. Hsiao, "Determination of Poly(4,4'-diphenylsulfonylterephthalamide) Crystalline Structure Via WAXD and Molecular Simulations", *Macromolecular Chemistry and Physics*, **(2013)**
    DOI: 10.1002/macp.201300369

11. Justin Che, Shigeyuki Toki, Christian Burger, Benjamin S. Hsiao, "Crystal and Crystallites Structure of Natural Rubber and Peroxide Vulcanized Natural Rubber by a Two Dimensional Wide Angle X-ray Diffraction Simulation Method. II. Strain-Induced Crystallization versus Temperature-Induced Crystallization," *Macromolecules*, **(2013),** accepted, in print

12. Posadas, P.; Malmierca, M. A.; Gonzalez-Jimenez, A.; Rodríguez, A.; Ibarra, L.; Valentín, J. L.; Nagaoka, T.; Yajima, H.; Toki, S.; Che, J.; Rong, L.; Hsiao, B. S. "Experimental study on the role of radicals during vulcanization process and during uniaxial deformation and strain-induced crystallization of natural rubber and synthetic polyisoprene rubber by in-situ Electron Spin Resonance (ESR) and synchrotron X-ray", *Polymer,* **(2013)**, submitted

13. Justin Che, Diana S. Smirnova, Benjamin S. Hsiao, Andy H. Tsou, "Morphological Effects of Swelling of Semi-Crystalline Polyethylene", **(2013)**, in progress

List of Presentations

1. **ACS National Meeting & Exposition**, Philadelphia, PA, August 2008
   "Investigating the Photophysics of a Conjugated Polymer Chemosensor in the Solid State," *Poster Presenter*

2. **ACS Rubber Division Meeting & Exposition**, Cleveland, OH, October 2011
   "Strain-Induced Crystallization of Pre- and Post-Vulcanized Natural Rubber Latex During Uniaxial Deformation by *in-situ* X-Ray Diffraction," *Oral Speaker/Paper*

3. **APS National Meeting & Exposition**, Boston, MA, March 2012
   "New Insights into Chain Order Dynamics and Structural Development in Sulfur-Vulcanized Natural Rubber Latex Using Multiple-Quantum NMR and Synchrotron X-ray Diffraction," *Poster Presenter*

4. **ACS Rubber Division Meeting & Exposition**, Cincinnati, OH, October 2012
   "Two-Dimensional Wide-Angle X-Ray Diffraction Simulation Study on Strain-Induced Crystallization and Temperature-Induced Crystallization of Un-Vulcanized Natural and Synthetic Rubber," *Oral Speaker/Paper*

5. **Graduate Chemical Society Student Seminar Series**, Stony Brook University, March 2013
   "Correlation Between Natural Rubber Network Structure and Mechanical Properties," *Oral Speaker*

6. **ACS National Meeting & Exposition**, Indianapolis, IN, September 2013
   "Plastic Deformation of Semi-Crystalline Polyethylene by X-ray Scattering: Comparison with Atomistic Simulations," *Oral Speaker/Paper,* Excellence in Graduate Student Research Symposium

7. **ACS National Meeting & Exposition**, Indianapolis, IN, September 2013
   "Two-Dimensional Wide-Angle X-Ray Diffraction Simulation Study on Strain-Induced Crystallization and Temperature-Induced Crystallization of Un-Vulcanized Natural and Synthetic Rubber," *Oral Speaker/Paper*

8. **ACS Rubber Division Meeting & Exposition**, Cleveland, OH, October 2013
   "New Insights into Strain-Induced Crystallization and Temperature-Induced Crystallization of Un-Vulcanized and Peroxide-Vulcanized Natural Rubber," *Oral Speaker/Paper*

Chapter 1

Introduction

In industry, it is crucial to first identify the driving physics and understand the relationships between structure and property before leading to materials design for potential applications. The performance of a material depends on the properties that it displays, which is determined heavily by its structural morphology. Therefore, it is important to first understand the structure of the materials and then correlate it with its overall properties. This dissertation will focus on the analysis of the morphology and property relationships in rubber and plastics. More specifically, the structure of natural rubber (NR) and polyethylene (PE) will be analyzed using synchrotron X-ray scattering techniques.

1.1 Introduction to Natural Rubber

Natural rubber (NR) is one of the most important natural resources in the world and is a vital raw material for industrial applications due to its excellent physical properties, such as elasticity, heat dispersion, and resistance to wear and tear. The global average annual NR production is about 11.5 million tons per year. NR is used in the manufacture of more than 40,000 products, especially as a key ingredient in automotive tires, dipped goods (medical and surgical items, gloves, balloons), rubber bearings, and adhesives[1-2]. Figure 1.1 shows the emerging applications for elastomers to 2017. More than 50% of NR is used in automotive tires and is therefore, essential to the national defense. NR has superior physical properties as compared to synthetic polyisoprene rubber (IR). This is attributed to the difference in their chemical structures and composition.

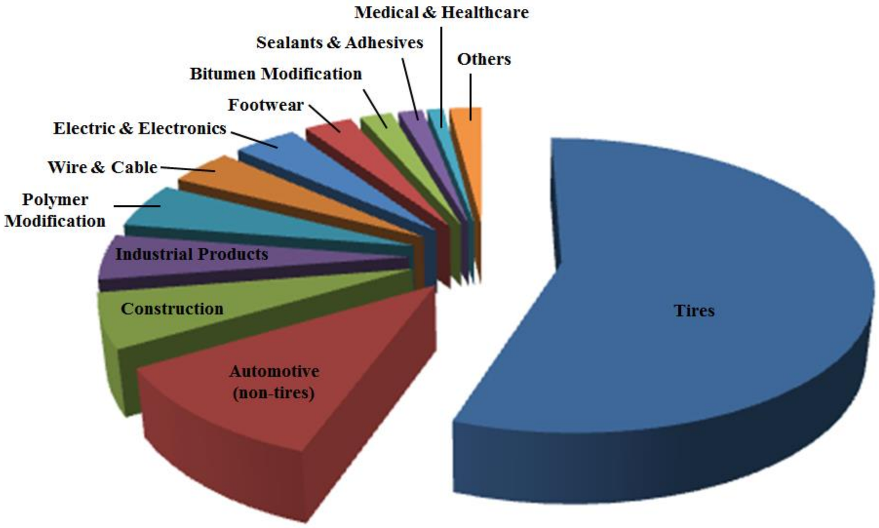

Figure 1.1 Emerging applications for elastomers to 2017.[3]

.

1.1.1 Structure of Natural Rubber

The main chemical unit of natural rubber is *cis*-1,4-polyisoprene as shown in Figure 1.2. NR is composed of 94% (by weight) *cis*-1,4-polyisoprene chains and 6% of the non-rubber components, including 2-3% proteins, 1-1.5% fatty acids, and 1-1.5% phospholipids[4-6]. A NR chain contains two different functional groups that are located at each individual ends of their chain: an α- and ω-terminal. These functionalized chain ends are postulated to interact with the non-rubber components to form a naturally occurring network (or pseudo-network) as shown in Figure 1.3. The α-terminal consists of mono- or di-phosphate groups that are linked with phospholipids, where networks can be formed between rubber chains. The ω-terminal is postulated to contain dimethyallyl units linked with a functional group to interact with the proteins and to form cross-linking networks through intermolecular bonding.

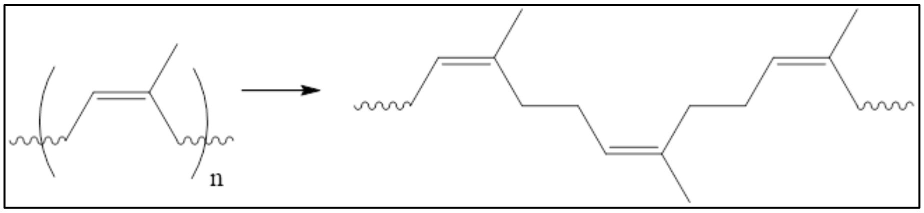

Figure 1.2 Chemical structure of natural rubber: *cis*-1,4-polyisoprene.

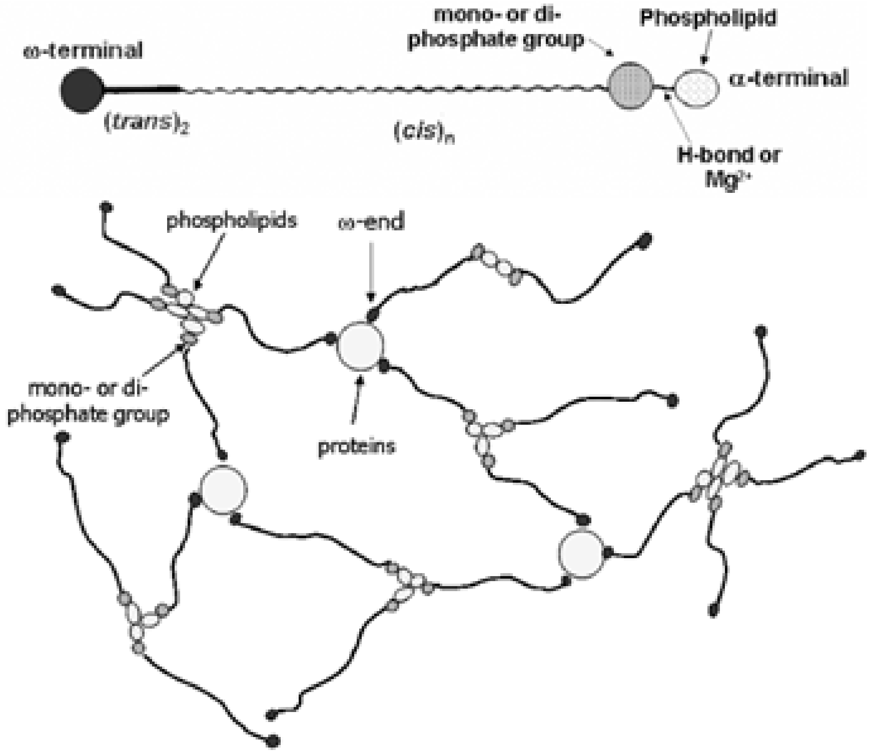

Figure 1.3 Proposed structures of a linear rubber chain and the naturally occurring network in NR.[5]

1.1.2 Natural Rubber Latex

All commercially-available NR is harvested from a single plant species called *Hevea Brasiliensis*. Natural rubber latex is defined as the stable dispersion of polymer micro-particles in an aqueous medium[7], or simply "rubber particles in water." Direct tapping of *Hevea Brasiliensis* barks produces a milky-white rubber latex emulsion that contains 40-45% rubber particles, 50-55% water, and 6% non-rubber components. Figure 1.4 shows the current concept on the structure of NR latex particles[8]. Rubber chain molecules are located inside the latex particle. Rubber chain polymerization takes place inside each individual latex particle, where intra-molecular cross-linking densities are formed. Furthermore, latex particles have a double layer of phospholipids and proteins, which can allow inter-particle interactions and inter-molecular network, can be formed between latex particles. The latex particles vary in sizes from 0.01 to 10 μm. The interactions of these latex particles will be discussed in detail in Chapter 2.

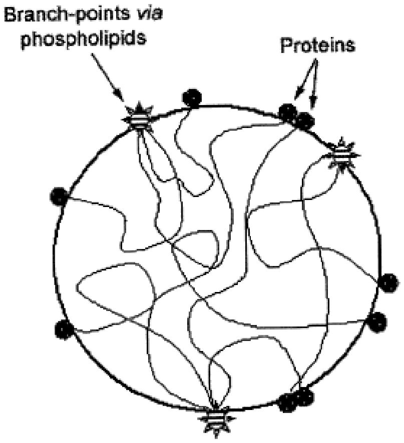

Figure 1.4 Structure and composition of natural rubber latex particles.[8]

1.1.3 Comparison Between Natural Rubber and Synthetic Polyisoprene Rubber

The different behaviors of NR and IR have been elucidated using several concepts. It has been well known that the superior properties and performance of NR as compared to IR are attributed to the presence of the pseudo-network in NR. In other words, certain non-rubber components play an essential role in determining the properties and performance of NR. Table 1.1 summarizes the composition of NR and IR. IR contains only *cis*-1,4-polyisoprene chains and do not possess any of the non-rubber components, and hence, there is a limited network in IR. In addition, the stereochemistry of the *cis*-1,4-polyisoprene is different between NR and IR. NR is composed of 100% *cis*-1,4 conformation, whereas the highest *cis*-1,4 conformation content in IR is composed of 98.5%. From gel permeation chromatography (GPC), the average molecular weights of the rubber chains in NR and IR are similar as shown in Figure 1.5, with values around $1x10^6$ g/mol. However, the molecular weight distributions are different. NR typically shows a bimodal distribution that is attributed to two different populations of average molecular weights resulting from the broad range of different size latex particles.

Natural Rubber (NR)	**Synthetic Rubber (IR)**
94% Polyisoprene (PI)	100% PI
3.4% Phospholipids and Fatty Acids	---
2.2% Proteins	---
0.4 % Carbohydrates and Metal Salts	---
100% *cis*-1,4-PI content	98.5% *cis*-1,4-PI

Table 1.1 Composition of natural rubber (NR) and synthetic polyisoprene rubber (IR).

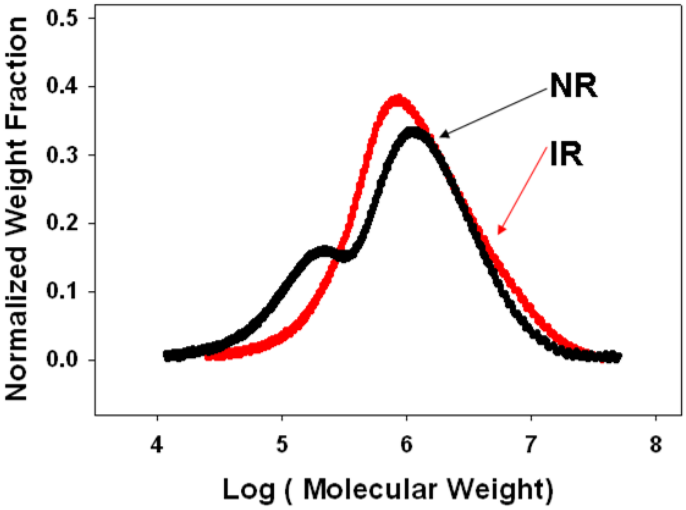

Figure 1.5 Molecular weight distribution of NR and IR determined from gel permeation chromatography.

1.1.4 Natural Rubber Derivatives

The non-rubber components in NR play an important role in the determination of its overall mechanical properties. The pseudo-network in NR can be chemically removed as shown in Figure 1.6.

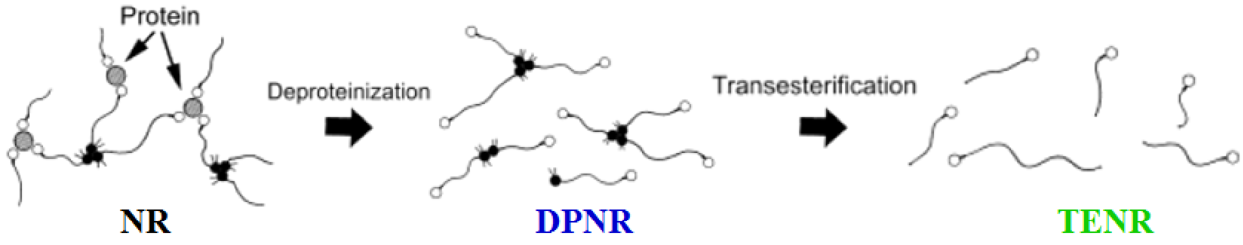

Figure 1.6 Removal of non-rubber components in NR.[6]

Deproteinization is the process to extract proteins from NR. This removes the protein interactions at the ω-terminal and breaks down the pseudo-network in NR. Deproteinized NR (DPNR) can be obtained by incubation of 30% w/v NR latex with 0.04% w/v proteolytic enzyme (KAO KP-3939) and 1% w/v Triton X-100 for 12 hours at 37 ˚C, followed by centrifugation at 13,000 revolutions per minute (rpm) for 30 minutes. After centrifugation, two phases are obtained: sol and cream. The sol fraction (or serum) contains the water soluble components, including proteins. The cream fraction contains the water-insoluble, rubber micelles. Figure 1.7 shows the centrifugation of NR latex[9]. About 50% of the soluble proteins can be removed from NR latex in the initial centrifugation. The cream fraction is then removed and re-dispersed in 0.5% w/v Triton X-100, followed by an additional centrifugation at 13,000 rpm for 30 minutes. The additional centrifugation can further remove the protein content.

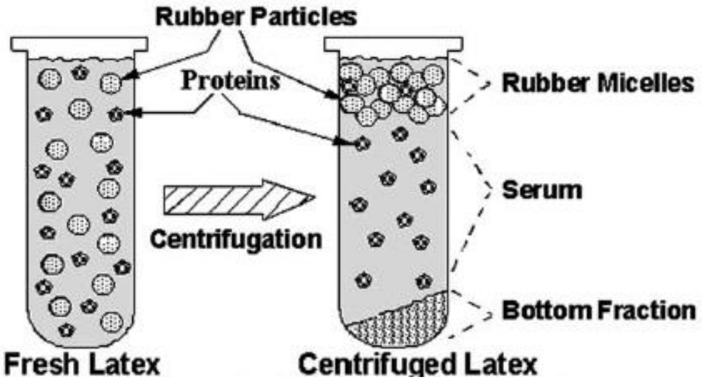

Figure 1.7 Centrifugation of NR latex.[9]

Transesterification, on the other hand, is the process to fully remove the non-rubber components in NR, including both the proteins and phospholipids. In this case, the interactions at both the α- and ω-terminals of NR are removed and the pseudo-network is completely destroyed. Transesterified NR (TENR) can be obtained by reacting NR with sodium methoxide in toluene at room temperature for 3 hours, followed by precipitation using an excess amount of methanol.

The protein and phospholipid contents in NR, DPNR, and TENR have been previously measured by Amnuaypornsri et al.[5] and are summarized in Table 1.2. The protein content was characterized by the nitrogen content, which was measured using a Leco Nitrogen Analyzer. The phospholipid content was characterized by the fatty acid and ester content, which was measured using Fourier Transform Infrared Spectroscopy (FTIR). The ester content was determined from the intensity ratio of peaks at 1739 cm^{-1} (C = O) to 1664 cm^{-1} (C = C). In addition, Table 1.2 includes the gel content of the samples, which were determined by toluene solubility measurements and estimated using the theory of rubber elasticity[28]:

$$\sigma = \upsilon k T(\alpha - \alpha^{-2}) \tag{1.1}$$

where σ is the stress measured by force per unit area, υ is the cross-link density that measures the number of network chains in unit volume, *k* is the Boltzmann constant, T is the absolute temperature, and α is the elongation ratio. The υ can be obtained from the slope of the linear plot of σ versus $(\alpha - \alpha^{-2})$.

As observed from Table 1.2, in DPNR, the nitrogen content is reduced to zero and the ester content remains the same as NR. The deproteination process successfully removes only the protein content. The gel content is significantly reduced as compared to NR, however, the gel content still remains. This indicates that there is still network present in DPNR, which is attributed to the phospholipid interactions at the α-terminal. In TENR, the nitrogen, ester, and gel content all reduce to zero. The transesterification process successfully removes the proteins and phospholipids at both terminals of NR, and hence, the pseudo-network is completely destroyed. The lack of non-rubber components and network in TENR closely resembles that of IR.

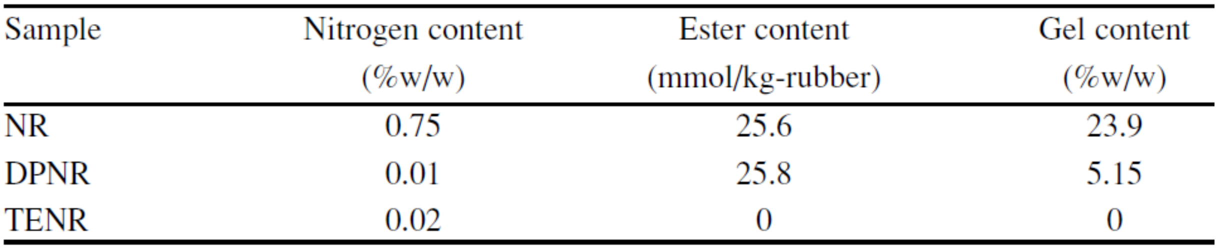

Sample	Nitrogen content (%w/w)	Ester content (mmol/kg-rubber)	Gel content (%w/w)
NR	0.75	25.6	23.9
DPNR	0.01	25.8	5.15
TENR	0.02	0	0

Table 1.2 Characterization of proteins and phospholipids in un-vulcanized NR, DPNR, and TENR.[5]

1.1.5 Effect of Natural Rubber Derivatives on its Mechanical Properties

Stress-strain relationships under uniaxial deformation are a basic measurement of rubber goods. Figure 1.8 shows the stress-strain relationships of NR, DPNR, TENR, and IR. The tensile strength, modulus, and absolute stress values are greater in NR as compared to DPNR, and the values for TENR closely resemble that of IR. It can clearly be seen that the removal of each constituent of the non-rubber component diminishes the pseudo-network in NR, and hence a reduction in the stress values.

NR shows an upturn of stress at higher deformation around strain 3.0, which is attributed to the presence of the pseudo-network and strain-induced crystallization (SIC), which will be discussed in detail in a later section. Although a minimal effect, the upturn of stress is also observed in DPNR. This indicates that a network still remains in DPNR, which is consistent with the gel content as shown in Table 1.2. The removal of only proteins does not fully destroy the pseudo-network in NR. On the other hand, the upturn of stress is not observed in TENR and IR, which is an indication of the lack of a network. IR is a polymer melt that shows a viscous response with yield stress that is related with entanglements[10].

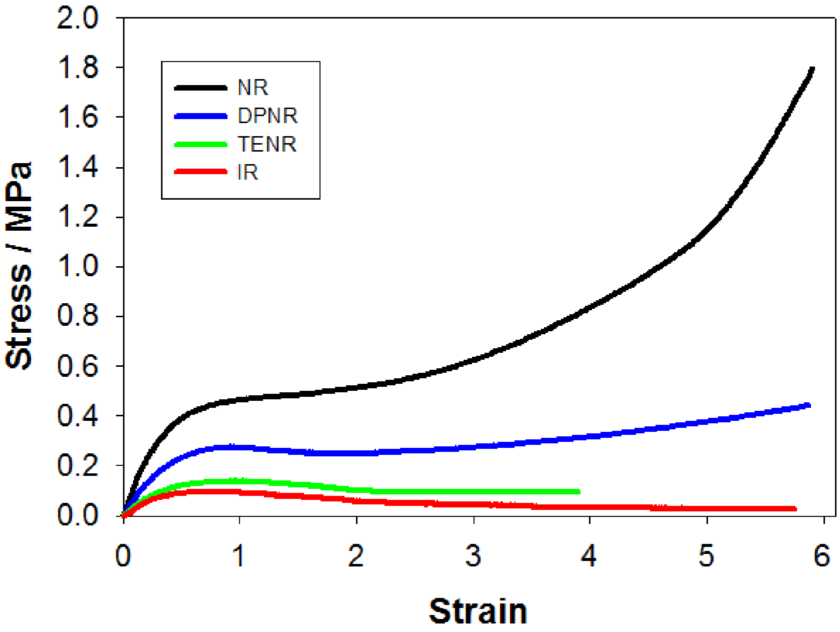

Figure 1.8 Stress-strain relationships during stretching and relaxation of NR, DPNR, TENR, and IR.

1.1.6 Rubber Vulcanization

Vulcanization is the most important process in the rubber manufacturing process. It was first discovered in the early-to-mid 1800s by Charles Goodyear. Vulcanization is a chemical process for converting rubber into more durable materials with superior mechanical properties by the addition of curatives to form crosslinks between rubber chains. Typical curing systems used in rubber vulcanization are sulfur and peroxide. Figure 1.9 shows a representation of the (a) sulfur and (b) peroxide vulcanization of rubber chains. Sulfur vulcanization is the process by which an olefin and sulfur reacts to increase the mechanical properties of rubber. Vulcanization takes place by forming sulfur bridges between polymer chains. These bridges can be composed of mono-, di-, or poly-sulfur molecules. Polymer chains of un-vulcanized rubber are cross-linked by sulfur bridges to give a three dimensional network, which is the main reason for the increase in elasticity of the vulcanized product. Peroxide vulcanization, on the other hand, is formed by free-radical reactions between peroxide and rubber chains. This creates C-C bonds that have higher energy than the C-S bonds in sulfur vulcanization, resulting in stronger bonds against heat and mechanical deformation. The vulcanization kinetics is much faster in peroxide as compared to sulfur and will be discussed in detail in Chapter 2. In addition, Chapter 2 will focus on the discussion of pre- and post-vulcanization, which are two important processes used widely in the rubber industry.

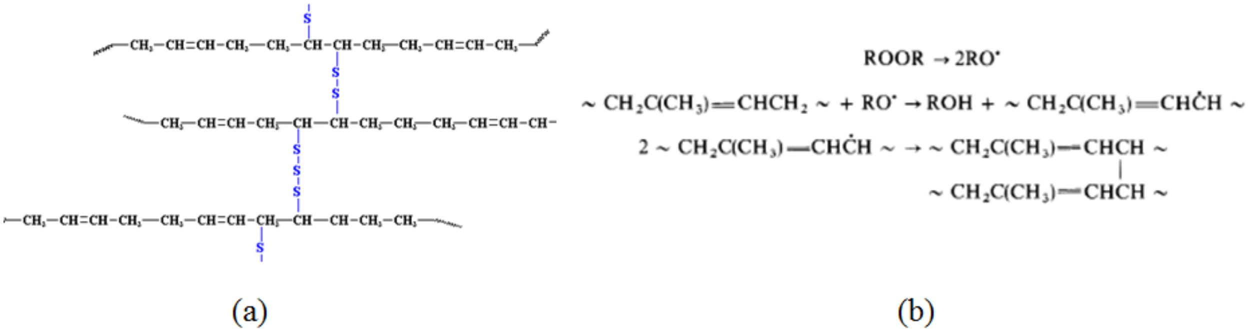

(a) (b)

Figure 1.9 (a) Sulfur[11] and (b) peroxide[12] vulcanization of rubber chains.

1.1.7 Strain-Induced Crystallization

The induction of strain-induced crystallization (SIC) in NR is believed to be primarily responsible for the outstanding properties in NR, such as outstanding tensile strength, tear strength, cut resistance, and durability. The underlying mechanism is believed to be due to the pseudo-network and the non-rubber components-polymer interactions in NR. The inhomogeneity of cross-linked topology in NR leads to a microfibrillar structure composed of crystalline segments between the cross-links during stretching[4], as shown in Figure 1.10. The strain-induced crystallites are highly oriented with excellent alignment along the stretching direction.

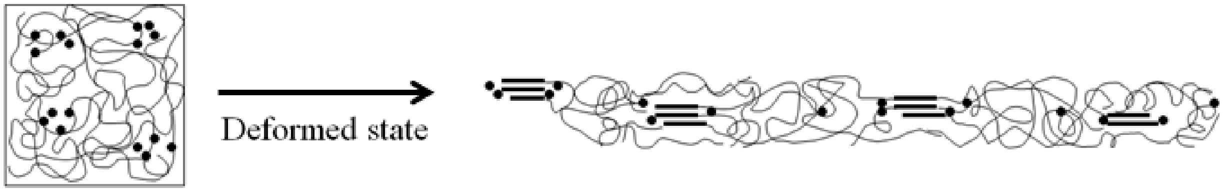

Figure 1.10 Strain-induced crystallization in a uniaxial deformed NR sample.[4]

Flory[13-14] proposed that SIC contributes to the stress in stress-strain relations. Chains that are deformed to their limit of extensibility make crystals. The length of a strain-induced crystallite chain is longer as compared to an oriented amorphous chain. The longer chain in a crystal (along the stretched direction) makes the amorphous chain relax. This mechanism decreases the stress and is one of the main contributions for the observed plateau at around strain 1.5 in Figure 1.8. In addition, SIC becomes giant network points that increase the stress, which contributes to the upturn of stress at higher strains[15].

Deformation along with *in-situ* synchrotron wide-angle X-ray diffraction (WAXD) has been recently used to study the development of molecular structures in rubber. Figure 1.11 shows WAXD patterns obtained at 25 ˚C for NR, DPNR, TENR, and IR at strain 0 and strain 6. Prior to deformation at strain 0, NR exists as a non-crystalline, amorphous polymer as indicated by the scattering ring. An external force is needed to deform the sample in order to induce crystallization as observed by the highly oriented crystal reflections at strain 6. Figure 1.12 quantitatively shows the SIC contents with respect to strain for NR, DPNR, TENR, and IR. The crystal fractions increase with strain during deformation. The reduction of non-rubber components in NR results in a decrease of SIC content. A full removal of the non-rubber components in TENR results in very small amounts of SIC content, which resembles that of IR. IR does not crystallize at 25 ˚C. As shown in Figure 1.12, the maximum crystal fraction for un-vulcanized NR is only about 10%, which indicates that the fraction of amorphous chains is about 90%. In vulcanized NR, the maximum crystal fraction is about 25%, with about 75% in the amorphous state. This suggests that the NR system is very inhomogeneous. The properties of these strain-induced crystallites will be discussed in great details in Chapters 2-5.

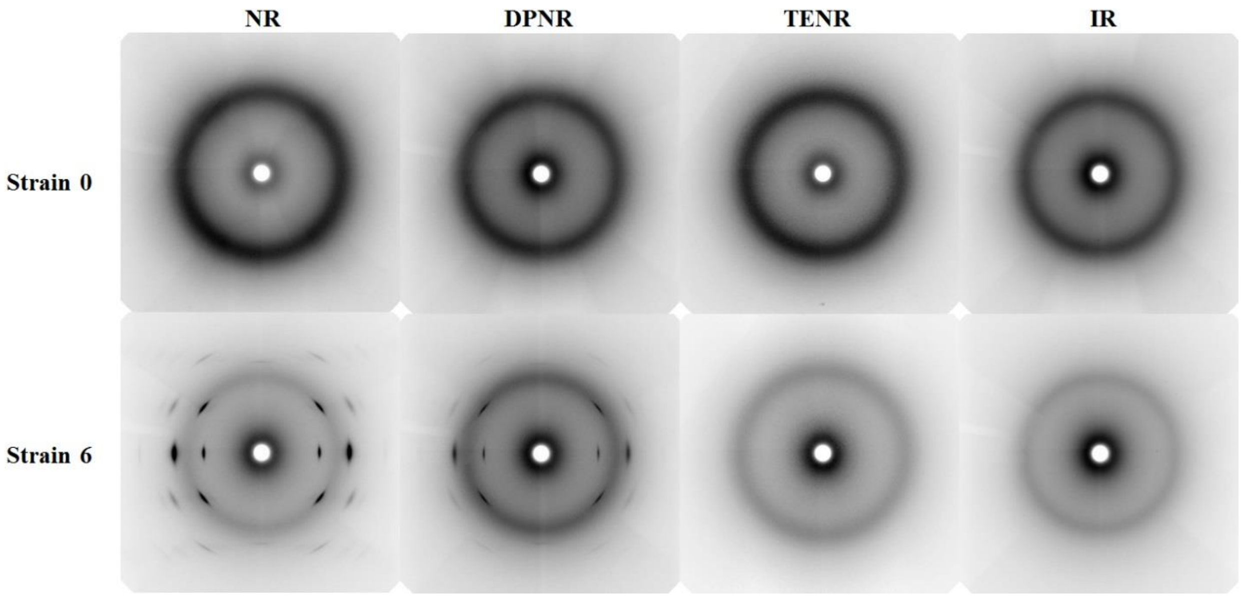

Figure 1.11 WAXD patterns obtained at 25 ˚C for un-vulcanized NR, DPNR, TENR, and IR at strain 0 and strain 6.

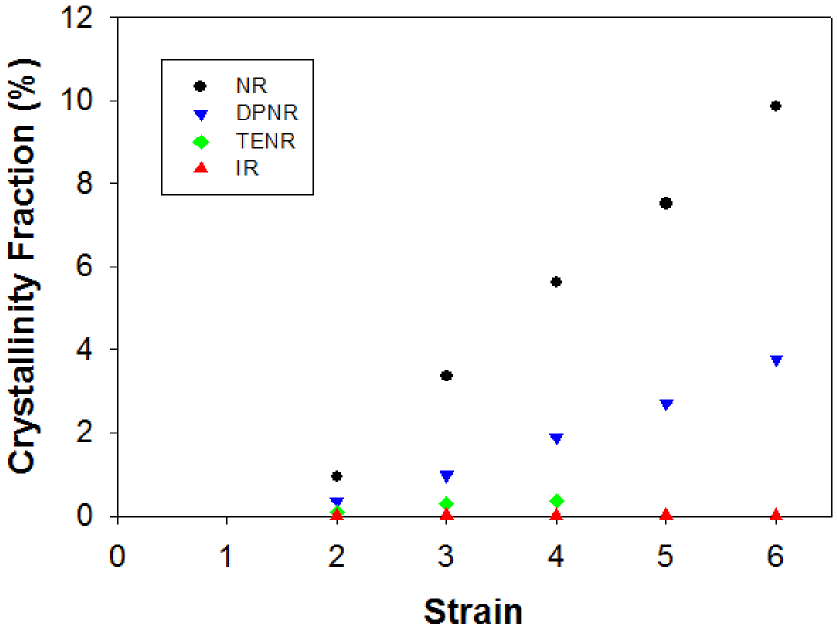

Figure 1.12 Strain-induced crystallization contents obtained at 25 ˚C for un-vulcanized NR, DPNR, TENR, and IR.

1.2 Introduction to Polyethylene

Polyethylene (PE) is the simplest hydrocarbon polymer, with the monomer unit ethylene, C_2H_4. It is the most widely used plastic with an annual production of about 90 million tons per year[16]. PE is a thermoplastic, semi-crystalline polymer that is used widely in diverse applications for bottles, bags, packaging, films, piping, laminates, cables and wires, liners, etc.[17] It has excellent toughness, impact resistance, stiffness, and processability. The properties of PE are determined and controlled by its structural morphology.

1.2.1 Semi-Crystalline Structure of Polyethylene

A summary of the structure of PE[18] is depicted in Figure 1.13. PE is a semi-crystalline polymer that consists of amorphous and crystalline phases that are packed together to form spherulitic structures. A spherulite consists of several lamellae that are separated by layers of amorphous and crystalline regions that are bounded together by tie-chains. The amorphous region is composed of disordered chains that are highly entangled. The crystalline region, on the other hand, is composed of highly ordered chains, where crystals are formed by folding chains alternately up and down and arranging the straight segments between folds into periodic arrays[19]. PE crystals, as shown in Figure 1.14, are reported[20-21] to be orthorhombic with lattice dimensions a = 7.41Å, b = 4.94 Å, and c = 2.55 Å. The crystalline regions have higher density as compared to the amorphous regions.

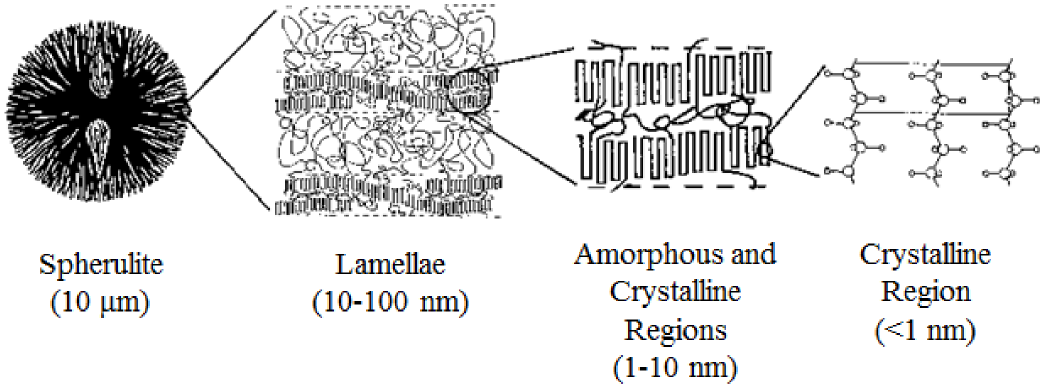

Figure 1.13 Structure of polyethylene: spherulite, lamellae, amorphous and crystalline regions.[18]

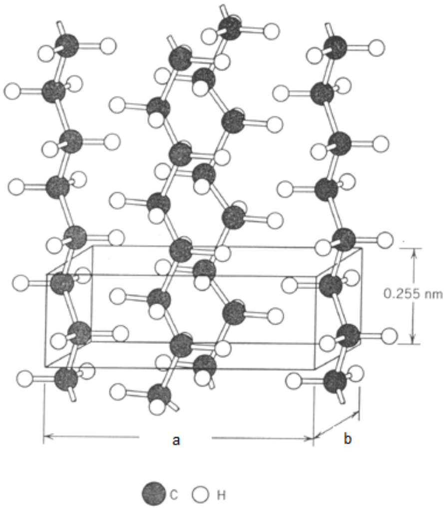

Figure 1.14 Orthorhombic crystal structure of polyethylene[20-21].

1.2.2 Different Density Systems of Polyethylene

The properties of PE depend on the overall chain lengths and the way monomers are ordered along the chain. The monomers in a polymer can be arranged in a number of different ways depending on the temperature, pressure, and catalyst conditions during polymerization. Figure 1.15 shows the linear, branched, or cross-linked arrangements in a polymer[19]. Linear polymers are made up of long continuous chains without any side attachments and are joined together at chain ends. Branched polymers occur by replacing some of the hydrogen atoms by covalently bonded polyethylene chains. A branched structure increases the tie-molecule (or tie-chain) density. Cross-linked polymers are made up when linear chains are joined to each other at various positions by covalent bonds, forming three-dimensional network molecules.

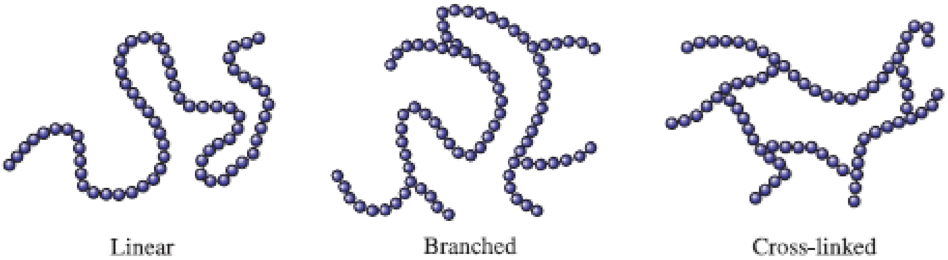

Figure 1.15 Linear, branched, and cross-linked arrangements in a polymer[19].

PE can be classified into several categories based on the density of the system. The difference in density of PE affects its overall properties, which can then be used in materials for various applications. An increase in density leads to an increase in tensile strength, stiffness, and hardness of the material. However, the increase in density leads to materials with a low impact strength and ductility. Table 1.3 summarizes the American Society for Testing and Materials (ASTM) and industrial polyethylene density-based classifications[19]. Low-density PE (LDPE) has long side chain branches on 1.5 to 2.5% of the carbon atoms. Therefore, the structure is dominated by the amorphous phase with crystallinity around 40-60%. These materials are mostly used in food and industrial packaging. Medium-density PE (MDPE) has crystallinity around 50-70%, and this material is used mostly in gas and water pipes. High-density PE (HDPE) has linear structures with very few branched chains, and the molecules are aligned into more compact arrangements with 60-80% crystallinity. HDPE is used in bags, bottles, containers, piping, and disposable goods. Ultra-high molecular weight PE (UHMWPE) has a very high crystalline structure around 85% that led to its outstanding modulus and toughness. This material is used mostly in applications for machinery parts, gears, and bearings.

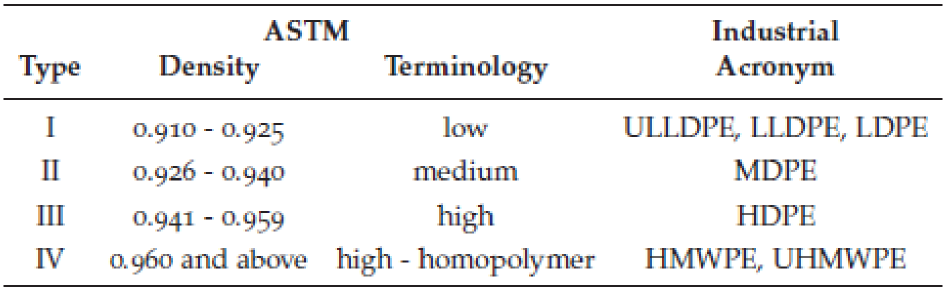

	ASTM		Industrial
Type	Density	Terminology	Acronym
I	0.910 - 0.925	low	ULLDPE, LLDPE, LDPE
II	0.926 - 0.940	medium	MDPE
III	0.941 - 0.959	high	HDPE
IV	0.960 and above	high - homopolymer	HMWPE, UHMWPE

Table 1.3 ASTM and industrial polyethylene density-based classification[19].

1.2.3 Deformation Mechanism in Polyethylene

Figure 1.16 shows a typical stress-strain curve for a thermoplastic, semi-crystalline polymer[22]. The yield point is also known as the local maximum in the stress-strain curve. Prior to the yield point, the material deforms elastically and the slope of this region is defined as the

Young's modulus. After the yield point, the material deforms inelastically and undergoes permanent plastic deformation until the breaking point. This is usually associated with a sharp necking of the materials. The ultimate tensile strength can be obtained at the maximum stress before breaking.

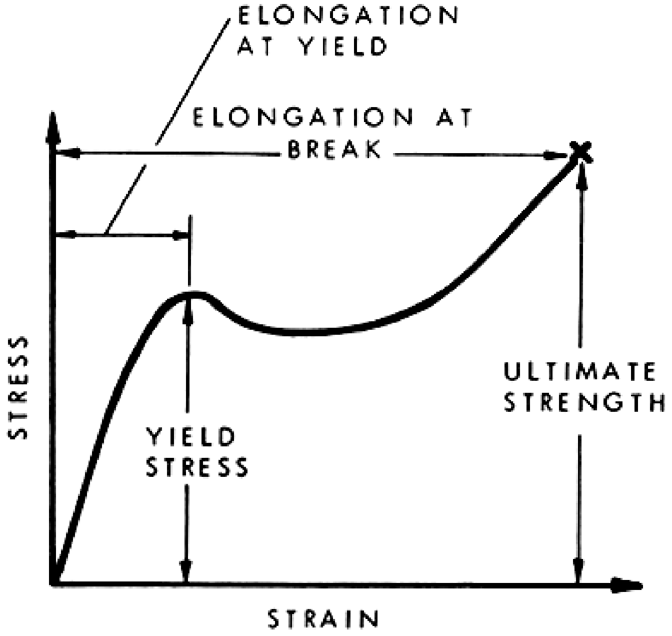

Figure 1.16 Typical stress-strain curve of a thermoplastic, semi-crystalline polymer[22].

The yielding phenomenon is associated with a change in the morphology from a spherulitic structure into a fibrillar structure[23-26]. The change occurs through shearing and fragmentation of the crystalline lamellae into blocks that rearrange to form parallel microfibrils. Figure 1.17 shows the proposed deformation mechanism in PE[27]. The elastic zone (up to the yield point) is attributed to an initial structural rearrangement by mechanical twinning and rotation. After the yield point, an initial decrease followed by an increase in stress is observed in the plastic zone. The onset of plastic deformation accompanied with the decrease in stress is attributed to intralamellar slippage, crystallographic slip, and deformation of the lamellar stacks. Finally, the increase in stress in the plastic deformation is attributed to strain hardening. The changes in the lamellae, crystalline and amorphous phases during deformation of PE have been characterized by using small-angle X-ray scattering (SAXS) and wide-angle X-ray diffraction (WAXD) and is discussed in detail in Chapter 5.

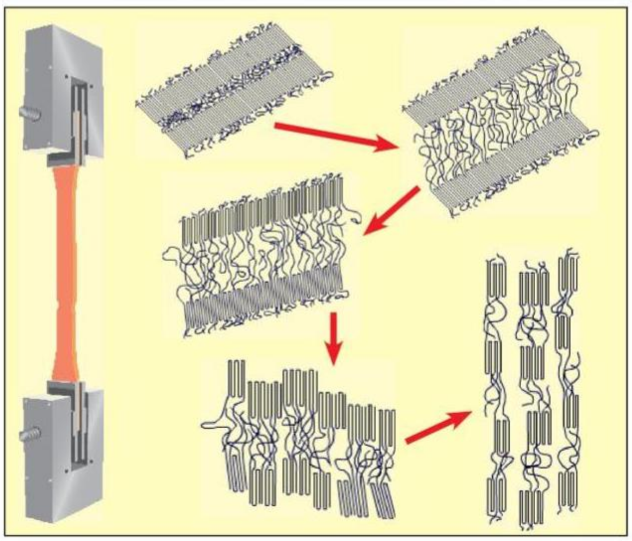

Figure 1.17 Proposed deformation mechanism in PE[27].

1.3 Chapter Contents

In industry, it is crucial to first identify the driving physics and understand the relationships between structure and property before leading to material design for potential applications. Therefore, it is important to first understand the structure of the materials and then correlate it with its overall properties. This thesis is divided into a total of 8 chapters. Chapters 2 through 5 discuss the morphology and property relationships in NR. Chapters 6 and 7 focus on the morphology and property relationships in PE.

- Chapter 2 focuses on the chain dynamics and SIC of vulcanized NR using Double-Quantum Nuclear Magnetic Resonance (DQ NMR) and WAXD. The interactions of the latex particles in pre- and post-vulcanized NR latex will be analyzed.
- Chapter 3 focuses on the stress-strain relations of unvulcanized and vulcanized NR at various temperatures from -50 to 75 ˚C. The effect of entanglements, pseudo end-linking

networks, chemical bond networks, and SIC on different parts of the stress-strain plot will be discussed.

- Chapter 4 focuses on the analysis of strain-induced crystallites of NR and IR. Here we present a novel 2D simulation to analyze WAXD patterns and obtain information about the crystallites. Properties of crystallites will be discussed, including crystal structure, crystallite size, fraction, orientation, and displacement disorder.
- Chapter 5 focuses on the SIC of un-vulcanized and vulcanized NR at various temperatures from -50 to 75 ˚C. The novel 2D WAXD simulation method presented in Chapter 4 will be applied here to understand the influence of temperature on SIC.
- Chapter 6 focuses on the plastic deformation of PE using experimental and atomistic simulations. The ability to define the deformation behavior of PE at room and at high temperatures through simulation will offer unique opportunities to examine the effect of the interlamellar amorphous topology on PE deformation.
- Chapter 7 focuses on solvent swelling of HDPE and LLDPE. Morphological changes in the lamellar structure will be analyzed using a two-phase stacking model and a 2D correlation analysis.
- Chapter 8 summarizes the conclusions of presented research and recommendations for future work.

1.4 References

1. Cornish, K. *Nat. Prod. Rep.* **2001**, *18*, 182
2. Cornish, K. "*Alternative Rubber Production*." Tire Technology Expo 2011, Cologne, Germany, **2011**
3. Smithers Rapra, Emerging Applications for Elastomers to 2017
4. Toki, S.; Sics, I.; Ran, S.; Liu, L.; Hsiao, B. S.; Murakami, S.; Senoo, K.; Kohjiya, S. *Polymer* **2003**, *44*, 6003
5. Amnuaypornsri, S.; Sakdapipanich, J.; Toki, S.; Hsiao, B. S.; Ichikawa, N.; Tanaka, Y. *Rubber Chem Technol.* **2008**, *81*, 753

6. Tanaka Y. *Rubber Chem Technol*. **2001**, *74*, 355
7. Encarta World English Dictionary, Bloomsbury Publishing Plc.: latex **2009**
8. Amnuaypornsri, S.; Sakdapipanich, J.; Tanaka, Y. *J. Appl. Polym Sci. Appl Polym.*, **2009**, *111*, 2127
9. Perrella, F. W.; Gaspari, A. A. *Methods*, **2002**, *27*, 77
10. Amnuaypornsri, S.; Toki, S.; Hsiao, B. S.; Sakdapipanich, J. *Polymer* **2012**, *53*, 3325
11. Diene Polymers, Polymer Sci, University of Southern Miss
12. L. Loan, Peroxide Crosslinking Reactions in Polymers, Bell Laboratories
13. Flory, P. J., *J. Chem. Phys.* **1947**, *15*, 397
14. Flory, P. J., Principles of Polymer Chemistry Cornell University Press, **1953**
15. Toki, S.; Che, J.; Rong, L.; Hsiao, B. S.; Amnuaypornsri, S.; Nimpaiboon, A.; Sakdapipanich, J. *Macromolecules*, **2013**, *46*, 5238-5248
16. Piringer, O. G.; Baner, A. L. *Plastic Packaging: Interactions with Food and Pharmaceuticals* **2008**, 2nd edition, Wiley-VCH
17. UL IDES, Polyethylene Plastic
18. Polymer Research Laboratory, Crystallizable Block Copolymers, 2010, Department of Chemical and Biological Engineering, The Trustees of Princeton University
19. Contreras, J. A. A. **2007**, *Micromechanical modelling of polyethylene* (Doctoral Dissertation), University of Waterloo, Waterloo, Ontario, Canada
20. Bunn, C. W. *Transactions of the Faraday Society*, **1944**, *40*, 23
21. Bunn, C. W. *Journal of Appl Phy*, **1954**, *25*, 820
22. National Research Council Canada. Properties and Behavior of Plastics, **2005**
23. O'Connell, P.A.; McKenna, G. B. *Yield and Crazing in Polymers*. Encyclopedia of Polymer Science and Technology (John Wiley & Sons, 2004)
24. Ward, I. M. *Mechanical Properties of Solid Polymers*, 2nd ed. (Wiley, New York, 1990)
25. Schultz, J. *Polymer Materials Science* (Prentice-Hall, Englewood Cliffs, 1974)
26. Uribe, A. R.; Manzur, A.; Olayo, R. *J. Mater. Res.*, **2012**, *27*, 1351
27. Essentials of Polymer Science & Engineering, Painter & Coleman, p.236
28. Treloar, L. R. G. "The Physics of Rubber Elasticity," Oxford University Press, London (1975)

(Chapter 2 reproduced with permission from *Macromolecules*, *45*, 6491-6503. Copyright **2012**. American Chemical Society.)

Chapter 2

Chain Dynamics and Strain-Induced Crystallization of Pre- and Post-Vulcanized Natural Rubber Latex Using Proton Multiple Quantum NMR and Uniaxial Deformation by In-Situ Synchrotron X-Ray Diffraction

2.1 Introduction

Vulcanized rubber has been a subject of intensive research interest since the 1940s[1,2]. However, it is only recently that NR latex has gained significant research interest in the rubber industry. It has been well known that natural rubber has superior strength as compared to synthetic rubber. In order to fully synthesize a rubber that can resemble the mechanical properties of NR, it is essential to begin at the fundamentals and start at the rubber latex state. As discussed in Chapter 1, NR latex is defined as the stable colloidal dispersion of polymeric particles in an aqueous medium[3], or simply "rubber particles in water." Rubber latex is derived from the sap of the *Hevea Brasiliensis* tree[4] and is composed of 30-40% rubber particles, 55-65% water, and about 6% non-rubber components, including proteins, fatty acids, phospholipids, etc. The proteins and phospholipids create the outside layer of the rubber particles, and the rubber chain molecules are located inside those particles[5].

Pre-vulcanization, drying/water evaporation (or film formation), and post-vulcanization are the most important processes in the rubber industry. They modify the rubber network structure and define their overall mechanical properties. Therefore, it is necessary to understand what truly happens during these processes in order to correlate network structure with the physical properties of rubber. In pre-vulcanization, it has been postulated that the process takes place inside the rubber particles that are dispersed in water.[3] A homogeneous solution containing natural rubber latex, activators, cure agents, antioxidants, and surfactants is mixed altogether. Vulcanization of rubber particles occurs inside each individual rubber particle, creating independent and non-connected cross-linked rubber particles (with a given network structure inside the rubber particle) dispersed in water. After pre-vulcanization, water is removed and the previously cross-linked particles become closer until they interact forming a coherent film. In post-vulcanization, excess chemicals and water-soluble proteins are further removed by heating up the films at high temperatures. The mechanism of each of these states is the main focus of this paper and will be analyzed using Double-Quantum Nuclear Magnetic Resonance (DQ NMR), also referred to as Multiple-Quantum (MQ) NMR, and wide-angle x-ray diffraction (WAXD).

DQ NMR is a powerful tool that can provide quantitative information regarding polymer network structure. More specifically, DQ NMR experiments are sensitive to the residual dipolar couplings (RDC) and their distributions, which can yield information on the number of cross-links and the spatial cross-links distribution. The existence of residual dipolar couplings (when the polymer is far away its characteristic T_g) on polymer networks is due to the presence of cross-links and entanglements that restrict fast segmental fluctuations, leading to non-isotropic orientation fluctuations that can be detected by using DQ-experiments.[6] The specific details of this procedure and analysis are discussed elsewhere.[6-8]

Deformation along with in-situ synchrotron X-ray scattering has been recently used to study the development of molecular structures in rubber. It has been well demonstrated that the roles of both molecular orientation and strain-induced crystallization are primarily responsible for the outstanding mechanical properties in natural rubber. The inhomogeneity of cross-linked topology in vulcanized natural rubber leads to a microfibrillar structure composed of crystalline segments between the cross-links (vulcanized points) during stretching.[1] The objective of this chapter is to study the structural development in un-vulcanized and vulcanized natural rubber latex in a relaxed state and under deformation by DQ NMR and synchrotron X-rays in both pre- and post-vulcanization states. DQ NMR studies the fluctuations of molecules at more local length scales, whereas synchrotron X-rays can analyze network structures at much larger length scales. The combination of both of these techniques can provide a considerable amount of information regarding rubber network structure.

2.2 Experimental Methods

2.2.1 Rubber Latex Samples

Recipes and cure conditions for rubber latex samples vulcanized with sulfur and peroxide are listed in Table 2.1 and Table 2.2, respectively. There were a total of 14 samples: latex, latex with heat treatment at 130 ˚C for 30 minutes, both sulfur and peroxide vulcanized latex at 60 ˚C for several hours depending on each sample's cure time (so-called pre-vulcanization) and samples that after several hours of pre-vulcanization and the subsequent film formation were submitted to an additional heating step at 130 ºC for 30 minutes (so-called post-vulcanization). For each sample, the optimum pre-vulcanization time (in latex-state) was determined by using proton Multiple-Quantum NMR (MQ NMR) spectroscopy carried out in an inexpensive low-field spectrometer.[8]

Dipentamethylenethiuram Tetrasulfide (DPTT) was used as the sulfur source for vulcanization at three different concentrations: 0.75, 1.50 and 2.25 parts per hundred of rubber (phr) (denoted as DPTT 0.5, 1.0, and 1.5 for pre-vulcanized latex, and 0.5, 1.0, and 1.5 PostV for post-vulcanized latex respectively). DPTT is an accelerator that has very active sulfur groups and good heat resistance. It is an excellent vulcanizing agent for latex.[9]

For pre-vulcanized latex with DPTT, a homogeneous dispersion containing natural rubber latex, activator (ZnO), cure agent (DPTT), antioxidant and dispersants is mechanically stirred together during the pre-vulcanization process. A commercial antioxidant named Wingstay-L was used to prevent the high temperature degradation of latex samples. The surfactants such as casein, Darvan 1 and potassium hydroxide were used to obtain a stable dispersion of DPTT, ZnO and antioxidant in water, whereas potassium caprilate gives better mechanical stability. The resulting dispersion was then stirred and heated at 60 ºC for various hours, depending on the sample's cure time, in order to vulcanize the individual rubber particles dispersed in water. Subsequently the pre-vulcanized samples were poured onto a glass petri-dish and the dispersion was dried overnight at room temperature, allowing further removal of water and film formation. However, some water still remains in the film, but in very small quantities. After a few days, the weight of the film was constant. Preparation of post-vulcanized samples included, after pre-vulcanization reaction and film formation, an additional heating at 130 ºC for 30 minutes. The thicknesses of all the films were around 1 mm after water evaporation.

Pre- and post-vulcanized latex with peroxide samples were prepared with the same methodology described previously. Tert-butyl hydroperoxide was used as the peroxide vulcanizing agent at three different concentrations: 0.6, 1.2 and 1.8 phr (denoted as Peroxide 0.6, 1.2, and 1.8 for pre-vulcanized latex, and Per 0.6, 1.2, and 1.8 PostV for post-vulcanized latex respectively). Activators and dispersants, including Iron (III), fructose and potassium caprilate, were used to prepare these samples. No antioxidants were added to the peroxide vulcanized samples.

For un-vulcanized latex and latex with post-heat treatment, no additives were mixed with the samples. The only difference between these two samples was that latex after film formation underwent an additional heat treatment at 130 ºC in order to compare it with the post-vulcanized samples. Both of these samples served as a control.

Table 2.1 Recipes and Curing Conditions for Rubber Latex Samples Vulcanized with DPTT

	Latex	**Latex Post-Heat Treatment**	**Latex DPTT 0.5**	**Latex DPTT 1.0**	**Latex DPTT 1.5**	**Latex DPTT 0.5 Post-V**	**Latex DPTT 1.0 Post-V**	**Latex DPTT 1.5 Post-V**
Pre-vulcanization (Cure Time)	No	No	Yes (18 hrs)	Yes (15 hrs)	Yes (11 hrs)	Yes (18 hrs)	Yes (15 hrs)	Yes (11 hrs)
Post-vulcanization (Cure Time)	No	Yes (30 mins)	No	No	No	Yes (30 mins)	Yes (30 mins)	Yes (30 mins)
DPTT, phr	No	No	0.75	1.50	2.25	0.75	1.50	2.25
ZnO,phr	No	No	0.30	0.60	0.90	0.30	0.60	0.90
Wingstay-L, phr	No	No	0.23	0.47	0.70	0.23	0.47	0.70
Dispersants	No	No	Potassium caprilate, casein, Darvan 1, KOH					

Table 2.2 Recipes and Curing Conditions for Rubber Latex Samples Vulcanized with Peroxide

	Latex Peroxide 0.6	**Latex Peroxide 1.2**	**Latex Peroxide 1.8**	**Latex Per 0.6 Post-V**	**Latex Per 1.2 Post-V**	**Latex Per 1.8 Post-V**
Pre-vulcanization (Cure Time)	Yes (3 hours)					
Post-vulcanization (Cure Time)	No	No	No	Yes (30 mins)	Yes (30 mins)	Yes (30 mins)
Tert-butyl hydroperoxide, phr	0.60	1.20	1.80	0.60	1.20	1.80
Activators	Iron (III), fructose					
Wingstay-L, phr	No					
Dispersants	Potassium caprilate					

2.2.2 Time-Domain NMR Measurements

Different time-domain proton NMR experiments under static conditions were carried out at 60 ºC (the optimum temperature for the analyzed samples) on a Bruker minispec mq20 spectrometer operating at 0.5 T with 90º pulses of 3 µs length and dead time of 11 µs.

2.2.2.1 Saturation Recovery Experiments

Recycle delay time for all experiments was always fixed as r.d. = $5T_1^{polymer}$, where $T_1^{polymer}$ is the spin-lattice relaxation time of the polymer as measured by saturation recovery experiments. This followed the same experimental procedure that was used to characterize hydrogels[10] because of its similarity with latex. This analysis (shown in Figure 2.1A) is important in rubber latexes because it allows the quantitative characterization of solid-like fractions (characterized by shorter spin-lattice relaxation time $T_1^{polymer}$ ~ 100 ms) dispersed in the liquid media (e.g. water with T_1^{water} ~ 2500 ms). As a consequence, this method could be considered a potential tool to be used in quality control measurements in the latex industry to more quickly (around 20 minutes) analyze the rubber content in latexes.

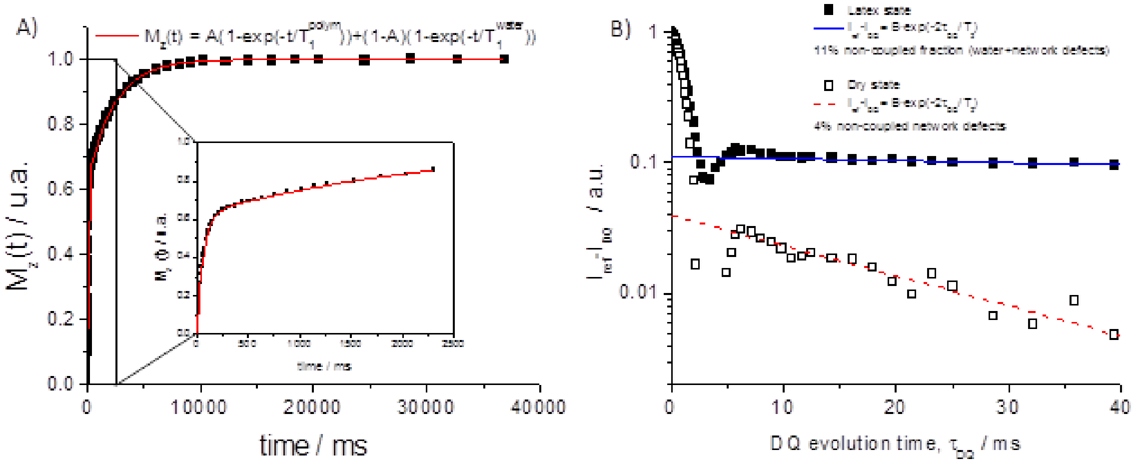

Figure 2.1 (A) Saturation recovery curve for NR latex state sample. Double exponential fits, where $M_z(t)$ is the longitudinal magnetization at the experiment time t and A represents the fraction of sample with solid-like behavior, were used to analyze the curves. (B) Identification and subtraction of non-coupled fraction tails in a latex sample after and before drying. In the latex samples, the non-coupled fraction is mainly composed by water (i.e. the small fraction of water that was magnetized caused by the short r.d. used in the experiments) and non-elastic network defects, whereas in dry samples, the slowly relaxed tails are mainly related with network defects.

2.2.2.2 ^{1}H DQ-NMR Experiments

Study of permanent network structure:

^{1}H DQ NMR experiments, based on enhanced Baum-Pines pulse sequences widely described elsewhere[6], were used to study the network structures of all samples in three different stages and states: pre-vulcanization in latex state, drying and film formation, and post-vulcanization. In order to analyze the network structure of rubber samples, the raw experimental data needs to be normalized in a way that the temperature-independent network structure effect (at temperatures far above the glass transition temperature) can be separated from the temperature dependent segmental dynamics. The initial raw data includes plots of the DQ build-up (I_{DQ}) and reference decay (I_{ref}) as a function of the DQ evolution time (τ_{DQ}). The sum of both components (I_{DQ} + I_{ref}) gives the full magnetization of the sample, which includes signals from dipolar coupled network segments (segments between constrains) and uncoupled isotropic mobile protons. Identification of both contributions is quite easy since coupled network segments typically relax faster than non-coupled protons (shown in Figure 2.1B). It is important to remark on the special characteristics of latex samples with respect to the usually analyzed rubber (in dry state) samples. Rubber networks usually contain non-elastic network defects (mainly dangling chains and loops), which are mainly responsible for the non-coupled slowly relaxing tails in DQ-experiments. In latex samples, rubber particles are dispersed in a water media, and therefore the non-coupled fraction of protons should be mainly composed of water (and small molecules dissolved or dispersed), which relax even slower than the non-elastic network defects. These tails were perfectly defined by a single exponential function and, after its subtraction, no evidence of additional non-coupled tails was observed.

Subtraction of the long-time contribution of the non-coupled fraction is needed to obtain the total MQ magnetization ($I_{\Sigma MQ}$) from the coupled segments (equation 2.1), which is dependent on chain dynamics:

$$I_{\Sigma MQ} = I_{DQ} + I_{ref} - Be^{-2\tau/T_2} \qquad (2.1)$$

where B is the non-coupled fraction of polymer chains and T_2 is the slow exponential decay factor of the non-coupled protons. The normalized DQ intensity (I_{nDQ}) is obtained by taking the ratio of the DQ intensity with respect to the total MQ magnetization (equation 2.2):

$$I_{nDQ} = I_{DQ} / I_{\Sigma MQ} \qquad (2.2)$$

This latter equation depends on the residual dipolar couplings (Dres), that reflects the long-time anisotropy arising from cross-links and topological constrains[11,12]. The proper analysis of I_{nDQ} provides quantitative information about the residual dipolar couplings (D_{res}) and their distribution. It was previously demonstrated[6-7] that an assumption of a Gaussian distribution of dipolar couplings is a robust and good approach for analyzing the cross-linked NR and butadiene rubber (BR) samples:

$$I_{nDQ}(D_{res},\sigma_G)=\frac{1}{2}\left(1-\frac{\exp\left\{-\dfrac{\frac{2}{5}D_{res}^2\tau_{DQ}^2}{1+\frac{4}{5}\sigma_{res}^2\tau_{DQ}^2}\right\}}{\sqrt{1+\frac{4}{5}\sigma_G^2\tau_{DQ}^2}}\right) \qquad (2.3)$$

where D_{res} is the average apparent residual dipolar coupling (in units of rad/s) and σ is its standard deviation that characterizes the distribution width. From D_{res}, the molecular weight between constraints, M_c, can be determined for NR samples by:

$$M_{\mathrm{c}}^{(\mathrm{NR})}=\frac{617\mathrm{Hz}}{D_{\mathrm{res}}/2\pi}\,\mathrm{kg/mol} \qquad (2.4)$$

In consequence, the cross-link density, ν, for 4-functional cross-links can be determined by:

$$\nu_{\mathrm{NMR}}=\frac{1}{2M_{\mathrm{c}}} \qquad (2.5)$$

Finally, an improved numerical inversion procedure based on fast Tikhonov regularization was used to determine the actual dipolar coupling distribution. The modified version of the numerical fit, which was described in a recent manuscript[8], provides a reliable, precise and quantitative picture of the actual distribution function of residual couplings, i.e. cross-links.

Study of vulcanization kinetics:

According to the previously explained statements, this experimental methodology is useful to quantitatively evaluate the invariant network structures of vulcanized samples (in latex or solid state), but it is not applicable to networks under evolution in the experimental time scale, e.g. rubber networks during the vulcanization process. In order to analyze the pre-vulcanization kinetics (in latex state), a faster but still quantitative modification of the DQ method was used. This method, which was previously used to analyze gelation kinetics[13], involves the evaluation of I_{nDQ} in a single DQ time (an experimental time around 1 minute) instead of the measurement of full DQ evolution time that needs longer measurement times (around 1 hour according to the experimental settings used in this work). For the most sensitive single-point measurement, τ_{DQ} should be selected for which I_{nDQ} or I_{DQ} attains its highest values in the fully vulcanized sample with the highest cross-link density. For a more robust and conservative analysis, the time was selected close to but before the maximum. Taking into consideration these statements, the best DQ time for single-point detection was selected at 2.2 ms in order to study the pre-vulcanization kinetics in latex state.

2.2.3 Synchrotron X-ray and Tensile Measurements

Wide-angle X-ray diffraction (WAXD) measurements were carried out at the X27C beam line in the National Synchrotron Light Source (NSLS), Brookhaven National Laboratory (BNL). The X-ray wavelength was set at 1.371 Å. Two-dimensional (2D) WAXD patterns were acquired using a MAR-CCD detector. The typical image acquisition time for each scan was 30 seconds. Al_2O_3 was used to calibrate the scattering angle in WAXD and the sample-to-detector distance was 124 mm. X-ray measurements for all samples were taken under the same conditions. All diffraction signals were corrected for beam fluctuations, sample absorption and background scattering. Data analysis was performed using the software Polar (Stony Brook Technology and Applied Research, Stony Brook, New York).

Rubber latex cast samples were pre-cut into a dumbbell-like shape and clamped onto a tensile stretching device. This device allowed symmetric deformation of the sample and monitoring the structure change of the sample by illuminating the same sample position during deformation. The samples were deformed to strains up to 6.4 and relaxed back to stress of 0. The deformation rate was 10 mm/min and was carried out at room temperature. The initial strain rate is 0.00556 sec^{-1} (or 0.333 min^{-1}). Time-resolved WAXD patterns during deformation and stress-strain relations were recorded simultaneously. The stress is defined as load divided by original cross section. The strain is defined as the distance of the two clamps divided by original length.

Quantitative evaluations of mass fractions of crystals were determined for all of the samples based on the integrated intensity patterns. The corrected WAXD patterns prior to stretching at strain 0 contain only an isotropic amorphous halo with no preferred orientation. With increasing strain values, crystalline reflections started to develop and WAXD patterns began to contain both crystalline peaks and the amorphous halo (both oriented and unoriented). The total molecules at the stretched state contain both the isotropic and anisotropic contributions as shown in the equations below:

$$\mathrm{I\ (total) = I\ (isotropic) + I\ (anisotropic)} \tag{2.6}$$

$$\mathrm{I\ (isotropic) = I\ (unoriented\ amorphous)} \tag{2.7}$$

$$\mathrm{I\ (anisotropic) = I\ (oriented\ amorphous) + I\ (oriented\ crystalline)} \tag{2.8}$$

The isotropic and anisotropic contributions in these patterns can be de-convoluted using the analytical method described by Toki et al.[1,2] The isotropic contribution of the WAXD patterns at the stretched state showed a similar feature to the WAXD pattern at strain 0. The de-convoluted anisotropic contribution of the WAXD pattern could be composed of oriented crystalline reflections and an oriented amorphous phase. Two-dimensional peak-fit software was used to fit all the crystal peaks and the amorphous halo. The mass fraction of strain-induced crystals was quantitatively determined by taking the ratio of the integrated crystal areas with the total integrated area.

2.3 Results

2.3.1 ^{1}H Double Quantum (DQ) Solid-State NMR

2.3.1.1 Pre-vulcanization Kinetics

Vulcanization kinetics is followed in rubber science and technology from the rheometer curves. Pre-vulcanization kinetics in NR latex cannot be measured by this methodology because it is dispersed in water. For that reason, this important step is usually indirectly studied by tedious mechanical measurements, i.e. samples pre-vulcanized at different times are dried and the tensile strengths for the obtained films are tested.

In this sense, application of time domain NMR is a step forward to the study of pre-vulcanization kinetics providing important benefits for both industrial and academic applications. Pre-vulcanization takes place inside the NMR spectrometer at the desired temperature, and the experimental method allowed us to observe *in-situ* how the intensity measured at a single DQ evolution time increases with the pre-vulcanization time due to the formation of cross-links (Figure 2.2). The shape of the pre-vulcanization process from the NMR measurements is quite similar to those obtained from the rheometer in "dry" rubber samples.[14]

Samples pre-vulcanized with DPTT show a scorch time where the accelerator chemistry takes place leading to the formation of the active sulfating agents but without the formation of cross-links. The second stage comprises the 'chemistry of cross-linking', which includes reactions leading to the formation of cross-links and the fast increment on the NMR signal. It is important to note that all studied samples do not show a clear plateau which indicates the end of the reaction. This is because the pre-vulcanization reaction depends on two competing processes, i.e. the diffusion of chemicals inside the rubber particles and their reactions to create cross-links. As the cross-linking reaction takes place, the diffusion mechanism is limited and the excess of the vulcanizing agent reacts slowly. These two competing processes will have an important impact on the network structure of each individual particle formed during the pre-vulcanization step, as will be discussed in the next sections. Nevertheless, it is clear that relative intensity increases with concentration of DPTT, which is indicative of an increase in cross-linking density.

Figure 2.2 also shows the relative intensity for the 1.2 phr peroxide vulcanized sample (other peroxide samples show almost identical behavior and they were not included in Figure 2.2). Vulcanization with peroxide is based on radical reactions. After thermal decomposition of peroxide, the formed radicals react with the polymer backbone and, subsequently, cross-links between polymer chains are created. This reaction pathway is so fast that it prevents the existence of scorch time. The reaction rates in sulfur vulcanized samples are much slower than peroxide vulcanized samples. The optimum vulcanization time (fixed as time for 90% conversion after 20 hours of reaction, t_{90}) for DPTT 0.5, 1.0, and 1.5 were 18, 15, and 11 hours respectively, whereas samples vulcanized with peroxide were all 3 hours.

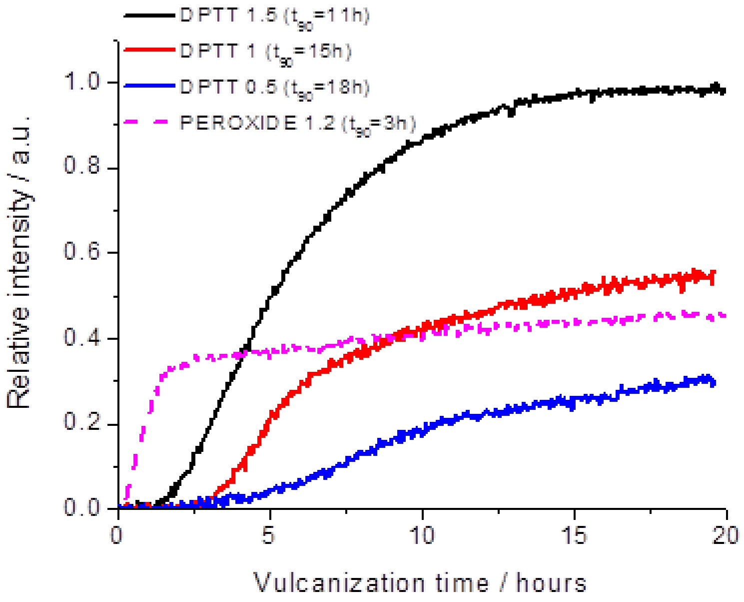

Figure 2.2 Relative intensity at the selected DQ evolution time of 2.2 ms as a function of pre-vulcanization time for various concentrations of DPTT. The 1.2 phr peroxide vulcanized sample is also shown. The optimum vulcanization time (t_{90}) is shown in parenthesis for each sample.

2.3.1.2 Rubber Network Structure

Following the usual manufacturing procedure, after pre-vulcanizing the NR latex at their optimum time (obtained from NMR analysis, see Figure 2.2), a rubber film was made by drying the water. Finally the films were thermally treated in the so-named post-vulcanization process. In all cases, DQ NMR methodology was used to analyze the evolution on the network structure through the three different states.

Non-coupled network defects:

Figure 2.3 shows the fraction of non-coupled network defects for the different samples in the different states. It is important to point out that pre-vulcanized samples in the latex state do not present any measurable non-coupled network defects, whereas they emerge (although in small fractions) after film formation and post-vulcanization.

Weak (albeit systematic) variations, between 2 and 6% in fraction of non-coupled network defect after the post-vulcanization process, were observed. This could be related with degradative processes promoted in this step, as will be discussed in the next sections.

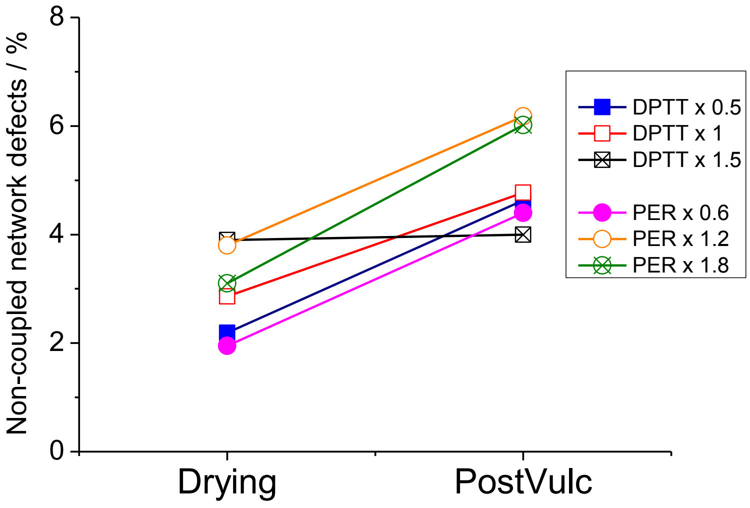

Figure 2.3 Percentage of non-coupled network defects in each state for the studied samples.

Pre-vulcanization process:

In previous works[6-7], the advantages of applying DQ NMR experiments for the complete analysis of rubber network structure, i.e. cross-link density and spatial distribution of cross-links, were pointed out. Nevertheless, in latex samples this methodology is even more important since it allows the study of rubber network structure in the latex state. It is an unresolved experimental challenge in this field, since well-established experimental methodologies for the analysis of cross-link density, e.g. equilibrium swelling experiments, uniaxial tensile strength, etc. are only applicable to dried samples.

Figure 2.4A shows the cross-linking density measured by NMR of various samples in the three different states. We can clearly see that the cross-linking density increases with concentration of DPTT in all three different states. Furthermore, at each concentration of DPTT, the cross-linking density for drying and post-vulcanization in the film state is higher than the cross-linking density for pre-vulcanization in the latex state.

These results demonstrate that conventional experimental methods for the analysis of rubber network structures just give information about the global process, e.g. the effect of pre-vulcanization and film formation on the rubber network structure. On the opposite hand, NMR spectroscopy is able to separate and independently analyze each individual step. In this sense, NMR results after pre-vulcanization reflect the network structure of the individual cross-linked rubber particles dispersed in water. They are direct experimental evidences about the effect of pre-vulcanization reaction without any disturbance caused by additional procedures. A linear relationship between cross-link density and concentration of vulcanizing agents was found (as shown in Figure 2.4B). In DPTT vulcanization, only the two central sulfur atoms are able to create cross-links. It means that the maximum efficiency on vulcanizing reaction should be 2 moles of cross-links (composed exclusively by monosulfidic bridges) per mole of DPTT. According to the slopes in Figure 2.4B, the reaction efficiency during the pre-vulcanization process is close to unity. This could be related to the formation of larger sulfidic cross-links (if a complete reaction of DPTT is supposed) or just by a partial reaction of DPTT. The latter emerged as the most reliable factor, as will be discussed later in this section. Finally, it is important to note that the spatial distribution of cross-links (measured as variation of the relative width of the distribution of cross-link density (σ) to the average value (D_{res}) assuming a Gaussian distribution of cross-links) became more homogeneous with the increase in amount of DPTT (shown in Figure 2.5).

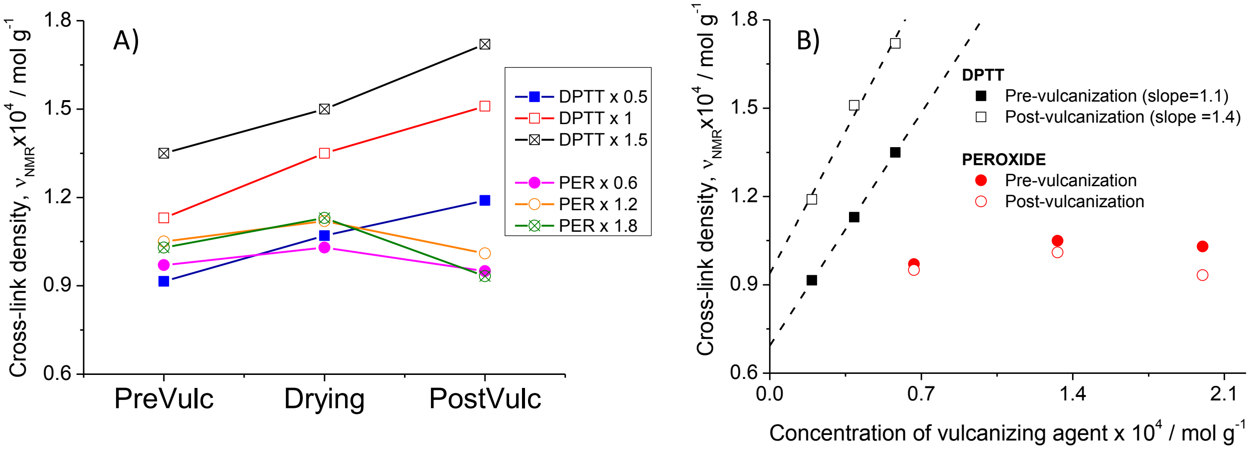

Figure 2.4 (A) Cross-linking density (ν) of various concentrations of DPTT and peroxide in the three different states: pre-vulcanization in latex state, drying and film formation, and post-vulcanization in film state. (B) Efficiency of pre- and post-vulcanization reactions for DPTT and peroxide as the relationship of cross-link density (measured by NMR) and the concentration of vulcanizing agent. Numbers in brackets represent the slope of the linear fit for DPTT vulcanization processes.

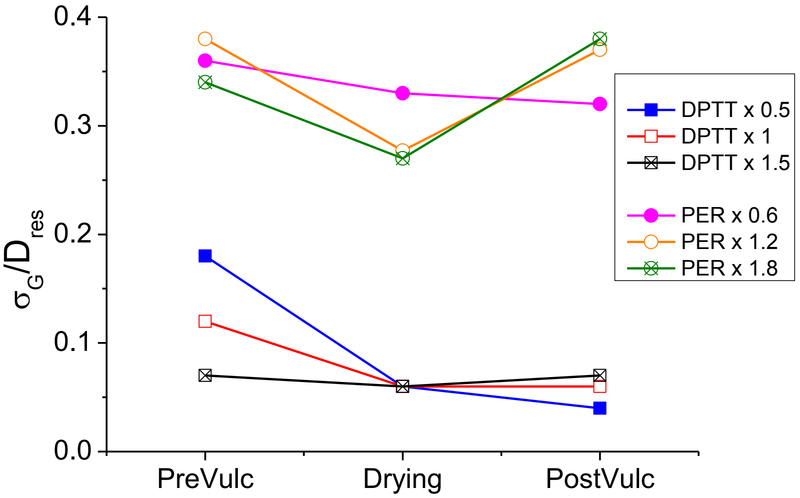

Figure 2.5 Variation of the relative width of the distribution of cross-link density (σ) to the average value ($D_{res)}$ for all three different states. A Gaussian distribution of cross-link density was assumed.

A different scenario takes place when peroxide was used as the vulcanizing agent. The reaction efficiency is very low and the addition of increased amounts of peroxide does not create additional cross-links, at least in the expected amount. To understand this behavior, it is necessary to take into mind that the pre-vulcanization process depends on both diffusion of the vulcanizing agent inside the rubber particle and the subsequent cross-linking reaction. According to pre-vulcanization kinetics explored in Figure 2.2, the reaction rates in sulfur vulcanized samples are much slower than peroxide vulcanized samples. Consequently, the different reactive molecules have enough time to diffuse inside the rubber particles; hence we observe the formation of homogeneous networks with increasing cross-link density according to the DPTT concentration (see Figure 2.6A). On the other hand, the reaction rate in peroxide vulcanization is very fast, where the cross-link density increases immediately after pre-vulcanization starts (see Figure 2.2). The time that peroxide molecules have to diffuse inside the rubber particle is reduced drastically before the cross-linking reaction starts. According to results shown in Figure 2.6A, the spatial distribution of cross-links on rubber particles (measured in latex state) for samples pre-vulcanized with peroxide are broader than the homogenous network structures obtained with DPTT. The heterogeneous networks formed during peroxide pre-vulcanization consist of highly cross-linked areas in combination with slightly cross-linked or even uncrosslinked polymer segments. These structural evidences support the formation of core-shell like structures. Highly cross-linked surfaces of rubber particles slow down the diffusion process. This could be the main reason for the limited cross-link density measured in the peroxide-vulcanized samples in opposition to the sulfur system. Independent of the peroxide concentration, the final network structure after pre-vulcanization process is almost the same in NR-latex.

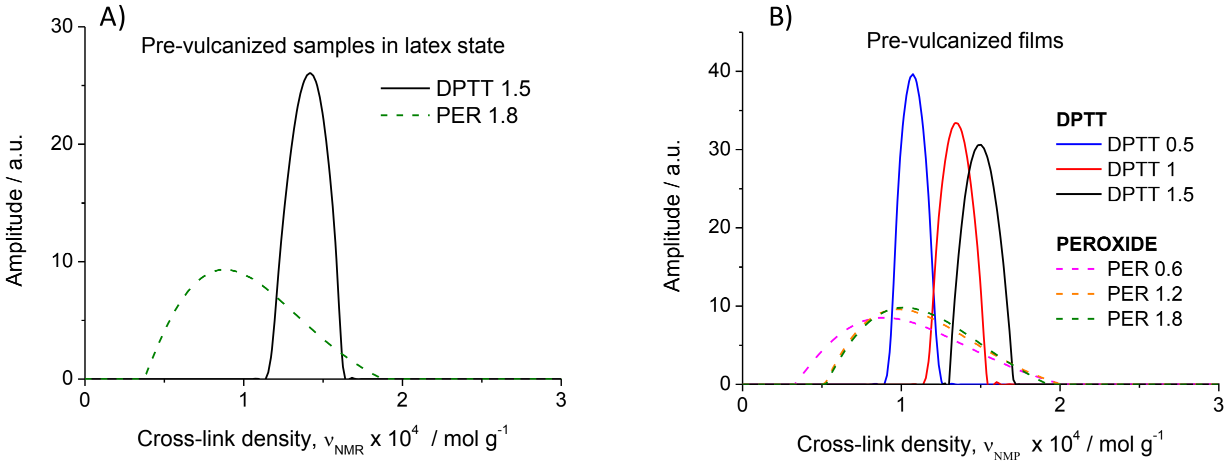

Figure 2.6 Actual spatial cross-link distribution for pre-vulcanized samples in latex state (A) and dried films (B) according to the regularization analysis of NMR data.

Film formation and post-vulcanization process:

The drying process promotes the inter-particle interaction and formation of coherent and continuous polymer film. Cross-linked rubber particles are packed and some interactions between them could take place. It provokes the formation of additional topological constraints measurable by NMR, as was demonstrated by the y-intercept value on Figure 2.4B. At this point, it should be pointed out that the interfusion of cross-linked particles is restricted to roughly one network mesh size. Therefore, the additional topological constrains measured by NMR should take place mainly in the bulk volume of the latex spheres because of the film formation. Cooperation and/or packing between polymer chains reduce and homogenize their conformational space, playing a key role in the elastic properties of those materials because of the reduction in chain entropy. As a consequence, the spatial distribution of cross-links is narrower as compared with the pre-vulcanized rubber particles. This fact hides the differences observed in the spatial distribution of cross-links caused by the DPTT concentration, as shown in Figure 2.5.

It is important to remark that peroxide vulcanized samples always show broader spatial distributions of cross-links compared with DPTT samples, even after film formation (see Figure 2.6B). This heterogeneous network structure on polymer films is a direct consequence of core-shell structure formed during pre-vulcanization, and it seems to be independent of the peroxide concentration.

The post-vulcanization process is a useful process in the latex industry because it accelerates the drying process and facilitates the rearrangement of polymer chains inside the films. However it causes opposite consequences on the network structure according to the recipe used. This thermal process (130ºC for 30 minutes) applied on samples pre-vulcanized with peroxide seems to promote the reaction of remaining peroxide, creating radicals that enhance the natural sensitivity of NR to thermo-oxidative processes[15]. It promotes chain scission reactions and in consequence, a slight reduction in the crosslink density (with a higher effect with increasing peroxide concentration) and the broadening on the spatial distribution of cross-links (Figure 2.4 and 2.5).

On the opposite side, samples pre-vulcanized with DPTT show higher cross-link density and narrower spatial distribution after post-vulcanization processes as compared to pre-vulcanized samples. It seems to indicate that post-vulcanization promotes both the inter-rearrangement of polymer chains in NR films and also the chemical interactions between rubber chains because of the reaction with the remaining DPTT (un-reacted DPTT molecules after the pre-vulcanization process). Post-vulcanization enhances the efficiency on the cross-linking reaction and achieves values close to 1.4 moles of cross-links per mole DPTT without modifying the homogeneity of the formed networks (see Figure 2.4 and 2.5). The lack of evidence that supports the well-known thermo-oxidative aging on NR has to be directly related to the presence of antioxidants (e.g. Wingstay-L) in those samples pre-vulcanized with DPTT.

This important point was confirmed after the analysis of washed samples. For that purpose, pre-vulcanized latex was diluted to 30% dry rubber content (DRC) and stabilized with 1% w/v of sodium dodecyl sulfate (SDS), followed by centrifugation at 12,000 rpm for 40 min. The cream fraction was re-dispersed in distilled water. This procedure was repeated 3 times to clean the excess reacting agents (DPTT and peroxide) and antioxidants (Wingstay-L). It is important to point out that the washing procedure does not modify the network structure after pre-vulcanization nor during the film formation, as was demonstrated in Figure 2.7. Nevertheless its effect is clear during post-vulcanization. Figure 2.7 shows that washed samples (including those pre-vulcanized with DPTT) suffer a considerable degradation during post-vulcanization.

As a consequence, the cross-link density decreases and its spatial distribution become broader. Thermo-oxidative degradation in NR leads to chain scission reactions via a radical mechanism. In addition, thermo labile sulfidic cross-links (characteristics on samples vulcanized with DPTT) could also be affected. For that reason, the sample pre-vulcanized with DPTT seems to be more degraded after post-vulcanization than the sample pre-vulcanized with peroxide. In any case, the natural tendency of NR to be degraded via thermo-oxidation processes emerges in the absence of antioxidants.

In conclusion, the post-vulcanization process improves formation and drying of NR latex films; but they should be properly protected against thermo-oxidative degradation. In that case, the excess of vulcanizing agent, e.g. DPTT, promotes the formation of additional cross-links without affecting the quite homogeneous network structure obtained after pre-vulcanization. This is because cross-linking and degradation reactions are two competing processes where cross-linking is favored and is able to hide any effect caused by the degradation reaction on NR samples. Without protection against aging, post-vulcanization has undesirable effects on the NR latex films.

On the opposite side, the excess of peroxide promotes formation of additional radicals that enhances the degradation of NR during post-vulcanization process. It leads to a complex network structure, since the original core-shell structure obtained after pre-vulcanization with peroxides becomes even more heterogeneous with lower cross-link density. Finally, it is important to remark on the difficulty to protect these samples against thermo-oxidative degradation with antioxidants because it could strongly affect the complex pre-vulcanization process via radical reactions.

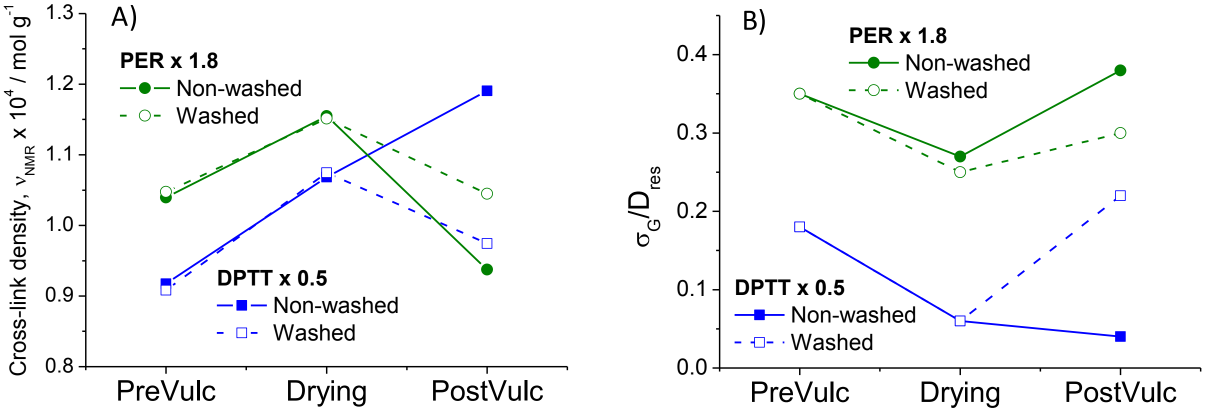

Figure 2.7 Effect of washing the excess of curing agent on the cross-linking density (A) and relative width of spatial cross-links distribution (B) in the three different states: pre-vulcanization in latex state, drying and film formation, and post-vulcanization in film state.

2.3.2 Stress-Strain Relations

The stress-strain relations of pristine latex and heat treated pristine latex (130 ˚C for 30 minutes) are compared in Figure 2.8. The heat condition is the same as the post vulcanization condition. The stress of pristine latex showed an upturn and increased significantly at the onset strain of 3.0, which may be attributed to the presence of the naturally occurring network structure. On the other hand, latex with post-heat treatment did not show the upturn of stress at large strain, indicative of the loss of an original network structure. Table 2.3 shows the 100% modulus, 300% modulus and tensile strength for all the samples. For the pristine latex, the modulus and tensile strength decreased with the post-heat treatment at 130 ˚C for 30 minutes. Since no antioxidants were added to this sample, the post-heat treatment at 130 ˚C provoked the thermo-oxidative aging of NR, where it may cause chain scission reactions (shown in Figure 2.7), and the decomposition of proteins and phospholipids, leading to the destruction of network points. The literature suggested that the removal of proteins and phospholipids destroyed the naturally occurring network, resulting in significant decreases in tensile properties.[16]

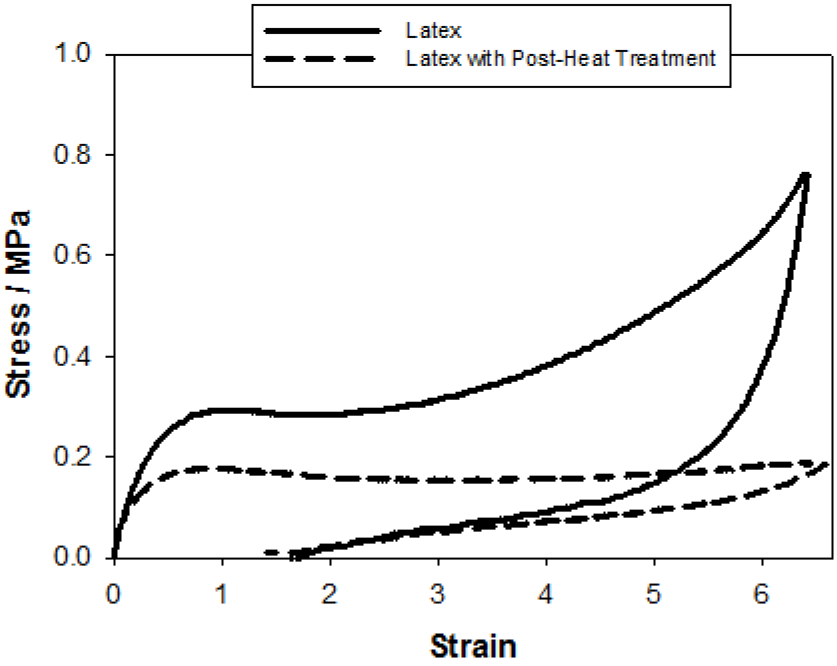

Figure 2.8 Stress-strain relationships during stretching and relaxation of Latex and Latex with post-heat treatment at 130 ˚C.

Table 2.3 100% modulus, 300% modulus and tensile strength of un-vulcanized and vulcanized latex samples at various concentrations and post-heat treatment 130 ˚C.

Sample	**100% Modulus (MPa)**	**300% Modulus (MPa)**	**Tensile Strength (MPa)**
Latex	0.29	0.32	0.76
Latex PostV	0.18	0.15	0.19
DPTT 0.5	0.41	0.74	3.95
DPTT 1.0	0.49	0.93	5.14
DPTT 1.5	0.59	1.11	6.60
DPTT 0.5 PostV	0.37	0.60	3.07
DPTT 1.0 PostV	0.51	0.86	5.10
DPTT 1.5 PostV	0.62	1.22	6.86
Per 0.6	0.41	0.66	3.27
Per 1.2	0.42	0.81	4.36
Per 1.8	0.40	0.72	3.74
Per 0.6 PostV	0.27	0.56	1.68
Per 1.2 PostV	0.33	0.80	2.00
Per 1.8 PostV	0.30	0.65	1.43

The pre-vulcanized samples used for measurements include the pre-vulcanization and drying/film formation processes after film formation, since pre-vulcanization takes place in the solution phase, we cannot measure the mechanical properties of real pre-vulcanized rubber samples. The stress-strain curves of pre-vulcanized latex and post-vulcanized latex for the different concentrations of DPTT are shown in Figure 2.9. The absolute stress values of the sulfur-vulcanized samples are much larger (almost ten times greater) than the un-vulcanized pristine NR latex. These sulfur-vulcanized samples are not affected by the thermal aging of the naturally occurring network because it was properly protected via the addition of anti-degradants. As shown in Figure 2.9, the stress-strain curve of sulfur-vulcanized latex showed a hysteresis, which was typically found in pure vulcanized natural rubber. The presence of network structure was confirmed with the upturn of stress at large strains. The absolute stress during retraction was much smaller than during stretching. This is attributed to the presence of stable crystallites that were formed during stretching. With increasing DPTT concentration, there was an increase in the modulus and tensile strength as shown in Table 2.3. This is in agreement with our DQ NMR measurements that at higher sulfur concentrations there was an increase in the cross-linking density and more network points were formed.

At low concentrations of DPTT, pre-vulcanized latex with DPTT has higher modulus and tensile strength than post-vulcanized latex. However, at higher concentrations of DPTT, the modulus and tensile strength of pre- and post-vulcanized latex are almost identical. The main difference between pre-vulcanization/film formation and post-vulcanization is the slight increase in cross-link density because of the thermal treatment (as it was demonstrated by the DQ NMR experiments). Since the modulus and tensile strength of the pre- and post-vulcanization are almost identical, this is an indication that slight variations on the network structure caused by the post-vulcanization process have no relevant effects on the mechanical properties of those samples.

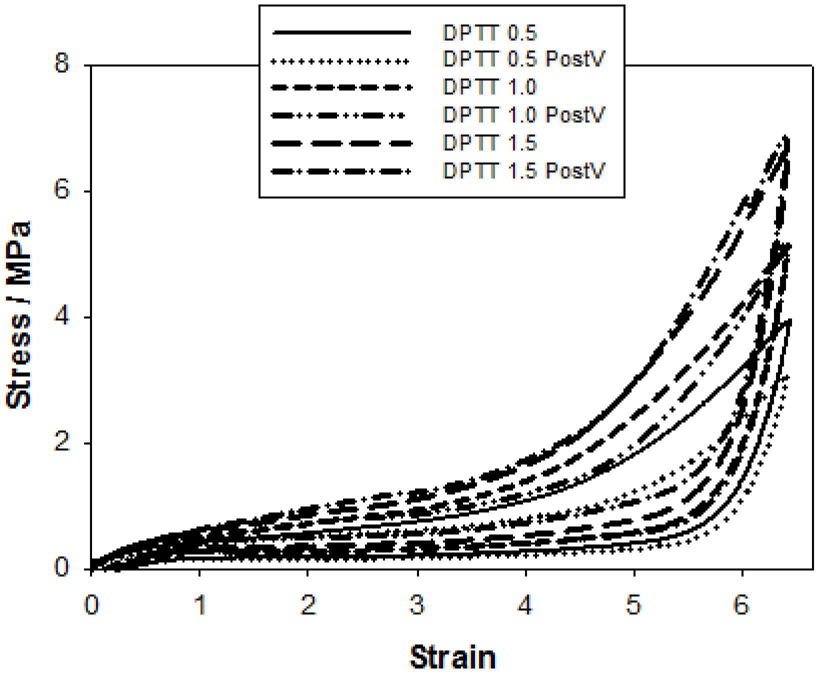

Figure 2.9 Comparison of the stress-strain relations of pre- and post-vulcanized latex with various concentrations of DPTT.

Figure 2.10 shows the stress-strain curves of pre-vulcanized latex and post-vulcanized latex for the different concentrations of peroxide. A hysteresis is also observed similar to that observed in sulfur vulcanized samples. The stress-strain relations are independent of the concentration of peroxide, which is in agreement with our DQ NMR measurements. Peroxide vulcanization may create a core-shell like structure that reduces the diffusion of vulcanizing agents to the inside of the latex particles; hence the cross-link density is unchanged even at higher concentrations. It is to be noted that the post-vulcanized samples with 1.2 and 1.8 phr of peroxide are stretched only up to strain 5 instead of 6. The modulus at small strain did not change by post vulcanization. The modulus and tensile strength are larger in pre-vulcanized than post-vulcanized samples. The additional thermal treatment in post-vulcanized peroxide samples may have caused chain scission reactions that reduced the cross-link density and increased the broadening of cross-link spatial distribution.

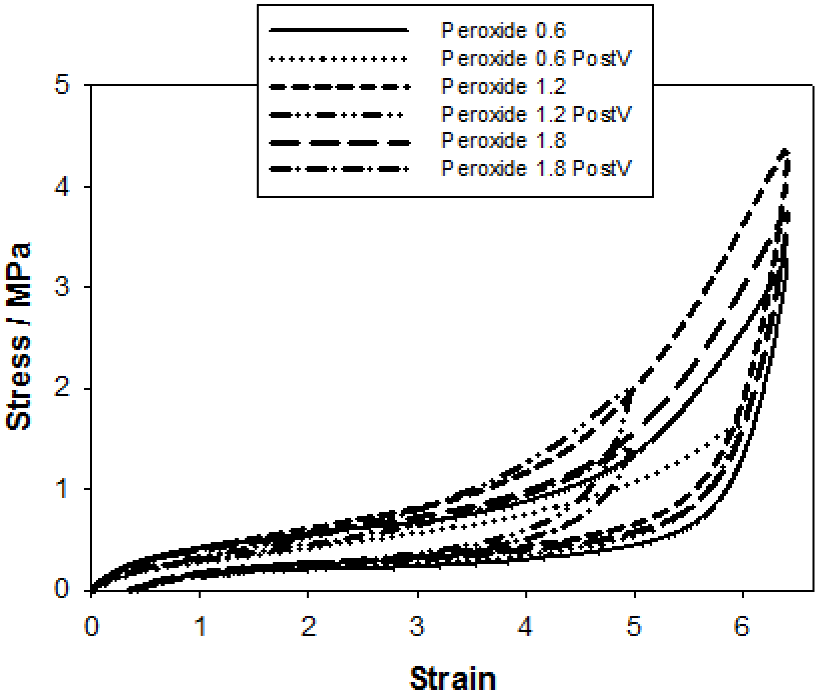

Figure 2.10 Comparison of the stress-strain relations of pre- and post-vulcanized latex with various concentrations of peroxide.

2.3.3 WAXD Results

WAXD of un-vulcanized and vulcanized samples (both pre- and post-vulcanized) are measured simultaneously under deformation. Figure 2.11 shows selected two-dimensional WAXD patterns of latex, latex with post-heat treatment at 130 ˚C, pre- and post-vulcanized latex with 2.25 phr of DPTT (labeled as DPTT 1.5 and 1.5 PostV respectively), and pre- and post-vulcanized latex with 1.8 phr of peroxide (labeled as Per 1.8 and Per 1.8 PostV respectively) during stretching. For the pre- and post-vulcanized samples with various concentrations of DPTT and peroxide, the WAXD patterns at each concentration were all similar and only the 2.25 phr DPTT and 1.8 phr peroxide are shown in the figure. An intense halo was observed both prior and during stretching. This halo is attributed to amorphous chains with no preferred orientation that was present prior to stretching and remained throughout stretching. Furthermore, highly oriented crystalline reflection peaks are observed at higher strains that were not observed prior to stretching at strain 0, indicating the occurrence of strain-induced crystallization (SIC).

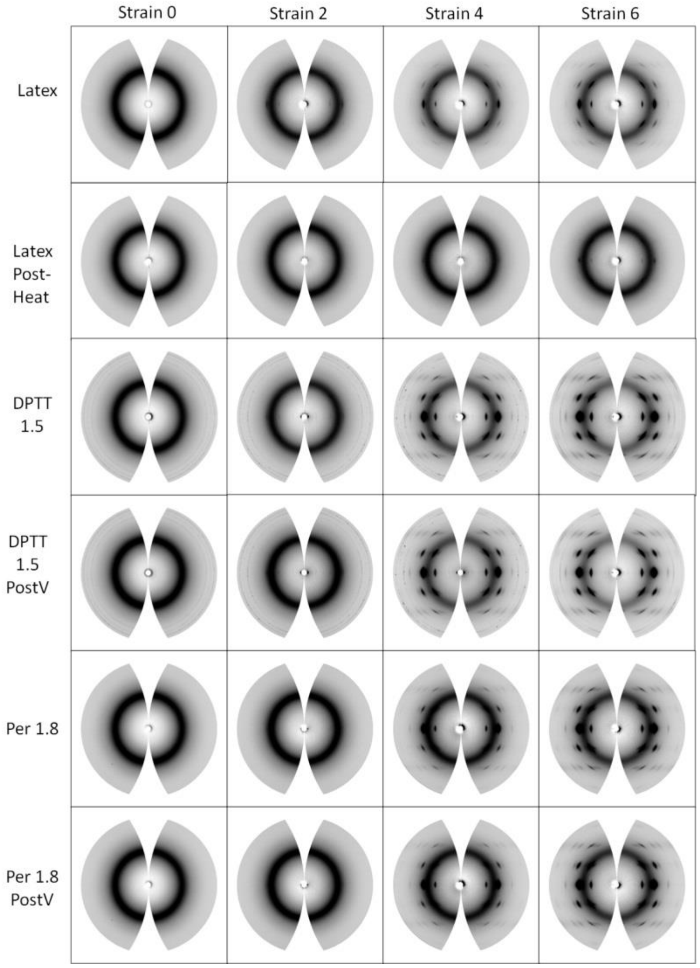

Figure 2.11 Selected two-dimensional WAXD patterns of latex, latex with post-heat treatment at 130 ˚C, pre- and post-vulcanized latex with 2.25 phr of DPTT (labeled as DPTT 1.5 and 1.5 PostV respectively), and pre-vulcanized latex with 1.8 phr of peroxide (labeled as Per 1.8 and Per 1.8 PostV respectively) during stretching.

Figure 2.12 shows the integrated intensities of the two-dimensional WAXD patterns for latex, latex with post-heat treatment, pre- and post-vulcanized latex with 2.25 phr of DPTT, and pre- and post-vulcanized latex with 1.8 phr of peroxide at strains 2 and 6. The intensities of the crystalline reflections increase with strain during stretching. The intensities of the amorphous halo decrease only slightly during stretching, indicating the persistence of sizable amorphous chains in the highly stretched sample. As reported in the literature by Toki et al.[1], during deformation of natural rubber, up to 75% of polymer chains remain in the unoriented state even at large strains, around 20% of chains are in the crystalline state, and 5% of the molecules are in the oriented amorphous state.

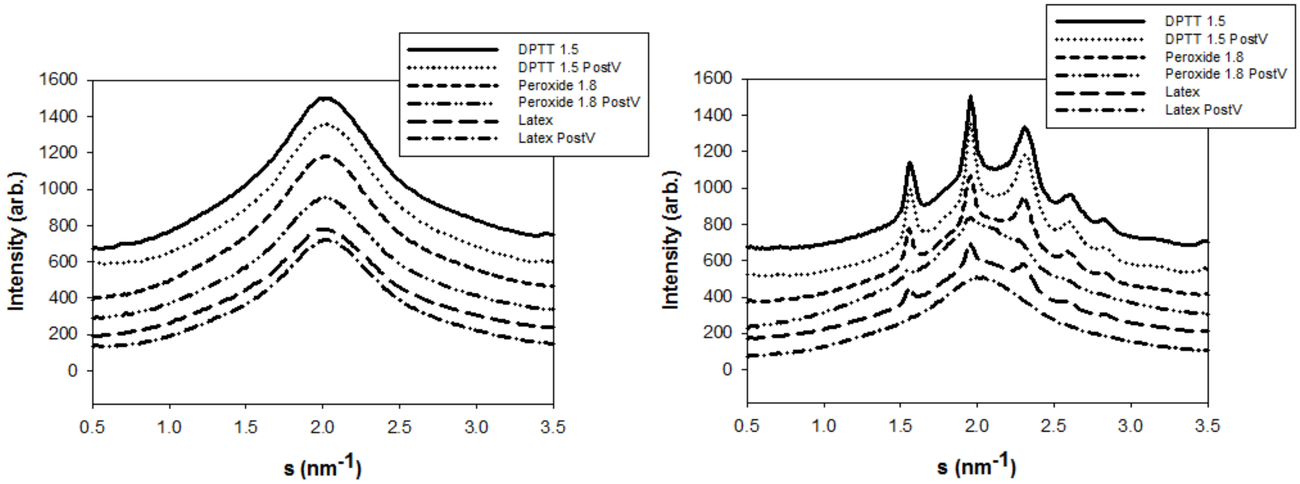

(a) Strain 2

(b) Strain 6

Figure 2.12 Integrated intensities of the two-dimensional WAXD patterns for latex, latex with post-heat treatment, pre- and post-vulcanized latex with 2.25 phr of DPTT, pre- and post-vulcanized latex with 1.8 phr of peroxide at strains 2 (a) and 6 (b).

Figure 2.13 shows the crystallinity fraction for all the samples as a function of strain. For pristine latex, the crystallinity fraction is lower for the latex with post-heat treatment at 130 ˚C. This is consistent with the previous stress-strain relation results, where the high temperature may have caused the destruction of the naturally occurring network, which is necessary for the induction of crystallite formation.

In vulcanized latex with DPTT, more amorphous chains were oriented during stretching and an increase in crystallinity fraction was observed. Furthermore, the crystallinity fraction increased with concentration of DPTT. This is in agreement with previous DQ NMR and stress-strain relation results, where the increase in sulfur concentration led to an increase in the cross-linking density and more network points were formed. As shown in Figure 2.13, for all the concentrations of DPTT, post-vulcanized latex has only a slightly higher crystallinity fraction than pre-vulcanized (and dried) latex films. This demonstrates that small changes on cross-link density during the post-vulcanization process do not have any effect on the strain induced crystallization nor on the mechanical properties of these samples. The further thermal treatment led to the slight increase in cross-linking density and network points for post-vulcanized latex, and hence a slightly higher crystallinity fraction.

As for samples vulcanized with peroxide, the crystallinity fraction is independent of the concentration of peroxide, which is consistent with the DQ NMR and stress-strain relation results. Furthermore, the crystalline intensities are much weaker than the intensities observed for the samples vulcanized with DPTT. This may be attributed to the inhomogeneous network structure formed on NR samples after vulcanization with peroxide. The post-vulcanized samples with peroxide have a smaller crystallinity fraction than the pre-vulcanized samples with peroxide, which is a consequence of the additional thermal treatment that might cause chain scission reactions and decrease the cross-linking density.

The onset strain of crystallization can be estimated from the best fit curve applied to each sample by extrapolating to the crystallinity at 0% position. It was found that the onset strain of crystallization of latex occurred much earlier than that of latex with post-heat treatment (strain 1.6 and 2.2 for latex and latex with post-heat treatment, respectively). Un-vulcanized latex with post-heat treatment resulted in less network points, late development of crystals, and low crystallinity fractions. The onset strain of crystallization of pre- and post-vulcanized latex at all three concentrations of DPTT occurred at the same strain of around 1.8, which tells us that the onset strain of crystallization is independent from the concentration of sulfur and the small changes on cross-link density created during post-vulcanization. The onset strain of crystallization of vulcanized-latex samples with DPTT was slightly higher than the onset strain of crystallization of un-vulcanized latex. This may be attributed to the bulky piperidine rings at the ends of DPTT that inhibit the extension of chains to form crystallites.

The onset strain of crystallization for pre-vulcanized latex with 0.6, 1.2, and 1.8 phr of peroxide is 2.23, 2.38, and 2.50 respectively. Unlike vulcanized samples with DPTT, the vulcanized samples with peroxide are dependent on concentration and temperature aging. With increasing concentration of peroxide, the onset strain of crystallization occurs at higher strains. Furthermore, the onset strain of crystallization occurs at larger strains for post-vulcanized than pre-vulcanized samples. This could be attributed to the enhanced thermo-oxidative degradation of network due to the presence of un-reacted peroxide during the post-vulcanization process.

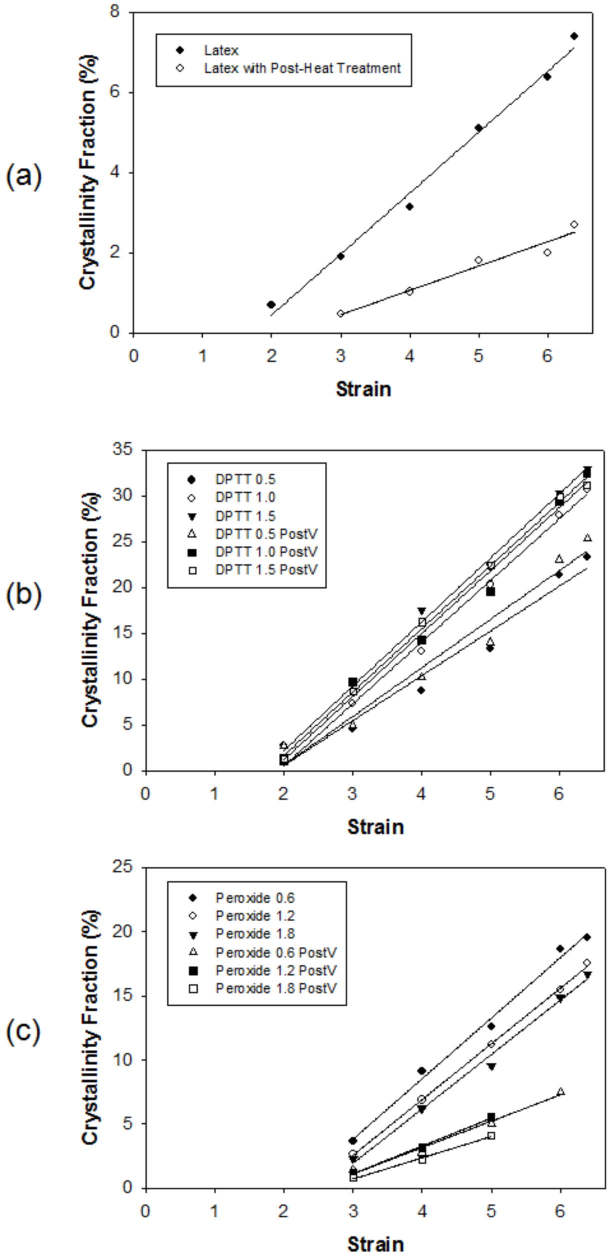

Figure 2.13 Crystallinity fraction with respect to strain for (a) latex and latex with post-heat treatment, comparison of crystallinity fraction between pre- and post-vulcanization with (b) DPTT and (c) peroxide.

2.4 Discussion

Pre-vulcanization with DPTT led to homogeneous network structures, whereas peroxide promotes core-shell structures that (after film formation) develop inhomogeneous network structures. The latter always show smaller crystallinity fractions with delayed onset strain of crystallization with respect to the homogeneous DPTT samples (always comparing samples with similar cross-link density). It demonstrates that in addition to cross-link density, spatial distribution of cross-links is a central factor to understand strain induced crystallization of NR.

These NMR and in-situ synchrotron X-ray diffraction results seem to be in contradiction with the conclusions described by Ikeda et al.[17] in a previous study. On the basis of strain-induced crystallization (SIC) studies, these authors found differences in the onset of SIC behavior as a function of the cross-link density. These differences were explained on the basis of assuming very homogeneous structures for peroxide-cured NR, yet even bimodal structures for sulfur-cured NR. Nevertheless in a most recent work[18] based on small-angle neutron scattering measurements (SANS), they conclude that the structure of peroxide cross-linked NR is inhomogeneous and is composed of several kinds of clusters with different sizes. In the same way, strain induced crystallization behavior of NR vulcanized with peroxide was then related to a progressive reduction of the overall size of inhomogeneities of these samples with the cross-link density. Therefore apparent differences and contradictions between these studies could be transformed into complementary results in perfect agreement based on the studied length scales. SANS[17-18] is used to detect inhomogeneities in the range of 20-50 nm. In sulfur-cured polyisoprene rubber, such inhomogeneities may partially be due to ZnO clusters, as found by transmission electron microscopy (TEM)[19]. The present NMR study provides more local information since it is sensible to spatial crosslinking inhomogeneities on scales of several nm and above. The network structures are obtained directly by simultaneous molecular-scale observation of the behavior of all monomers in the rubber. They suppose clear experimental evidence about the link between the actual local rubber network structure and strain induced crystallization without invoking any model.

It is possible to conclude that the NR samples vulcanized with sulfur exhibit a rather homogeneous rubber matrix down to very local scales, with inhomogeneities at larger scales arising from the non-rubber components. In contrast, vulcanization with peroxides always creates inhomogeneous network structures on all scales, because of radical reactions. These differences on the local network structure led to variations on more complex phenomena like strain induced crystallization.

Figure 2.14 shows a schematic model of the different states using DPTT as the vulcanizing agent: pre-vulcanization in latex state, drying and film formation, and post-vulcanization in film state. During pre-vulcanization, latex particles are dispersed in water. DPTT diffuse inside the rubber particles and then react with the rubber chains. Cross-linking reaction of rubber particles takes place inside each individual rubber particle (intra-particle cross-link density), creating independent and non-connected vulcanized rubber particles. During this process, the protein and phospholipid layers stabilize the rubber particles dispersed in water.

During drying and film formation, water evaporation plays a significant role in network formation. As water evaporates to form a film, rubber particles come in contact with each other and additional entanglements and cross-linking reaction takes place between rubber particles (inter-particle cross-link densities), which are not seen in NMR due to their low volume fraction. According to Figure 2.4, during film formation, slight increases in the cross-linking density as compared to pre-vulcanization in the latex state were observed. According to previous DQ NMR results, inter-particle constraints (entanglements and cross-links) and chain rearrangements created during film formation, homogenize the conformational space of rubber chains. This fact tends to create a continuous rubber media, where proteins and phospholipids are pushed away from the particle boundaries creating aggregates. Nevertheless, the chain ends on the highly cross-linked particles (during the pre-vulcanization process) usually show higher difficulties to diffuse out the original particle to interact with the neighbor particle. In this case, rubber particles retain the particle-shape after film formation (SEM images are not shown). This step should be strongly influenced by the network structure developed on the individual rubber particles as it was suggested by atomic force microscopy[20]. It is of central importance to correlate the network structure after pre-vulcanization (e.g. perfect homogeneous network structure in DPTT samples or core-shell structures in peroxide samples) with the formation and evolution of polymer films. The main inconvenience to develop this investigation was lack of experimental techniques to analyze the rubber network structure on latex state. Nevertheless, time-domain NMR experiments have shown their potential to overcome this problem and reveal the actual network structure on latex state. It will take part in an upcoming study.

During post-vulcanization in the film state, the high temperature (130˚C for 30 minutes) promoted film drying and, in addition, it caused further interactions between rubber particles and additional reaction of DPTT. In this case, samples were protected (by addition of antioxidants) against the thermo-oxidation and, consequently, an increase in intra-particle cross-links and inter-particle cross-links takes place as compared to the drying/film formation state. In addition, the high temperature may have caused the decomposition of protein and phospholipid layers, and therefore, it makes easier the interactions between particles. According to Figure 2.4, the cross-link density is higher than the pre-vulcanization and drying states. Overall, drying from latex state to dry films improved the homogeneity of the samples and promoted the creation of new interactions.

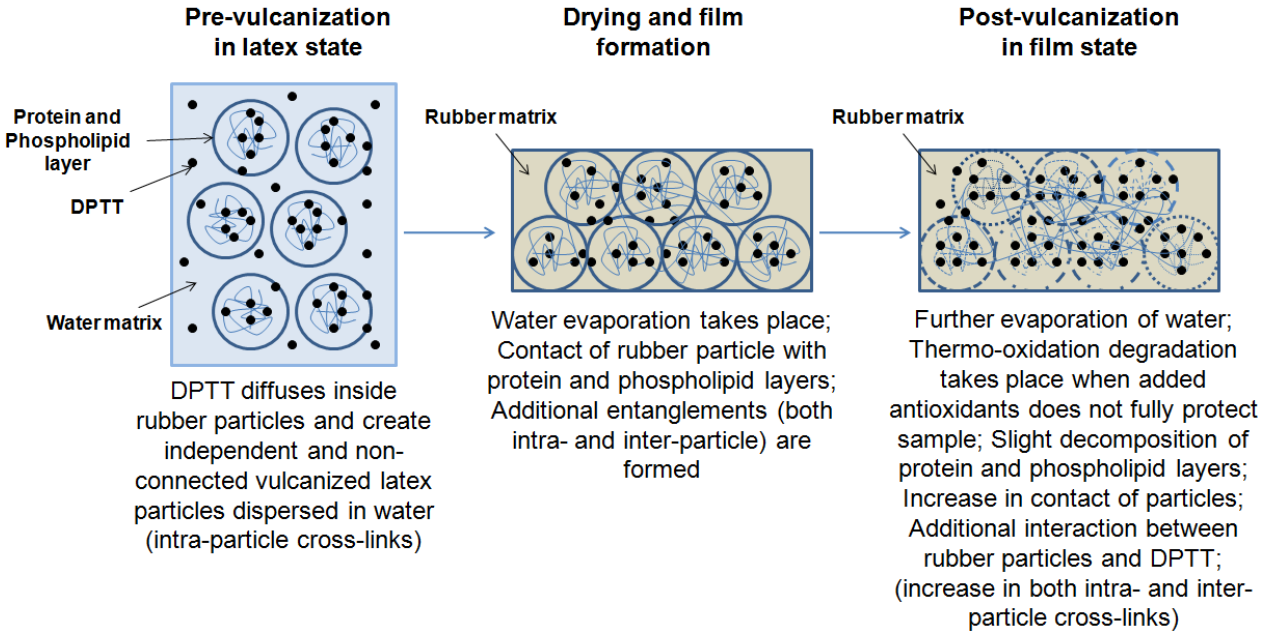
Pre-vulcanization in latex state

Drying and film formation

Post-vulcanization in film state

DPTT diffuses inside rubber particles and create independent and non-connected vulcanized latex particles dispersed in water (intra-particle cross-links)

Water evaporation takes place; Contact of rubber particle with protein and phospholipid layers; Additional entanglements (both intra- and inter-particle) are formed

Further evaporation of water; Thermo-oxidation degradation takes place when added antioxidants does not fully protect sample; Slight decomposition of protein and phospholipid layers; Increase in contact of particles; Additional interaction between rubber particles and DPTT; (increase in both intra- and inter-particle cross-links)

Figure 2.14 A schematic model of the 3 different states for vulcanized latex: pre-vulcanization in latex state, drying and film formation, and post-vulcanization in film state.

2.5 Conclusion

The combination of ^{1}H DQ NMR and WAXD experiments provided us with quantitative information regarding rubber network structure along the different steps on the usual manufacturing procedure of NR latex. It consists of three different states: pre-vulcanization in latex state, drying and film formation, and post-vulcanization in film state. These three states play a large role in the overall vulcanization process and they can affect both network structure and mechanical properties. From DQ NMR and synchrotron X-ray results, a schematic model for each of these processes was proposed. The network structure at each of these states was correlated with its physical properties.

In this sense, time domain NMR experiments have been shown as an easy and quantitative tool to overcome the lack of experimental techniques to characterize the network structure of individual rubber particles that conform the NR latex. ^{1}H DQ NMR experiments, performed on inexpensive and easy-to-use low-field spectrometers, were used to obtain qualitative information about the pre-vulcanization kinetics and the actual network structure of rubber particles dispersed on water. It promotes this experimental approach as valuable methodology to be applied in basic research on academic and technological developments in the industry.

Un-vulcanized latex (without any additive) and latex heated at 130°C during 30 minutes (similar to post-vulcanization process) were tested in order to analyze the intrinsic thermal behavior of NR without the interference of any chemicals. Latex after the thermal treatment always shows lower mechanical properties and crystallization fraction than latex due to high temperature degradation of polymer chains, proteins and phospholipids. Chain scission may reduce the molecular weight of macromolecules, whereas removal of proteins and phospholipids may destroy the naturally occurring network, resulting in significant decreases in tensile properties.

NR latex vulcanized with the sulfur donor DPTT always shows better elastic properties (higher modulus and tensile strength) than those samples vulcanized with peroxides. In pre- and post-vulcanized latex with DPTT, an increase in the DPTT concentration led to more network points with extremely narrow spatial distribution. As a consequence, an increase in modulus and crystal fraction was observed. According to these results and pre-vulcanization kinetics, it was demonstrated that cross-linking reaction of DPTT is slow enough to allow the diffusion of vulcanizing agent inside the rubber particle. It promotes the formation of a highly homogeneous rubber network with excellent physical properties.

On the opposite hand, the peroxide vulcanization process occurs very fast. The diffusion of the vulcanizing agent into the latex particle is limited where vulcanization takes place on the surface. This creates a core-shell like structure that prevents additional peroxide to penetrate into the latex particle. For these reasons, pre- and post-vulcanized latex with peroxide show lower crystallinity fraction (independent on the concentration of peroxide) that affect the stress-strain properties.

Film formation enhances the inter-particle interactions and formation of additional topological constraints between polymer chains without the assembly of chemical cross-links. It increases the dynamic order parameter (related with the lower entropy on the system) and homogenizes the segmental conformational space as compared with the pre-vulcanized rubber particles. Drying process and film formation is usually enhanced by post-vulcanization treatment at higher temperatures. That effect is shown by post-vulcanized latex with DPTT that has slightly higher cross-linking density, mechanical properties and crystallinity fraction than pre-vulcanized latex. In this case, the slight improvement is caused by two positive effects: the addition of antioxidant minimizes the natural aging tendency of NR and the further reaction of (unreacted) DPTT increases the cross-link density without changing the narrow spatial distribution.

By comparing pre- and post-vulcanized latex with peroxide, pre-vulcanized latex with peroxide has a higher cross-linking density, mechanical property and crystallinity fraction than post-vulcanized latex. In these samples without antioxidant protection, the additional thermal treatment for post-vulcanization led to negative effects on network structure and elastic properties. Reaction of peroxide in excess, facilitate the chain scissions of NR that resulted in a decrease in cross-link density.

Improved elastic properties on latex samples seem to be directly related with formation of homogeneous network structures that facilitates the strain induced crystallization of NR. To achieve that objective it is important to select the proper recipe (e.g. vulcanizing systems that allow diffusion inside rubber particles before cross-linking reaction and addition of antioxidants) and optimized pre- and post-vulcanization conditions (time and temperature). Application of time-domain NMR facilitates and rationalizes this complex work, giving quantitative information about the actual network structure in every step of latex manufacturing. Network structure in sulfur vulcanized latex is rather homogeneous than peroxide vulcanized one, though previous NMR studies using C^{13} and deuterium on vulcanized NR reported that carbon filled vulcanized compounds seems to be homogeneous [21, 22] and oriented rubber chains in vulcanized pure compounds is aligned with the stretched direction at less than 200% strain[23, 24].

2.6 References

1. Toki, S.; Sics, I.; Ran, S.; Liu, L.; Hsiao, B. S.; Murakami, S.; Senoo, K.; Kohjiya, S. *Polymer* **2003**, *44*, 6003
2. Toki, S.; Sics, I.; Ran, S.; Liu, L.; Hsiao, B. S.; Murakami, S.; Senoo, K.; Kohjiya, S. *Macromolecules* **2002,** *35*, 6578
3. Keddie, J.; Routh, A. **“**Fundamentals of Latex Film Formation: Processes and Properties,” *UK: Canopus Academic Publishing Limited* **2010**
4. Perrellaa, F.; Gaspari, A. *Methods* **2002**, *27*, 77
5. Amnuaypornsri, S.; Sakdapipanich, J.; Tanaka, Y. *Jour. Appl. Polym Sci. Appl Polym.* **2009**, *111*, 2127
6. Saalwachter, K. *Prog. Nucl. Magn. Reson. Spectrosc*. **2007**, *51*, 1
7. Valentin, J. L.; Posadas, P.; Fernandez-Torres, A.; Malmierca, M. A.; Gonzalez, L.; Chasse, W.; Saalwachter, K. *Macromolecules* **2010**, *43,* 4210
8. Chasse, W.; Valentin, J. L.; Genesky, G. D.; Cohen, C.; Saalwachter, K. *J. Chem. Phys* **2011**, *134*, 044907
9. Lewis, A. “Accelerator DPTT,” *AkroChem Corporation* **2009**
10. Valentín, J. L.; López, D.; Hernández, R.; Mijangos, C.; Saalwächter, K. *Macromolecules* **2009**, *42*, 263
11. Vaca-Chavez, F.; Saalwachter, K. *Phys. Rev. Lett.* **2010,** *104***,** 198305
12. Vaca-Chavez, F.; Saalwachter, K. *Macromolecules* **2011**, *44***,** 1560

13. Saalwachter, K.; Gottlieb, M.; Liu, R.; Oppermann, W. *Macromolecules* **2007**, *40*, 1555

14. Posadas, P.; Fernández-Torres, A.; Valentin, J. L.; Rodríguez, A.; González, L.; *J Appl. Polym. Sci.* **2010**, *115*, 692

15. Lemayev, N. V.; Kurbatov, V. A.; Liakumovich, A. G. *Polymer Science URSS* **1981**, *23, 419*

16. Amnuaypornsri, S.; Sakdapipanich, J.; Toki, S.; Hsiao, B. S.; Ichikawa, N.; Tanaka, Y. *Rubber Chemistry and Technology* **2008**, *81*, 753

17. Ikeda, Y.; Yasuda, Y.; Hijikata, K.; Tosaka, M.; Kohjiya, S. *Macromolecules* **2008**, *41*, 5876

18. Suzuki, T.; Osaka, N.; Endo, H.; Shibayama, M.; Ikeda, Y.; Asai, H.; Higashitani, N.; Kokubo, Y.; Kohjiya, S. *Macromolecules* **2010**, *43*, 1556

19. Dohi, H.; Horiuchi, S. *Polymer* **2007,** *48*, 2526

20. Ho, C.C.; Khew, M.C. *Langmuir* **2000**, *16*, 2436

21. Rault, J., Marchal, J., Judeinstein, P., Albouy, P. A., *Macromolecules* **2006**, *39*, 8356

22. Dupres, S., Long, D. R., Albouy, P. A., Sotta, P., *Macromolecules* **2009**, *42*, 2634

23. Kimura, H., Dohi, H., Kotani, M., Matsunaga, T., Yamauchi, K., Kaji, H., Kurosu, H., Asakura, T., *Polymer journal* **2010**,*42*, 25

24. Kameda, T., Asakura, T., *Polymer* **2003**, *44*, 7539

(Chapter 3 reproduced in part with permission from *Macromolecules, 46*, 5238-5248. Copyright **2013** American Chemical Society.)

Chapter 3

Entanglements and Networks of Strain-Induced Crystallization in Natural Rubber at Various Temperatures

3.1 Introduction

Vulcanized natural rubber (NR) has been studied enormously because its mechanical performance is superior to vulcanized synthetic rubbers, including polyisoprene rubber (IR), polybutadiene rubber (BR), and styrene-butadiene rubber (SBR). Strain-induced crystallization (SIC) has been considered as a key factor of the superiority of vulcanized NR. The stress-strain relation and SIC have been discussed under uniaxial deformation since 1925, when SIC was founded by Katz[1]. The stress-strain relation of sulfur vulcanized NR (SVNR) has been simulated by non-Gaussian chain network models with the classic theory of rubber elasticity[2-3]. Arruda and Boyce[4-5] succeeded to simulate the stress-strain relation of Treloar's experimental data at 20 °C under simple elongation, equal bi-axial extension, and pure shear deformation[6]. The success of their simulation of the stress-strain relation of SVNR from small strains to the strain at break suggests that SIC has no contribution to the stress.

In 1947, Treloar[7] also measured the stress-strain relation and the birefringence of SVNR at various temperatures. He suggested that at lower temperatures, the extensibility of molecular chains decrease and birefringence increase, in which both of these effects increase the upturn of stress at smaller strains. At -50 °C, the extensibility increases owing to the reduction in birefringence that compensates for the increase in mechanical cohesion. The birefringence of the sample increases with strain during extension and decreases with strain during retraction. Although the stress during extension is larger than the stress during retraction, the birefringence during extension is smaller than that during retraction. The birefringence is the total of the amorphous orientation and crystal orientation, which cannot be separated. However, Treloar[6] suggested that most of the birefringence comes from SIC and concluded that SIC is one of the main causes of the temperature dependency of the stress-strain relation of SVNR. However, he wrote in 1975, "to regard the effect of crystallization as secondary, producing only minor modifications"[2].

The stress in stress-strain relation of rubber at various temperatures has been elucidated by the theory of rubber elasticity[2-3]. The entropy force of a non-Gaussian chain[2,8] can be expressed as:

$$f = (kT / b_K)\, L^{-1} (r / N\, b_K) \qquad (3.1)$$

where f is the force, b_K is the Kuhn statistical segment length, N is the number of Kuhn segments of a chain, r is the end-to-end distance at the deformed state, and $L^{-1}(x)$ is the inverse Langevin function. Several network models, which are composed of non-Gaussian chains, were proposed, including the three chain, four chain, eight chain and full chain models[2-5,9]. The upturn of stress at large strains of rubber is elucidated by the limited extensibility of non-Gaussian statistical chains between network points[2,4-5] and by a singularity of the tube theory[10]. The force from the theory of rubber elasticity at the deformed ideal network of non-Gaussian chains is expressed as follows[2-5,8] :

$$f = (\nu\, kT / 3)\, N^{1/2} \left(\left(L^{-1} (\lambda / N^{1/2}) - \lambda^{-3/2} L^{-1} (\lambda^{-1/2} / N^{1/2}) \right) \right) \qquad (3.2)$$

where ν is the number of chains per unit volume, and λ is the extension ratio. The equation suggests that the stress increases linearly with temperature.

During vulcanization, molecular chains are fixed by crosslink points, but molecular chains between crosslink points could be considered as a random coil. At lower temperatures, polymer chains between crosslink points may become stiff, i.e., "Kuhn statistical segment length" increases, and therefore, the number of randomly movable segments decreases as a first approximation that neglects thermal expansion. The Kuhn statistical segment length, $b_{K,}$ is defined by:

$$b_K = \langle \mathbf{R}^2 \rangle / R_{max} \qquad (3.3)$$

where $(\langle \mathbf{R}^2 \rangle)^{1/2}$ is the mean squared end-to end distance and R_{max} is the maximum length of the end to end vector. Stiffer chains have larger values of b_K, where $b_K = R_{max}$ for a perfectly stiff chain[8], $\langle \mathbf{R}^2 \rangle$ is expressed with a fixed bond angle θ between the nth and (n-1)th bond and with a mean rotation angle $\langle \cos \varphi \rangle$ between (n-1)th, nth and (n+1)th bonds[11-13]:

$$\langle \mathbf{R}^2 \rangle = N\, b_K{}^2\, [(1+\cos\theta) / (1-\cos\theta)] \times [(1 + \langle \cos\varphi \rangle) / (1- \langle \cos\varphi \rangle)] \qquad (3.4)$$

Since polymer chains in the polymer melt can be considered as Gaussian chains[8,13], the end-to-end distance of chains in polymer melts is applicable for rubber. The temperature dependency of molecular size is included in $\langle \cos \varphi \rangle$, since $\langle \cos \varphi \rangle = 0$ for the case of free rotation. According to Edwards and Vilgis[11], a maximum extensibility λ_{max} is defined as $(R_{max} / b_K)^{½}$ by the Kuhn theory and (a / b_K) by the tube theory, where a is the radius of the tube. The limit of extensibility depends on the stiffness (b_K) of the polymer chains at its melt state. At lower temperatures, the extensibility may be smaller than at higher temperatures due to the increase of stiffness.

According to literature[10], the molecular weight between entanglements of the *cis*-1,4-polyisoprene structure is 3120 g/mol at 25 °C. This value suggests that each rubber chain may have more than 300 entanglements at 25 °C, since the molecular weight is around 10^6 g/mol. In the case of occurrence of entanglements, the molecular weight dependency of the zero shear viscosity of polymer melt is expressed as $\eta_0 \sim M^{3.4}$, which is well established experimentally at large molecular weights, where η_0 is the zero-shear viscosity and M is molecular weight. This behavior is elucidated to consider the effect of entanglement by the tube model and the reptation model[14-15]. According to Doi[15], these theories elucidate that the behavior is rather universal, independent of temperature and molecular species (as long as the polymer is linear and flexible). Therefore, these theories treat entanglements at constant temperatures, and the degree of entanglement does not change at various temperatures.

Stress-strain relation and a crystal peak intensity of wide angle X-ray diffraction (WAXD) of SVNR were measured simultaneously by a conventional X-ray instrument[16]. The crystal peak intensity increases with strain during extension and decreases with strain during retraction. The crystal peak intensity during extension is lower than that during retraction, although the stress during extension is larger than that during retraction. Both hysteresis of the stress-strain and the crystal peak intensity are closed at the same strain. It means that SIC contributes to the hysteresis of the stress-strain relation. A shoulder in the stress-strain relation was observed during extension at -3 °C and 7 °C, in spite of no shoulder at 22 °C. Synchrotron X-ray made it possible to measure the stress-strain relation and obtain 2D WAXD pictures simultaneously[17-20]. The crystal fraction, oriented amorphous fraction and non-oriented amorphous fraction in SVNR were calculated from 2D WAXD pictures[17]. The maximum crystal fraction is around 25% and the fraction of non-oriented amorphous fraction is around 70%. This result suggests that the system is very inhomogeneous.

Trabelsi et. al.[19] observed a plateau in the stress-strain relation at the onset strain of SIC in SVNR. They claimed that the plateau is created by SIC and depends on the rate of extension and network density. Flory[21-22] proposed that SIC contributes to the stress in stress-strain relations. Chains that are deformed to their limit of extensibility make crystals. The chain length in SIC is longer than the chain length in the oriented amorphous. The longer chain in a crystal (along the stretched direction) makes the amorphous chain relax. This mechanism decreases the stress and is one of the main contributions for the observed plateau. In addition, SIC become giant network points that increase the stress, which contributes to the upturn of stress at higher strains.

In this chapter, we discuss the temperature dependency of stress-strain relations and the contribution of SIC of un-vulcanized and vulcanized NR at various temperatures. We propose structural models for un-vulcanized and vulcanized NR, which are attributed to the presence of entanglements, pseudo-network, and chemical-bond network.

3.2 Experimental Methods

3.2.1 Sample Preparation

Raw NR sample used in this study was fresh field latex provided by the Thai Rubber Latex Co, Thailand. The fresh NR latex was preserved with 0.6 v/v% NH_3 (NR latex 100 ml: NH_3 solution 0.6 ml) at room temperature for 3 months. The preserved NR latex was cast on glass dishes and dried in an oven at 60 °C for 48 hours. These samples were dissolved in toluene as 3 w/v% solution. These solutions were cast onto glass dishes, creating cast films about 1 mm in thickness after solvent evaporation.

Peroxide vulcanized NR (PVNR) samples were prepared as follows. Un-vulcanized rubber samples were first masticated by a two-roll mill at 50 °C for 2 minutes. Subsequently, 1 phr (parts per hundred rubber) dicumyl peroxide (DCP) was added to these samples and thoroughly mixed for 3 minutes. The rubber compounds were vulcanized at 160 °C for 30 minutes in a 1 mm depth mold by compression.

3.2.2 Sample Characterization

Synchrotron X-ray measurements were carried out at the X27C beam line in the National Synchrotron Light Source (NSLS), Brookhaven National Laboratory (BNL). The wavelength of the X-rays used was 1.371 Å. Two-dimensional WAXD patterns were recorded by a MAR-CCD detector (MAR USA). The image acquisition time for each frame was 30 sec. The diffraction angle in WAXD was calibrated by Al_2O_3 standard. All measured images were corrected for beam fluctuations and sample absorption. The data analysis software POLAR (Stony Brook Technology and Applied Research, New York) was used to analyze the WAXD images. The onset strain of SIC was determined from the plot of crystalline fraction versus strain by extrapolating the best fit curve to a crystalline fraction value of zero. A 2D simulation method has been developed to analyze the crystal structure, crystallinity fraction, size, orientation, and defects in the SIC of NR and PVNR. This will be discussed in Chapter 5 and elsewhere[33].

Stress-strain measurements were recorded simultaneously with the time-resolved WAXD measurements during tensile deformation at various temperatures from -50 to 75 ˚C. A modified

Instron 4442 tensile stretching instrument was used that allowed the uniaxial and symmetric deformation of the sample, while monitoring the structural changes of the sample by illuminating the same sample position during deformation. The samples were deformed up to strains of 6.0 at a stretching rate of 10 mm/min. The temperature is controlled using dry air or liquid nitrogen that flows through a heater. The samples were deformed after stabilizing at the set temperature for a few minutes. The stress is defined as the measured load value divided by the original cross section area of the sample. The strain is defined as the difference of the deformed length and the original length divided by the original length.

3.3 Results and Discussion

Commercially available raw natural rubber is classified into latex grade and solid rubber grade. Solid rubber is made from latex through cohesion, extrusion, centrifugation and sheeting (smoking in ribbed smoked sheet (RSS)) in order to kill virus, to remove dust and sand, and to control the Mooney viscosity in rubber manufacturing factories. The content of non-rubber impurities is reduced from 6 % to 2 %. The molecular weight and molecular weight distribution (MWD) are controlled at rubber factories. The experiments presented here focus on fresh latex to avoid the effects from manufacturing processes[23-25].

3.3.1 Un-vulcanized State

The stress strain relations of un-vulcanized NR at temperatures from -50 to 75 ˚C are shown in Figure 3.1. The stress values at lower temperatures are larger than the stress at higher temperatures. The upturn of stress at large strains and the “S” shape figures in all the stress-strain curves, except 75 ˚C, suggest that un-vulcanized NR is composed of a pseudo-network. At temperatures lower than 25 ˚C, the stress upturn at large strains is more pronounced as compared to higher temperatures.

Figure 3.1 also shows the WAXD images obtained at various temperatures. These images shown were obtained at the largest strain before breaking. SIC was observed in the WAXD patterns at all temperatures. The SIC reflections were more apparent and pronounced at lower temperatures. The vertical arrows show the onset strains of SIC at each of the temperatures. The onset strains of SIC decreased with the decrease of temperature, except at -50 ˚C. Polyisoprene chains may slide at entanglements at 25 ˚C during extension. However, at temperatures lower than 0 ˚C, chains may not slide at entanglements and may be aligned into crystalline order. At -50 ˚C, chains may be more difficult to slide at the entanglement and are stiffer than at -25 ˚C. Chapter 5 will discuss the properties of these crystals in greater details.

A schematic model of un-vulcanized NR that is composed of entanglements (blue circles), pseudo end-linked networks (green squares), and SIC (gray squares) is shown in Figure 3.2. Although the network density of the pseudo end-linked network is very low, the whole entanglement seems to become a permanent entanglement that is not loosened by chain movements. It is reported that the end-linked network and entanglements induce SIC differently at different deformation rates[25].

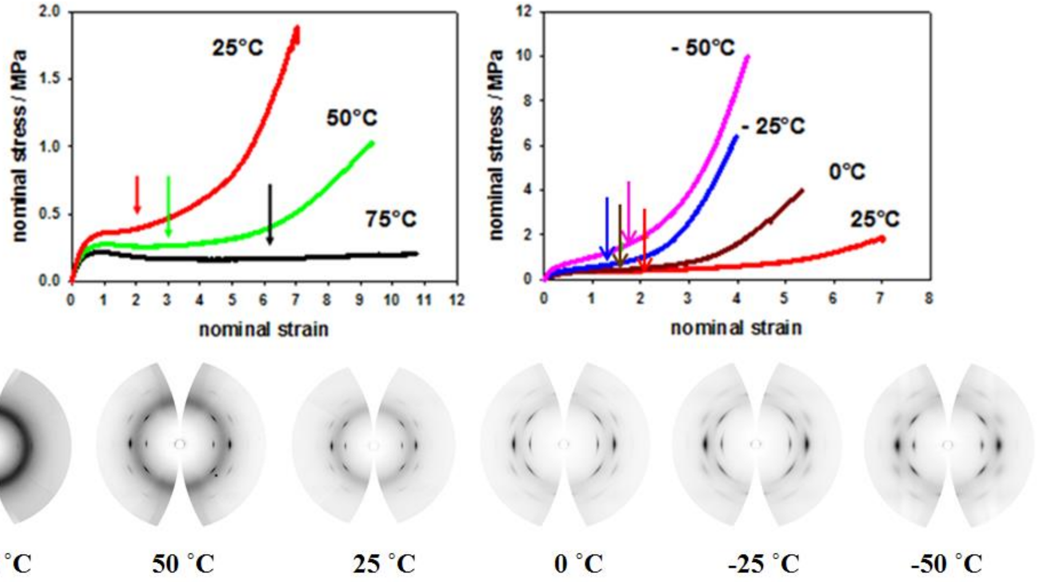

Figure 3.1 Stress strain relations of un-vulcanized NR at temperatures from -50 to 75 ˚C. The WAXD images at each temperature were obtained at the largest strain before breaking. The vertical arrows show the onset strains of SIC at the temperatures.

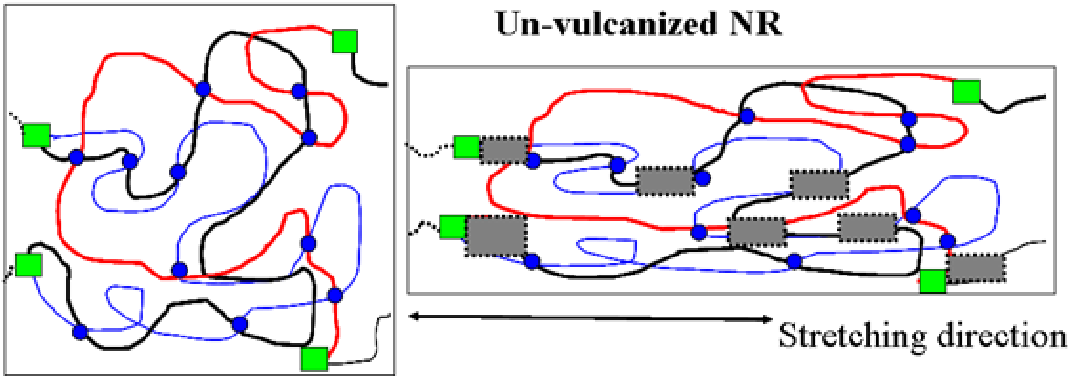

Figure 3.2. A schematic model of un-vulcanized NR prior to deformation (left) and after deformation (right). Entanglements (blue circles), pseudo end-linking networks (green squares), and SIC (gray squares) are shown.

3.3.2 Vulcanized State

The final properties of the rubber materials are determined by the vulcanization conditions. Before vulcanization, the mixing of raw rubber (solid material) and vulcanization agent (solid powder) with accelerators (solid powder) in an internal mixer or a two role mill is necessary. It is difficult to obtain a good dispersion of vulcanization agents through the mixing process. During vulcanization, chemical reaction between double bonds of polyisoprene and vulcanization agents are occurred randomly. When the vulcanization process begins, the viscosity increases and the vulcanization agents cannot move to other places where vulcanization has not yet started. This mechanism makes the network inhomogeneous. Vulcanization changes un-vulcanized rubber to an elastic material.

The stress-strain relations and WAXD images at large strains of PVNR from -50 to 75 ˚C are shown in Figure 3.3. SIC is observed in the WAXD images at all temperatures and the vertical arrows indicate the onset strain of SIC at various temperatures. Chapter 5 will focus on the discussion of the SIC of PVNR. The stress values at lower temperatures are larger than the stress values at higher temperatures. A slight shoulder can be observed at -25 ˚C and 0 ˚C, but at the other temperatures, the stress increases with strain and does not show shoulders[17-19]. Trabelsi et al.[19] discussed that the appearance of shoulders of are limited to the certain conditions of network density, rate of extension, and temperature. The stress-temperature dependencies of PVNR at strain 1.0, 3.0 and 5.0 are shown in Figure 3.4. The stress values at lower temperatures are larger than the stress values at higher temperatures. The stress values at -50 °C do not follow the same tendencies as the other temperatures. More importantly, the stress does not increase linearly with temperature.

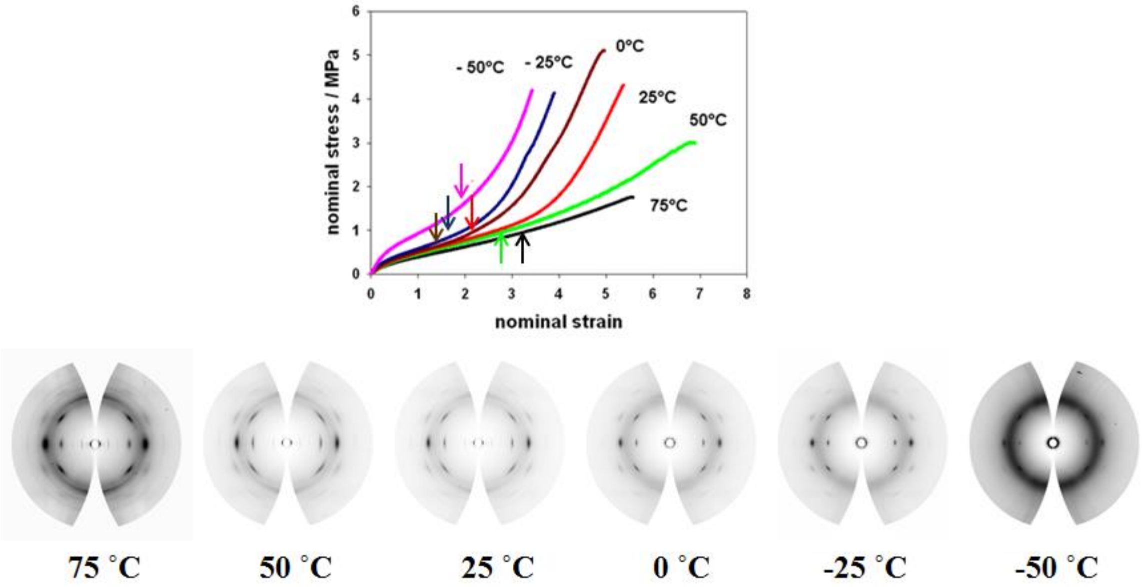

Figure 3.3 Stress strain relations of peroxide vulcanized NR (PVNR) at temperatures from -50 to 75 °C. The WAXD images at each temperature were obtained at the largest strain before breaking. The vertical arrows show the onset strains of SIC at the temperatures.

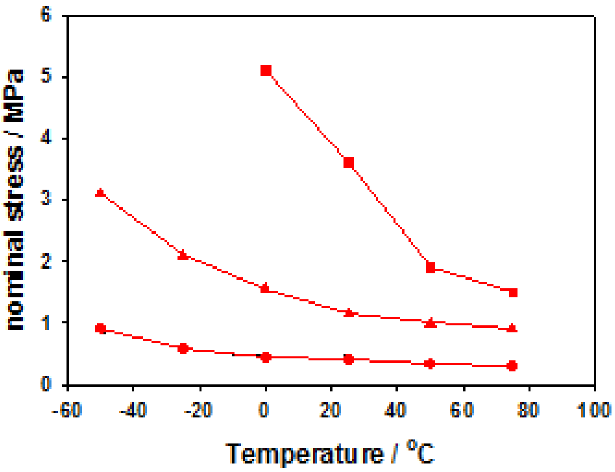

Figure 3.4 Stress-temperature relations of PVNR at strain 1.0 (●), 3.0 (▲), 5.0 (■).

A schematic model of vulcanized NR that is composed of entanglements (blue circles), pseudo networks (green squares), chemical bond networks (red circles), and SIC (gray squares) is shown in Figure 3.5. Vulcanized NR has three kinds of networks that influences the mechanical properties and SIC content. It is not known whether the pseudo networks are still present in vulcanized NR after vulcanization, since the pseudo network may be damaged during the vulcanization process. Nonetheless, the three kinds of network, including entanglements, create rubber elasticity and the limited extensibility of chains.

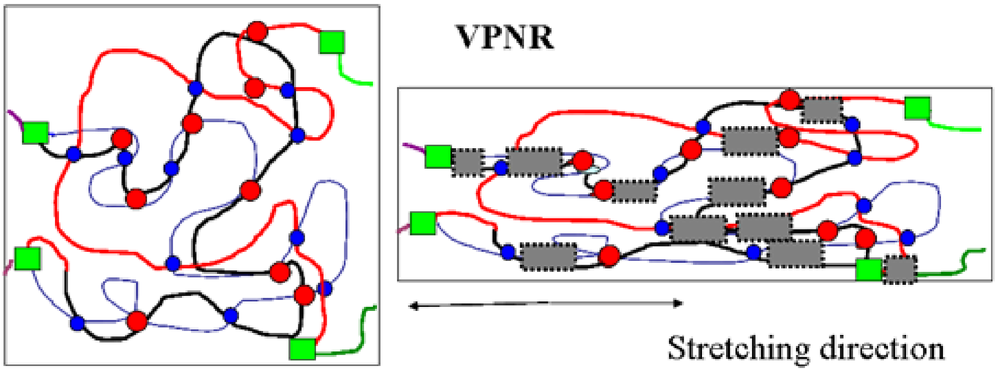

Figure 3.5 A schematic model of peroxide vulcanized NR (PVNR) prior to deformation (left) and after deformation (right). Entanglements (blue circles), pseudo end-linking networks (green squares), chemical bond networks (red circles), and SIC (gray squares) are shown.

3.3.3 Theory of Rubber Elasticity: Stress-Temperature Relation

Stress relaxation experiments at various temperatures have proved the theory of rubber elasticity (Equation 3.2) such that stress increases linearly with temperature, and the force is originated by the reduction of entropy at the deformed state[13,26]. At the strain where SIC is induced, Trabelsi et al.[19] reported that the stress at strain 3.0 at -25 °C reduced to zero in 30 hours, and the crystallinity fraction reached 30%. Toki et al.[27] studied stress relaxation and WAXD patterns simultaneously at temperatures from -20 °C to 100 °C by synchrotron X-ray scattering. The VSIR sample was stretched to strain 4.0 and set at 30 °C. The sample was then heated immediately up to 100 °C or cooled down to -20 °C at the rate of 2 °C/min. The stress was normalized by the stress at 30 °C. According to the theory of rubber elasticity in Equation 3.2, the force at temperature T (f(T)) and the force at the reference temperature To of 30 °C (f(To)) at the same strains should follow f(T)/f(To) = T/To. At temperatures higher than 30 °C, the stress increased with the increase in temperature, accompanied with the melting of SIC. The melting of SIC seemed to increase the stress more than a linear relation due to the increase of the number of amorphous chains, since Equation 3.2 indicates the increase of mobility of amorphous chains at higher temperatures. On the other hand, at temperatures lower than 30 °C, the stress values decreased with the decrease in temperature, accompanied with the increase of SIC. The increase of SIC decreased the stress lower than the linear stress-temperature relation, since

Equation 3.2 indicates the decrease of the mobility of chains at lower temperature. Although SIC seems to have an effect on the results[27], the stress increases with temperature. Therefore, the theory of rubber elasticity seems to be correct under equilibrium conditions (at constant strain) with SIC. However, the temperature dependency of stress-strain relation cannot be elucidated by the theory of rubber elasticity as shown in Figures 3.1 and 3.3. Since the stress-strain measurement is not executed in the equilibrium state, the deformation effect should be considered. In addition, the temperature effect to the stress should include the effect of the stiffness of chains.

3.3.4 Proposed Model on the Stress-Strain Relation

A hypothetical model on the stress-strain relation is proposed in Figure 3.6. Since vulcanized rubber is composed of a hierarchy of networks as shown in Figure 3.5, the mechanical response with deformation differs at certain strains. The stress-strain relation may be divided into five regions that can be attributed to the molecular response with entanglements, pseudo end-linked network, chemical bond network, and SIC.

I. At un-deformed state, small-angle X-ray diffraction (SAXS) and small-angle neutron scattering (SANS) revealed in-homogeneity in SVNR due to zinc oxide and sulfur combination[28-29]. As shown in Chapter 2, Double-Quantum NMR revealed that PVNR create a rather inhomogeneous distribution of cross-links than SVNR[30-31]. At very small strains, random coil chains between network points and permanent entanglements are displaced in an elastic way. However, the displacements of network points and entanglements may not follow affine deformation, since the system is inhomogeneous due to the non-rubber impurities, lots of entanglements, inhomogeneously distributed chemical bond network points, and far apart pseudo end-linked network points.

II. Chains slide at entanglements, and network points dislocate from their positions to adjust the concentrated force. ESR studies revealed that the radical content due to breakage of sulfur-carbon linkage increases with strain[32].

III. Network points and entanglements are dislocated to reduce the concentrated force and to avoid failure. This is a preparation process for SIC.

IV. SIC takes place. The stress-strain relation shows a plateau because of SIC. The presence of the pseudo end-linked network in NR assists the induction of SIC.

V. SIC increases with the increase of the number of crystallites. SIC become a network point and reduce the molecular weights between network points. Non-Gaussian chains are extended to the limit of extensibility. At lower temperature, the limit of extensibility decreases with the higher stiffness of polymer chain.

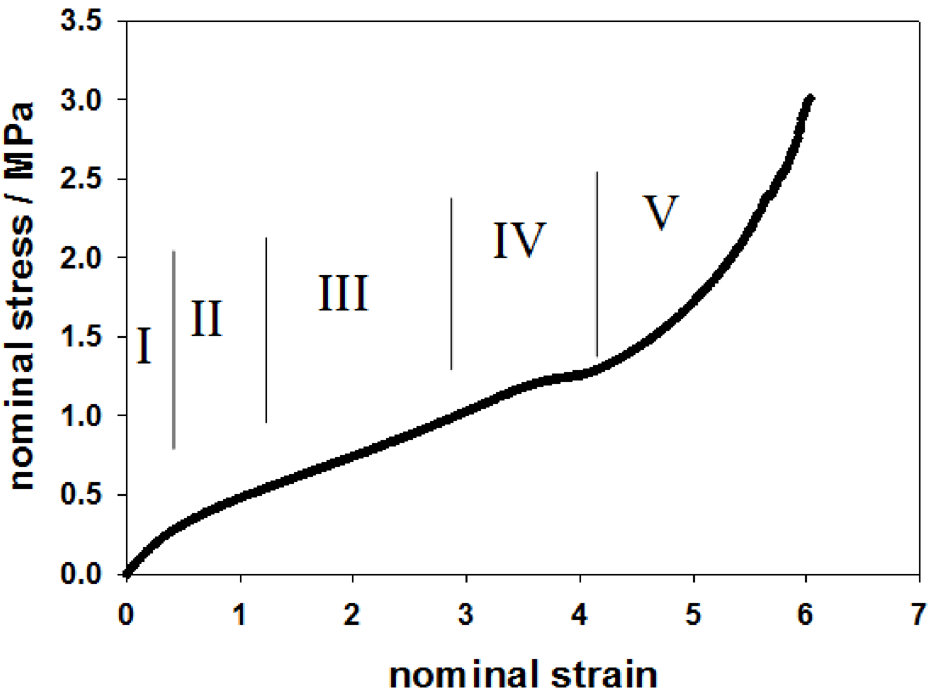

Figure 3.6 A hypothetical model on the stress-strain relation.

3.4 Conclusion

The different behaviors of SIC and stress-strain relations between un-vulcanized and vulcanized NR can be elucidated by entanglements, pseudo end-linked network, chemical bond network, and non-rubber components in the inhomogeneous matrix. Stress at higher temperatures is lower than the stress at lower temperatures in the stress-strain relations in a polymer melt, pseudo endlinked network, and vulcanized rubbers. The theory of rubber elasticity does not seem to be applicable to the stress-strain relation under deformation at various temperatures.

Entanglements can be pivotal points to align rubber chains and to induce SIC. The pseudo end-linked network in NR makes entanglements as permanent entanglements, which can induce SIC and stress upturns. The chemical bond network renders PVNR as an elastic material. During deformation at large strains, polymer chains adjust the concentrated force in order to avoid the failure in the inhomogeneous matrix. SIC reduces tension and energy levels at the local area. As a consequence, SIC delays a stress upturn and increases the strain at break. The stress-strain relation of vulcanized NR is affected by SIC. SIC become a network point and reduce the molecular weights between network points and the limit of extensibility.

3.5 References

1. Katz, J. R., (1925b), *Kolloid Zeitschrif.*, **1925,** *36*, 300
2. Treloar, L. R. G., The physics of rubber elasticity, 3rd ed., Oxfrd press, **1975**
3. Mark, J. E., Erman, B., Rubberlike elasticity. A molecular premier. Wiley-Interscience, New York, **1988**
4. Arruda, E. M., Boyce, M. C. *J. Mechanic. Physic. Solid*, **1993**, *41*, 389
5. Boyce, M. C., Arruda, E. M. *Rubber Chem. Technol.* **2000**, *73*, 504
6. Treloar L. R. G., *Trans. Faraday Society*, **1944**, *40*, 59
7. Treloar, L. R. G., *Trans. Faraday Society*, **1947**, *43*, 284
8. Doi, M and Edwards, S. F., The theory of polymer dynamics. Clerendon press, Oxford, London. **1986**

9. James, H. M., Guth, E., *J. Chem. Phys.* **1943**,*11*, 455
10. Fetters, L. J., Lohse, D. J., Richter, D., Witten, T. A., Zirkel, A. *Macromolecules* **1994**, *27*, 4639
11. Edwards, S. F., Vilgis, T. A., *Rep. Prog. Phys.*, **1988,** *51*, 243
12. Eyring, H., *Physi. Rev*. **1932,** *39*, 746
13. Oka, S. *Proc. Phys-Math. Soc. Japan*, **1942,** *24*, 657
14. deGennes, P. G. *J. Chem. Physi.* **1971**, *55*, 572
15. Doi, M. *J. Polym. Sci. part C : Polym. Letter.* **1981**, *19*, 265
16. Toki, S., Fujimaki, T., Okuyama, M. *Polymer* **2000**, *41*, 5423
17. Toki, S., Sics, I., Ran, S., Liu, L., Hsiao, B, Murakami, S., Tosaka, M.,Senoo, K., Kohjiya, S. *Macromolecules* **2002**, *35*, 6578
18. Murakami, S., Senoo, K., Toki, S., Kohjiya, S. *Polymer* **2002** *43*, 2117
19. Trabelsi S., Albouy. P. A., Rault, J. *Macromolecules* **2003**, *36*, 7624
20. Tosaka, M.; Murakami, S.; Poompradub, S.; Kohjiya, S.; Ikeda, Y.; Toki, S.; Sics, I.; Hsiao, B. S. *Macromolecules* **2004**, *37*, 3299
21. Flory, P. J., *J. Chem. Phys.* **1947**, *15*, 397
22. Flory, P. J., Principles of Polymer Chemistry Cornell University Press, **1953**
23. Toki S., Hsiao S. H., Amnuaypornsri S., Sakdapipanich J. *Polymer* **2009**, *50*, 2142
24. Toki S., Hsiao S. H., Amnuaypornsri S., Sakdapipanich J., Tanaka Y. *J. Polym. Sci. Polym. Phys*. **2008**, *46*, 2456
25. Amnuaypornsri, S.,Toki, S., Hsiao, B. S., Sakdapipanich, J. *Polymer* **2012**, *53*, 3325
26. Anthony. B. L., Caston, R. H., Guth, E. *J. Phys. Chem*., **1942**, *46*, 826
27. Toki, S., Sics, I., Liu, L., Hsiao, B. S., Murakami, S., Tosaka, M., Poompradub, S., Kohjiya, S., Ikeda, Y. *Macromolecules*, **2005**, *38*, 7064
28. Karino, T., Ikeda, Y., Yasuda, Y., Kohjiya, S., Shibayama, M. *Biomacromol.* **2007**; *8,* 693
29. Ikeda, Y; Higashitani, N; Hijikata, K; Kokubo, Y; Morita, Y; Shibayama, M; Osaka, N; Suzuki, T; Endo, H; Kohjiya, S. *Macromolecules* **2009**, *42*, 2741
30. Che, J.; Toki, S.; Valentin, J.; Brasero, J. Nimpaiboon, A.; Rong, L.; Hsiao, B. S. *Macromolecules* **(2012)** *45*, 6491-6503

31. Valentin, J. L., Posadas, P., Fernandez-Terres, A., Malmierca, M. A, Gonzalez, L., Chasse, W., Saalwachter, K. *Macromolecules* **2010**, *43*, 4210
32. Toki, S., Takagi, R., Ito, M., Hsiao B. S. *Polymer* **2011**, *52*, 2453
33. Che, J.; Burger, C.; Toki, S.; Rong, L.; Hsiao, B. S. *Macromolecules*, **(2013)** *46*, 4520-4528

(Chapter 4 reproduced with permission from *Macromolecules, 46*, 4520-4528. Copyright **2013** American Chemical Society.)

Chapter 4

Crystal and Crystallites Structure of Natural Rubber and Synthetic *cis*-1,4-Polyisoprene by a New Two Dimensional Wide Angle X-ray Diffraction Simulation Method: Strain-Induced Crystallization

4.1 Introduction

The significant superiority in mechanical properties of natural rubber (NR) as compared to synthetic rubbers has been considered to originate from strain-induced crystallization (SIC) in NR. In 1925, Katz[1-2] discovered crystals in stretched NR (both un-vulcanized and vulcanized) by wide angle X-ray diffraction (WAXD). In the early to mid-decades between 1930's to 1950's, the crystal structure of stretched and frozen NR was studied intensively and different models of the unit cell were proposed. Mark and von Susich[3] reported an orthorhombic unit cell composed of four molecular chains, with each chain having two isoprene units. Morss[4] and Bunn[5] proposed a monoclinic unit cell (β = 92°) with an internal screw axis symmetry. Nyburg[6] reported an orthorhombic unit cell and internal glide plane symmetry. Natta and Corradini[7] reported a structure similar to Nyburg's model, but with an orthorhombic unit cell of P_{bac} space group with glide plane symmetry. In 2004, Takahashi and Kumano[8] modified Bunn's model slightly and reported a monoclinic unit cell (β = 93.1˚) with space group $P2_1/a$. Immirzi et al.[9] modified Takahashi's model with a pseudo-orthorhombic structure. Rajkumar et al.[10] proposed an orthorhombic unit cell with a space group $P2_12_12_1$ and a glide plane symmetry. These researchers measured un-vulcanized NR and un-vulcanized de-proteinized NR (DPNR) at low temperature such as -25°C or -50°C. The samples were stretched 5-8 times its original length and then set to a sample fixture. This sample with the fixture was frozen and exposed to X-rays for several hours in order to acquire strong X-ray diffraction intensities measured by conventional X-ray instruments. These researchers assumed that SIC can be treated as a fiber symmetry system.

On the other hand, the mechanical properties and strain dependency of SIC has been studied extensively since the 1940s. Gent[11] reported that the stress of peroxide vulcanized NR, after stretching to a certain strain, relaxes to zero in a short period of time at -26°C. During the stress relaxation, the volume of the sample decreases significantly. This suggests that SIC is accompanied with stress relaxation. SIC of NR starts at strain around 2.0 and its crystalline fraction reaches around 30% of all the molecular chains at room temperature. Around 70% of the molecules still remain amorphous even at the highest strain[12-15]. Synchrotron X-ray makes it possible to measure stress-strain relation and WAXD pictures simultaneously. SIC increases with strain during extension and delays to diminish with decreasing strain during retraction. The fiber axis of crystals (c-axis) is parallel to the extension direction[13-14]. The dimensions of SIC crystals increase slightly along the c-axis and decreases along the a- and b- axis during extension[15-16]. The dimensions of crystallites are also changed with extension with the same trends[14-16], however, the volume of crystallites remains constant[14] or slightly decrease with strain[15]. Therefore, the increase of crystalline fraction is caused by the increase of the number of the crystallites[14-15].

Flory[17] elucidated the mechanism of the occurrence of SIC from thermo-mechanics, that is, SIC is caused by the rise of the melting temperature (Tm) due to a decrease in entropy by forced deformation. Therefore, SIC is accelerated at lower temperature because of super cooling conditions. On the other hand, it is known that un-vulcanized NR preserved in a refrigerator shows whitening due to crystallization. Since the Tm is around room temperature, and the crystallization temperature (Tc) is around -10°C, the preserved un-vulcanized rubber shows crystallization that can be called as temperature-induced crystallization (TIC). Previous researcher's samples may be affected by TIC, since TIC could be occurred in the sample after the stress relaxes to zero. The initiation of SIC at a certain strain is very fast, such as 60 millisecond[18] and around 100 millisecond[16,19]. Therefore, SIC might be completed at a certain strain during extension.

As discussed in Chapter 1, NR is a compound of *cis*-1,4-polyisoprene with functional groups at both chain ends and non-rubber components (6 wt.% in fresh latex and 2 wt.% in solid rubber) including proteins, phospholipids, quebrachitol, stearic acid, metal ions, etc. With these functional groups and non-rubber components, NR forms a pseudo-network that shows high tensile strength and elasticity[20-22]. On the other hand, synthetic polyisoprene is a polymer melt that shows only a viscous response. Some of the non-rubber components in NR, such as quebrachitol and stearic acid, make crystals and some, such as phospholipids and proteins, make agglomerates or aggregates[20-21, 23]. These components and pseudo-networks may become constraints for movement of polymer chains in NR. This chapter aims to apply a two dimensional WAXD simulation method to SIC in un-vulcanized NR and synthetic *cis*-1,4-polyisoprene (IR) at -50˚C in order to determine the most plausible crystal structure, crystallite size, crystalline fraction, crystallite orientation and crystal disorder.

4.2 Experimental Methods

4.2.1 2D WAXD Pattern Simulation

Two dimensional WAXD images include information of not only unit cell dimension, atomic coordinates, space group and symmetry, but also crystallite size, crystallite orientation, crystalline fraction and disorder in crystal. Our group has developed a method to analyze whole information in two dimensional images rather than the integrated one dimensional data[24]. Burger[24-25] and Mao[26] have applied their two dimensional WAXD pattern simulation method on collagen, cellulose fibers and propylene-1-butylene random copolymer. The scattering X-ray intensity of an individual (*hkl*) plane in reciprocal space is directly proportional to the square of the structure factors $F_{hkl}(s)$:

$$I_{hkl}(s) \sim [F_{hkl}(s)]^2 \qquad (4.1)$$

where s is the absolute value of the scattering vector **s**. We assume simple fiber symmetry in SIC. An orientation distribution function $F(\varphi,\varphi_{hkl})$ can be introduced to calculate the scattering intensity distribution of the entire fiber system $J(s, \varphi)$:

$$J(s,\varphi) = \int_0^{\pi/2} I(s,\varphi_{hkl})\,F(\varphi,\varphi_{hkl})\,\sin\varphi_{hkl}\,d\varphi_{hkl} \tag{4.2}$$

Here φ and φ_{hkl} denote the polar angle of the fiber and the individual structural unit, respectively. Figure 4.1 shows the geometric relationships between s and the primary axes of the fiber $J(s, \varphi)$ and individual structural unit $I(s,\varphi_{hkl})$, which is adopted from Ruland[27].

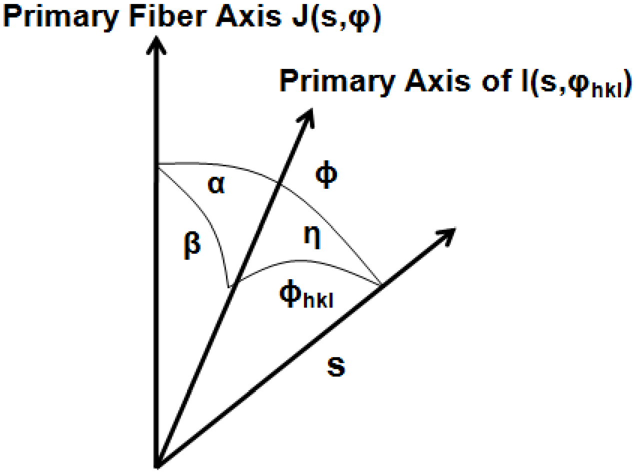

Figure 4.1 Geometric relationship between the scattering vector s and the primary axes of the fiber $J(s, \varphi)$ and individual structural unit $I(s,\varphi_{hkl})$.

In order to calculate the size of crystallites, we introduce a term w which is the width in the radial direction and its reciprocal value gives an estimate for the average crystallite size. The scattering intensity distribution $I(s,\varphi_{hkl})$ of an (hkl) plane with radius s_{hkl} and polar angle φ_{hkl} can be given as:

$$I(s,\varphi_{hkl}) = (4\pi w s^2_{hkl})^{-1}\ I_{hkl}(s)\ Ho[(s - s_{hkl})/\ w] \tag{4.3}$$

where Ho is a one-dimensional normalized peak distribution function. In this simulation work, we used a Lorentzian distribution function that takes the form $Ho(t) = (1+\pi^2 t^2)^{-1}$.

In order to estimate the orientation of crystallites, we introduced a term $g(\beta)$ which is the orientation distribution function, where β is the angle between the primary fiber axis and the primary axis of the structural unit. In this simulation, we used a modified Onsager distribution function for $g(\beta)$ that was proposed by Burger[25]:

$$g(\beta) = p_0 + (1-p_0)\ p \cosh(p \cos\beta)/\sinh(p) \tag{4.4}$$

where p_0 is the isotropic un-oriented fraction, and p is the width of the distribution of the oriented fraction. The function $F(\varphi,\varphi_{hkl})$ can now be written as:

$$F(\varphi,\varphi_{hkl}) = p_0 + (1-p_0)\ (p \cosh\ (p \cos\varphi \cos\varphi_{hkl})\ /\ \sinh(p))\ \ I_0(p \sin\varphi\ \sin\varphi_{hkl}) \tag{4.5}$$

where I_0 is the modified Bessel function of the first kind of order 0. In this case, the Hermans' orientation factor P_2 is given by[25]:

$$P_2 = (1-p_0)\{1 - 3p^{-1}[\coth(p)-p^{-1}]\} \tag{4.6}$$

P_2 is equal to 1 for a perfectly oriented system parallel to the stretching direction, 0 for random orientation, and -0.5 for a perfected oriented system perpendicular to stretching direction. The shape of the crystal can be obtained from the combination of the size and orientation of the crystal.

In order to estimate the crystal lattice disorder, we introduce the Debye-Waller factor (DWF), which corrects for lattice disorder and displacement due to thermal motion The DWF describes the lattice vibrations on Bragg-peak intensities and can be given by[28-29]:

$$\mathrm{DWF} = \exp\ (-Bs^2) \tag{4.7}$$

where B is proportional to the mean square displacement of the atoms, and s is the scattering vector. A highly ordered crystal lattice leads to low values for B that does not suppress the scattering intensity.

Finally, the overall fiber averaged intensity distribution can now be written as a combination of equations 4.3, 4.5, and 4.7:

$$J(s, \varphi) = (4\pi w s^2_{hkl})^{-1}\, I_{hkl}(s)\, H_0[(s - s_{hkl})/ w] \cdot (p_0 + (1-p_0)\, (p \cosh (p \cos \varphi \cos \varphi_{hkl}) /\sinh(p))\, I_0(p \sin \varphi \sin \varphi_{hkl})) \cdot \exp(-\boldsymbol{B} s^2) \tag{4.8}$$

In order to estimate the crystalline fraction, the amorphous halo could be described by three separate Gaussian intensity distribution functions. The crystalline fraction is determined by taking the ratio of the integrated crystal areas with the total integrated area in the simulated intensity distribution.

4.2.2 Materials and Sample Preparation

Two samples were used in this study: un-vulcanized natural rubber (NR) and synthetic *cis*-1,4-polyisoprene (IR). Raw NR latex sample was provided by the Thai Rubber Latex Company, Thailand. The fresh NR latex was preserved in ammonia for 3 months at room temperature. The preserved NR was then casted on glass dishes and dried in an oven at 60˚C for 48 hours. The synthetic IR used in this study was IR2200 manufactured by JSR. Both of these samples were dissolved in toluene and then casted onto glass dishes. After the evaporation of the solvent, the films created were 1 mm in thickness.

Prior to stretching, the samples were pre-cut into dumbbell-like shapes. The total lengths of the samples were 50 mm. The narrow section of the dumb-bell shaped samples were 30 mm in length and 4 mm in width.

4.2.3 Time-Resolved WAXD Measurements and Tensile Deformation

Stress-strain measurements were recorded simultaneously with the time-resolved WAXD measurements during tensile deformation. The strain is defined as the difference of the deformed length and the original length divided by the original length ((l-lo)/ lo). A modified Instron 4442 tensile stretching instrument was used that allowed the uniaxial and symmetric deformation of the sample, while monitoring the structural changes of the sample by illuminating the same sample position during deformation. The samples were deformed up to strains of 6.0 at a stretching rate of 10 mm/min. Tensile deformation was carried out at -50˚C. The samples were set in a heat chamber at -50˚C for 3 minutes before stretching. The time for stretching is about 20 minutes. This condition does not allow for the additional effect of temperature and time.

Synchrotron X-ray measurements were carried out at the X27C beamline in the National Synchrotron Light Source (NSLS), Brookhaven National Laboratory (BNL). The X-ray wavelength was set at 1.371 Å. Two-dimensional (2D) wide-angle X-ray diffraction (WAXD) patterns were acquired using a MAR-CCD detector. The acquisition time for each frame was 30 seconds. Al_2O_3 standard was used to calibrate the scattering angle. The sample-to-detector distances for WAXD was 114 mm. X-ray data analysis was performed using the software Polar (Stony Brook Technology and Applied Research, Stony Brook, New York). All diffraction signals were corrected for beam fluctuations and background scattering. It is to be noted that the observed WAXD patterns were also corrected for the distortion due to the curvature of the Ewald sphere (Fraser correction[30]).

4.3 Results and Discussion

The experimentally obtained, with Fraser corrected, WAXD images at strain 6.0 for un-vulcanized NR and IR at -50˚C are shown in Figure 4.2. The images were obtained for 30 sec exposing time. The sample may not have the influence of TIC and stress relaxation. Since the Tg of NR and IR (-70˚C and -65˚C respectively) are close to the measuring temperature, the stresses at the strain 6.0 are more than 10 MPa. The detail of stress-strain relation and mechanism of SIC at low temperature will be discussed elsewhere. The peaks are named by the index of the diffraction planes of crystal according to previous researcher's data[9]. With the Fraser correction, the patterns show an empty area along the meridian where the intensity distribution will not intersect with the Ewald sphere. In this case, information regarding the (001), (002) crystal plane peaks, and partial information about the crystal size along the *c*-axis may be lost. Trabelsi et al.[14] and Tosaka et. al.[16,19] built a stretching machine that can be tilted to the X-ray in order to obtain information along the meridian. They confirmed that the presence of the (002) plane peak in the crystal, along with the absence of the (001) peak. The peak positions between the NR and IR samples look similar, even though NR and IR are of different origin and stereo-regularity. The WAXD pattern shown for this IR sample only contains the SIC of pure *cis*-1,4-polyisoprene, since no impurity is included in IR. On the other hand, it is clear that the shapes of the crystal peaks are different (round and crescent) between the two samples. These differences are attributed to the size, orientation, and disorder of the crystal and crystallites, which affects the shapes along the lateral and phi direction. The peak positions of (110) and (200) are close to each other. It is impossible to separate the intensity of these unit cell planes from the 2D images. The peaks (020) and (120) are of the same situation. Immirzi[9] showed the close relations of these two peaks in their table of structure factors.

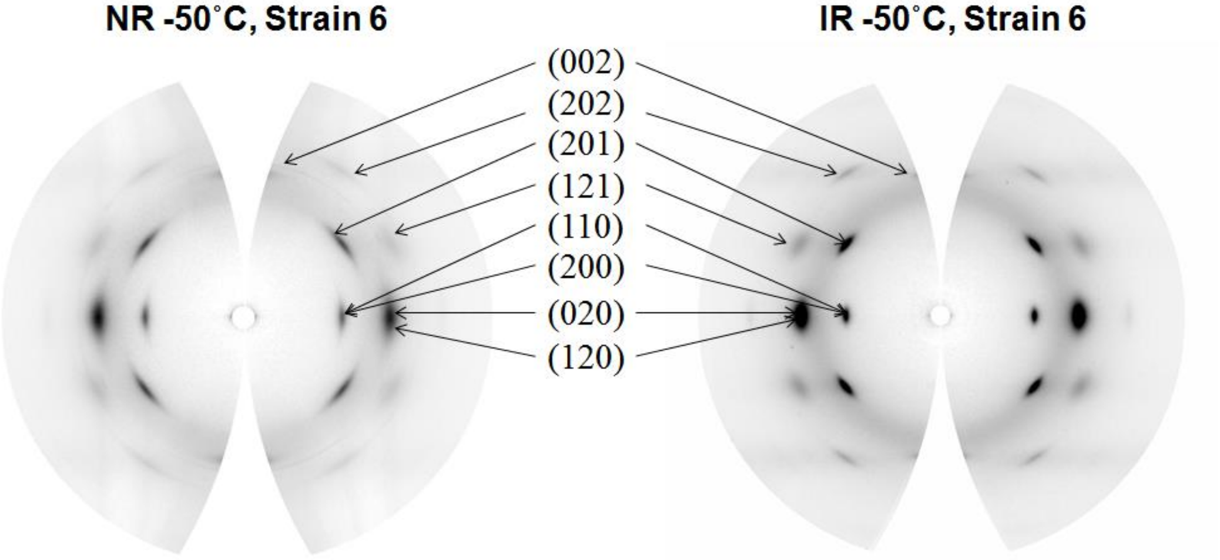

Figure 4.2 Observed WAXD images, with Fraser correction, at strain 6.0 for un-vulcanized NR and IR at -50˚C.

In order to determine the unit cell dimensions, space group and space symmetry, we integrated the 2D images into the one-dimensional profile in Figure 4.3. A general software for crystallography, Bruker TOPAS, was applied to analyze the one-dimensional profile and concluded that the strain-induced crystallite is an orthorhombic unit cell with space group $P2_12_12_1$. This conclusion is consistent with Rajkumar et.al.[10].

The reported crystal peak positions and relative intensities of (200), (201), and (120) by Takahashi[8], Immirzi[9], and Rajkumar[10] are presented as points and bars in Figure 4.3. Figure 4.3 also shows our observed data on the NR and IR diffraction profiles, including the amorphous diffraction (called as amorphous halo). Takahashi did not show the peak positions in his table of observed and calculated structure factors, but Immirzi analyzed Takahashi's data and determined the Bragg d-spacings. Therefore, they both started from the same observed data, but their conclusions were different, i.e., Takahashi chose a monoclinic unit cell and Immirzi selected a pseudo-orthorhombic unit cell. On the other hand, the peak positions and measured structure amplitudes for Rajkumar's observed data is shown in their table 1. The peak positions of Takahashi-Immirzi, Rajkumar and our observed data are slightly different from each other. The difference in peak positions lead to different atomic coordinates and unit cell dimensions.

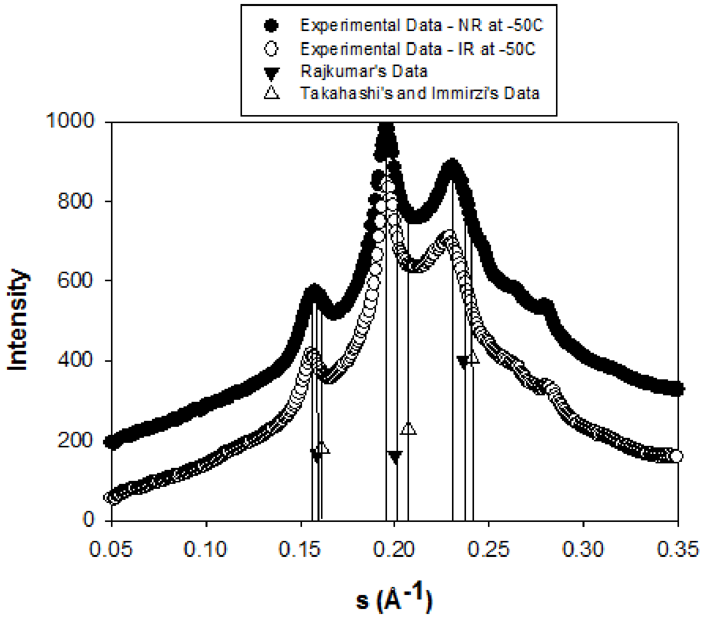

Figure 4.3. The scattering peak positions and relative intensities in one dimensional profile of Takahashi-Immirzi's data (Δ), Rajkumar's data(▼) and our observed profile of NR and IR.

Our observed NR and IR profiles showed the same peak positions as shown in Figure 4.3. The crystal unit cell of *cis*-1, 4-polyisoprene seems to be not affected by the stereo-regularity and impurity differences. The observed WAXD intensities of NR at different strains are shown in Figure 4.4. The WAXD intensities are composed of amorphous halo and crystalline peaks. At strain 0, all molecules are in the amorphous state. SIC is observed at higher strains, and the peak positions do not change during extension.

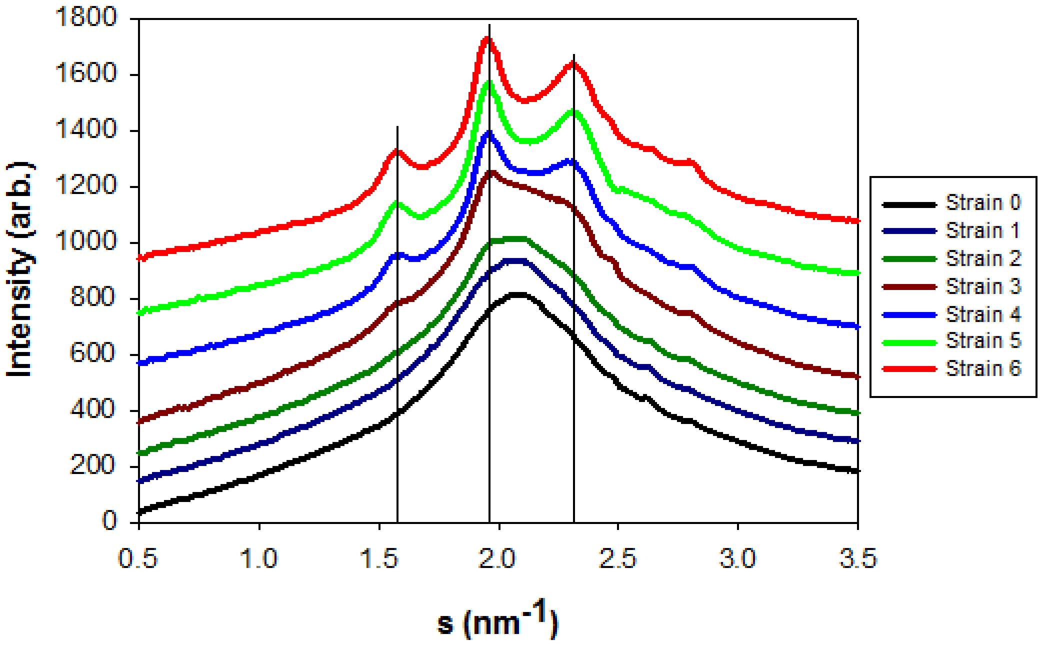

Figure 4.4 One-dimensional integrated intensities of NR at -50˚C at various strains. From strains 0.0 to 3.0, the amorphous halo is observed. From strains 4.0 to 6.0, both the crystal peaks and amorphous halo are observed.

Previous researchers picked up more than 40 peak positions in order to determine the unit cell dimensions and atom coordinates. On the other hand, we focused only on the three strong peak positions (200), (201), and (120), since the intensities at other positions are significantly weaker. In the case of an orthorhombic unit cell, these three positions are enough to determine the unit cell dimensions. Takahashi and Kumano measured un-vulcanized DPNR (3 mm thick and 3 mm wide) with 7 times the extension at -50°C using a conventional X-ray instrument.

Rajkumar et al. measured un-vulcanized NR at room temperature by a conventional X-ray instrument, but there was no mention on the extension ratio and the exposing time. In the case of un-vulcanized NR at room temperature, it may take several hours in order to acquire enough intensity to analyze the data of more than 6 times the extension, and the stress may decrease quickly.

We adopted the carbon atom coordinates from Rajkumar et al. From the peak positions of (200), (201), (120), we determined our unit cell dimension as a = 13.048 Å, b = 9.391 Å, and c = 8.551 Å. The dimensions of our unit cell are slightly larger than the dimensions of Rajkumar, which are a = 12.586 Å, b = 8.985 Å, and c = 8.205 Å. As a consequence, a linear expansion of unit cell and affine displacements of carbon atoms of Rajkumar's unit cell structure is assumed. Our unit cell model is shown in Figure 4.5.

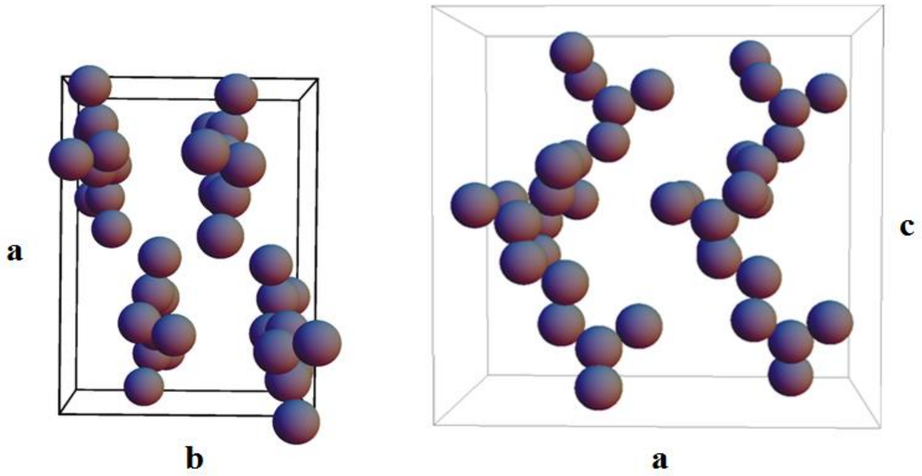

Figure 4.5 Orthorhombic unit cell of *cis*-1,4-polyisoprene with $P2_12_12_1$ symmetry. The unit cell dimensions are a = 13.048 Å, b = 9.391 Å, and c = 8.551 Å. These carbon atom coordinates are modified Rajkumar's coordinates.

Based on our atomic coordinates and unit cell dimensions, the scattering X-ray intensity of an individual (hkl) plane in reciprocal space were calculated using Equation 4.1. Table 4.1 shows the scattering positions s, Bragg spacing d, the total observed and calculated WAXD intensities for each specific (hkl) plane of NR at strain 6.0. It is to note that the scattering intensities shown in Table 4.1 also includes the intensities of the amorphous halo, although previous researchers did not concern the amorphous molecules' contribution.

By comparing the observed and calculated WAXD intensities, these values are in close correspondence with each other, which is an indication that our modified Rajkumar's unit cell structure is a suitable model for SIC of *cis*-1,4-polyisoprene at -50°C. We have also compared Takahashi's and Immirzi's model, but we have found that the correspondence is not as closely as our modified Rajkumar's model. We also confirmed that calculated and observed of NR at strain 3.0 and 4.0 with our modified Rajkumar's model are very close.

In order to determine crystallites size, crystallites orientation and crystal disorder, we simulate the calculated values with *w*, p, and B in Equation 4.8 to match the experimentally observed peaks in the 2D WAXD images and its corresponding one-dimensional integration. During the simulation process, *w*, p, and B were varied to improve the fitting. Each parameter varies the fiber patterns differently, and each individual parameter tells a specific aspect of the crystallite. Varying *w* will change the width of the peaks along the radial direction, which can tell us information about the sizes of the crystallite. A larger *w* used in the diffraction pattern indicates a smaller size crystallite in real space. Varying p will change the width of the peaks along phi. A p value close to zero will produce a powder diffraction pattern with rings that have no orientation, whereas a large p value will produce sharp diffraction reflections that have high orientation. Varying B will change the intensity of certain Bragg peaks, where the relative ratios of the diffraction peak intensities can be adjusted. The best combinations of *w*, p, and B were obtained for each sample at specific strains after matching the simulated pattern to the observed pattern with the highest R^2 value and with R^2 values greater than 0.98.

Table 4.1 Observed and calculated WAXD intensities for each specific (*hkl*) planes

s (Å^{-1})	d (Å)	I_{obs}	I_{sim}	h	k	l
0.1312	7.622	237.7	237.1	-1	-1	0
				-1	1	0
				1	-1	0
				1	1	0
0.1533	6.524	571	563.2	-2	0	0
				2	0	0
0.1582	6.323	470	469.2	0	-1	1
				0	1	1
0.1758	5.690	476.4	478.6	-1	-1	1
				-1	1	1
				1	-1	1
				1	1	1
				-1	-1	-1
				-1	1	-1
				1	-1	-1
				1	1	-1
0.1866	5.358	640.1	679.6	-2	-1	0
				-2	1	0
				2	-1	0
				2	1	0
0.1928	5.187	918.2	878.2	-2	0	1
				2	0	-1
				-2	0	1
				2	0	-1
0.2130	4.695	750.9	768.7	0	-2	0
				0	2	0
0.2203	4.540	878.3	886.6	-2	-1	1
				-2	1	1
				2	-1	1
				2	1	1
				-2	-1	-1
				-2	1	-1
				2	-1	-1
				2	1	-1
0.2263	4.418	983.4	989.7	-1	-2	0
				-1	2	0
				1	-2	0
				1	2	0
0.2339	4.276	832.4	806.0	0	0	2
				0	0	-2
0.2534	3.947	463.3	476.4	-3	-1	0
				-3	1	0
				3	-1	0
				3	1	0
0.2548	3.925	461.7	469.4	-1	-2	1
				-1	2	1
				1	-2	1
				1	2	1
0.2624	3.811	432.0	408.4	-2	-2	0
				-2	2	0
				2	-2	0
				2	2	0
0.2682	3.729	383.7	352.9	-1	-1	2
				-1	1	2
				1	-1	2
				1	1	2
				-1	-1	-2
				-1	1	-2
				1	-1	-2
				1	1	-2
0.2791	3.583	368.4	303.4	-3	-1	1
				-3	1	1
				3	-1	1
				3	1	1
				-3	-1	-1
				-3	1	-1
				3	-1	-1
				3	1	-1
0.2796	3.576	367.5	300.1	-2	0	2
				2	0	2
				-2	0	-2
				2	0	-2
0.2873	3.481	301.3	276.2	-2	-2	1
				-2	2	1
				2	-2	1
				2	2	1
				-2	-2	-1
				-2	2	-1
				2	-2	-1
				2	2	-1
0.2992	3.342	255.3	248.8	-2	-1	2
				-2	1	2
				2	-1	2
				2	1	2
				-2	-1	-2
				-2	1	-2
				2	-1	-2
				2	1	-2
0.3281	3.048	190.8	217.5	-4	0	1
				4	0	1
				-4	0	-1
				4	0	-1
0.3285	3.044	189.3	216.3	-1	-3	0
				-1	3	0
				1	-3	0
				1	3	0
0.3345	2.989	183.7	208.9	-3	-2	1
				-3	2	1
				3	-2	1
				3	2	1
				-3	-2	-1
				-3	2	-1
				3	-2	-1
				3	2	-1
0.3066	3.262	242.5	239.7	-4	0	0
				4	0	0
0.3134	3.191	230.0	231.5	-3	-2	0
				-3	2	0
				3	-2	0
				3	2	0
0.3163	3.161	221.9	228.7	0	-2	2
				0	2	2
				0	-2	-2
				0	2	-2
0.3245	3.081	197.9	221.8	-4	--1	0
				-4	1	0
				4	-1	0
				4	1	0
0.3255	3.072	196.5	220.8	-1	-2	2
				-1	2	2
				1	-2	2
				1	2	2
				-1	-2	-2
				-1	2	-2
				1	-2	-2
				1	2	-2
0.3402	2.940	179.2	195.3	0	-3	1
				0	3	1
				0	-3	-1
				0	3	-1
0.3448	2.900	179.0	188.8	-3	-1	2
				-3	1	2
				3	-1	2
				3	1	2
				-3	-1	-2
				-3	1	-2
				3	-1	-2
				3	1	-2
0.3450	2.899	179.0	186.7	-4	-1	1
				-4	1	1
				4	-1	1
				4	1	1
				-4	-1	-1
				-4	1	-1
				4	-1	-1
				4	1	-1

The simulated two-dimensional WAXD patterns were compared with the observed patterns. Figure 4.6 shows the observed and simulated WAXD patterns at strain 6.0 for NR and IR at -50˚C. The WAXD patterns for other strains look similar and are not shown here. In all these images, the top and bottom portions of the images represent the observed and simulated WAXD pattern, respectively. It is to be noted that the observed images were the Fraser corrected images, where a portion of the (002) peak information may be lost. On the other hand, the simulation can produce the full (002) crystal peak and information on the crystallite size of the c-axis can be determined. From Figure 4.6, it is clear that the simulated WAXD image demonstrate an excellent fit to the experimental image for both samples. The different shapes of peaks in NR and IR are simulated, such as crescent and round, based on crystallites size and orientation.

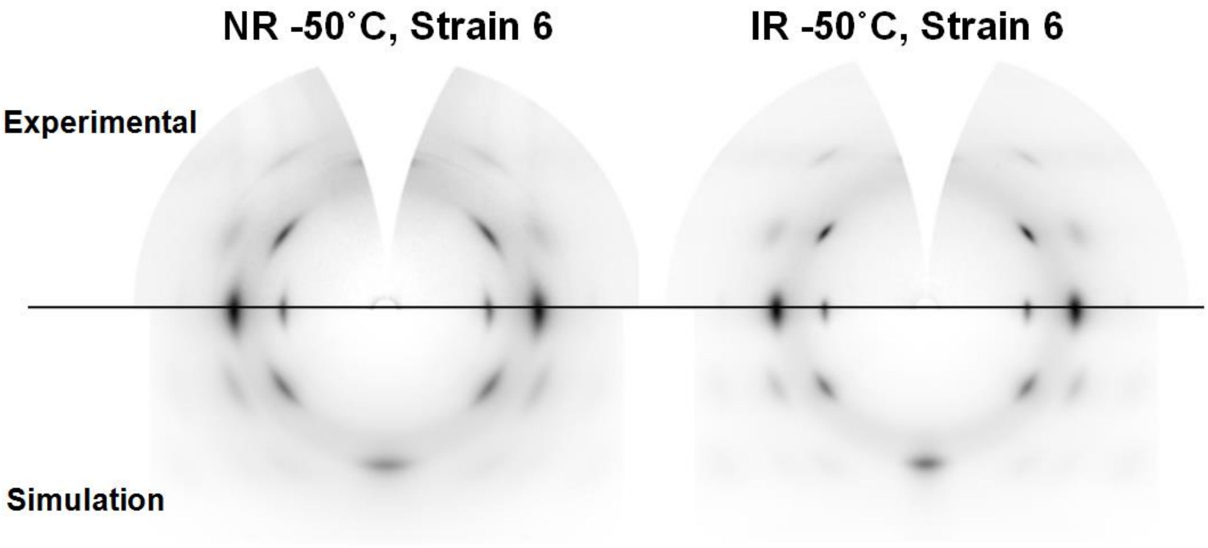

Figure 4.6 Two-dimensional observed and simulated WAXD patterns at strain 6.0 for NR and IR at -50˚C. The top and bottom portions of the images represent the observed and simulated WAXD pattern, respectively.

Since the two-dimensional patterns show a good agreement between the simulated and observed, it is also important that it fits well in the one-dimensional space. Figure 4.7a shows the one-dimensional integrated intensity profile of the experimental (solid line) and simulated (long dashed line) WAXD pattern at strain 6.0 for NR and IR at -50˚C. The small dashed lines represent the separated simulated peaks of the total integrated intensity, which is composed of the amorphous halo (fitted using three Gaussian peaks) and oriented crystalline peaks.

In order to determine the goodness of fit between the simulation and observed, the standardized residuals and R^2 values were calculated. The standardized residual is defined as $(I_{sim}-I_{obs.})/\sigma$, where I_{sim} and $I_{obs.}$ are the intensities obtained from the simulation and observed respectively, and σ is the standard deviation. Figure 4.7b shows the one-dimensional standardized residual plots calculated from the difference between the simulation and observed intensities in Figure 4.7a. The R^2 values were calculated for these fittings for NR and IR at -50˚C to be 0.988 and 0.986 respectively. The residual plots show random patterns with no trends, which indicate a good fitting of our simulation intensities to the observed.

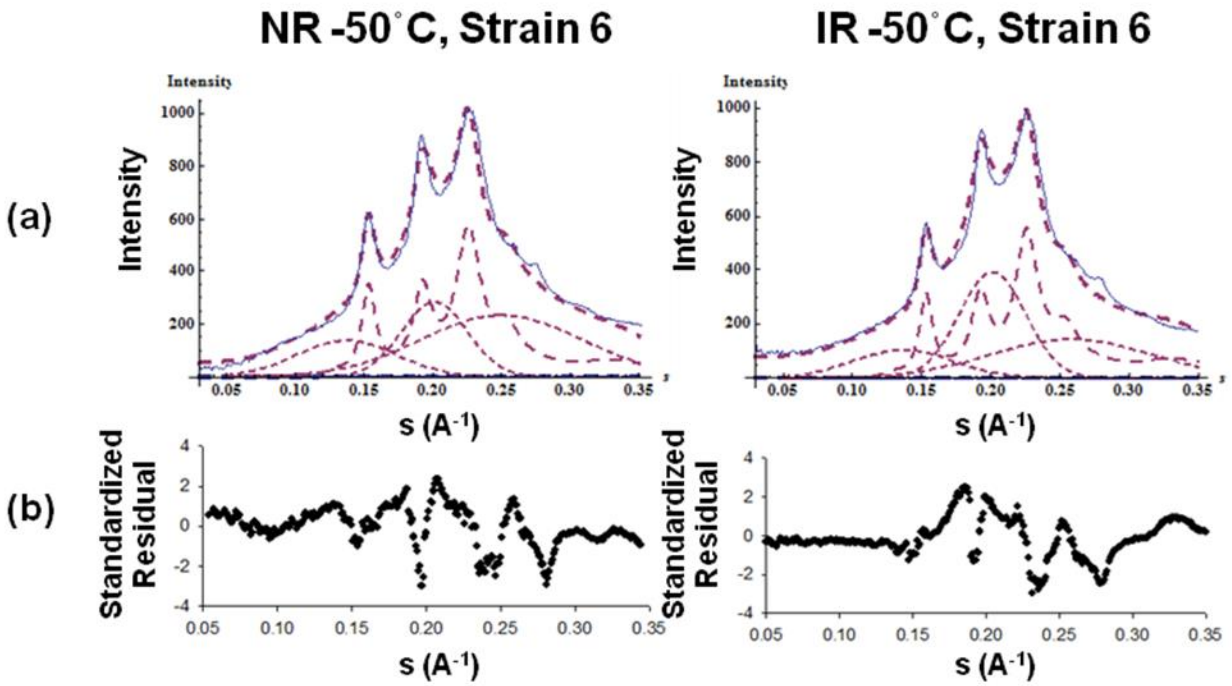

Figure 4.7 (a) One-dimensional integrated intensity profile of the observed (solid line) and simulated (long dashed line) WAXD pattern at strain 6.0 for NR and IR at -50˚C. The separated simulated peaks are shown in small dash lines. (b) One-dimensional standardized residual plots calculated from the difference between the simulation and observed intensities in (a).

4.3.1 Crystalline Fraction

The crystalline fractions were determined from the one-dimensional integrated profiles of the simulated WAXD patterns by taking the ratio of integrated areas of the crystal peaks to the total integrated area. The crystalline fraction increases with strain as shown in Figure 4.8. NR at -50˚C has the larger crystalline fraction than IR at any strain, and this tendency have been reported in vulcanized NR and IR at +25 ˚C [31-33]. Therefore, it is noteworthy that the difference in SIC between NR and IR is prevailed from -50 C to +25 ˚C, in both the vulcanized and un-vulcanized state. The onset strain (initial strain where crystallization start to be observed) of crystallization can be determined from the best fit curve applied to each sample by extrapolating the plot of crystalline fraction versus strain to the crystalline fraction at 0% position. The crystalline fraction starts at strain 1.61 in NR and strain 3.97 in IR.

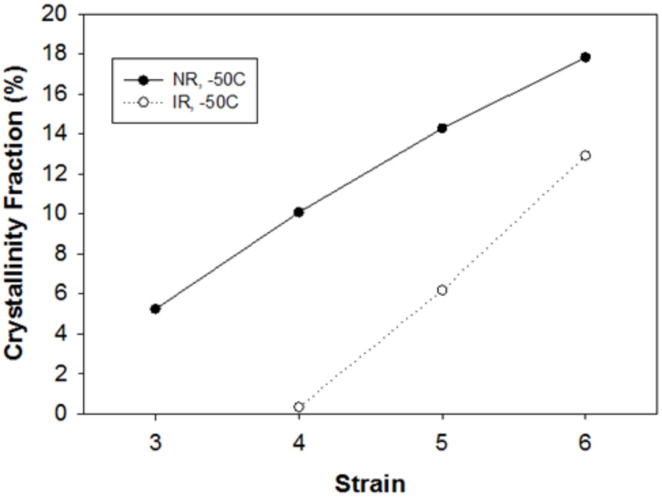

Figure 4.8 Crystalline fractions as a function of strain for NR and IR at -50˚C. The onset strains of SIC in NR and IR are 1.61 and 3.97, respectively.

4.3.2 Crystallite Size

Conventional one-dimensional WAXD analysis to determine lateral crystallite sizes (L) includes the use of the Scherrer's equation, i.e., $L_{hkl} = K \cdot \lambda /(\beta \cos \theta)$. Because Scherrer's equation uses the averaged one-dimensional integrated WAXD intensity, this equation leads to some limitations and inaccuracies in determining crystallite sizes. This averaged intensity approach typically contains closely spaced peaks that are partially blended together, such as (200) blended with (110), and (120) blended with (020) as shown in Table 4.1. Therefore, it can be difficult to separate these peaks and determine the exact peak widths, leading to inaccurate determinations of the apparent crystallite sizes. Furthermore, a peak-broadening effect can also be attributed to micro-strains (or other types of lattice disorder) and instrumental effects. All these effects must be accounted for in order to obtain accurate crystallite sizes. Another major inaccuracy of the Scherrer equation is the determination of the true value of K. The value of K is determined by the shape of the crystal and influences how the width is determined. Typical K values for natural rubber have been reported to range from 0.8 to 1.0, where 1.0 signifies a perfectly symmetric peak shape profile. The values in this range essentially assume spherical crystals which may not be an accurate description for the present more anisotropic situation.

In the new two-dimensional simulation approach, exact scattering angles are defined and do not require the use of the true value of K. For the simulated WAXD patterns, the lateral crystallite sizes were estimated from taking the reciprocal value of the width, w, obtained in Equation 4.8. The lateral crystallite sizes were estimated using the (*200*) and (*120*) diffraction peaks. Figure 4.9a shows the lateral crystal sizes for (*200*) and (*120*) diffraction peaks as a function of strain for NR and IR at -50˚C. For all the samples, the lateral crystallite size decreased only slightly with increasing strain, even up to strains 6. The unit cell contracts slightly in the direction perpendicular to the deformation (the *a*- and *b*-directions), as Trabelsi et. al.[14] and Tosaka et. al.[15] reported. The size of the (*200*) crystallite is almost doubled that of the (*120*) crystallite. The *c*-axis crystallite size can be estimated using the (002) diffraction peak and shown in Figure 4.9b. The size in the c-axis seems to be not changed in spite of being extended to this direction. The crystallites sizes do not seem to be changed. They are almost constant as Trabelsi reported, although they used Scherrer's equation. Since the crystallite sizes are almost constant, the larger crystalline fraction is attributed to the increase of the number of crystallites. From the width of L_{200}, L_{120} and L_{002}, the crystallites dimensions are calculated as 5.51nm x 3.12nm x 3.00 nm in the a, b, and c direction respectively. This may suggests that there are around four unit cells in the crystallites along the three directions. The size is very small as compared to the dimensions at +25˚C[14-15]. We will report the dimensions at higher temperature elsewhere.

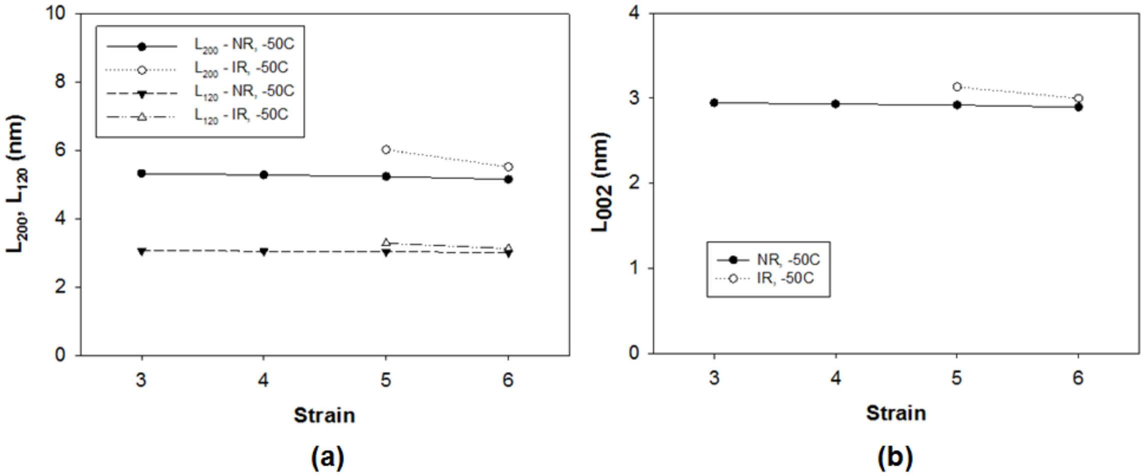

Figure 4.9 Crystallite sizes of the (*200*), (*120*) and (002) diffraction peaks as a function of strain for NR and IR at -50˚C

4.3.3 Crystallite Orientation

The crystallite orientations throughout deformation were determined using the Hermans' orientation parameter (P_2) in Equation 4.6. The comparison of the P_2 orientation factors with respect to strain for NR and IR at -50˚C is shown in Figure 4.10. The orientation increases with strain and approaches a value close to 1, which indicates the increase in alignment of crystallites along the stretching direction during deformation. The orientation of IR is higher as compared to NR at -50˚C. We (along with previous researchers) assumed that SIC are completely parallel to the extension direction and fiber symmetry. But this result suggest that SIC are not completely aligned and NR seems to have more constraint to be parallel than IR. These phenomena must be accelerated at -50˚C since molecules are more rigid than at +25˚C. The results can be expected from Figure 4.2, since NR peaks have shapes that are crescent and IR peaks are round. The difference between NR and IR may be caused by pseudo network and impurities in NR, such as the large crystals of quebrachitol and stearic acid, and big agglomerates including proteins and phospholipids.

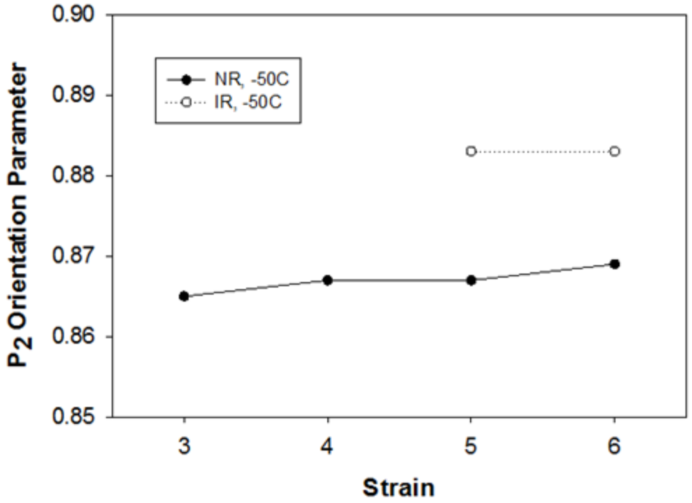

Figure 4.10 P_2 orientations of the crystallites as a function of strain for NR and IR at -50˚C.

4.3.4 Displacement Disorder in Crystal

A plot of the Debye-Waller factor, *B,* in Equation 4.7 with respect to strain for NR and IR at -50˚C is shown in Figure 4.11. The value of *B* decreases with strain, which is an indication of higher order at large strains. This is consistent with the increase in orientation with strain as shown in Figure 4.10. Therefore, crystallites become oriented and less disordered during extension. The magnitude of disorder is around a few angstroms according to the *B* value, since *B* can be expressed as $2\pi^2/3 \times \Delta u^2$, where Δu is the displacement of atoms in the case of an ideal free lattice and atoms can move independently from unit cell[26]. In the case of polymer crystals, there are defects/dislocations located inside of the crystals and folding of chains located on the surface. Therefore, the structure disorder may contribute to the B factor. We consider the value of B as a measure of disorder of SIC. The NR samples have a higher *B* as compared to IR at -50 ˚C. This is against the fact that NR is composed of a more perfect stereo-regularity (100 %) of *cis*-1,4-polyisoprene than IR (98.5%). The non-rubber components and pseudo network in NR may lead to more constraints that may affect the B-factor. SIC in NR may be activated by the pseudo-network or non-rubber components rather than perfect stereo-regularity.

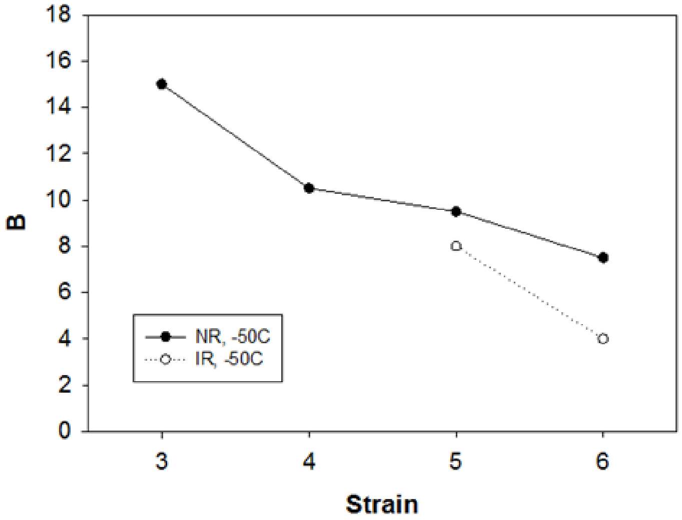

Figure 4.11 Debye-Waller factors, B, as a function of strain for NR and IR at -50˚C.

4.3.5 Proposed SIC Model

From the two-dimensional WAXD simulations, we found the same unit cell dimensions for both NR and IR at -50˚C and have showed an excellent agreement between the simulation and observed results. The average number amount of unit cells per crystallite (*n*) in the *a*, *b*, and *c* direction (denoted as *a* x *b* x *c*) were determined from the unit cell lattice constants and the lateral crystallite sizes. Since the crystallite sizes and unit cell constants of NR and IR at -50˚C were almost identical even up to strain 6.0, they both contain 4 x 4 x 4 unit cells per crystallite at -50˚C. Only the crystallite size for NR at -50˚C is shown in Figure 4.12. The model for IR at -50˚C look similar, but with smaller amounts of crystallites since the crystalline fraction is smaller than NR at -50˚C.

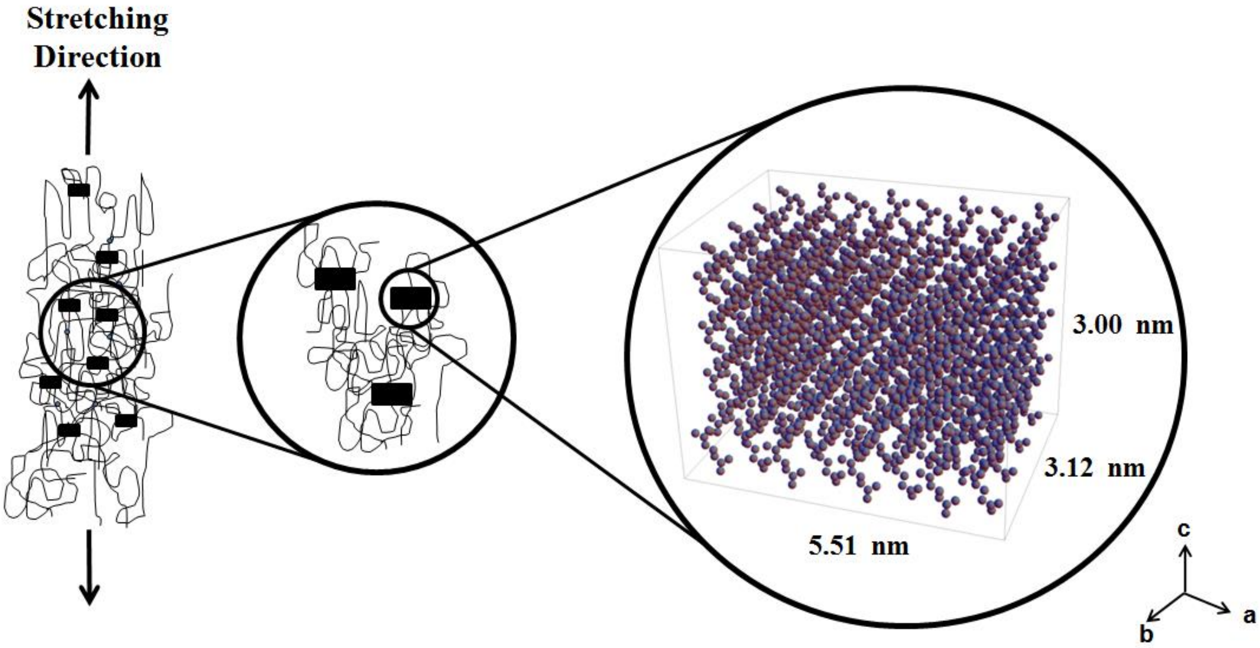

Figure 4.12 A model of the average crystallite size for the SIC of un-vulcanized NR at -50˚C.

4.4 Conclusion

A new two-dimensional simulation approach has been presented to generate the WAXD patterns for SIC of un-vulcanized NR and IR at -50 C. The calculated scattering intensities based on the modified atomic coordinates of Rajkumar et. al. are very close to our observed data. We concluded that the unit cell of SIC is orthorhombic, $P2_12_12_1$ symmetry, with lattice constants of a = 13.04 Å, b = 9.39 Å, and c = 8.55 Å. The dimensions of unit cell of NR and IR are the same and do not change during deformation.

The simulation of 2D WAXD images with the width of crystallites w, the orientation of crystallites p, the crystal disorder B, following calculated scattering intensities depict the observed 2D scattering patterns successfully. The different styles of peaks in NR and IR (crescent and round) are caused by crystallites dimension and orientation. IR crystallites are more aligned towards the extension direction than NR crystallites. The sizes of crystallites do not change during extension. The increase of crystalline fraction is attributed to the increase in the number of crystallites during extension. The order of crystal in NR is lower than in IR, which suggests that the different behavior of SIC in NR and IR is caused by pseudo network rather than stereo-regularity.

4.5 References

1. Katz, J. R. *Kolloid Zeitschrif*. **1925**, *36*, 300
2. Katz, J. R. *Kolloid Zeitshrif*. **1925**, *37*, 10
3. Mark, H.; von Susich, G. *Kolloid Zeits*. **1928**, *46*, 11
4. Morss Jr, H. A. *J. Amer. Chem. Soc.* **1938**, *60*, 237
5. Bunn, C. W. *Proc. R. Soc. London A* **1942**, *180*, 40
6. Nyburg, S. C. *Acta Crystal.* **1956**, *7*, 385
7. Natta, G.; Corradini, P. *Angew. Chem*. **1956**, *68*, 615
8. Takahasi, Y.; Kumano, T. *Macromolecules* **2004**, *37*, 4860
9. Immirzi, A.; Tedesco, C.; Monaco, G.; Tonelli, A. E. *Macromolecules* **2005**, *38*, 1223
10. Rajkumar, G.; Squire, J. M.; Arnott, S. *Macromolecules* **2006**, *39*, 7004
11. Gent, A. N. *Trans. Faraday Society,* **1954**, *50*, 521
12. Mitchell, G. R. *Polymer,* **1984**, *25*, 1563
13. Toki, S.; Sics, I.; Ran, S.; Liu, L.; Hsiao, B. S.; Murakami, S.; Senoo, K.; Kohjiya, S. *Macromolecules* **2002**, *35*, 6578
14. Trabelsi, S.; Albuoy, P. A.; Rault, J. *Macromolecules* **2003,** *36*, 7624
15. Tosaka, M.; Murakami, S.; Poompradub, S.; Kohjiya, S.; Ikeda, Y.; Toki, S.; Sics, I.; Hsiao, B. S. *Macromolecules* **2004**, *37*, 3299
16. Tosaka, M.; Senoo, K.; Sato, K.; Noda, M.; Ohta, N. *Polymer,* **2012**, *53*, 864
17. Flory, P. J. *J. Phys. Chem*., **1947**, *15*, 397
18. Mitchell, J. C.; Meier, D. J. *J. Polymer Science,* **1968**, *6*, 1689
19. Tosaka, M.; Kawakami, D.; Senoo, K.; Kohjiya, S. *Macromolecules* **2006**, *39*, 5100
20. Tanaka, Y. *Rubber Chem. Technol.* **2001**, *74*, 355

21. Karino, T.; Ikeda, Y.; Yasuda, Y.; Kohjiya, S.; Shibayama, M. *Biomacromolecules* **2007**, *8*, 693
22. Amnuaypornsri, S.; Toki, S.; Hsiao, B. S.; Sakdapipanich, J.; Tanaka, Y. *Rubber Chem. Technol.* **2008**, *81*, 753
23. Toki, S.; Burger, C.; Hsiao, B. S; Amnuaypornsri, S.; Sakdapipanich, J.; Tanaka Y. *J. Polym. Sci. Part B: Polym. Phys.* **2008**, *46*, 2456
24. Burger, C.; Hsiao, B. S.; Chu, B. *Polymer Reviews* **2010**, *50*, 91
25. Burger, C.; Zhou, H.; Sics, I.; Hsiao, B. S.; Chu, B.; Graham, L.; Glimcher, M. J. *J. Appl. Cryst.* **2008**, *41*, 252
26. Mao, Y.; Burger, C.; Zuo, F.; Hsiao, B. S.; Mehta, A.; Mitchell, C.; Tsou, A. H. *Macromolecules* **2011**, *44*, 558
27. Ruland, W. *Colloid Polym. Sci.* **1977**, *255*, 833
28. Guinier, A. X-Ray Diffraction: In Crystals, Imperfect Crystals, and Amorphous Bodies; W. H. Freeman: San Francisco, CA, and London, **1963**
29. Sears, V. F.; Shelley, S. A. *Acta Crystal.* **1991**, *47*, 441
30. Fraser, R. D. B.; Macrae, T. P.; Miller, A.; Rowlands, R. J. *J. Appl. Cryst.* **1976**, 9, 81
31. Toki, S.; Fujimaki, T.; Okuyama, M. *Polymer,* **2000** *41*, 5423
32. Toki, S.; Sics, I.; Ran, S.; Liu, L.; Hsiao, B. S.; Murakami, S.; Senoo, K.; Kohjiya, S. *Polymer* **2003**, *44*, 6003
33. Toki, S.; Sics, I.; Hsiao, B. S.; Murakami, S.; Tosaka, M.; Poompradub, S.; Kohjiya, S.; Ikeda, Y. *J. polym., Sci., B, Polym. Phys*. **2004**, *42*, 956

(Chapter 5 reproduced with permission from *Macromolecules*, in press. Unpublished work copyright **2013** American Chemical Society.)

Chapter 5

Crystal and Crystallites Structure of Natural Rubber and Peroxide Vulcanized Natural Rubber by a Two Dimensional Wide Angle X-ray Diffraction Simulation Method:

Strain-Induced Crystallization Versus Temperature-Induced Crystallization

5.1 Introduction

In the past few decades, significant research has been done in analyzing the crystal structure of natural rubber (NR), more specifically *cis*-1,4-polyisoprene. Crystallization of polymer chains in rubber can be temperature-induced or strain-induced[2]. Temperature-induced crystallization (TIC) is a common method for natural rubber to crystallize under static conditions, where polymer chains can crystallize over time at low temperatures (at 0˚C or lower). TIC is created by the energy pathway from the melting temperature (T_m) to the crystallizing temperature (T_c).[3] X-ray wide-angle diffraction with a two-dimensional (2D) detector shows a series of sharp rings without any preferred orientation, similar to a crystalline powder pattern. In strain-induced crystallization (SIC), the entropy of the rubber chains are reduced by deformation and the transition from the amorphous to crystalline state occurs by the rise of melting temperature[4-6]. Flory[4] and Toki[10] reported that strain-induced crystallites are considered as extended chain crystal that reduces the stress, where the crystals grow parallel to the stretching direction. The increase in stress and crystallinity with strain is attributed to the limited extensibility of network chains.

The main difference between TIC and SIC is that the crystallites observed in SIC show a preferred orientation with their crystallographic *c*-axes preferentially oriented about the stretching direction, and that the degree of crystallinity increases with increasing strain. As Treloar[7] suggested, a major distinction between crystallization by SIC and TIC is the rate (or time scale) at which the process takes place. Crystallization for SIC is observed immediately after higher extensions around 50-200 msec[8-9]. On the other hand, the rate of crystallization for TIC depends on the temperature and duration of crystallization. It may take several hours up to days before crystallites are observed, depending on the temperature. The rate of crystallization is an important factor that will influence the size and number of the crystallites in SIC and TIC.

As discussed in Chapter 1, SIC is known to be primarily responsible for the outstanding mechanical properties in NR as compared to synthetic polyisoprene rubber (IR). Toki et al.[15] studied the effect of temperature on the stress-strain behavior and onset strain of SIC in un-vulcanized and vulcanized NR and IR from -50 to 75 ˚C. The authors reported that the stress values at higher temperatures are less than the stress values at lower temperatures, which does not follow the theory of rubber elasticity under deformations at various temperatures. It is of particular interest to determine the strain-induced crystallites' properties at these temperatures and its effect on the overall mechanical properties. In addition, the onset strain of SIC is delayed with the increase in temperature. These differences may be governed by entanglements, the pseudo end-linked network in NR with the non-rubber components, and the chemical bond network from vulcanization.[15-16] Entanglements can act as pivotal points to align rubber chains and induce SIC. Functionalized chain ends and other non-rubber components (proteins, phospholipids, carbohydrates, metal salts and oxides, etc.) in un-vulcanized NR are assumed to play a role in the formation of a pseudo end-linked network that makes the entanglements as permanent entanglements that can induce SIC and cause the stress upturn. On the other hand, un-vulcanized IR is a polymer melt at room temperature and SIC has not been observed even up to large strains of 600%. Deformations at low temperatures or the addition of vulcanization agents are required for SIC to initiate in synthetic rubber[1]. Even without the presence of network, IR can show SIC at low temperatures, and therefore, chain entanglements may be the only source of pivot points, which may act as physical network points at low temperatures for the nucleation of crystals.[17] The chemical bond network from vulcanization renders IR as an elastic material similar to that of NR.

In Chapter 4, a novel 2D simulation method to analyze a wide-angle X-ray diffraction (WAXD) pattern was applied to the crystal and crystallites of SIC in un-vulcanized NR and IR at -50 ˚C. The crystallites' dimensions in NR and IR are the same at -50 ˚C, and the sizes of the crystallites do not change with strain. The orientation of the crystallites in NR is lower than in IR. The order of crystals in NR is lower than in IR. The crystalline fraction increases with strain because of the increase in the number of crystallites. The onset strain of SIC in NR is smaller than in IR. The different behavior of SIC in NR and IR is caused by the pseudo-network of NR.

This chapter aims to apply the novel two-dimensional WAXD simulation method to the SIC and TIC in both un-vulcanized and peroxide vulcanized NR. The two-dimensional simulated WAXD patterns are directly compared with experimentally obtained WAXD patterns. Information on the crystallites' structure is then obtained from the WAXD simulation, including crystallite size, volume, orientation, displacement disorder, and crystallinity fraction. The SIC samples are deformed at various temperatures from -50 to 50 ˚C. The purpose of this work is to differentiate the effects of temperature and vulcanization on the crystallites' structure during deformation. We will compare the different crystallization processes of SIC and TIC and determine its effects on the crystallite structures. In addition, corresponding SAXS experiments and analysis are carried out to determine the long-range ordering in SIC and TIC. A two-phase stacking model is applied to the observed lamellar structures in order to determine the thicknesses of the crystalline and amorphous layers, and the long-period spacings.

5.2 Experimental Methods

5.2.1 Materials and Sample Preparation

Two samples were used in this study: un-vulcanized natural rubber (NR) and peroxide vulcanized natural rubber (PVNR). These samples were provided by the Thai Rubber Latex Company, Thailand. The fresh NR latex was preserved in 0.6% v/v ammonia (ammonia solution 0.6 mL; NR latex 100 mL) for 3 months at room temperature. The preserved NR was then casted on glass dishes and dried in an oven at 60 ˚C for 48 hours. The preparation of the PVNR sample included several steps. First, the un-vulcanized NR sample was masticated by a two-roll mill at 50 ˚C for 2 minutes. 1 part per hundred rubber (phr) of dicumyl peroxide (DCP) was then added to the sample and thoroughly mixed for 3 minutes. The rubber compound was then cured at 160 ˚C for 30 minutes in a 1 mm depth mold under pressure.

For SIC experiments, the samples were pre-cut into dumbbell-like shapes prior to deformation. The total lengths of the samples were 50 mm. The narrow section of the dumb-bell shaped samples were 30 mm in length and 4 mm in width. For TIC experiments, samples were cut and placed into a sample holder of about 5 mm in diameter. These samples were stored in a refrigerator freezer for one month at -11 ˚C prior to the X-ray measurements.

5.2.2 Time-Resolved WAXD Measurements and Tensile Deformation

Synchrotron X-ray measurements were carried out at the X27C beamline in the National Synchrotron Light Source (NSLS), Brookhaven National Laboratory (BNL). The X-ray wavelength was set at 1.371 Å. Two-dimensional (2D) wide-angle X-ray diffraction (WAXD) and small-angle X-ray scattering (SAXS) patterns were acquired using a MAR-CCD detector. The acquisition time for each frame was 30 seconds. Aluminum oxide (Al_2O_3) and silver behenate ($AgC_{22}H_{43}O_2$) standards were used to calibrate the scattering angle for WAXD and SAXS, respectively. The sample-to-detector distances for WAXD and SAXS were 114 and 1756 mm, respectively. All diffraction and scattering signals were corrected for beam fluctuations and background scattering. X-ray data analysis was performed using the software Polar (Stony Brook Technology and Applied Research, Stony Brook, New York).

For SIC experiments, stress-strain measurements were recorded simultaneously with the time-resolved WAXD and SAXS measurements during tensile deformation at various temperatures from -50 to 50 ˚C. A modified Instron 4442 tensile stretching instrument was used that allowed the uniaxial and symmetric deformation of the sample, while monitoring the structural changes of the sample by illuminating the same sample position during deformation. The samples were deformed up to strains of 6.0 at a stretching rate of 10 mm/min. The temperature is controlled using dry air or liquid nitrogen that flows through a heater. The samples were deformed after stabilizing at the set temperature for a few minutes. The stress is defined as the measured load value divided by the original cross section area of the sample. The strain is defined as the difference of the deformed length and the original length divided by the original length.

For TIC experiments, static WAXD and SAXS measurements were recorded for the NR and PVNR samples. Samples were removed from the refrigerator and kept in a dry ice box before obtaining WAXD and SAXS measurements in order to keep the samples crystallized. In addition, the X-ray sample chamber was kept at -25 ˚C to further prevent the possibility of the melting of the crystals.

5.2.3 WAXD Data Analysis

The WAXD data analysis is briefly discussed here, but a more detailed analysis can be found in Chapter 4.[1,18-19] By assuming simple fiber symmetry, the scattering intensity distribution of the entire fiber system $J(s, \varphi)$, with s as the scattering vector [$s = (2/\lambda)\sin(\theta/2)$, where λ is the wavelength and θ is the scattering angle] and φ as the polar angle of the fiber, can be explained as a combination of the scattering intensity distribution $I(s,\varphi_{hkl})$ of an (*hkl*) plane, with radius s_{hkl} and polar angle φ_{hkl}, and the orientation distribution function $F(\varphi,\varphi_{hkl})$:

$$J(s, \varphi) = \int_{0}^{\pi/2} I(s, \varphi_{hkl})\, F(\varphi, \varphi_{hkl})\, \sin\varphi_{hkl}\, d\varphi_{hkl} \qquad (5.1)$$

This equation can be expanded into:

$$J(s, \varphi) = (4\pi \mathbf{w} s^2_{hkl})^{-1}\ I_{hkl}(s)\ H_0[(s - s_{hkl})/\ w] \cdot (p_0 + (1-p_0)\ (p \cosh (p \cos\varphi \cos\varphi_{hkl})\ /\sinh(p))\ I_0(p \sin\varphi \sin\varphi_{hkl})) \cdot \exp(-\boldsymbol{B}s^2) \qquad (5.2)$$

where *w* is the width of the peak in the radial direction and its reciprocal value gives an estimate for the average crystallite size, Ho is a one-dimensional normalized peak distribution function that takes the Lorentzian function as $Ho(t) = (1+\pi^2t^2)^{-1}$, p_0 is the isotropic un-oriented fraction, p is the width of the distribution of the oriented fraction, I_0 is the modified Bessel function of the first kind of order 0, and $\exp(-\boldsymbol{B}s^2)$ is the Debye-Waller factor for crystal lattice disorder where *B* describes the lattice vibrations on Bragg-peak intensities and is proportional to the mean square displacement of the atoms. Two-dimensional simulated WAXD patterns were obtained from Equation 5.2. During the simulation process, the fitting parameters *w*, p, and B were systematically varied to improve the fitting in order to match the experimental two-dimensional patterns and the one-dimensional integration. The optimal values of w, p, and B were obtained with the highest R^2 value agreement between the experimental and simulated patterns. Each parameter varied the WAXD fiber pattern differently. The width of the peaks in the fiber pattern was varied with *w*, and the size of the crystallite in real space was obtained from the reciprocal value of *w*. A large value of *w* indicated a smaller crystallite size. The orientation of the peaks was varied with p, and the Hermans' orientation factor P_2 was obtained by:

$$P_2 = (1-p_0)\{1 - 3p^{-1}[\coth(p)-p^{-1}]\} \qquad (5.3)$$

A P_2 value of 1 indicated a perfectly oriented system parallel to the stretching direction; a value of 0 for random orientation; and a value of -0.5 for a perfectly oriented system perpendicular to stretching direction. The mean square displacement of the atoms due to thermal motion was varied with *B*, which changed the intensity of certain Bragg peaks. Small values of *B* indicated a highly ordered crystal lattice.

In addition to the crystal scattering intensity distribution described from equation 5.2, the amorphous halo was described using three separate Gaussian intensity distribution function:

$$I\,(\text{amorphous}) = I(s_a) + I(s_b) + I(s_c) \qquad (5.4)$$

Each intensity distribution function takes the form:

$$I(s_x) = (4\pi w_x s^2_x)^{-1}\, I_x(s)\, H_0[(s - s_x)/\, w_x] \qquad (5.5)$$

where s_x and w_x is the scattering position and width of the intensity distribution function respectively. The crystallinity fraction determined from WAXD (X_{cw}) was then obtained by taking the ratio of the integrated area of the crystal distribution function (A_c) to the total integrated area of the crystal and amorphous distribution (A_a) functions.

$$X_{cw} = [A_c/(A_c+A_a)]*100 \qquad (5.6)$$

5.2.4 SAXS Data Analysis

In order to determine the thicknesses of the crystalline and amorphous layers, a stacking model[20-23], which considers a two-phase lamellar system with their planar faces oriented parallel to each other, was applied to the experimentally obtained one-dimensional integrated raw SAXS intensities. The intensity distribution through an infinite stack height of lamellae is given as:

$$I_{1D}(s) = \frac{f}{s^4}\,\mathrm{Re}\left\{\frac{(1 - H_1(s))(1 - H_2(s))}{1 - H_1(s)H_2(s)}\right\}, \qquad (5.7)$$

where $I_{1D}(s)$ is the intensity in the one-dimensional reciprocal space, s is the scattering vector, f is a proportionality constant, $\mathrm{Re}\{\ \}$ takes the real part of the complex number, and $H_1(s)$ and $H_2(s)$ are the Fourier transforms of the thickness distributions of the two phases. A narrow

Gaussian distribution was chosen as the thickness distributions of the crystalline layer and can be given as:

$$H_1(s) = \exp(2\pi i\langle T\rangle s - 2\pi^2\sigma_T{}^2 s^2) \tag{5.8}$$

where <T> is the average thickness of the crystalline layer and σ_T is the standard deviation of the thickness distribution. A Gamma distribution was chosen as the thickness of the amorphous layer, since it typically has a broader distribution, and can be given as:

$$H_2(s) = (1 - 2\pi i\sigma_t{}^2 s/\langle t\rangle)^{-\langle t\rangle^2/\sigma^2} \tag{5.9}$$

where <t> is the average thickness of the amorphous layer and σ_t is the standard deviation of the thickness distribution. The lamellar long spacing was obtained from the sum of <T> and <t>. In addition, the crystallinity fraction determined from SAXS (X_{cs}) was also obtained this way by:

$$X_{cs} = (\langle T\rangle/L)*100 \tag{5.10}$$

5.3 Results and Discussion

5.3.1 WAXD Results

The carbon atom coordinates of the orthorhombic unit cell with space group $P2_12_12_1$ were adopted from the works of Rajkumar et al.[30] The unit cell dimensions of SIC and TIC were determined from the scattering peak positions. The details of this procedure are discussed elsewhere[1]. For the SIC samples, the temperature at which the samples are deformed did not affect the unit cell lattice parameters. Furthermore, the addition of peroxide vulcanization also did not affect the unit cell lattice parameters. The PVNR samples have the same unit cell as the un-vulcanized NR samples. The unit cell lattice parameters for un-vulcanized NR and PVNR at -50, -25, 0, 25, and 50 °C were determined to be a = 13.048 Å, b = 9.391 Å, and c = 8.551 Å.

For the TIC samples, the unit cell lattice parameters were different as compared to those for SIC. Also, the lattice parameters for the TIC of NR and PVNR were different. The lattice parameters for the TIC of un-vulcanized NR were determined to be a = 12.292 Å, b = 8.833 Å, and c = 8.158 Å. The lattice parameters for the TIC of PVNR were determined to be a = 12.205 Å, b = 8.723 Å, and c = 8.068 Å. These lattice constants are significantly smaller than those observed for SIC. This may be attributed to the difference in crystallization processes between SIC and TIC.

Figure 5.1 shows the two-dimensional (2D) WAXD patterns of the SIC of (a) NR and (b) PVNR at various strains and temperatures (-50, -25, 0, 25, and 50 ˚C), and (c) the TIC of NR and PVNR. It is to be noted that the WAXD patterns shown for the SIC samples were obtained at the maximum strain during deformation before breaking, and the WAXD patterns for other strains are not shown in the figure. The top and bottom portions of all the patterns represent the experimentally observed and simulated WAXD patterns, respectively. The experimental patterns have been corrected for distortion and curvature of the Ewald sphere (Fraser correction[24]), where some information along the meridian may be lost. However, the simulated WAXD patterns can produce information in the regions along the meridian, and the crystallite sizes along the c-axis can be obtained. The WAXD patterns that are obtained for SIC are different than those that are obtained for TIC. The SIC samples show crystal reflections with preferred orientation along the stretching direction. On the other hand, the TIC samples show a series of rings that corresponds to the specific (hkl) planes, which indicates that the crystallites have random orientation.

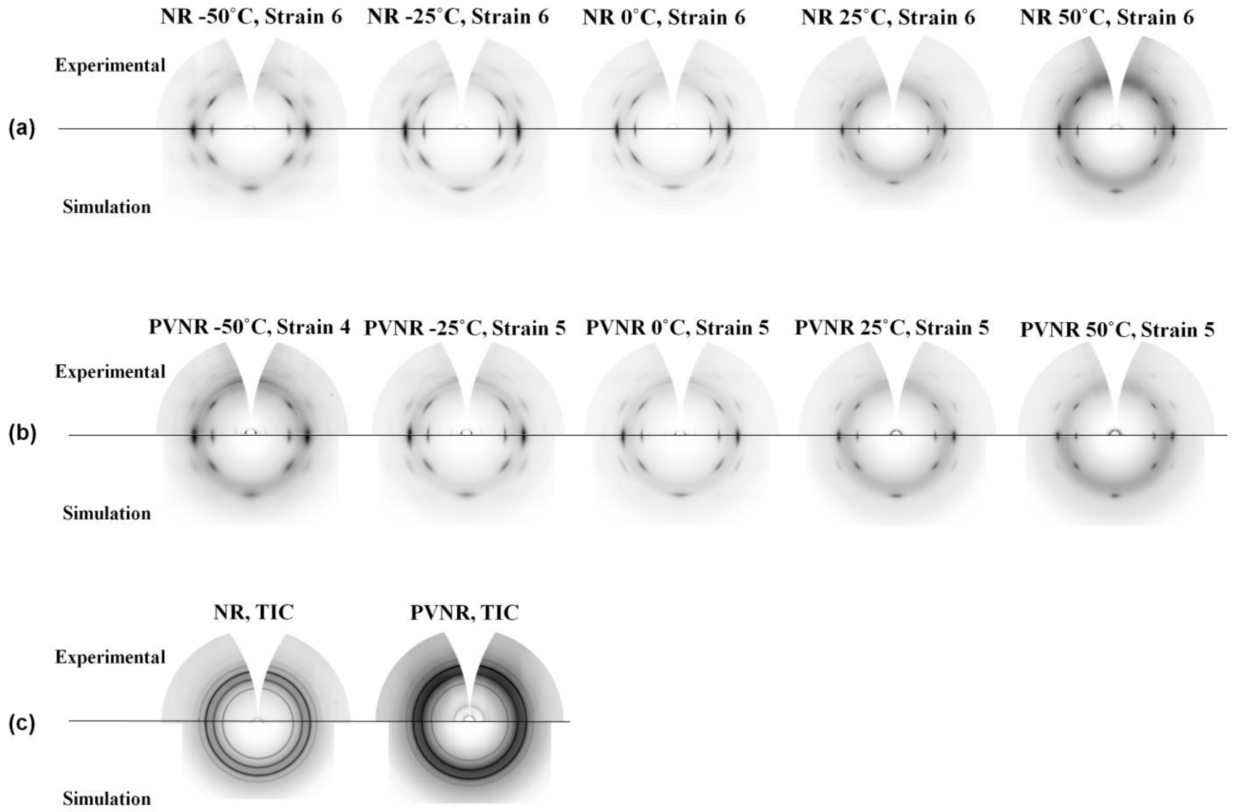

Figure 5.1 Two-dimensional observed and simulated WAXD patterns of the SIC of (a) NR and (b) PVNR at various strains and temperatures (-50, -25, 0, 25, 50 ˚C), and (c) the TIC of NR and PVNR. The patterns shown for SIC are those that are obtained at the maximum strain during deformation before breaking. The top and bottom portions of all the images represent the experimentally observed and simulated WAXD pattern, respectively.

Figure 5.2 shows the corresponding one-dimensional (1D) integrated intensity profile of the experimental (solid line) and simulated (long dashed line) WAXD patterns from Figure 5.1 for the SIC of (a) NR and (b) PVNR at various strains and temperatures, and (c) the TIC of NR and PVNR. The small dashed lines represent the separated simulated peaks of the total integrated intensity, which is composed of the amorphous halo (fitted using three Gaussian peaks) and oriented crystalline peaks. In addition, in order to quantify the goodness of fit, the standardized residuals and R^2 values were calculated. The standardized residual is defined as $(I_{sim}-I_{obs.})/\sigma$, where I_{sim} and I_{obs} are the intensities obtained from the simulation and observed respectively, and σ is the standard deviation. In Figure 5.2, the one-dimensional standardized residual plots were calculated from the difference between the simulation and observed intensities. The residual plots show random patterns with no trends, which indicate a good fitting of our simulation intensities to the observed intensities. The R^2 values were calculated for all these fittings for NR and PVNR at various strains and temperatures to be 0.99.

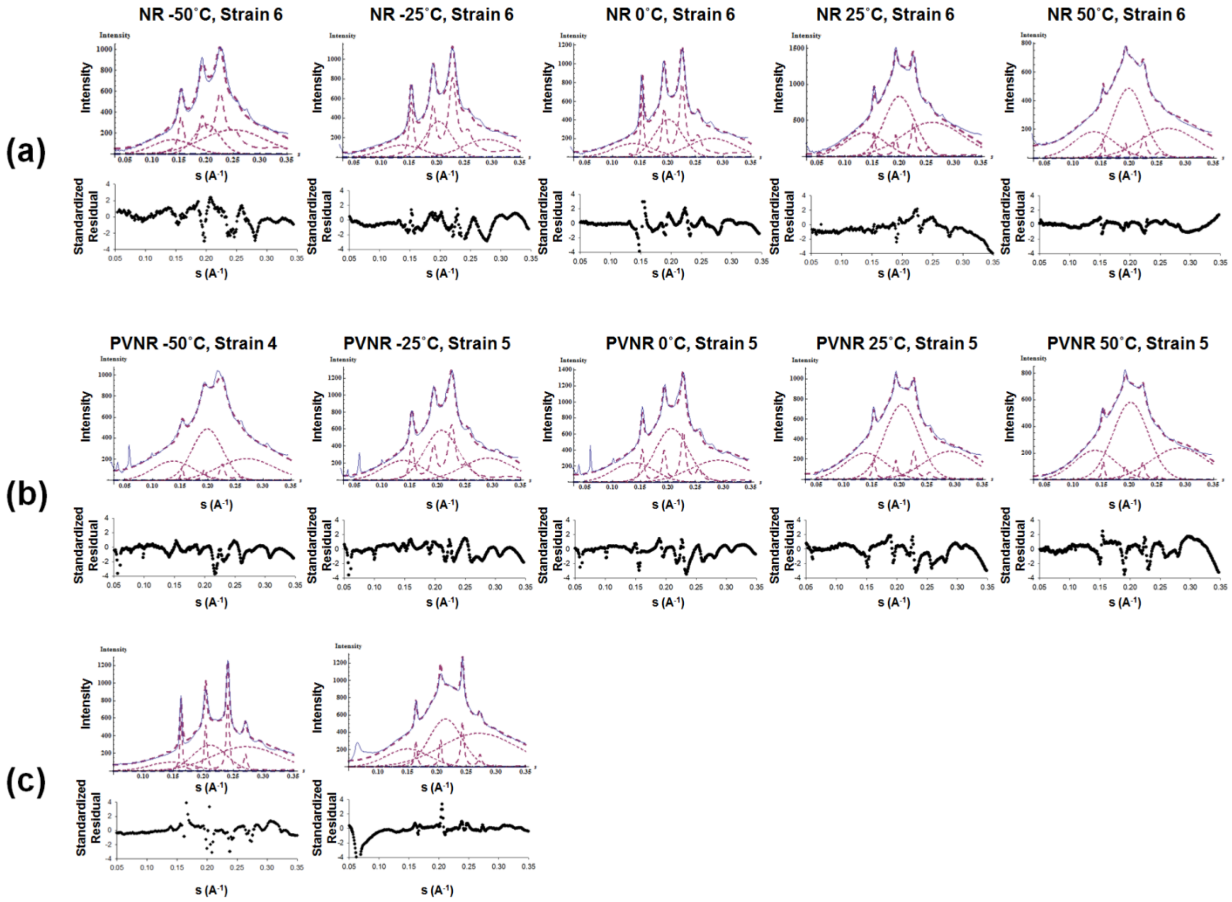

Figure 5.2 One-dimensional (1D) integrated intensity profile of the experimental (solid line) and simulated (long dashed line) WAXD patterns from Figure 5.1 for the SIC of (a) NR and (b) PVNR at various strains and temperatures, and (c) the TIC of NR and PVNR. The separated simulated peaks are shown in small dash lines. The standardized residual plots are calculated from the difference between the simulation and observed intensities.

5.3.1.1 Crystallite Size and Crystalline Fraction

Information about the crystallites' size and volume were obtained from the WAXD simulations using the *w* parameter in Equation 5.2 after fitting the simulation to the experimentally observed 2D and 1D pattern. The crystallites dimensions along the *a*-, *b*-, and c-directions were estimated using the (*200*), (*120*), and (*002*) diffraction peaks respectively. Figure 5.3 shows the lateral crystallite sizes for the (*200*), (*120*), and (*002*) diffraction peaks as a function of temperature for the SIC (left) and TIC (right) of NR and PVNR. For the SIC samples, the data shown are obtained at the maximum strain during deformation before breaking as indicated in Figure 5.1. For NR, all data points shown are at strain 6. For PVNR, the data shown are at strain 4 for -50 ˚C and strain 5 for all the other temperatures. The size of the (*200*) crystal is almost doubled that of the (*120*) and (*002*) crystals. This is consistent with the results reported by Tosaka et al.[25], which is attributed to the statistical displacement of molecular chains in the crystal structure of *cis*-1,4-polyisoprene. Table 5.1 summarizes the average number amount of unit cells per crystallite (*n*) in the *a*-, *b*-, and *c*-direction (denoted as *a* x *b x c*), the volume of the crystallite (V_c), and the crystallite fraction determined from WAXD (X_{cw}) for the SIC (at various temperatures) and the TIC of NR and PVNR. The average number amount of unit cells per crystallite was calculated from the unit cell lattice constants and the crystallite sizes. The volume of the crystallite was calculated from the products of $L_{200}L_{120}L_{002}\cos\alpha$, where α is the angle between the directions of (020) and (120) and has a value of 70˚.[31] The crystallinity fraction determined from WAXD was obtained using Equation 5.6. For SIC, the lateral crystallite sizes, average number of unit cells per crystallite, and volume of the crystallite at each temperature were calculated from the WAXD patterns obtained at the maximum strain during deformation before breaking, since the crystallite sizes did not change significantly with deformation.

For both the SIC and TIC samples, NR and PVNR showed similar crystallite sizes and volume. The addition of vulcanizing agents did not significantly contribute to the crystallite size. The lateral crystallite size L_{200} was smaller in PVNR as compared to NR. For the SIC samples, the cross-linking network in PVNR may decrease the mobility of the chains, prevent the rearrangement of crystallites, and therefore reduce the crystallite size. For the TIC samples, since the WAXD measurements for these samples were obtained at static conditions, the crystallite sizes and volume were similar, although slightly greater for NR as compared to PVNR. The presence of the cross-linking network in PVNR decreased the molecular weight of the chains between network points. In addition, the cross-linking points may act as a physical barrier for the growth of crystallites.

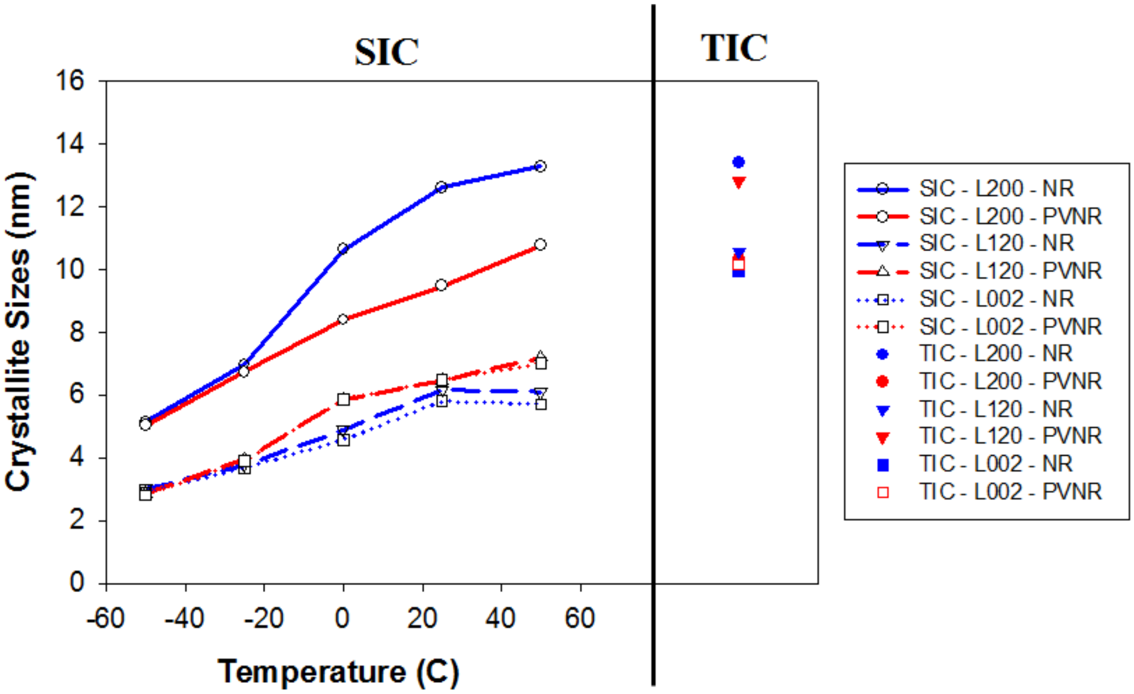

Figure 5.3 The crystallite sizes for the (*200*), (*120*), and (*002*) diffraction peaks as a function of temperature for the SIC (left) and TIC (right) of NR and PVNR. For the SIC samples, the data shown are obtained at the maximum strain during deformation before breaking as indicated in Figure 5.1. For NR, all data points shown are at strain 6. For PVNR, the data shown are at strain 4 for -50 ˚C and strain 5 for all the other temperatures.

Sample		**# of Unit Cells (*a* x *b* x *c*)**		**V_c (nm^3)**		**X_{cw} (%)**	
		NR	**PVNR**	**NR**	**PVNR**	**NR**	**PVNR**
SIC	**-50˚C**	4 x 4 x 4	4 x 4 x 4	15	14	17.3	15.9
	-25˚C	5 x 4 x 4	5 x 4 x 4	34	36	25.5	22.4
	0˚C	8 x 5 x 5	6 x 6 x 6	81	100	22.3	19.5
	25˚C	10 x 7 x 7	7 x 7 x 7	154	137	6.9	13.0
	50˚C	10 x 7 x 7	8 x 8 x 8	158	186	5.5	6.3
TIC		11 x 12 x 13	11 x 11 x 13	502	442	16.2	10.4

Table 5.1 Summary of the average number amount of unit cells per crystallite (*n*) in the *a*-, *b*-, and *c*-direction (denoted as *a* x *b* x *c*), the volume of the crystallite (V_c), and the crystallite fraction determined from WAXD (X_{cw}) for the SIC (at various temperatures) and the TIC of NR and PVNR. For the SIC samples, the data shown are obtained at the maximum strain during deformation before breaking as indicated in Figure 5.1. For NR, all data shown are at strain 6. For PVNR, the data shown are at strain 4 for -50 ˚C and strain 5 for all the other temperatures.

For the SIC samples, the lateral crystallite sizes, average number amount of unit cells, and volume of crystallite decreased with decreasing temperature. The mobility of chains to reorient from amorphous chains to crystallites is significantly reduced at low temperatures, and therefore, limits the size of the crystallites. Furthermore, even though the size and volume of the crystallites were greatest at 50 ˚C, the overall crystallinity fraction was lowest at 50 ˚C. From previous works, the sizes of the crystallites were almost independent of stretching, and the increase in stretching resulted in more amounts of crystallites rather than larger size crystallites[1,2,26]. The onset strain of crystallization was estimated from the best-fit curve of crystallinity fraction versus strain for NR at -50, -25, 0, 25, and 50 ˚C to be 1.79, 1.44, 1.66, 2, and 2.83 respectively. The onset strain of crystallization for PVNR at -50, -25, 0, 25, and 50 ˚C was 1.74, 1.59, 1.51, 2.47, and 2.87 respectively. In SIC, the melting temperature of molecular chains is elevated above the ambient temperature by stretching. Here at higher temperatures, only the highly stretched large crystals can exist, leading to a small amount of larger size crystallites. A larger strain is necessary to induce crystallization with increasing temperatures. On the other hand, at low temperatures, there is a significantly large amount of smaller size crystallites. Smaller size crystallites are more readily crystallized at low temperatures, and hence, a smaller onset strain of crystallization. It is interesting to note that the crystallinity fraction at -50 ˚C was smaller as compared to at -25 ˚C and 0 ˚C. Also, the volumes of the crystallite of NR and PVNR at -50 ˚C were 100 times smaller as compared to the volumes at 50 ˚C. The rate of crystallization increases sharply with the degree of supercooling[29]. At -50 ˚C, the rate of crystallization is significantly reduced[7] since it is very close to the T_g of NR of -70 ˚C. This tells us that temperature plays a large role in the formation of the strain-induced crystallites, which leads to the significant differences in the mechanical properties at various temperatures.[15]

For the TIC samples, the crystallite sizes, volumes of the crystallite, and the average number of unit cells per crystallite were larger as compared to the SIC samples at any temperature. This is attributed to the differences in the rate of crystallization between the two processes as discussed in the introduction. The duration of crystallization is an important factor that will influence the size and number of the crystallites. Since the TIC experiments were held in the refrigerator at -11˚C for one month, these samples were compared with the SIC samples at -25 ˚C and 0 ˚C. The crystallinity fraction was much smaller in TIC as compared to SIC. In TIC, there is a small amount of larger size crystallites, whereas in SIC, there is a large amount of smaller size crystallites.

5.3.1.2 Crystallite Orientation and Displacement Disorder in Crystal

Figure 5.4 shows the comparison of the P_2 orientation factors of the SIC samples with respect to temperature for NR and PVNR. The orientation increased with respect to temperature and approached a value close to one, which represent an almost perfect alignment of crystallites along the stretching direction during deformation. At high temperatures, a larger strain is needed to induce crystallization, which leads to higher orientation. At low temperatures, the mobility of chains is significantly reduced, which leads to the low orientation function of small crystallites. PVNR has a larger orientation parameter as compared to NR. The cross-linking points in PVNR help align molecules and to induce crystallization during deformation[15]. Furthermore, the P_2 orientation factors for the TIC samples were close to zero and were not shown in the figure, which represent random orientation of the crystallites as compared to the highly oriented crystallites for SIC.

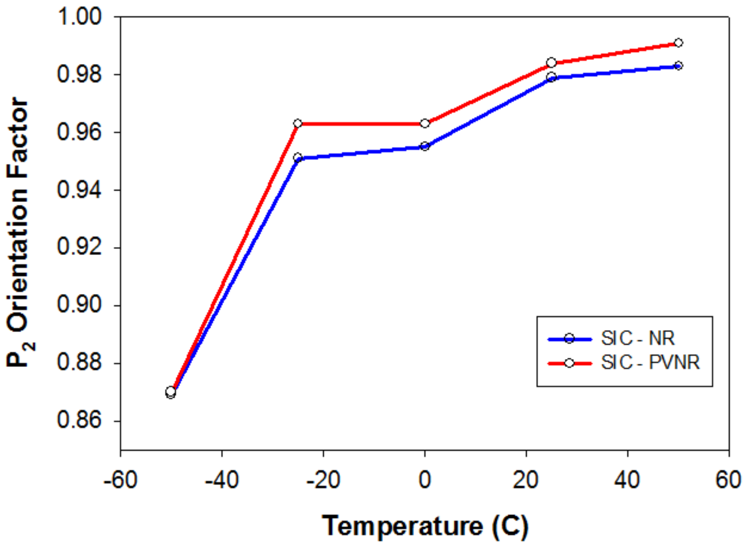

Figure 5.4 P_2 orientation of the crystallites as a function of temperature for the SIC of NR and PVNR. For NR, all data points shown are at strain 6. For PVNR, the data shown are at strain 4 for -50 ˚C and strain 5 for all the other temperatures.

Figure 5.5 shows the displacement disorder factor, *B*, as a function of temperature for the SIC (left) and TIC (right) of NR and PVNR. *B* is proportional to the mean square displacement of the atoms, where a highly ordered crystal lattice leads to low values for *B* that does not suppress the scattering intensity[27,28]. For the SIC samples, the *B* factor increased with increasing temperature, which is attributed to the increase in lattice vibrations and also the thermal expansion of the crystals at higher temperatures. In addition, the *B* factors were larger for PVNR as compared to NR at any given temperature for SIC and TIC. In NR and PVNR, there are non-rubber components and lots of entanglements that disrupt the packing of atoms[15]. However, PVNR also contains an inhomogeneous distribution of cross-links and far apart pseudo end-linked network points that further disrupt the packing of atoms, which leads to a less ordered crystallite system and a larger value for *B*. In addition, the larger B factor for PVNR in TIC may be attributed to the latent internal tension between crystallites. The crystallization in unvulcanized NR does not induce internal strain among the adjacent crystallites because molecular chains can be reeled into the crystallites by reptation motion. On the other hand, in PVNR, molecular chains among the crystallites are connected, and therefore, the crystallites may feel tension from the adjacent counterparts. This tension can slightly distort the crystal structure leading to the larger B factors in PVNR.

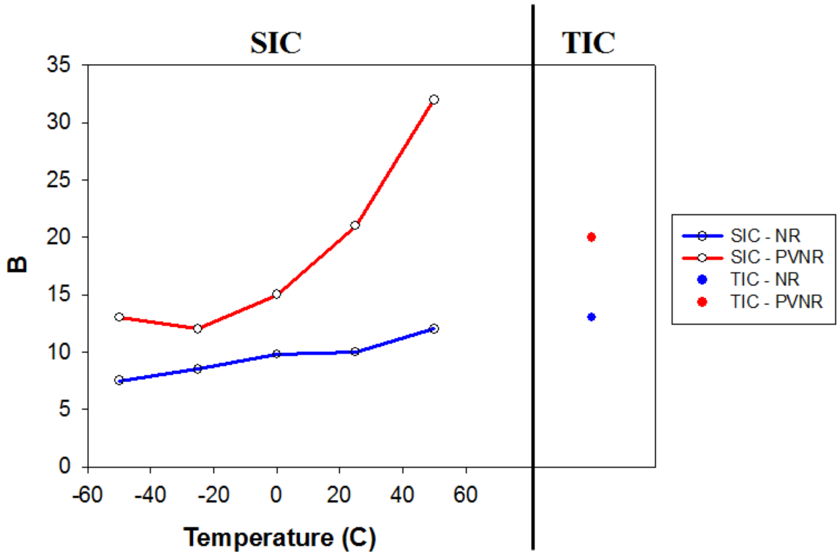

Figure 5.5 The displacement disorder factor, *B*, as a function of temperature for the SIC (left) and TIC (right) of NR and PVNR. For the SIC of NR, all data points shown are at strain 6. For the SIC of PVNR, the data shown are at strain 4 for -50 ˚C and strain 5 for all the other temperatures.

5.3.2 SAXS Results

Figure 5.6 shows the raw two-dimensional SAXS patterns of the SIC at various strains and temperatures (-50, -25, 0, 25, 50 ˚C), and the TIC of NR and PVNR. For the SIC samples, the samples shown at higher strains were obtained at the maximum strain during deformation before breaking. Figure 5.7 shows the corresponding one-dimensional SAXS integrated intensity profiles of the experimental SAXS patterns from Figure 5.6 for the SIC at (a) strain 0 and (b) strain 5 or 6, and (c) TIC of NR and PVNR. For SIC, the SAXS patterns were shown at strains 0 and 6 for two purposes. One purpose was to show the effect of deformation on the changes in the SAXS patterns with the presence of SIC at strain 6. A second purpose was to compare between the TIC samples with the SIC samples at strain 0. The only difference between the TIC samples and the SIC samples at strain 0 is that a low temperature treatment was applied to the TIC samples at -11 ˚C for one month, whereas the SIC samples did not have this treatment.

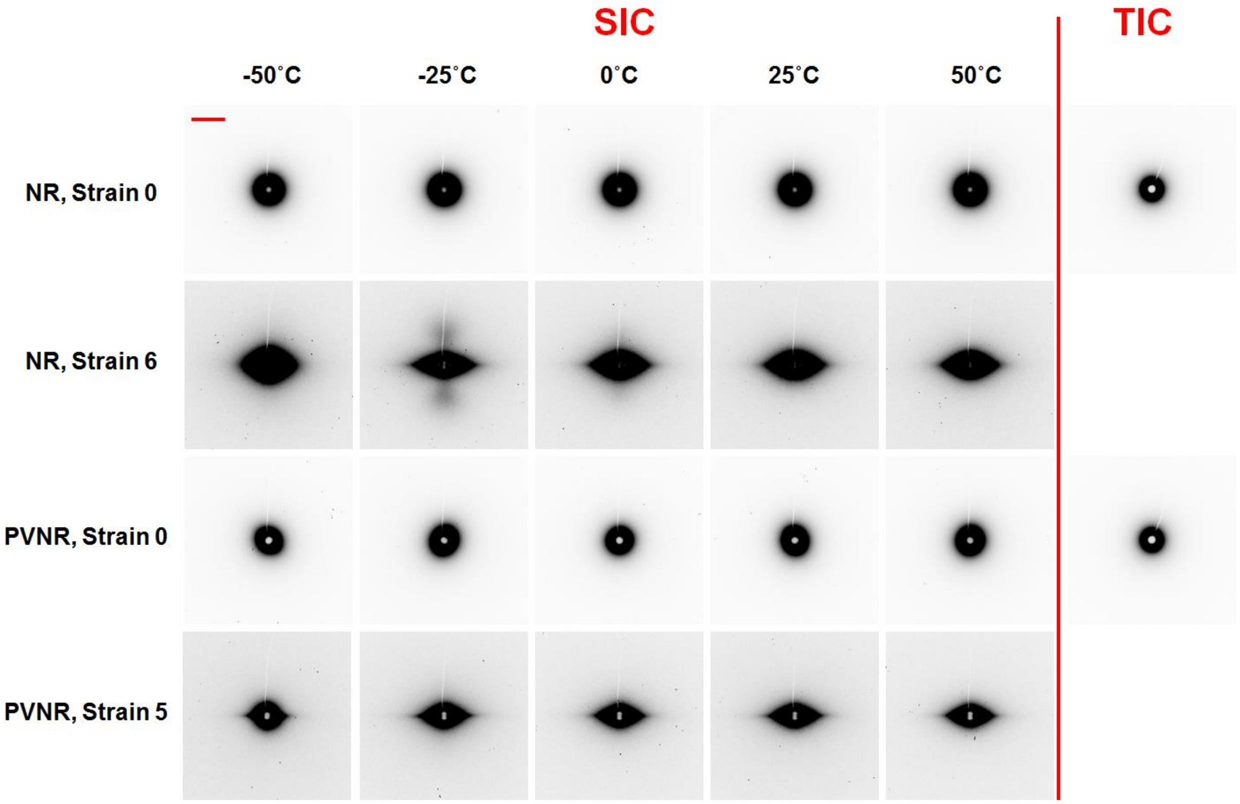

Figure 5.6 Two-dimensional SAXS patterns of the SIC at various strains and temperatures (-50, -25, 0, 25, 50 ˚C), and the TIC of NR and PVNR. A scale bar for the SAXS patterns are shown as the red line in the top left at NR strain 0 at -50 ˚C. The scale bar represents 0.05 nm^{-1}.

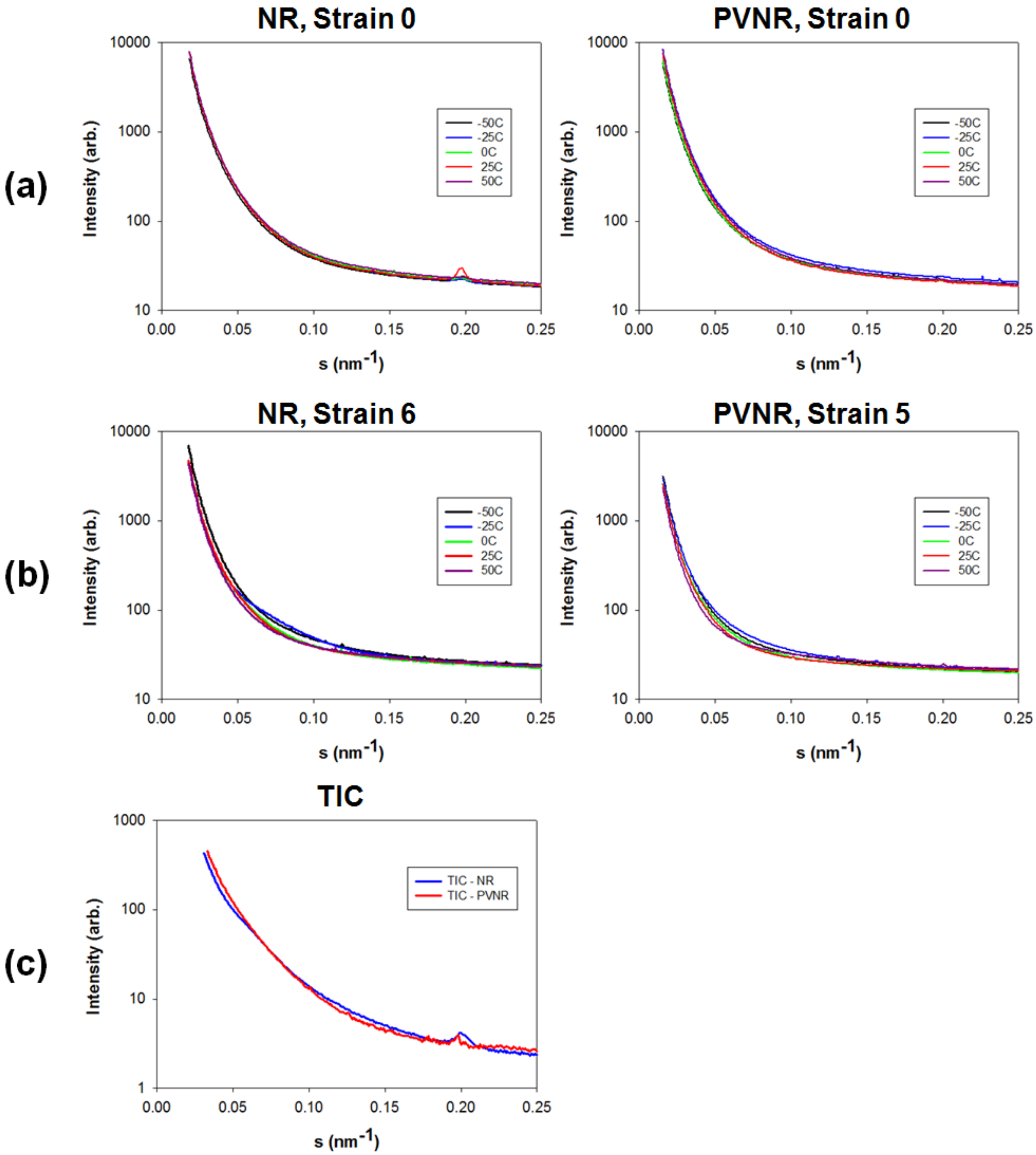

Figure 5.7 The corresponding one-dimensional SAXS integrated intensity profiles of the experimental SAXS patterns from Figure 5.6 for the SIC at (a) strain 0 and (b) strain 6, and (c) TIC of NR and PVNR.

Since only amorphous chains are present in the SIC samples at strain 0, we expect to have no scattering features from the SAXS patterns. The SAXS patterns of NR and PVNR at strain 0 changed from a spherical to an ellipsoidal-shaped morphology at higher strains. At higher strains, a two-point meridional scattering appeared only for NR at -25 and 0 ˚C at strain 6, which is attributed to the presence of a lamellar structure and the difference in the crystalline-amorphous electron density contrast. In SIC, the crystalline regions are formed by adjacent extended-chains that are deformed to the limit of extensibility. This scattering feature was most discrete for NR at -25 ˚C and eventually disappeared as room temperature at 25 ˚C was reached. Any diffuse scattering from the crystalline-amorphous composite in the s range from 0.05 to 0.10 nm^{-1} are either very weak or inexistence at higher temperatures. The lamellar structure can only exists at temperatures below the isotropic melting point[11-14]. However, this was not observed at -50 ˚C, since chains are very close to the T_g.

Since the two-point meridional scattering appeared only for NR at -25 and 0 ˚C at strain 6, a two-phase stacking model fitting was applied to the raw experimental SAXS intensities in order to determine the thickness of the crystalline (<T>) and amorphous layers (<t>), and the long-period spacings (L). Figure 5.8a shows the two-phase stacking model fitting (shown in red) applied to the raw integrated SAXS intensities for the SIC of NR at -25 ˚C (black) and 0 ˚C (blue) at strain 6. The R^2 values of the model fitting to the experimental were both 0.999, which demonstrated an excellent fit. The results of the fitting are summarized in a table in Figure 5.8b. By assuming fiber symmetry, the two-phase stacking model considers a two-phase lamellar system with their planar faces oriented parallel to each other and stacked along the fiber axis. Therefore, the crystalline layer thickness obtained from the stacking model can be directly compared to the L_{002} crystallite along the *c*-direction (fiber axis direction). As observed in the WAXD results in Figure 5.3, the size of the L_{002} crystallite at -25 and 0 ˚C is around 4 nm, which are within the ranges obtained here from the stacking model. The crystalline layer thickness, amorphous layer thickness, and longer periods are larger at 0 ˚C as compared to the values at -25 ˚C. The increase in long period with increasing temperature is mainly contributed by the larger amorphous layer thickness at 0 ˚C, since the crystalline layer thicknesses are almost identical. Furthermore, the increase in long period with increasing temperature is accomplished with the decrease in the number of crystalline lamellae as observed from the reduction in the crystallinity fraction determined from SAXS (X_{cs}). The increase in temperature promotes the gradual melting down of the crystalline regions, which results in the translation of chains from the crystalline to the amorphous state[13]. This resulted in the thickening of the amorphous layer and in consequence, a larger long period.

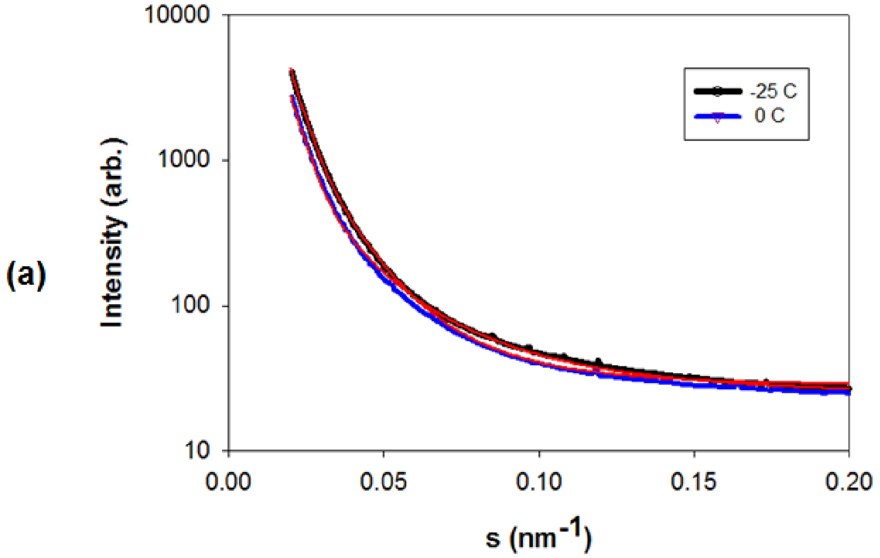

(b)

Sample	<T> (nm)	<t> (nm)	L (nm)	X_{cs} (%)
SIC – NR, -25 ˚C	5.3 ± 2.3	14.8 ± 3.7	20.1 ± 4.4	26.3 ± 0.5
SIC – NR, 0 ˚C	5.4 ± 2.3	22.6 ± 2.9	28.0 ± 3.7	19.3 ± 0.5

Figure 5.8 (a) Two-phase stacking model fittings (shown in red) applied to the raw integrated SAXS intensities for the SIC of NR at -25 ˚C (black) and 0 ˚C (blue) at strain 6. (b) Summary of parameters obtained from the fitting in (a), including crystalline layer thickness (<T>), amorphous layer thickness (<t>), long-period spacing (L), and crystallinity fraction determined from SAXS (X_{cs}).

The lamellar structure was not observed for PVNR at all the temperatures. Increased cross-link densities tend to suppress and discourage the formation of the lamellar structure. Luch and Yeh[13] reported the observation of a lamellar structure for peroxide vulcanized NR, however, the authors used 0.2 phr of the vulcanizing agent, DCP, as compared to the 1 phr of DCP used here in this work. In addition, the authors first elongated the sample, followed by holding the sample fixed at a certain temperature for a significantly long period of time prior to X-ray measurements. This allowed stress-relaxation to occur, which promoted the increase in the lamellar structure.

5.3.3 Proposed Models

Figure 5.9 shows a schematic model of the SIC of NR at strain 6 that are deformed at various temperatures. The sizes, volume of the crystallite, number of unit cells, number of chains per crystallite, crystallite orientation, and crystal displacement disorder increased with increasing temperature. However, the crystallinity fraction decreased with increasing temperature. Temperature plays a significant role in the SIC process. Temperature can affect the movement of chains in order to orient from the amorphous to crystalline state. At low temperatures (below 0˚C), chain movements are restricted and there are numerous amounts of smaller size crystallites. At higher temperatures (25˚C and above), it is more difficult to form crystallites due to an increase in chain movements, and only a small amount of larger size crystallites exist.

For the TIC samples, both the amorphous chains and crystallites are present as observed from the WAXD patterns in Figures 5.1 and 5.2. However, no discernible scattering features were observed in the SAXS patterns. From the combination of the WAXD and SAXS data, a schematic representation of the TIC of NR is shown in Figure 5.9. The TIC process creates a wide distribution of crystallite sizes, since the crystallization process occurs under static conditions where random regions are crystallized. Furthermore, since the crystallinity fractions of the TIC samples are less than 20%, there are only a small amount of these large size crystallites that are distributed inhomogeneously and randomly throughout the sample, and therefore, no long-range ordering is present in these samples. The sizes, volume, and number of chains per crystallite of the TIC of NR is larger as compared to the SIC samples.

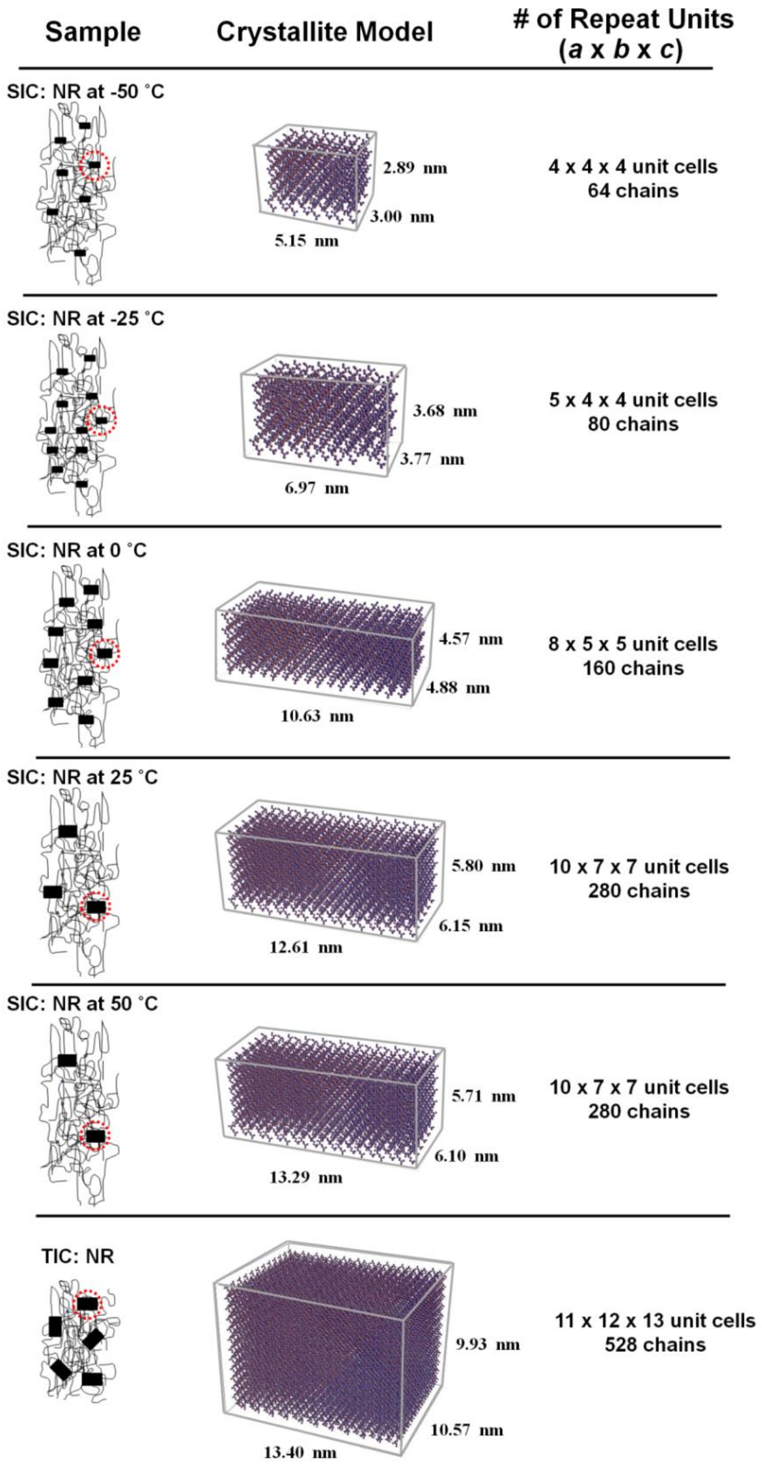

Figure 5.9 A schematic representation of the SIC at strain 6 at various temperatures and the TIC of NR. The crystallites circled in red are enlarged and shown in the center of the figure. The average number of unit cells in the *a*, *b,* and *c* direction (denoted as *a* x *b* x *c*) and the number of chains per crystallite are also shown.

5.4 Conclusion

A two-dimensional WAXD simulation method was used to generate the WAXD patterns for the SIC and TIC of un-vulcanized NR and PVNR. These simulated two-dimensional WAXD patterns were in excellent agreement with the experimentally obtained WAXD patterns. Corresponding SAXS experiments were also carried out to determine the long-range ordering in the samples. A two-phase stacking model was applied to the one-dimensional SAXS in order to characterize the lamellar structure and to determine the thicknesses of the crystalline and amorphous layers, and the long-period spacings. The difference in the crystallization process in SIC at various temperatures and TIC are revealed as follows:

1. For SIC, the crystalline regions are formed by adjacent extended-chains that are deformed to the limit of extensibility. The increase in temperature led to larger crystallite sizes, volume, number of chains per crystallite, crystallite orientation, and crystal displacement disorder. However, the number of crystals decreased with increasing temperature. A lamellar structure was observed at low temperatures and the long period increased with increasing temperature, which was attributed to the reduction in the number of crystallites and the translation of chains from the crystalline regions to an amorphous state.
2. For TIC, the crystallites were randomly oriented and distributed inhomogeneously in the sample since these were measured under static conditions, and therefore, no lamellar structure was observed. The sizes, volume, and number of chains per crystallite are larger as compared to the SIC samples.

5.5 References

1. Che, J.; Burger, C.; Toki, S.; Rong, L.; Hsiao, B. S.; Amnuaypornsri, S.; Sakdapipanich, J. *Macromolecules* **2013**, *46*, 4520
2. Kroon, M. *Mech of Materials* **2010**, *42*, 873

3. Toki, S.; Kohjiya, S.; Ikeda, Y. "Chapter 7: The effect of strain-induced crystallization on the physical properties of natural rubber." *Chemistry, Manufacture, and Applications of Natural Rubber*. Woodhead Publishing Ltd, **2013** (in print)
4. Flory, P. J. *J. Phys. Chem*. **1947**, *15*, 397
5. Yamamoto, M.; White, J. L. *J. Poly. Sci. A-2* **1971**, *9*, 1399
6. Tosaka, M. *Macromolecules* **2009**, *42*, 6166
7. Treolar, L. R. G. *The Physics of Rubber Elasticity*. New York: Oxford University Press, **2005**
8. Mitchell, J. C.; Meier, D. J. *J. Polymer Science, part A-2*, **1968**, *6*, 1689
9. Tosaka, M.; Senoo, K..; Sato, K.; Noda, M.; Ohta, N. *Polymer* **2012**, *53*, 864
10. Toki, S.; Fujimaki, T.; Okuyama, M. *Polymer* 2000, *41*, 5423
11. Andrews, E. H. *Proc. Roy. Soc.***1964**, *277*, 562
12. Luch, D.; Yeh, G. S. Y. *J. Appl. Phys*. **1972**, *43*, 4326
13. Luch, D.; Yeh, G. S. Y. J. *Macomol. Sci. Phys* .**1973**, *B7*, 121
14. Luch, D.; Yeh, G. S. Y. *J. Polym. Sci. Polymer Phys* **1973**, *11*, 467
15. Toki, S.; Che, J.; Rong, L.; Hsiao, B. S.; Amnuaypornsri, S.; Nimpaiboon, A.; Sakdapipanich, J. *Macromolecules* **2013**, *46*, 5238
16. Che, J.; Toki, S.; Valentin, J. L.; Brasero, J.; Nimpaiboon, A.; Rong, L.; Hsiao, B. S. *Macromolecules* **2012**, *45*, 6491
17. Amnuaypornsri, S.; Toki, S.; Hsiao, B. S.; Sakdapipanich, J. *Polymer* **2012**, *53*, 3325
18. Burger, C.; Hsiao, B. S.; Chu, B. *Polymer Reviews* **2010**, *50*, 91
19. Burger, C.; Zhou, H.; Sics, I.; Hsiao, B. S.; Chu, B.; Graham, L.; Glimcher, M. J. *J. Appl. Crystallogr.* **2008**, *41*, 252
20. Hermans, J. J. *Recl. Trav. Chim. Pays-Bas* **1944**, *63*, 211
21. Stribeck, N. *Macromolecules* **1996**, *29*, 7217
22. Ruland, W.; Smarsly B. *J. Appl. Crystallogr.* **2004**, *37*, 575
23. Burger, C.; Zhou, H.; Wang, H.; Sics, I.; Hsiao, B. S.; Chu, B.; Graham, L.; Glimcher, M. J. *Biophys. J.* **2008**, *95*, 1985
24. Fraser, R. D. B.; Macrae, T. P.; Miller, A.; Rowlands, R. J. *J. Appl. Cryst*. **1976**, 9, 81
25. Tosaka, M.; Senoo, K.; Kohjiya, S.; Ikeda, Y. *J. Appl. Phys*. **2007**, *101*, 084909

26. Gehman, S. D.; Field, J. E. *J. Appl. Phys*. **1939**, *10*, 564
27. Guinier, A. X-Ray Diffraction: In Crystals, Imperfect Crystals, and Amorphous Bodies; W. H. Freeman: San Francisco, CA, and London, **1963**
28. Sears, V. F.; Shelley, S. A. *Acta Crystal*. **1991**, *47*, 441
29. Bukhina, M. F. *Rubb Chem and Tech*. **1964**, *37*, 404
30. Rajkumar, G.; Squire, J. M.; Arnott, S. *Macromolecules* **2006**, *39*, 7004
31. Trabelsi, S.; Albouy, P. A.; Rault, J. *Macromolecules* **2003**, *36*, 7624

(Chapter 6 reproduced with permission from *Macromolecules, 46*, 5279-5289. Copyright **2013** American Chemical Society.)

Chapter 6

Plastic Deformation of Semi-Crystalline Polyethylene by X-ray Scattering: Comparison with Atomistic Simulations

6.1 Introduction

While it is widely speculated that the strength and mechanical deformation mechanisms of polyethylene (PE) derive from the microscopic topology of the non-crystalline regions in the semi-crystalline solid, it is difficult to probe this mainly amorphous region directly through experiment. By combining Raman spectroscopy, differential scanning calorimetry (DSC), and X-ray measurements, the mechanical properties were proposed to be directly correlated with an intermediate phase that links the phases between the crystallites[1-5]. Data from experiments such as in situ uniaxial tensile deformation small angle x-ray scattering (SAXS)[6-9] and other x-ray diffraction studies[10-15] led to proposed deformation mechanisms of crystallographic slip and mechanical melting, respectively, in the crystalline regions. However, the interpretation of deformation in the amorphous phase is model dependent and amorphous phase contributions to the deformation of a semi-crystalline polymer cannot be quantified directly. Molecular-level simulations of a semi-crystalline model (SM) with fully thermalized and deformable crystalline and amorphous components have been conducted to determine the deformation mechanisms of a stacked lamellar unit cell under two deformation modes and strain rates of semicrystalline PE at

350 K[16]. An interphase Monte Carlo (IMC) molecular simulation methodology[17] was applied to create initial configurations for the SM model with proper treatment of chain connectivity and packing density. These configurations were then subjected to molecular dynamics (MD) simulations to explore the temporal evolution of the combined noncrystalline/crystalline system in tensile deformation with large strains. The yielding and plastic flow mechanisms were found to be sensitive to the deformation mode and deformation rate. This simulation approach provides experimentally inaccessible insight into how the amorphous region within the semicrystalline solid deforms plastically. In order for the simulation results to be interpreted in the context of real polyethylene deformation scenarios, the mechanical properties and deformation mechanisms identified in these molecular simulations must be validated by comparison to experimental deformation of model materials. While several experimental X-ray scattering studies have probed the *in situ* deformation of PE in the linear elastic regime[7-9,18], deformation beyond yielding is required to understand the plastic deformation mechanisms identified in the simulations. To this end, a tensile deformation X-ray scattering study was conducted on a PE fiber with uniaxially aligned stacked lamellar morphology beyond yielding to plastic flow at a constant strain rate and for two temperatures. The small and wide angle scattering data were analyzed to examine morphological changes and orientation in the noncrystalline and crystalline phases in order to establish the deformation mechanisms of polyethylene fibers and to compare the experimental observations with the simulation results.

Two main yielding mechanisms were identified in the simulations of the SM model. Fast deformations and deformations with constant lateral sides were found to yield through cavitation. Slow deformations where the simulation cell was kept at a constant volume resulted in yielding through crystallographic slip. This molecular level SM model is used as a probing tool to identify mechanism(s) for plastic deformation and to understand the stress origins in the semicrystalline lamellar morphology. This SM model acts as a mechanical "microscope" for examining the effects of amorphous topology on plastic deformation. In order to validate the model and to define the bounds of interpretation, a cognate experimental system is essential. In this study, tensile deformation of a model HDPE (High Density Polyethylene) uniaxially oriented fiber was followed and examined by synchrotron X-ray scattering. The experimental deformation results were compared to simulation findings to validate the simulation protocol, to assess any limitations, if present, and to relate simulation conditions of a given deformation mechanism to corresponding experimental conditions.

6.2 Experimental Methods

6.2.1 Sample Preparation

Linear polyethylene, or HDPE, with Mn of 15,400 and Mw of 122,000, with an entanglement molecular weight of 860, is obtained from ExxonMobil Chemical Company. HDPE fibers were prepared using a Rosand RH7 Capillary Rheometer (Malvern Instruments) at a low pull rate of 0.6 m/min to form 1-mm thick monofilament with uniaxially oriented stacked lamellae. To repair any potential defects and to ensure uniaxial alignment, these fibers were stretched using a tensile machine at 1 mm/min to 50% elongation and then relaxed back to 0% while clamping in place for thermal annealing at 80°C for 1 hour. SAXS and WAXD were performed afterward on the fibers to confirm uniaxial symmetry without any microvoids.

6.2.2 X-ray Scattering

Synchrotron X-ray measurements were carried out at the X27C beamline in the National Synchrotron Light Source (NSLS), Brookhaven National Laboratory (BNL). The X-ray wavelength was set at 1.371 Å. Two types of X-ray measurements were performed: wide-angle X-ray diffraction (WAXD) and small-angle X-ray scattering (SAXS). Two-dimensional (2D) WAXD and SAXS patterns were acquired using a MAR-CCD detector. The typical image acquisition time for each scan was 1 minute. Al_2O_3 and silver behenate standards were used to calibrate the scattering angle in WAXD and SAXS, respectively. The sample-to-detector distances for WAXD and SAXS were 133.7 mm and 1783 mm, respectively. X-ray measurements for all samples were taken under the same conditions. All scattering/diffraction signals were corrected for beam fluctuations and background scattering. X-ray scattering data analysis was performed using the software Polar (Stony Brook Technology and Applied Research, Stony Brook, New York). The sample length used in this study was 30 mm. A tensile stretching device that could deliver symmetric sample deformation was used. Structural changes in the sample were monitored by X-ray illuminating the same sample position throughout deformation. The samples were deformed at 25˚C and 100˚C at a rate of 10 mm/min. Time-resolved WAXD/SAXS patterns and stress/strain values during deformation were recorded simultaneously. The stress is an engineering stress as defined with load divided by the original cross section. The strain is defined as the displacement of the two clamps divided by the original length.

6.2.3 Scattering Data Analysis

For WAXD analysis, quantitative evaluations of crystal mass fractions were determined from the corrected WAXD patterns. The corrected WAXD pattern contains contributions from both the unoriented isotropic and the oriented anisotropic crystalline and amorphous domains. The isotropic and anisotropic contributions in these patterns can be obtained by de-convoluting the corrected WAXD patterns into these separate contributions using the Polar software. The isotropic contribution consists of unoriented amorphous and unoriented crystalline components. The anisotropic contribution consists of the oriented amorphous and oriented crystalline components.

$$I\,(\text{total}) = I\,(\text{isotropic}) + I\,(\text{anisotropic}) \tag{6.1}$$

$$I\,(\text{isotropic}) = I\,(\text{unoriented amorphous}) + I\,(\text{unoriented crystalline}) \tag{6.2}$$

$$I\,(\text{anisotropic}) = I\,(\text{oriented amorphous}) + I\,(\text{oriented crystalline}) \tag{6.3}$$

The integrated intensities of the isotropic and anisotropic contributions were obtained and a two-dimensional peak-fit software was applied to fit all the observed crystal peaks and the amorphous halo. The crystallinity was quantitatively determined by taking the ratio of the integrated crystal peak area (both unoriented and oriented components) by the total integrated peak area. The P_2 orientation factors of the polymer chains along the fibril axis (c-axis) were calculated using the Hermans' orientation function:

$$P_2 = 0.5(3 <\cos^2\varphi> - 1) \tag{6.4}$$

where φ is the angle between the chain axis and the reference axis, and $<\cos^2\varphi>$ is the averaging over all φ given by:

$$<\cos^2\varphi> = \frac{\int_0^{\pi/2} I(\varphi)\cos^2\varphi \sin\varphi \, d\varphi}{\int_0^{\pi/2} I(\varphi)\sin\varphi \, d\varphi} \tag{6.5}$$

Since no crystal reflections along the (001) diffraction plane can be observed from the WAXD patterns, an indirect method described by Wilchinsky[19] and Desper *et al.*[20] was used to determine the fibril axis orientation. Using a combination of two or more diffraction planes containing the c-axis, which are the (hk0) planes, the crystallites' orientation with respect to the filament axis can be calculated. In this study, the combination of the (110) and (200) planes were used.

For SAXS analysis, the integrated SAXS pattern was first cleaned up with a Lorentz correction. Afterward, the long period (L) was obtained from the inverse of the scattering vector, s, at the peak maximum. The thicknesses of the crystalline and amorphous layers can be determined from analyzing the combined WAXD and SAXS results using a simple calculation. The crystalline layer thickness (<T>) is calculated from the product of the crystallinity and the long period. The amorphous layer thickness (<t>) is then obtained from the difference of the long period and the crystalline layer thickness.

For a more in-depth SAXS analysis, an additional two-phase stacking model, which is adopted from Hermans[21], Stribeck[22], Ruland[23] and Burger[24], was applied to the experimentally obtained one-dimensional integrated raw SAXS intensities. The stacking model considers a two-phase lamellar system with their planar interfaces oriented parallel to each other. The intensity distribution through an infinite stack height of lamellae in the one-dimensional reciprocal space ($I_{1D}(s)$) is given by:

$$I_{1D}(s) = \frac{f}{s^4}\,\mathrm{Re}\left\{\frac{(1-H_1(s))(1-H_2(s))}{1-H_1(s)H_2(s)}\right\} \tag{6.6}$$

where s is the scattering vector in reciprocal space [$s = 2(\sin\theta)/\lambda$, θ is the Bragg angle, λ is the wavelength], f is a proportionality constant, $\mathrm{Re}\{\ \}$ takes the real part of the complex number, and $H_1(s)$ and $H_2(s)$ are the Fourier transforms of the thickness distributions of the two phases. A Gaussian function was chosen as the thickness distributions of the two phases and can be given as:

$$H_1(s) = \exp(2\pi i\langle T\rangle s - 2\pi^2\sigma_T{}^2 s^2) \tag{6.7}$$

$$H_2(s) = \exp(2\pi i\langle t\rangle s - 2\pi^2\sigma_t{}^2 s^2) \tag{6.8}$$

where σ_T and σ_t are the standard deviations of the thickness distributions. The long period can then be obtained from the sum of <T> and <t>. An example of the stacking model fitting to the experimental raw SAXS intensity is shown in Figure 6.1. The structural parameters obtained from stacking model were compared with those obtained from experiments using the simple calculation.

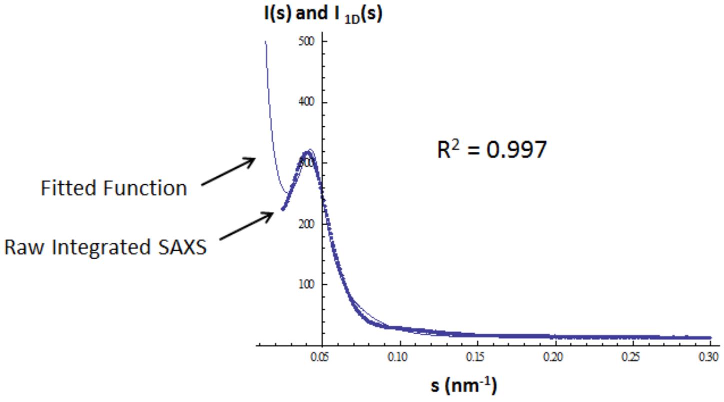

Figure 6.1 An example of the two-phase stacking model fitting to the experimental integrated raw SAXS intensity.

6.2.4 Simulation Models and Methods

Summaries of the simulation model and protocol are presented here, while details can be found in Reference 16. Semicrystalline polyethylene (PE) was modeled using united atom polymer chains, organized into a periodic lamellar stack with alternating crystalline and noncrystalline layers. The stacked lamellae configurations were generated using the Interphase Monte Carlo algorithm[25], and they were subsequently subjected to molecular dynamics simulations with boundary conditions that simulate uniaxial deformation. The stress tensors, velocities and coordinates of each bead were monitored to compute the stress, degree of crystallinity, crystal orientation and local orientation (Hermans' orientation factor) as a function of strain. Two different strain rates and two different modes of deformation were explored.

The individual PE chains were modeled with a united atom model where each bead represents one methylene group with the following potential energy function[17]]:

$$E = E_b + E_\theta + E_\varphi + E_{nb} \tag{6.9}$$

where E_b, E_θ, and E_ϕ represent bond stretching, bond bending, and torsional twisting along the chain, respectively. E_{nb} represents pairwise Van der Waals interactions between non-bonded beads. The exact forms of each term and the parameters used in this model are discussed in Reference 17. This model has been shown to reproduce experimentally observed structure, thermodynamics and dynamics of amorphous PE melts. It has also been shown to capture the melting point and heat of fusion as well as crystal growth kinetics for n-alkanes. Nevertheless, some caution should be exercised when comparing simulation results from this potential energy function directly to PE experiments. The experimentally observed crystal unit cell is orthorhombic with hexagonal symmetry in the *ab*-plane, while the model crystal phase exhibits pseudohexagonal symmetry in the *ab*-plane. This difference is due to the reduced phase space in the model system caused by combining the carbon and attached hydrogen atoms to create a methylene bead, which apparently stabilized the rotator phase with respect to the orthorhombic phase. All-atom simulations of these systems of interest are computationally more expensive, so the united atom system results should be interpreted as a comparable, if not identical system when compared to experiment. It should be noted that the model provides a very good description of n-alkanes where the rotator phase is indeed observed experimentally.

A semicrystalline simulation cell with stacked lamellar morphology was created from a single crystal cell using the Interphase Monte Carlo algorithm[25]. This protocol is illustrated in Figure 6.2. Thirty individual 100-mer chains were packed into the simulation cell with crystalline order, in a lattice of 3x5x50 unit cells. The lattice was oriented so that the normal to the (201) lattice plane aligned approximately with the z-direction of the simulation cell. The cell dimensions were adjusted so the stresses in the chains match the experimentally measured stresses in the crystal phase at atmospheric pressure and T=350 K. In order to create the stacked lamellar morphology within the simulation cell, 6 chains were randomly selected in the center of the cell and cut to form 12 free ends. Beads were then randomly removed from the tails to reach a noncrystalline density of ~0.8 g/cm^3, slightly higher than that of the amorphous melt extrapolated to 350 K. The first and last 10 beads on each PE chain were held fixed in 3D space to create a crystalline boundary for the interlamellar domain. The system was then randomized under a high temperature (10,000K) Monte Carlo (MC) simulation with local and global displacements that allow changes in chain connectivity[25]. The randomized structure was then annealed with the same MC algorithm and equilibrated at 350 K to identify topologies in the noncrystalline region consistent with the lowest free energy ensemble. The resulting topology in the noncrystalline region consisted of tails (free ends), loops (both ends of the chain are anchored within one crystallite), and tie-chains/bridges (each chain end is anchored in a different crystallite). Finally, the z-dimension within the interlamellar domain was adjusted to obtain near-atmospheric pressure of 0.1 MPa over the entire simulation cell. The resulting amorphous region flanked by the short crystalline domains is shown in Figure 6.2a. Crystalline ends were then added to each chain in the crystalline domain to yield a simulation cell with 65% crystallinity, number average molecular weight of 13,100 g/mol and polydispersity index of 1.62. MD simulations in the canonical ensemble with no constraint on the motion of the crystalline beads showed that the constructed configurations were stable over at least 8 ns. A total of 18 independent semicrystalline configurations were generated using this method. The configurations were then subjected to uniaxial tensile deformation in the z-direction using two deformation rates ("fast": 5x10^7 s^{-1}, "slow": 5x10^6 s^{-1}) and two boundary conditions (constant lateral dimensions, and constant volume where the x and y cell dimensions shrink with the elongation in the z-direction).

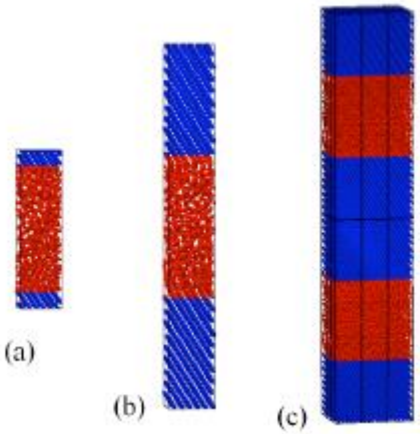

Figure 6.2 Reproduced from Reference 16. (a) Amorphous topology (red) generated from Interphase Monte Carlo algorithm. (b) Semicrystalline model simulation cell with crystalline beads added at chain ends to give realistic degree of crystallinity, average molecular weight and polydispersity in the model polyethylene system. (c) Visualization of the repeated stacked lamellae resulting from periodic boundary conditions in the Monte Carlo and molecular dynamics simulations.

6.3 Results and Discussion

6.3.1 X-ray Results During Deformation

Figure 6.3a and 6.3b shows the experimentally obtained stress-strain curves of HDPE fibers deformed in tension at 25°C and 100°C. Here, the strain value denotes the ratio of the deformed length to its initial length. For example, strain 1 and strain 2 refers to 100% and 200% respectively to its original length of the sample. For deformation at 25°C, several regions of melting and reconstruction were revealed from strains 0.5 to 3.5 of the stress-strain curve. A significant reduction in stress was observed around strain 3.5 which may be attributed to changes in the microstructure. For deformation at 100°C, only a region of melting and reconstruction at strain 0.5 was observed, followed by a region of strain-hardening.

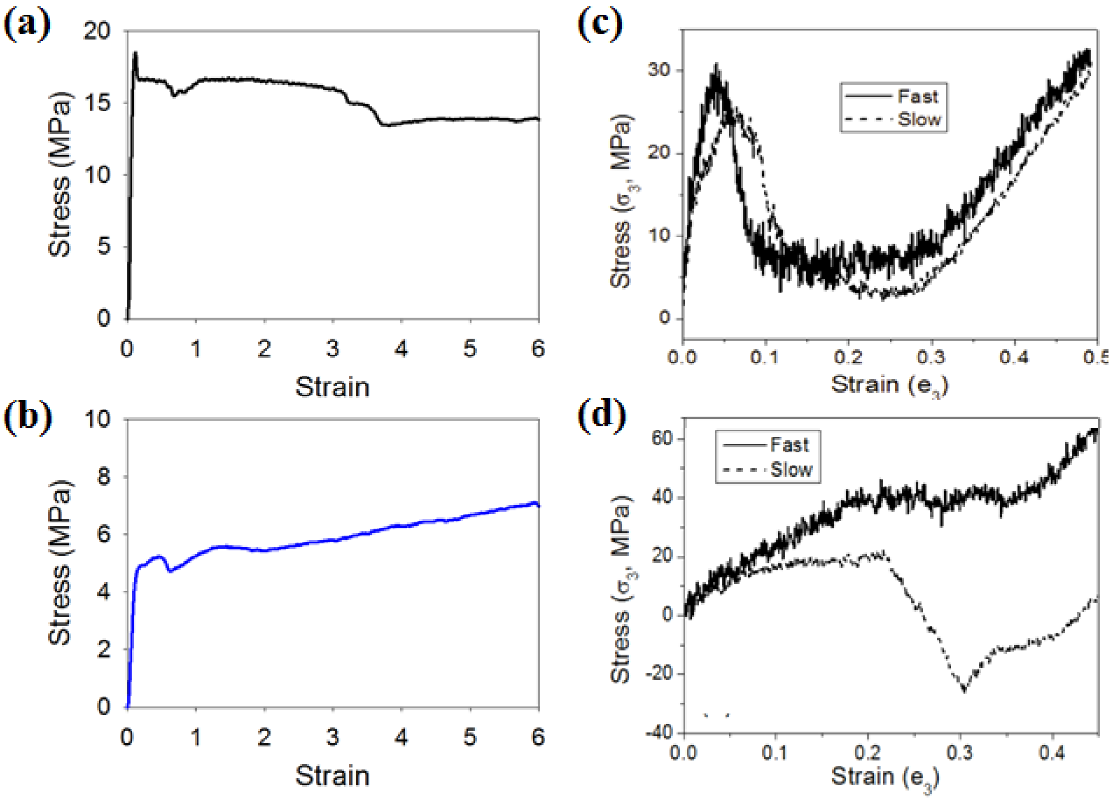

Figure 6.3 Stress-strain curves for (a) 25°C experiment, (b) 100°C experiment, (c) simulation with constant lateral sides, and (d) simulation with constant volume. The simulations in (c) exhibit similar features (yield, plastic deformation, and strain hardening) as the 25°C experiment, but they tend to occur at lower strains and are more pronounced. Similarly, the slow simulation in (d) shows yield, melting, and strain hardening features also seen in the 100°C experiment, and the simulated features tend to be more pronounced and occur at lower strains.

Figure 6.4 shows the 2D WAXD and SAXS patterns of HDPE at various strains. The corresponding 1D integrated intensities are shown in Figure 6.5. Prior to deformation at 25°C, only the orthorhombic crystal structure can be found in the sample as observed in the integrated WAXD by the presence of the (110) and (200) crystal peaks. Upon deformation to strains above 200% at 25°C, a mixture of the orthorhombic and monoclinic crystal structures were identified by the presence of additional crystal peaks that co-exists and overlaps each other. At strain 6, the peaks of both phases are separated and more apparent, which is due to the increase in the monoclinic phase and a decrease in the orthorhombic phase. On the other hand, only the presence of the orthorhombic structure was observed throughout deformation at 100˚C. From each WAXD pattern, the fractions of unoriented isotropic and oriented anisotropic contributions as a function of strain were determined and shown in Figure 6.6. Similar trends were observed at both temperatures. The unoriented fractions of both amorphous and crystalline domains were found to decrease with increasing strain. The conversion from unoriented amorphous domain to oriented amorphous domain was small, whereas significantly more oriented crystalline domains developed during deformation. The conversions from unoriented to oriented crystalline and amorphous fractions were far more pronounced at 100˚C than those changes observed at 25˚C. This is expected since the higher temperature system exhibits faster polymer chain dynamics.

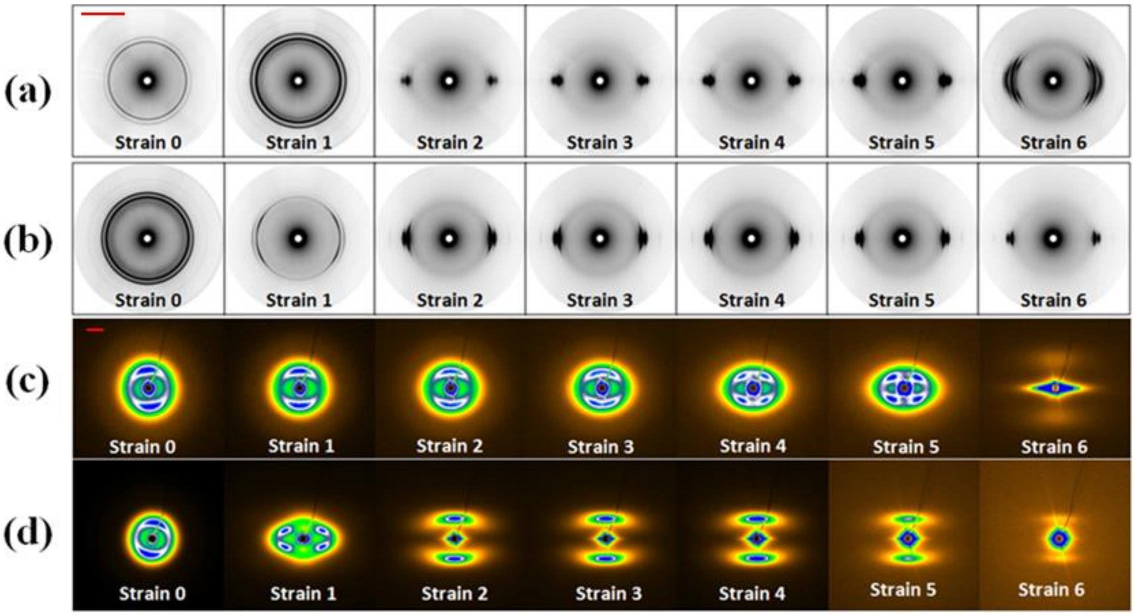

Figure 6.4 2D WAXD patterns for the deformation at (a) 25˚C and (b) 100˚C. 2D SAXS patterns for the deformation at (c) 25˚C and (d) 100˚C. Scale bars for the WAXD and SAXS patterns are shown as the red line in (a) and (c) at strain 0. The scale bars for WAXD and SAXS represents 2.35 nm^{-1} and 0.05 nm^{-1} respectively.

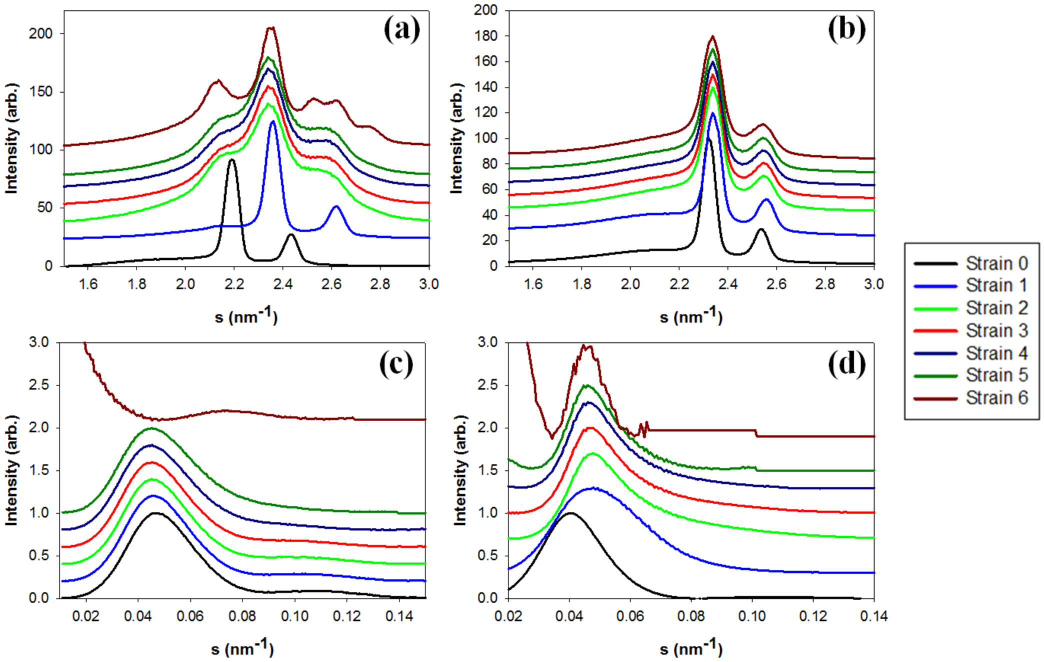

Figure 6.5 1D integrated WAXD intensities for the deformation at (a) 25°C and (b) 100°C. 1D integrated SAXS intensities for the deformation at (c) 25°C and (d) 100°C.

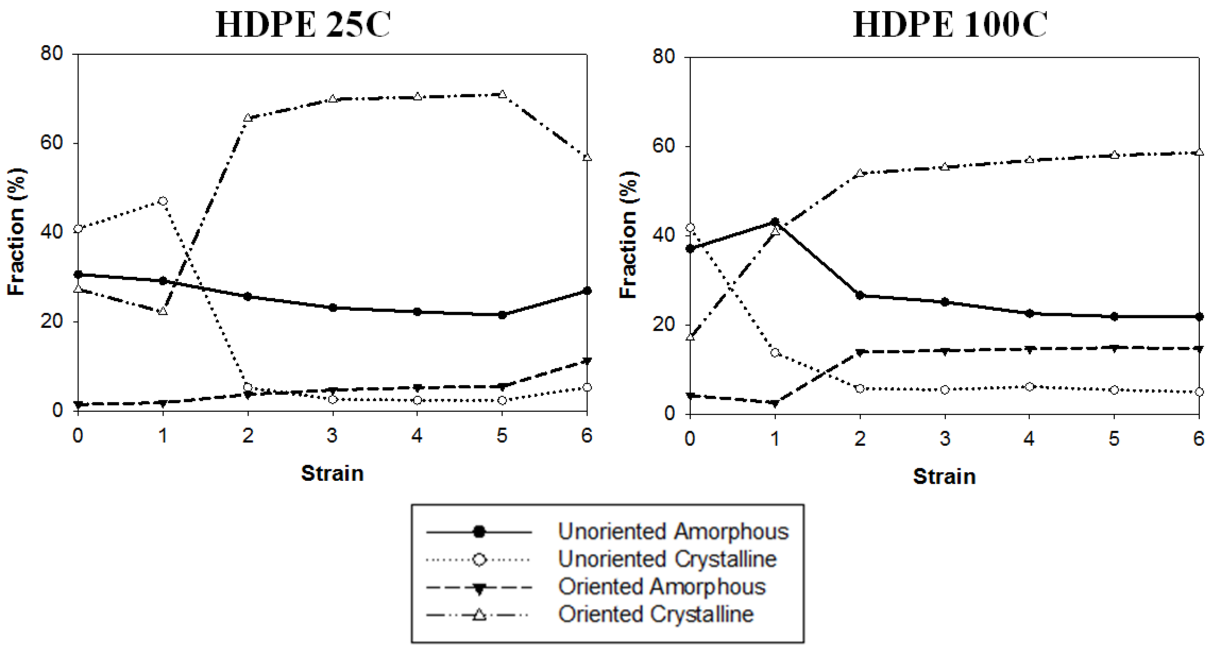

Figure 6.6 Unoriented isotropic and oriented anisotropic fractions as a function of strain for the deformation of HDPE at 25°C and 100°C.

From the WAXD patterns, the P_2 orientation factor of the polymer crystals with respect to the filament axis can be calculated. Figure 6.7 shows the P_2 orientation factor of the polymer crystals as a function of strain for the deformation at 25°C and 100°C. The orientation factor prior to deformation was about 0, suggesting random orientation of polyethylene crystals. During deformation, the orientation factor was raised to about 0.9, indicating high alignment of polymer crystals along the stretching direction. The orientation factor was found to be higher during 100°C deformation than that obtained during deformation at 25°C.

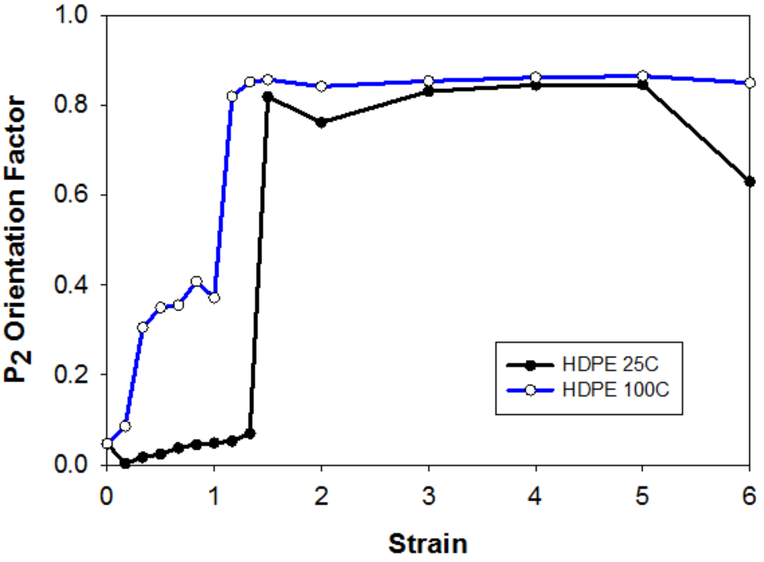

Figure 6.7 P_2 orientation factor of the polymer crystals with respect to the filament axis as a function of strain for the deformation at 25°C and 100°C.

From the SAXS patterns, prior to deformation at both temperatures, an initial two-point pattern along the meridional axis with an additional ring was observed. Figure 6.8 shows the polar azimuthal scans at the peak maximum of the lamellar long period at varying strains for the deformation at 25°C and 100°C. The P_2 orientation factor of the lamellar stacks can then be calculated from these polar azimuthal scans of the lamellar long period. The P_2 orientation factors of the lamellar stacks prior to deformation were determined to be 0.30 and 0.32 for the deformation at 25˚C and 100˚C respectively. This indicated the presence of a very slightly oriented lamellar structure along the meridional axis, which was formed by the uniaxial pulling of the sample during the preparation process.

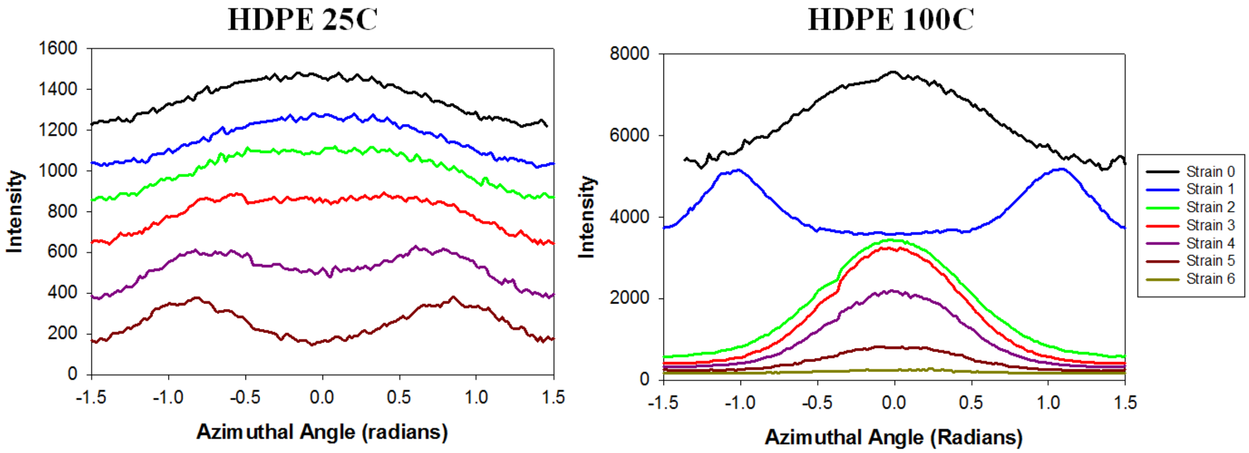

Figure 6.8 Polar azimuthal scans at the peak maximum of the lamellar long period at varying strains for the deformation at 25˚C and 100˚C. The intensities were offset to increase clarity.

Figure 6.9 shows the long period, crystalline layer thickness (represented by <T>) and amorphous layer thickness (represented by <t>) as a function of strain for the deformation of HDPE at 25˚C and 100˚C from (a) the simple calculation method using the experimental WAXD and SAXS results, and (b) the two-phase stacking model fitting. Similar trends in structural parameters were observed in Figure 6.9a and 6.9b. Upon deformation at 25˚C, the long period was determined to increase with deformation, which arises from the increase in the crystalline layer thickness and the reduction in amorphous layer thickness. Structural rearrangement of the lamellar stacks was observed around strain 3 by the transformation of the two-point pattern into a four-point pattern, representing the presence of chevron morphologies. This is also observed in the polar azimuthal scans with the transformation of the single peak into two peaks at higher strains. During this transformation, changes to the structural morphology of the lamellar stacks were observed as represented by the significant drop in mechanical stress and a very slight reduction in the long period. With the increase in deformation, the four point reflections begin to develop away from the meridional axis and towards the equatorial axis. Intralamellar slippage along with rotation and slight deformation of the lamellar stacks are occurring with the increase in deformation. Further increase in deformation after the four point pattern produces a new two-point pattern along the meridional axis. This new meridional axis reflection has a significantly lower long period, crystalline and amorphous layer thicknesses, which is an indication of the destruction of the original lamellar stacks with the mechanical stretching force.

For the deformation at 100˚C, an initial decrease in the long period, amorphous and crystalline layer thicknesses was observed that can be attributed to the melting and rearrangement of the lamellar stacks around strain 0.5. The transformation into a four-point pattern occurs at much smaller strains at 100˚C (around strain 1) as compared to the deformation at 25˚C (around strain 4), which can also be observed from the polar azimuthal scans. This is consistent with the faster polymer chain dynamics at higher temperatures. After the development of the four-point pattern, the new two-point pattern along the meridional axis was observed in the strain hardening region. An increase in the long period was observed that can be attributed to the increase in the crystalline thickness and decrease in the amorphous thickness. The opposite trend was observed for the deformation at 25˚C, where the new two-point reflection produced a long period that is much lower than the original lamella. Here at 100˚C, the melting and recrystallization create the formation of a more perfect crystal as confirmed with the increase in crystallinity and orientation of crystals with deformation. In addition, the orientation of the lamellar stacks also increased with strain, as shown by narrowing of the distribution of the polar azimuthal scans of the lamellar period with the increase in strain. A P_2 value of 0.61 was observed at strain 6 for the lamellar stacks, which is larger than the initial P_2 value of 0.32 prior to deformation.

Furthermore, for the deformation at higher strains for both temperatures, we can observe the presence of equatorial streaks and a diamond shaped morphology around the center of the beam stop in the SAXS patterns, which is attributed to the presence of needle-shaped microvoids between fibrils that are elongated along the fiber axis direction during deformation.

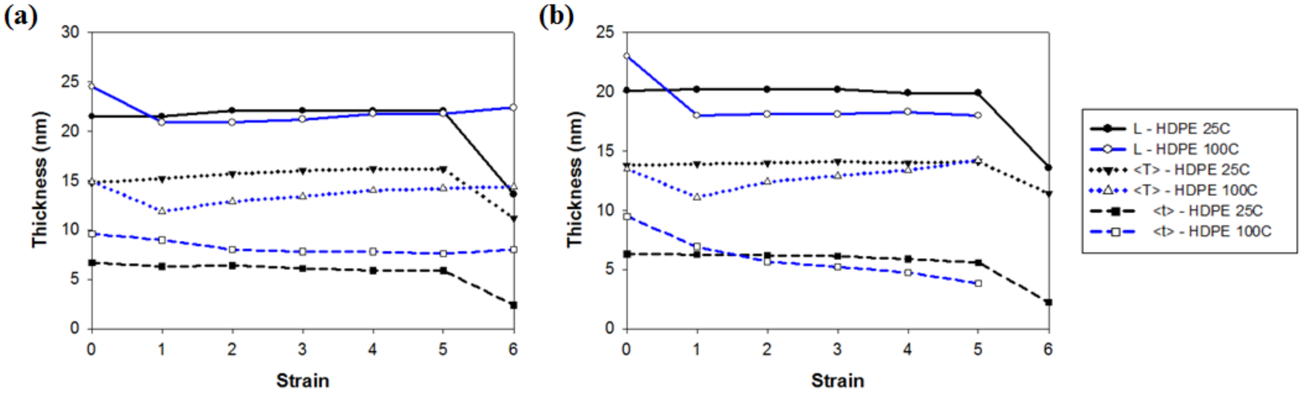

Figure 6.9 Long period (L), crystalline layer thickness (<T>), and amorphous layer thickness (<t>) as a function of strain for the deformation of HDPE at 25˚C and 100˚C from (a) the simple calculation method using the experimental WAXD and SAXS results, and (b) the two-phase stacking model fitting.

6.3.2 Comparison Between Simulation and Experiment

The simulation results presented here are originally reported in Reference 16. Although simulations can capture molecular re-arrangement details during the deformation, the united atom model used was found to yield a different crystal packing structure. Additionally, a relationship between the modeling boundary conditions and experimental stretching conditions under dynamic, or non-equilibrium, deformation has not been developed. Thus, the simulation time scales and the deformation strain rates do not necessarily form a one-to-one correspondence with experimental time scales and strain rates. Indeed, a qualitative comparison between the stress-strain curves in simulation and experiment, as shown in Figure 6.3, indicates that while several qualitative features of yield, melting, and strain hardening can be identified in both simulation and experiment, these features happen at larger strains and later times during the experiment than predicted by the simulations. This can be attributed to the differences in experimental and simulation temperatures, strain rates and degree of initial lamellar alignment. Nonetheless, the qualitative similarities in the stress-strain curves suggest that the united atom model can capture the important deformation features albeit on shorter timescales and at lower strains.

The Eyring model[26] has been used in other studies[27,28] to superpose data collected at different temperatures (T) and strain rates ($\dot{\varepsilon}$) via an activated process, $\dot{\varepsilon} = \dot{\varepsilon}_0 e^{\frac{\Delta E - \sigma v^*}{k_b T}}$, where the activation energy associated with the yield process, ΔE, is modified by the additional work required for the deformation (σv^*, where σ is the applied stress and v^* is the activation volume), and k_b is Boltzmann's constant. This model assumes that the activation energy required for yield is independent of the applied stress, and the pre-exponent, $\dot{\varepsilon}_0$, depends on the temperature and the ensemble of configurations available to surmount the barrier. One could, in principle, use this model to map the simulation stress to experiment. However, the assumptions of constant activation energy and pre-exponential hold over a range of strain rates that is much smaller than the 10^7 s^{-1} range studied in the current simulations. A multiple process Eyring model would likely work, but the problem is ill-defined with only two strain rates to define the curve. An alternate approach is to map the phase space of the experimental system onto the simulation phase space by assuming a linear relationship between the two. By choosing a prominent feature in the stress-strain curve (namely, the time and strain at yield) to match the experimental data to the simulations, the data can be compared explicitly. Linear correlation curves in time and strain for the two experimental conditions (25°C and 100°C) and the pertinent simulation conditions are shown in Figure 6.10.

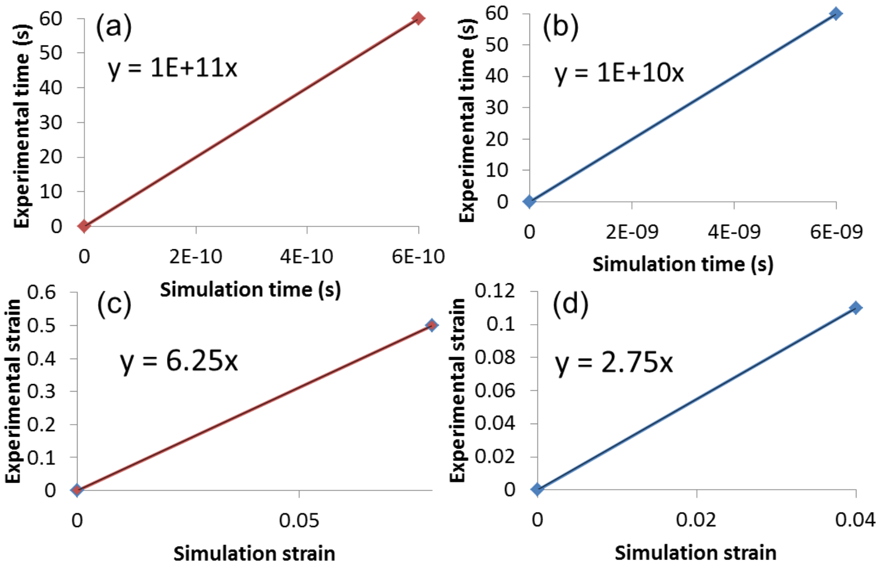

Figure 6.10 Linear maps between experimental and simulation time and strain. (a) and (c) map the constant volume, slow deformation simulation to the 100°C experiment. (b) and (d) map the fixed lateral sides, fast deformation simulation to the 25°C experiment. Initial points correspond to zero time and strain, final points correspond to time to yield and yield strain for the time and strain maps, respectively.

Detailed comparisons of the stress-strain curves, crystallinity and evolution of lamella with strain (*vide infra*) suggest that the fast deformation simulation with fixed lateral sides can be mapped to the 25°C experiment, and that the slow deformation simulation with constant volume can be mapped to the 100°C experiment. These are the conditions that will be compared and contrasted in the subsequent analysis. Since yielding is the key feature on the stress-strain curve signifying the end of the linear material response, yielding time and strain were chosen as the features to map the simulation time and strain space to the experimental space. The slow simulation with constant volume is mapped to the 100°C experiment and the fast simulation with constant lateral sides is mapped to the 25°C experiment. The positive slopes indicate that yield tends to happen faster and at lower strains during the simulation. The fast simulation with constant lateral sides deformed the sample to a mapped strain of e_m=1.35 and the slow simulation with constant volume deformed the sample to a mapped strain of e_m=3.07. Since the HDPE samples were strained to 600% at both experimental temperatures, the comparisons of experimental data and simulation results are restricted to deformations up to a mapped strain of 1.35 and 3.07 for the constant lateral sides and the constant volume simulations, respectively.

The simulation results can be presented in the "experimental space" by plotting all quantities of interest against the mapped strains. The experimental and simulation stresses as a function of mapped strain are plotted in Figure 6.11. As a result of the mapping, the experimental yield strain at 25°C is the same value as that for the fast deformation with fixed lateral sides, shown in Figure 6.11a. Although the qualitative features are similar, there is no evidence that the fast deformation in Figure 6.11a more closely follows the low temperature experiment than does the slow deformation simulation. Later comparison of the evolution of crystallinity during deformation will make this similarity between low temperature experiment and fast deformation simulation more apparent. The experimentally measured yield stress of 19 MPa is lower than the simulated yield stress of 29 MPa. This is likely a consequence of the lateral periodic boundary conditions employed in the simulations leading to infinite lamellae in the x- and y-directions which are effectively more resistant to yielding. There is a strain softening and plastic flow after yielding as indicated by simulation and by experiment between e_m=0.3 and 0.8 followed by a strain hardening region beyond e_m=0.8. However, these phenomena are not as pronounced in the experimental data. These observations are likely the result of the differences in morphology between the simulation and experimental systems. The lamellae in the experimental system are only partially aligned initially, with an average Hermans' orientation factor of 0.3, whereas the perfectly aligned lamellae in the simulation box have a Hermans' orientation factor of 1.0. Thus, the lamellae in the experimental system are not all subjected to perfect uniaxial deformation. In Figure 6.11b, it is apparent that the 100°C experimental stress-strain curve most closely resembles the slow, constant volume deformation simulation curve. The yield stress of 5 MPa in the 100°C experiment is lower than the yield stress of 10 MPa in the slow and constant volume simulation. After yield, there is a stress plateau followed by a drop in stress that involves melting and, as evidenced in the simulations, significant reconstruction of the crystal domains. The melting starts at a lower strain during the experiment (e=0.6) than the mapped strain predicted from the simulation (e_m=1.4). Additionally, the experimentally observed stress reduction during melting and reconstruction is much lower (~4%) than that calculated by the simulation (~200%). This suggests that the melting and reconstruction are not as pervasive in the experiment, or that they are distributed over a broader range of strain. Melting is followed by strain hardening, which is less pronounced in the experiment than in the simulations. This is also likely due to the partial melting in the experiment.

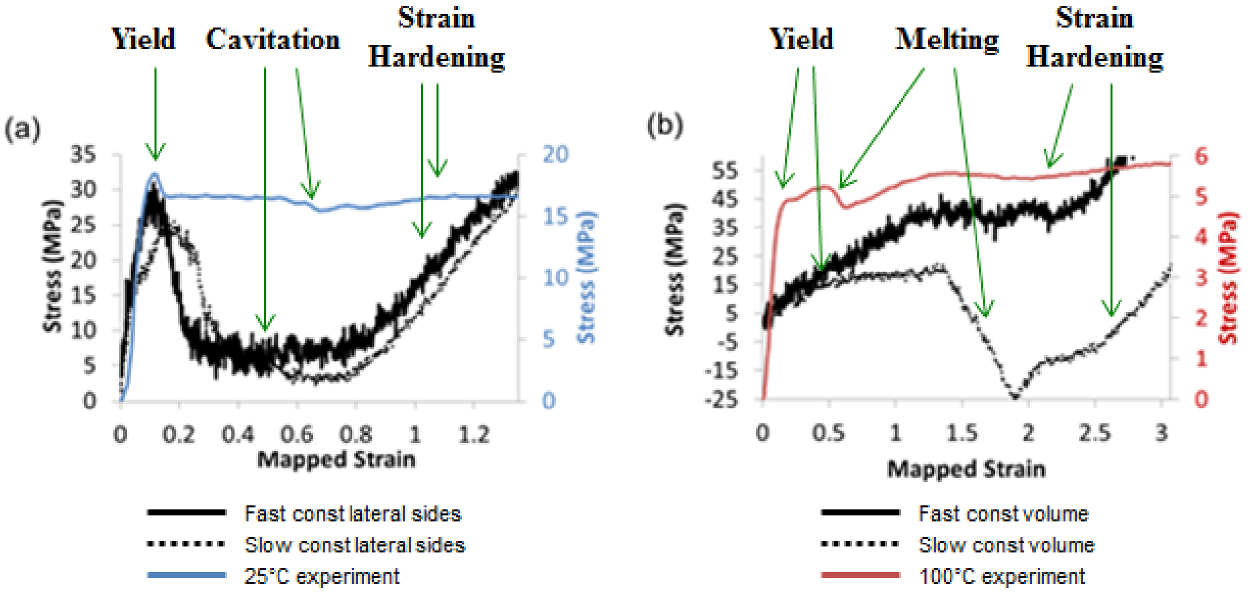

Figure 6.11 Stress-strain curves for (a) simulation with constant lateral sides (black) and the 25°C experiment (blue), (b) simulation with constant volume and the 100°C experiment (red). The simulation strain is mapped to experimental strain space using the linear maps for time and strain in Figure 6.9 (d) and (c), respectively. The simulations in (a) exhibit similar features (yield, plastic deformation, and strain hardening) as the 25°C experiment, but both post-yield softening and subsequent strain hardening are more pronounced. Similarly, the slow simulation in (b) shows yield, melting, and strain hardening features also seen in the 100°C experiment, and the simulated features tend to be more pronounced and occur at higher (mapped) strains.

Changes in morphology associated with the uniaxial tensile deformation can be assessed by computing the % crystallinity as a function of deformation strain. A comparison of the computed change in % crystallinity from the simulations and from the experimental WAXD patterns is shown in Figure 6.12. The crystallinity from the simulations was determined first by computing a local Herman's orientation factor, $P_2(r)$, of each bead, where $r<0.4$nm, in three dimensions. Beads are considered crystalline if $P_2(r)>0.6$. As discussed in Reference 16, the choice of order parameter and the cutoff of 0.6 for crystallinity calculations are somewhat arbitrary and thus, the comparisons of calculated crystallinity changes to those of experimental findings are qualitative.

Experimentally determined crystallinity values during deformation at 25°C are consistently higher than the values obtained from the simulations with constant lateral dimensions. This is expected since the simulations were conducted at T=77°C, ensuring more thermal energy and a subsequent lower crystallinity. However, the *change* in crystallinity during simulated deformation should be comparable to the experimentally measured change in crystallinity. Figure 6.12 shows that the changes in crystallinity during the simulated deformations depend on both the simulation strain rate and the boundary conditions. Under simulation conditions with fixed lateral sides, the crystallinity stays relatively constant during the fast deformation, but decreases markedly during the slow deformation, as shown in Figure 6.12a. The crystallinity during the 25°C deformation experiment remains relatively constant up to e=0.7, although it does increase at higher strains by about 3%. Hence, the 25°C experiment more closely resembles the fast deformation simulation with constant lateral dimensions. However, the experimentally observed transition from an orthorhombic crystalline unit cell to a mix of monoclinic and orthorhombic structure at e=1.0 is not observed in the simulation because the UA PE model only exhibits one low energy crystal packing structure. The fast deformation simulation with fixed lateral sides was expected to coincide with the low temperature deformation experiment because both are likely exploring similar configuration space that gives rise to similar deformation mechanisms. At low temperatures where the ground state energy dominates, the crystalline regions would persist upon deformation. Thus, the crystallites could act as a natural barrier to constriction in the lateral dimension. This effectively corresponds to a deformation with constant lateral dimensions in the mechanical unit cell. In addition, the lower temperature experimental system lacks thermal energy required to surmount free energy barriers and to fully explore available conformation space. A similar phenomenon happens in the fast deformation simulation where exploration is restricted because deformation is faster than the average relaxation time of the polymer chains.

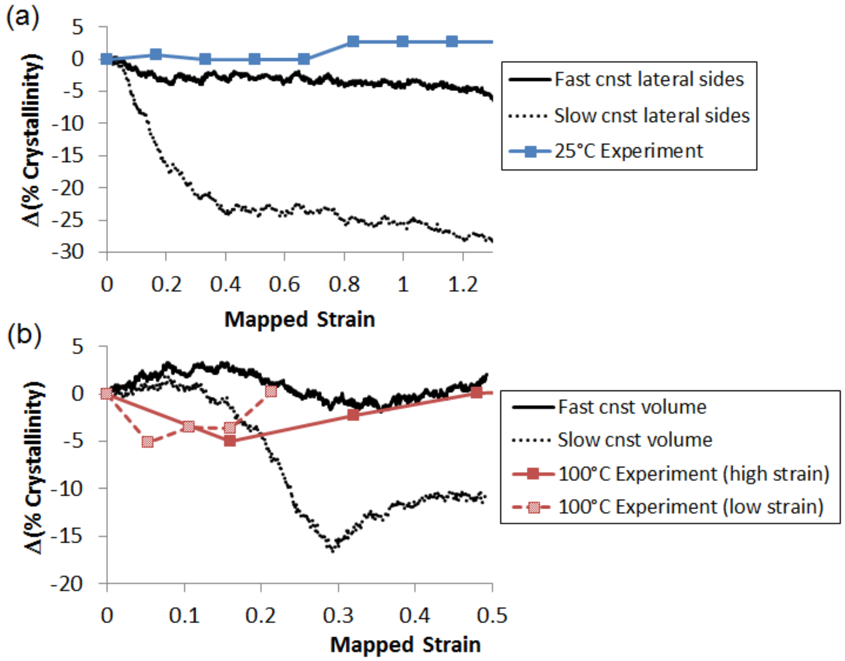

Figure 6.12 The change in percent crystallinity in simulations of deformation with (a) constant lateral dimensions and the 25°C experiment, and (b) constant volume simulations and two 100°C experiments. Two experiments were performed at 100°C; one with a higher collection frequency deformed to 1.5 strain (dashed red line) and one with a lower collection frequency deformed to 3.0 strain (solid red line).

The crystallinity during the slow, constant volume simulation and during the 100°C deformation experiment both exhibit a decrease in crystallinity with strain followed by a reconstruction phase, as shown in Figure 6.12b. This trend is consistent with the observed similarity in the stress-strain curves in Figure 6.11b. Both simulation and experimental results show an initial crystallinity near 60% with more melting after yielding indicated from simulations (almost a 30% drop in degree of crystallinity versus the 9% drop observed experimentally). Unlike comparisons with other deformation features, the melting of the crystalline regions occurs at higher strains in the simulation than observed from the experiment. This may be attributed to the “infinite” lamellae resulting from the crystallite periodic boundary conditions imposed in the simulation that would resist melting from the lateral planes. The probability of observing this melting mechanism is thus much lower in the simulations than in the experiment.

The similarity between the high temperature deformation experiment and the slow and constant volume simulation is also consistent with physical interpretation. The crystalline regions during the high temperature deformation could exhibit strain-induced melting and the lateral dimensions of a lamellar stack would then decrease proportional to the increase in the deformation axis. This effectively corresponds to a deformation with constant volume where the lateral dimensions are decreasing with increasing strain in the stretching direction. Additionally, the higher temperature system has enough thermal energy to surmount free energy barriers and to explore more conformation space. The slow deformation simulations allow enough time for the system to similarly explore more conformations. Thus, the high temperature deformation experiment corresponds to the slow deformation simulation with a constant volume.

The evolution of the lamellar morphology with strain was analyzed for the constant volume simulations by considering the Gibbs dividing surface between the crystalline and noncrystalline regions. In this analysis, the mass density profile is computed along the deformation (z-) axis. The transition between crystalline (high mass density) and noncrystalline regions is fit to a step function and the location of the step is the Gibbs dividing surface[29]. Unlike the calculation of crystallinity, this procedure is purely based on mass density and does not take into account local chain orientation. Thus, the interfacial region between crystalline and amorphous regions, where the packing density of united atoms is still high but the chains are not well aligned, are interpreted as crystalline. During deformation where the crystalline region melts, as is the case for the slow and constant volume simulation, this interfacial region will rapidly "melt out" leading to a growth in the amorphous region.

As shown in Figure 6.13a, the amorphous region grows more than an affine deformation (marked as a red line, representing equal strain in crystalline and noncrystalline regions) during the slow and constant volume simulated deformation. This amorphous thickness reaches a maximum around a simulated strain of 0.27, which is the strain at the completion of melting where the stress is minimal in Figure 6.11b. After a reconstruction period (simulated e=0.3), the amorphous region grows at a rate similar to an affine deformation. This finding implies that the softer, noncrystalline region contributes more to the deformation strain. However, this interpretation is tempered since the Gibbs dividing surface may underestimate the initial number of beads within the noncrystalline region. Because of this reason, it is difficult to compare the crystalline and amorphous thicknesses during the 100°C experimental deformation, shown in Figure 6.13b, with the simulation results. The experimental results, mapped onto the simulated strain, show an initial drop in both crystalline and amorphous thicknesses up to e_m=0.2. The long period also decreases during this low strain period, which is likely caused by residual alignment in the strain direction. This residual alignment could cause a drop in amorphous thickness and may explain why it is not observed in the simulations. The drop in crystalline thickness can be attributed to melting during deformation. At higher strains, the crystalline regions grow by the imposed chain alignment.

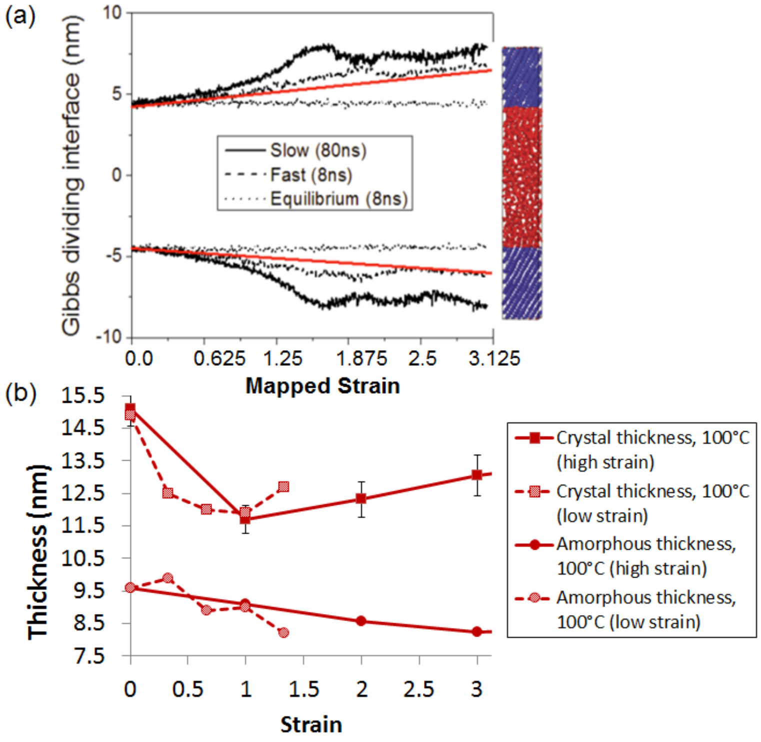

Figure 6.13 Evolution of lamellar morphology. (a) Gibbs dividing interfaces between crystalline (shown as the two blue regions on the right side of the figure) and noncrystalline domains (shown as the red region on the right side of the figure) as a function of strain for the constant volume "slow" and "fast" deformation simulations. The red line represents a hypothetical affine deformation, and the equilibrium data is from a simulation with no deformation. (b) Crystal (squares) and amorphous (circles) thickness of the HDPE computed from SAXS and WAXD data collected from two experiments during 100°C uniaxial deformation. As in Figure 6.12, the two experiments employed different collection frequencies to capture the low strain behavior.

6.4 Conclusion

The controlled in situ SAXS/WAXD deformation experiment on a uniaxially oriented PE fiber provides a system to directly compare to the plastic deformation simulation results of a semi-crystalline lamellar model. This comparison provides bounds in which to interpret further simulation results. In general, discernable features in the simulated stress-strain curves happen with higher and more pronounced changes in stress, and at lower strains as a consequence of the united atom model used for PE and the periodic boundary conditions imposed. Also, the simulations average over only 18 different structures, all of which are perfectly aligned. Thus, the changes in simulated stress occur at similar strains and tend to be abrupt. Nonetheless, simulations were shown to be able to capture a full range of observed experimental behavior by varying deformation rate and boundary conditions. The correspondence of rate with experimental temperature is simply a time-temperature superposition. The dependence on the simulation boundary conditions highlights the different observed experimental deformation mechanisms—crystallographic slip and strain-induced melting. One could likely find similar deformation mechanisms by varying the simulation temperature rather than the boundary conditions. With these performance boundaries in mind, one can now devise systematic studies using this SM model in order to understand how amorphous topology affects plastic deformation and the stress within the system.

6.5 References

1. Kolgjini, B.; Schoukens, G.; Kiekens, P. *Intern. J. Poly. Sci.* **2011**, 731708, 1-7.
2. Na, B.; Zhang, Q.; Fu, Q.; Men, Y.; Hong, K.; Strobl, G. *Macromolecules* **2006**, 39, 2584-2591.
3. Fu, Q.; Men, Y.; Strobl, G. *Polymer* **2003**, 44, 1927-1933.
4. Hobeika, S.; Men, Y.; Strobl, G. *Macromolecules* **2000**, 33, 1827-1833.
5. Stribeck, N.; Alamo, R. G.; Mandelkern, L.; Zachmann, H. G. *Macromolecules* **1995**, 28, 5029-5036.
6. Fu, Q.; Men, Y.; Strobl, G. *Polymer* **2003**, 44, 1941-1947.

7. Jiang, Z.; Tang, Y.; Men, Y.; Enderle, H.; Lilge, D.; Roth, S. V.; Gehrke, R.; Rieger, J. *Macromolecules* **2007**, 40, 7263-7269.
8. Tang, Y.; Jiang, Z.; Men, Y.; An, L.; Enderle, H.; Lilge, D.; Roth, S. V.; Gehrke, R.; Rieger, J. *Polymer* **2007**, 48, 5125-5132.
9. Uribe, A.; Manzur, A.; Olayo, R. *J. Mater. Res.* **2012**, 27, 1351-1359.
10. Bowden, P. B.; Young, R. J. *J. Mater. Sci* **1974**, 9, 2034-2051.
11. Goderis, B.; Reynaers, H.; Koch, M. H. J.; Mathot, V. B. F. *J. Poly. Sci: Part B: Poly. Phys.* **1999**, 37, 1715-1738.
12. Hiss, R.; Hobeika, S.; Lynn, C.; Strobl, G. *J. Macro Sci, Part B: Phys* **1999**, 38, 847-858.
13. Hiss, R.; Hobeika, S.; Lynn, C.; Strobl, G. *Macromolecules* **1999**, 32, 4390-4403.
14. Moysés S. C.; Machado, R. *Eur. Poly. Journ.* **2002**, 38, 2041-2044.
15. Hong, K.; Strobl, G. *Macromolecules* **2006**, 39, 268-273.
16. Lee, S.; Rutledge, G. C. *Macromolecules* **2011**, 44, 3096-3108.
17. Veld, P. in't; Rutledge, G. C. *Macromolecules* **2003**, 36, 7358-7365.
18. Humbert, S.; Lame, O.; Chenal, J.; Rochas, C.; Vigier, G. *J. Poly. Sci: Part B: Poly. Phys.* **2010**, 48, 1535-1542.
19. Z. Wilchinsky, *J. Appl. Phys.* **1960**, 31, 1969-1972.
20. Desper, C.; Stein, R. *J. Appl. Phys.* **1966**, 37, 3990-4002.
21. Hermans, J. J. *Rec. Trav. Chim. Pays-Bas.* **1944**, 63, 211-218.
22. Stribeck, N. *Macromolecules* **1996**, 29, 7217-7220.
23. Ruland, W.; Smarsly, B. *J. Appl. Crystal.* **2004**, 37, 575-584.
24. Burger, C.; Zhou, H.; Wang, H.; Sics, I.; Hsiao, B. S.; Chu, B.; Graham, L.; Glimcher, M. J. *Biophysical Journ.* **2008**, 95, 1985-1992.
25. Veld, P. in't; Hutter, M.; Rutledge, G. C. *Macromolecules* **2006**, 39, 439-447.
26. Eyring, H. *J. Chem. Phys.* **1936**, 4, 283-291.
27. Sweeney, J.; Shirataki, H.; Unwin, A. P.; Ward, I. M. *J. App. Poly. Sci.* **1999**, 74, 3331-3341.
28. Capaldi, F. M.; Boyce, M. C.; Rutledge, G. *Polymer* **2004**, 45, 1391-1399.
29. Hutter, M.; Veld, P. in't ; Rutledge, G. C. *Polymer* **2006**, 47, 5494-5504.

Chapter 7

Morphological Effects on Swelling in Semi-Crystalline Polyethylene

7.1 Introduction

Solvent and vapor swelling of semi-crystalline polyethylene has been examined quite thoroughly before. Vapor diffusion coefficient was found to decrease with increasing polyethylene crystallinity and sorbed vapor concentration was proportionally lowered with decreasing amorphous content[1-3]. It was thus concluded that vapor and solvent uptakes occur only in the amorphous region. Additionally, it was found that both diffusion coefficient[4] and total uptake[5] decrease with increasing orientation in an oriented polyethylene. In situ vapor sorption SANS (Small Angle Neutron Scattering) has been successfully applied to examine the structural changes in polyethylene with sorption and has verified the assumption that vapor selectively diffuses into only the amorphous regions[6]. With solvent and vapor selectively diffusing into the amorphous regions of a semi-crystalline polyethylene (PE), the swelling or sorption of PE could potentially be used to examine the amorphous phase.

The structure of a semi-crystalline polyethylene is in the form of stacked lamellae with alternative layers of crystalline and amorphous regions where chain folds, tie chains, entanglements, and loose ends can be found in the amorphous phase. The Huang-Brown theory[7] computes the probability of forming a tie chain as a function of PE backbone composition, including molecular weight and co-monomer content, and has been applied to explain the observed enhancements in toughness in LLDPE (Linear Low Density PE) as compared with that of HDPE (High Density PE)[8] and the change in impact toughness of LLDPE as a function of its density[9]. The tie chains and trapped entanglements in the amorphous phase behave like network connecting chain segments in a crosslinked rubber during deformation where the crystallites can be treated as crosslinks. The rubber elasticity theory can be and has been applied to understand the deformation behavior of semicrystalline PE, specifically the mechanical strain hardening during uniaxial tensile deformation[10]. Through the measurements of strain hardening slope and the conversion from strain hardening to rubber elasticity modulus, network segment concentrations in semi-crystalline PE have been determined and were found to compare favorably with the tie chain probabilities calculated from the Huang-Brown theory[9]. Those network-chain-equivalent tie chains and entanglements in the amorphous phase are expected to equally affect the amorphous swelling[11]. In this work, swelling and corresponding morphological changes in HDPE and LLDPE were examined and quantified by a combination of x-ray scattering and calorimetric methods. Constrained swelling was found in LLDPE and can be related to its higher tie chain concentration.

7.2 Experimental Methods

7.2.1 Materials and Sample Preparation

Linear and short-chain-branched polyethylene fibers were supplied by ExxonMobil Chemical Company. The provided HDPE fiber had M_n of 15,400 g/mol and M_w of 122,000 g/mol. The entanglement molecular weight of this HDPE is about 860 g/mol. The provided LLDPE fiber had M_n of 24,300 g/mol and M_w of 96,600 g/mol. The entanglement molecular weight of this LLDPE is about 880 g/mol. Both HDPE and LLDPE fibers were prepared using a capillary rheometer at a low pull rate of 0.6 m/min to form 1-mm thick fibers with uniaxially oriented stacked lamellae. Based on the experimentally measured polymer melt coil dimensions, crystallite thickness, and amorphous spacing in the fibers, tie chain probabilities calculated based on the Huang-Brown theory for the HDPE fiber and LLDPE fiber were 0.0036 and 0.165, respectively. Significantly higher tie chain concentration is expected in LLDPE. For both DSC and x-ray experiments, fresh samples were soaked in toluene for specified amounts of time and gently dried with Kimwipes® prior to experiments. Samples were soaked for various time intervals up to 24 hours.

7.2.2 Differential Scanning Calorimetry

Samples having approximate length of 0.5 cm were used. Sample weight before and after soaking was determined using a Mettler-Toledo XS3DU Microbalance to within ±0.001 mg. Samples were immediately cut roughly in half and sealed in standard aluminum pans of known weight. Samples were heated at 10 °C/min between -60 and 160 °C using a TA Instruments Q2000 DSC equipped with a liquid nitrogen accessory. Limits of integration for heat of fusion determination were held constant for each analysis. Degree crystallinity[12] was calculated compared to 100% crystalline polyethylene having a heat of fusion of 293 J/g.

7.2.3 X-ray Scattering

Samples having approximate length of 1 cm were used. Sample weight, before and after soaking, was determined to within ±0.01g. Samples were soaked for time periods ranging between 0 and 6 hours every 30 min, between 6 and 12 hours every hour, and between 12 and 24 hours every 6 hours. SAXS and WAXS data was collected at beamline X27C, National Synchrotron Light Source (NSLS) at Brookhaven National Lab (BNL). A MARCCD detector with 158-µm pixel size was used to record two-dimensional scattering patterns generated with x-rays of wavelength, λ, of 1.371 Å and 30 seconds acquisition time period. The camera length was calibrated by using aluminum oxide (Al_2O_3) for WAXS and silver behenate for SAXS. SAXS and WAXS camera distances were 1775.7 and 128.2 mm, respectively.

X-ray data pre-treatment included the subtraction of a background and adjustment for incident flux and acquisition time. The azimuthally-averaged intensity, $I(q)$, was extracted as a function of scattering vector, $q = 2\pi s = 4\pi\sin(\theta)/\lambda$, where θ is half the scattering angle. Since orientation in the samples was negligible, a Lorentz correction was applied to SAXS data by multiplying the scattering intensity[13], $I(q)$, by the scattering vector, q, squared: $J(q) = I(q)q^2$. The

SAXS long period, L_p, was determined from the position of the peak in $J(q)$, q_{max}, as: $L_p = 2\pi/q_{max}$. The long period is a measure of the periodicity within the sample resulting from electron density differences and is interpreted as a characteristic spacing of crystalline and non-crystalline domains for a two-phase system. The WAXS crystallinity index, X_c, was determined as the ratio of the area of the crystalline peaks, Ac, to the combined area of the amorphous halo, A_a, and the crystalline peaks: $X_c = A_c/(A_a+A_c)$. Areas were obtained after fitting the amorphous halo and the orthorhombic crystal reflections attributed to the (110) and (200) planes with Lorentzian functions.

Assuming a two-phase model, the average thickness of the crystalline layer, <T>, was calculated from WAXS crystallinity, X_c, and long period, L_p (obtained from SAXS) as:

$$\langle T \rangle = X_c * L_p \tag{7.1}$$

Consequently, the average thickness of the amorphous layer, <t>, is given as

$$\langle t \rangle = L_p - \langle T \rangle \tag{7.2}$$

7.2.4 SAXS Stacking Model Fitting

The experimentally obtained one-dimensional integrated raw SAXS intensities were fitted with a two phase stacking model that was adopted from Burger[14], Ruland[26], Hermans[27], Stribeck[28], and is given by:

$$I_{1D}(s) = \frac{f}{s^4} \mathrm{Re}\left\{ \frac{(1 - H_1(s))(1 - H_2(s))}{1 - H_1(s) H_2(s)} \right\}, \tag{7.3}$$

where $I_{1D}(s)$ is the intensity in the one-dimensional reciprocal space, s is the scattering vector, f is a proportionality constant, $\mathrm{Re}\{\ \}$ takes the real part of the complex number, and $H_1(s)$ and

$H_2(s)$ are the Fourier transforms of the thickness distributions of the two phases. A Gaussian distribution was chosen as the thickness distributions of the two layers and can be given as:

$$H_1(s) = \exp(2\pi i\langle T\rangle s - 2\pi^2\sigma_T{}^2 s^2) \text{ and} \tag{7.4}$$

$$H_2(s) = \exp(2\pi i\langle t\rangle s - 2\pi^2\sigma_t{}^2 s^2), \tag{7.5}$$

where σ_T and σ_t are the standard deviations of the thickness distributions. These structural parameters were obtained for both HDPE and LLDPE fibers at various sorption time intervals. The structural parameters obtained from model fitting were compared with those obtained from experiments.

7.2.5 2D Correlation Analysis

Two-dimensional (2D) correlation analysis was applied to examine subtle changes in the SAXS and WAXS scattering curves in response to the perturbation variable—here, swelling time. Two-dimensional correlation spectra were calculated using Noda's generalized method[15-17] from the discrete set of intensity curves ($J(q)$ or $I(q)$; $J(q)$ shown) measured at m unequally swelling times, t_i:

$$J_i(q) = J(q,t_i) \qquad i= 1,2,3\ldots m. \tag{7.6}$$

The discrete dynamic spectra, $\tilde{J}(q,t_i)$, were calculated with respect to a time-averaged spectrum, $< J(q) >$:

$$\tilde{J}(q,t_i) = J(q,t_i) - < J(q) > i = 1,2,3,\ldots, m. \tag{7.7}$$

$$< J(q) >= \frac{\sum_{i=1}^{m} J(q,t_i)(t_{i+1} - t_{i-1})}{\sum_{i=1}^{m}(t_{i+1} - t_{i-1})}. \tag{7.8}$$

By defining

$$t_0 = 2t_1 - t_2 \text{ and} \tag{7.9}$$

$$t_{m+1} = 2t_m - t_{m-1}, \tag{7.10}$$

equation 7.8 simplifies to:

$$< J(q) >= \frac{\sum_{i=1}^{m} J(q,t_i)(t_{i+1} - t_{i-1})}{3t_m - t_{m-1} + t_2 - 3t_1}\,. \tag{7.11}$$

The synchronous 2D correlation intensity, demonstrating simultaneous or coincidental changes in intensity, is given by:

$$\Phi(q_1, q_2) = \frac{1}{2(t_m - t_1)} \sum_{i=1}^{m} \tilde{J}_i(q_1) \cdot \tilde{J}_i(q_2)(t_{i+1} - t_{i-1})\,. \tag{7.12}$$

The asynchronous 2D correlation spectra, showing changes in intensity that lag/lead one another, is given by

$$\Psi(q_1, q_2) = \frac{1}{2(t_m - t_1)} \sum_{i=1}^{m} \tilde{J}_i(q_1) \cdot \tilde{z}_i(q_2)(t_{i+1} - t_{i-1})\,, \tag{7.13}$$

where $\tilde{z}_i(q_2)$ are the discrete orthogonal spectra defined as the time-domain Hilbert transform of the dynamic spectra, $\tilde{J}(q,t_i)$. We used the approximation introduced by Noda[17] that permitted $\tilde{z}_i(q_2)$ to be expressed in terms of a linear transformation of discrete dynamic spectra, $\tilde{J}_i(q_2)$,

$$\tilde{z}_i(q_2) = \sum_{j=1}^{m} N_{ij} \cdot \tilde{J}_j(q_2)\,, \tag{7.14}$$

where N_{ij} is the Hilbert-Noda transformation matrix for unevenly spaced data,

$$N_{ij} = \begin{cases} 0 & \text{if } i = j \\ \dfrac{t_{j+1} - t_{j-1}}{2\pi(t_j - t_i)} & \text{otherwise} \end{cases}. \tag{7.15}$$

7.3 Results and Discussion

7.3.1 DSC and WAXD

Gravimetrically, LLDPE exhibited greater percent uptake of toluene compared with HDPE (Figure 7.1a). Additionally, LLDPE attained saturation faster in about 4 hours, compared with about 6.5 hours for HDPE, due largely to the higher amorphous content of the polymer. When the data was normalized by the amorphous fraction calculated by DSC, HDPE exhibited slightly greater toluene uptake (Figure 7.1b). This observation is consistent with a less constrained amorphous phase found in HDPE compared with LLDPE[2]. The differences in rates of saturation may be attributed to the larger crystals found in HPDE which would adversely impact permeability compared with LLDPE.

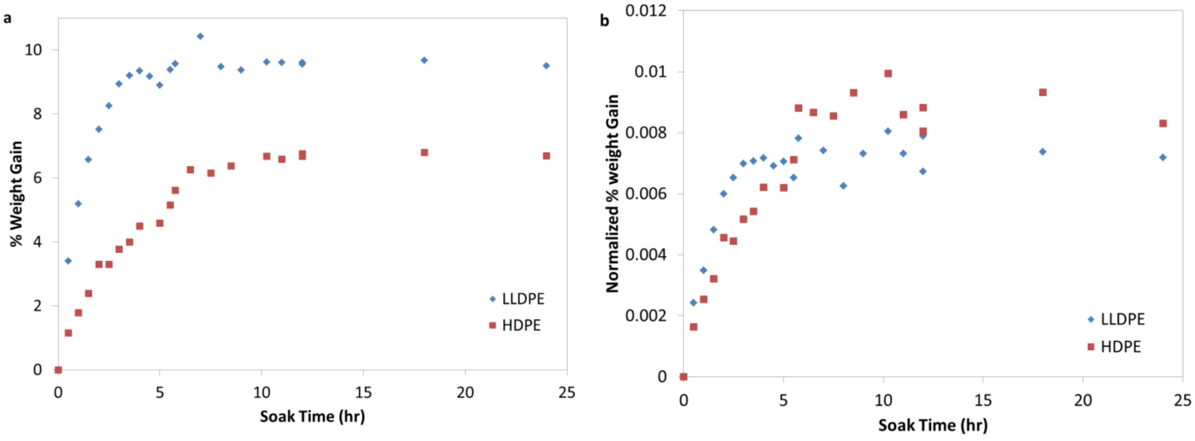

Figure 7.1 (a) Percent weight gain and (b) percent weight gain normalized by amorphous fraction by DSC of LLDPE compared with HDPE after soaking in toluene for different periods of time.

Neither crystallinity nor peak melting temperature by DSC exhibited a dependence on soaking time for either material as shown in Figure 7.2. Crystallinity measured by WAXD (not shown) also remained constant with soaking time. Furthermore, no change was observed in either the *a* or *b* axis of the orthorhombic unit cell, as shown in Figure 7.3. These observations could suggest that toluene uptake did not significantly alter the crystal phase of either polymer and occurred primarily in the amorphous phase, consistent with previous literature[3-5].

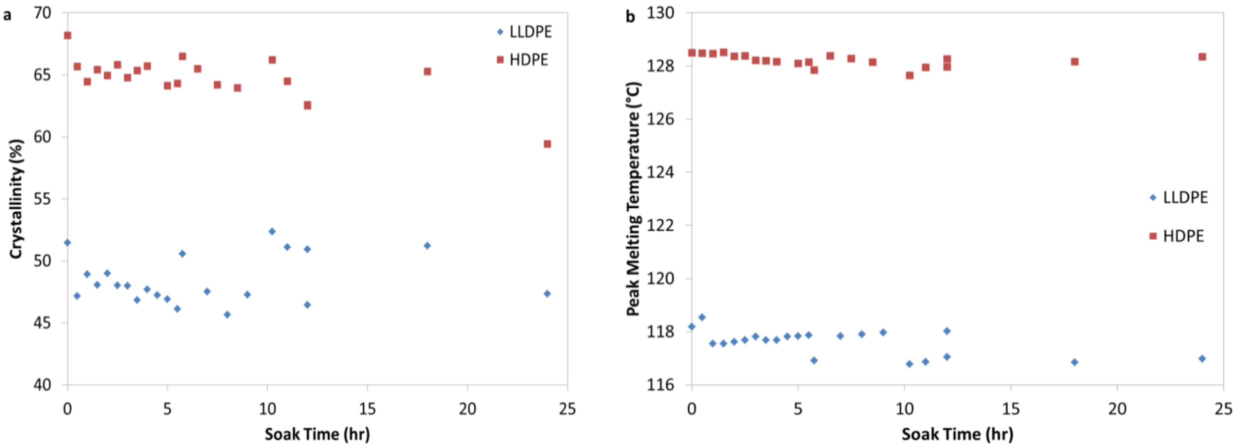

Figure 7.2 (a) Crystallinity and (b) peak melting temperature by DSC of LLDPE compared with HDPE after soaking in toluene for different periods of time.

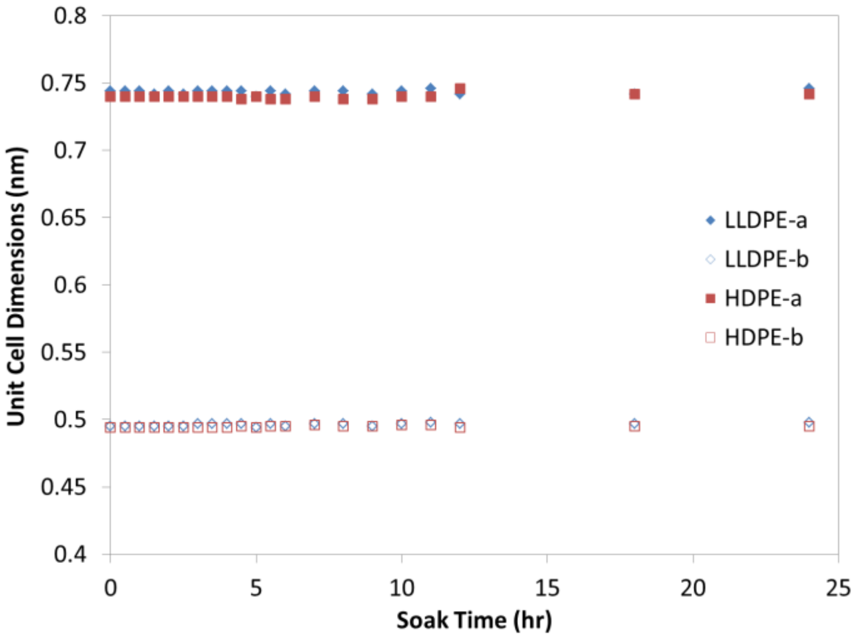

Figure 7.3 Orthorhombic unit cell dimensions by WAXD of LLDPE compared with HDPE after soaking in toluene for different periods of time.

7.3.2 Diffusion Coefficient

The diffusion coefficient of toluene in LLDPE and HDPE was calculated by assuming 1D Fickian diffusion and calculating the initial slope of the relationship between molar percent uptake of solvent per gram of polymer (Q_t) and square root of soak time ($t^{1/2}$)[18-19]. The initial slope of this plot, m, could be related to the diffusion coefficient, D, of a solvent molecule in a network of polymer using Fick's second law of diffusion:

$$D = \pi\,(lm/4Q_\infty), \tag{7.16}$$

where l is the fiber thickness and Q_∞ is the equilibrium absorption at long times. D is assumed to be independent of soaking time. The resulting diffusion coefficients were 1.7×10^{-7} and 6.3×10^{-8} for LLDPE and HDPE, respectively. Consistent with literature, we could see a decrease in the diffusion coefficient with increasing crystallinity[4].

7.3.3 SAXS Stacking Model

Long period, L_p, determined by traditional SAXS/WAXS methods was found to increase with soaking time for both materials (Figure 7.4a). Consistent with total toluene uptake, saturation was found to occur at shorter time for LLDPE compared with HDPE. Analysis using the stacking model yielded similar results. In both cases, the long period was found to increase by approximately 6% (Table 7.1). Most of this change was due to an increase of the average amorphous layer thickness, <t>, of about 8%. Surprisingly, the average crystalline layer thickness, <T>, was also found to increase by approximately 5% for both materials. This small change could likely occur due to an increase in alignment and crystallization in the interfacial region between the crystalline and amorphous layers as a consequence of the expansion of the amorphous layer[20].

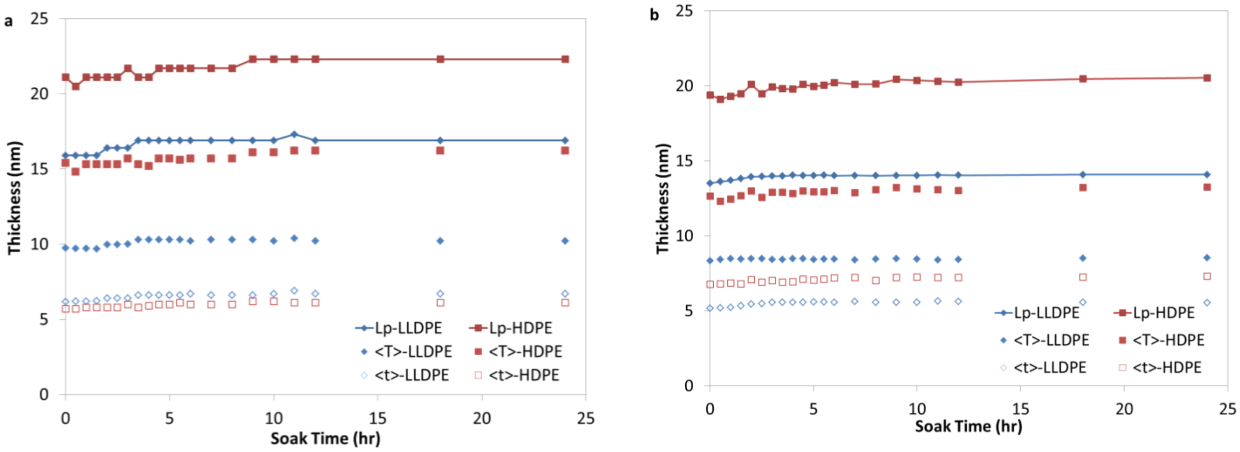

Figure 7.4 Long period, L_p, average crystalline, <T>, and amorphous <t> layer thicknesses calculated by (a) traditional SAXS/WAXS method and (b) fitting to a stacking model.

	Sample	**% Increase (WAXD/SAXS)**	**% Increase (Stacking Model)**
Lp	LLDPE	6	4
	HDPE	6	6
<T>	LLDPE	5	3
	HDPE	5	5
<t>	LLDPE	9	7
	HDPE	7	8

Table 7.1Total percent increase after soaking in toluene for 24 hours of long period, L_p, average crystalline layer thickness <T> and average amorphous layer thickness <t> obtained by tradition WAXS/SAXS analysis and with Stacking model.

7.3.4 2D Correlation Analysis

Two-dimensional correlation analysis was applied to both WAXS and SAXS intensity curves in order to examine subtle changes in the scattering profiles[21-22]. Figure 7.5a shows a 2D synchronous plot obtained from SAXS scattering profiles during swelling of HDPE with toluene. Average scattering intensities are shown on the sides. The 2D plot was dominated by a positive feature along the diagonal at approximately 0.36 nm^{-1}. A secondary positive cross-peak was evident at (0.78, 0.36) indicating there was a second autocorrelation peak at 0.78 nm^{-1} (due to the nature of the calculation of the 2D synchronous plot, the intensity of these feature was below the threshold of the contour plot). The autocorrelation spectra depicted in Figure 7.6a, which is the intensity profile along the diagonal of the 2D synchronous plot in Figure 7.5a, confirmed a small change in scattering near 0.78 nm^{-1}. This second feature was also evident in the average spectra shown on the sides of Figure 7.5a and corresponded to the secondary reflection due to well-ordered lamellae found in HDPE. The presence of these features in the 2D synchronous spectra indicated changes of the SAXS peaks, and hence long period, in response to toluene soaking. Furthermore, negative cross-peaks were evident at (0.36, 0.22), indicating changes in intensity at 0.22 nm^{-1} occurring in the opposite direction to those at 0.36 and 0.78 nm^{-1}. These features were consistent with the shifting of the SAXS peaks to lower q-values and hence increasing long period with toluene uptake.

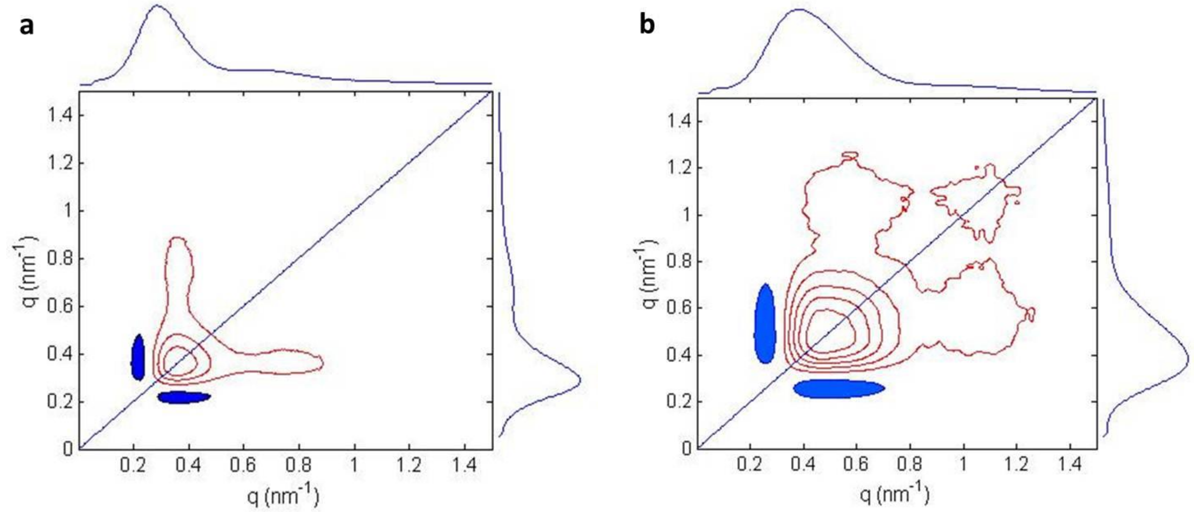

Figure 7.5 2D synchronous correlation plots of SAXS profiles as a function of soaking time for (a) HDPE and (b) LLDPE. Positive contours are outlined in red and negative contours are filled blue. Average profiles are shown on the side.

Two-dimensional correlation analysis was applied to both WAXS and SAXS intensity curves in order to examine subtle changes in the scattering profiles[21-22]. Figure 7.5a shows a 2D synchronous plot obtained from SAXS scattering profiles during swelling of HDPE with toluene. Average scattering intensities are shown on the sides. The 2D plot is dominated by a positive feature along the diagonal at approximately 0.36 nm^{-1}. A secondary positive cross-peak was evident at (0.78, 0.36) indicating there was a second autocorrelation peak at 0.78 nm^{-1} (due to the nature of the calculation of the 2D synchronous plot, the intensity of these feature was below the threshold of the contour plot). The autocorrelation spectra depicted in Figure 7.6a, which was the intensity profile along the diagonal of the 2D synchronous plot in Figure 7.5a, confirmed a small change in scattering near 0.78 nm^{-1}. This second feature was also evident in the average spectra shown on the sides of Figure 7.5a and corresponded to the secondary reflection due to well-ordered lamellae found in HDPE. The presence of these features in the 2D synchronous spectra indicated changes of the SAXS peaks, and hence long period, in response to toluene soaking. Furthermore, negative cross-peaks were evident at (0.36, 0.22), indicating changes in intensity at 0.22 nm^{-1} occurring in the opposite direction to those at 0.36 and 0.78 nm^{-1}. These features were consistent with the shifting of the SAXS peaks to lower q-values and hence increasing long period with toluene uptake.

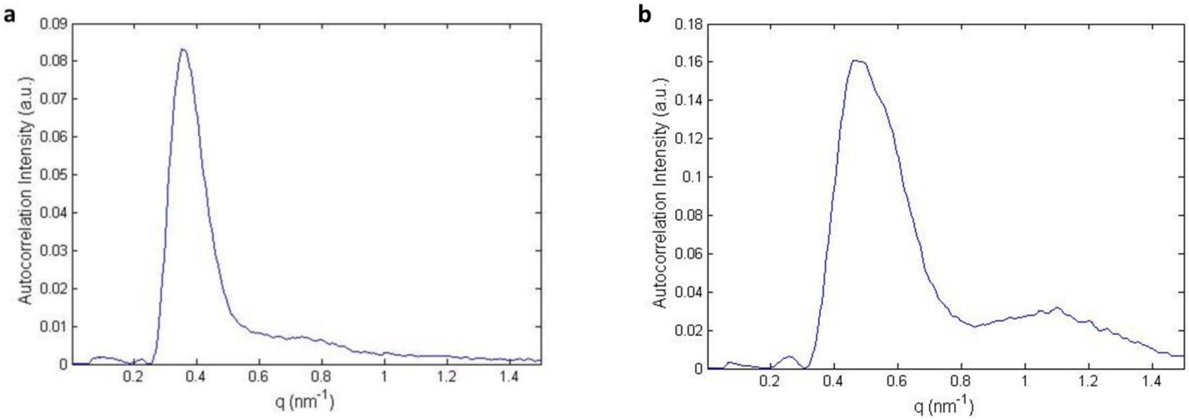

Figure 7.6 Autocorrelation intensity along diagonal of 2D synchronous correlation plots of SAXS profiles as a function of soaking time for (a) HDPE and (b) LLDPE.

The 2D synchronous plot for LLDPE (Figure 6.5b) also contained a prominent positive feature along the diagonal; this feature was at about 0.5 nm^{-1} corresponding to the smaller long period found in this material compared with HDPE. Again, the negative cross-peaks were evident at (0.25, 0.5), consistent with the SAXS peak shifting to lower q-values. For this material, an additional autocorrelation feature was evident at about 1.1 nm^{-1}, along with the corresponding cross-peaks at (1.1, 0.5). The significant change in intensity near 1.1 nm^{-1} was even more apparent upon examination of the autocorrelation intensity (Figure 6.6b). Furthermore, a secondary reflection near 1.1 nm^{-1} was *not* evident in the average scattering curves depicted on the sides of Figure 7.5b for LLDPE. Consequently, one could not associate the change in the scattering intensity near 1.1 nm^{-1} with the change in the long period due to swelling as was done for HDPE. An alternative interpretation is a change in scattering from entities with a characteristic long spacing of approximately 6 nm, which are most likely fringed micelles[22-25].These morphological entities could also likely swell in response to toluene soaking and hence the broad 2D feature could likely be due to shifting of intensity from high to low q-

values. This shift could not be confirmed because of the breadth of this feature and the limited amount of SAXS profiles available to convolute the 2D asynchronous plot (not shown).

Application of 2D correlation analysis to WAXS data (not shown) did not reveal features of interest. Even implementation of several normalization schemes failed to provide significant features corresponding to the amorphous halo, suggesting that even though there were changes in the amorphous region due to swelling and in the interfacial region due to crystallization, these were relatively small for both materials.

7.4 Conclusion

Solvent and vapor swelling of semi-crystalline PE have been examined and quantified by SAXS, WAXD, and DSC. The morphological changes in the lamellar structure of HDPE and LLDPE were analyzed using a two-phase stacking model and a 2D correlation analysis. The lamellar structure contained alternative layers of crystalline and amorphous regions, where chain folds, tie chains, entanglements, and loose ends could be found in the amorphous phase. An increase in long spacing during swelling was found in both HDPE and LLDPE. The diffusion coefficient and the solvent uptake were found to occur mainly in the amorphous regions. The constrained swelling in LLDPE may be attributed to its higher tie chain and trapped entanglement concentrations in its amorphous phase as compared to HDPE.

7.5 References

1. McCall, D. W.; Anderson, E. W. *Journal of Polymer Science Part A: General Papers*, **1963**, *1*, 1175
2. Rogers, C. E.; Stannett, V.; Szwarc, M. *Journal of Polymer Science*, **1960**, *45*, 61
3. McCall, D.W. *Journal of Polymer Science*, **1957**, *26*, 151
4. Ng, H. C.; Leung, W. P.; Choy, C. L. *Journal of Polymer Science: Polymer Physics Edition*, **1985**, *23*, 973
5. Kwei, T. K.; Wang, T. T. *Macromolecules*, **1972**, *5*, 128

6. Kim, M. H.; Glinka, C. J. *Journal of Applied Crystallography*, **2005**, *38*, 734
7. Huang, Y. L.; Brown, N. *Journal of Polymer Science, Part B: Polymer Physics*, **1991**, *29*, 129
8. Seguela, R. *Journal of Polymer Science, Part B: Polymer Physics*, **2005**, *43*, 1729
9. Patel, R. M.; Sehanobish, K.; Jain, P.; Chum, S. P.; Knight, G. W. *J. Appl. Polym. Sci.*, **1996**, *60*, 749
10. Howard, R. N. *Macromolecules*, **1993**, *26*, 5860
11. Flory, P. J. *"Principle of Polymer Chemistry"*, **1953**, Cornell University Press, Ithaca, NY, Chapter 13, 577-584
12. Wunderlich, B.; Czornyj, G. *Macromolecules*, **1977**, *10*, 906
13. Cser, F. *Journal of Applied Polymer Science*, **2001**, *80*, 2300
14. Burger, C.; Zhou, H.; Wang, H.; Sics, I.; Hsiao, B. S.; Chu, B.; Graham, L.; Glimcher, M. J. *Biophysical Journal*, **2008**, *95*, 1985
15. Noda, I. *Applied Spectroscopy*, **1993**, 47, 1329
16. Noda, I., *Applied Spectroscopy*, **2000**, *54*, 994
17. Noda, I.; Ozaki, Y. "*Two-Dimensional Correlation Spectroscopy: Applications in Vibrational and Optical Spectroscopy"*, **2004**, England John Wiley & Sons Ltd
18. Mathew, A. P.; Packirisamy, S.; Kumaran, M. G.; Thomas, S. *Polymer*, **1995**, *36*, 4935
19. Igwe, I. O. *Journal of Applied Polymer Science*, **2007**, *104*, 3849
20. Chalykh, A. Y.;. Shreder, V. L ; Krivoshei, V. N. *Polymer Science U.S.S.R.*, **1989**, *31*, 976
21. Guo, L.; Spegazzini, N.; Sato, H.; Hashimoto, T.; Masunaga, H.; Sasaki, S.; Takata, M.; Ozaki, Y. *Macromolecules*, **2012**, *45*, 313
22. Smirnova, D. S.; Kornfield, J. A.; Lohse, D. J. *Macromolecules*, **2011**, *44*, 6836
23. Bensason, S. *Journal of Polymer Science: Part B: Polymer Physics*, **1996**, *34*, 1301
24. Crist, B.; Williams, D. N. *Journal of Macromolecular Science-Physics*, **2000**, *B39*, 1
25. Alizadeh, A. *Macromolecues*, **1999**, *32*, 6221
26. Ruland, W.; Smarsly, B. *J. Appl. Crystal.* **2004**, 37, 575-584
27. Hermans, J. J. *Rec. Trav. Chim. Pays-Bas.* **1944**, 63, 211-218
28. Stribeck, N. *Macromolecules* **1996**, 29, 7217-7220

Chapter 8

Conclusion

The structure-property relationships of polymers can be tailored to meet the specific needs for a variety of applications. Recent developments in X-ray measurements at a synchrotron radiation facility (the X27C beamline in NSLS, BNL) have enabled time-resolved X-ray measurements during tensile deformation of polymeric soft matter materials. The advantage of a synchrotron source is to use its high intensities to minimize the relaxation effect by setting the irradiation time of X-rays on the sample much shorter than that of conventional X-ray measurements[1]. In this thesis, the structure, morphology and property relationships of NR and PE under external forces were studied using in situ synchrotron X-ray scattering techniques.

In Chapter 1, the importance and structure of NR and PE was discussed. The properties of these materials were determined by its structural morphology. In NR, the pseudo-network composed by the non-rubber components was mainly responsible for inducing SIC during deformation. The presence of SIC in NR could significantly alter its properties, where the crystallites could act as natural reinforcers to enhance the resistance to fracture and failure[2]. In PE, the differences in molecular weight and density of the semi-crystalline structure primarily determined its properties. In addition, the properties were governed by the presence of entanglements and tie chains between the crystallites.

In Chapter 2, the structural development and morphology in un-vulcanized and vulcanized (both pre- and post-vulcanized) natural rubber latex was studied in a relaxed state and under deformation by DQ-NMR and in-situ WAXD, respectively. Vulcanization was carried out using both sulfur and peroxide, showing important differences on the spatial distribution of cross-links according to the source of vulcanizing agents. Sulfur pre-vulcanization promotes the formation of highly homogeneous networks in the dispersed rubber particles, whereas peroxide vulcanization makes broader spatial cross-link distributions. The latter is compatible with the formation of core-shell network structures. Molecular orientation and strain-induced crystallization was analyzed by both stress-strain relations and WAXD. An increase in the vulcanizing agent concentration led to an increase in modulus and crystalline fractions. For sulfur vulcanization, the additional heat treatment (post-vulcanization) increased the interactions between rubber particles and un-reacted vulcanizing agents. For peroxide vulcanization, the additional heat treatment led to chain scission reactions and degradation of network points.

In Chapter 3, stress-strain relations and strain-induced crystallization (SIC) of un-vulcanized and vulcanized NR were studied using synchrotron X-ray at various temperatures from -50 +75 ˚C. Un-vulcanized and vulcanized NR showed SIC and stress upturns in the stress-strain relations. Since a permanent set was observed after large extension and retraction, un-vulcanized NR exhibited a pseudo end-linked network. The pseudo end-linked networks made entanglements as permanent entanglements and showed stress upturn and SIC. The stress values at higher temperatures were significantly lower than the stress values at lower temperatures. This tendency did not seem to follow the theory of rubber elasticity. The onset of SIC delayed the upturn of stress as a shoulder or plateau in the stress-strain relation. SIC contributed to the stress, even though the stress increased smoothly with strain. At higher strain, SIC became big network points to bind many chains and reduced the limit of extensibility.

In Chapter 4, a novel two-dimensional simulation method to analyze a WAXD pattern was introduced. The 2D WAXD simulation method was applied to the crystal and crystallites of SCI of un-vulcanized NR and IR at -50 ˚C. The unit cell dimensions of SIC were determined by calculation of scattering factors based on atomic coordinates and symmetry, and were compared with the observed data. The unit cell dimensions were identical in NR and IR, and did not change during extension. The crystallites' dimensions in NR and IR were almost the same at -50 C. The orientation of crystallites in NR was lower than in IR. The order of crystals in NR was lower than in IR. The crystalline fraction increased with strain because of the increase in the number of crystallites. The onset strain of SIC in NR was smaller than in IR. The different behaviors of SIC in NR and IR are caused by the pseudo-network of NR.

In Chapter 5, new insights into the SIC and TIC of un-vulcanized NR and PVNR were obtained by WAXD and SAXS. The SIC samples were deformed at various temperatures (from -50 to 50 ˚C) in order to determine the effect of temperature on the crystallite structure. In the WAXD patterns, highly oriented sharp crystal reflections were observed for the SIC samples, whereas sharp rings without preferred orientation were observed for the TIC samples. The novel 2D method to calculate WAXD patterns discussed in Chapter 4 was applied here to obtain information on the crystallite structure at various temperatures. For the SIC samples, the crystallite sizes, volume, number of chains per crystallite, crystallite orientation, and crystal displacement disorder increased with increasing temperature, but with a decrease in the number of crystals. The crystallite sizes and volume were much larger for the TIC samples as compared to the SIC samples. In the SAXS patterns, the presence of a lamellar peak was observed only for the SIC samples at low temperatures, whereas diffuse scattering was observed for the SIC samples at high temperatures and for the TIC samples. A two-phase stacking model was applied to the 1D integrated intensities of the TIC samples in order to determine the thicknesses of the crystalline and amorphous phases, and the long period spacing. The long period increased with increasing temperature, which was attributed to the reduction in the number of crystallites and the translation of chains from the crystalline regions to an amorphous state.

In Chapter 6, plastic deformation of uniaxially PE fiber was examined by SAXS and WAXD. Morphology changes of the lamellar stack with deformation beyond yielding have been characterized and quantified. Atomistic simulations of tensile deformation of the lamellar stack in the longitudinal direction compared favorably to the experimentally observed morphological changes in the PE fiber. Experimental deformations at 100 °C exhibited responses comparable to those observed by simulation of deformation with constant total volume at 77 °C and a strain rate of 5 x 10^6 s^{-1}. Experimental deformations of the PE fiber at 25 °C were found to be comparable to simulated tensile deformation with constant lateral dimensions at 77 °C and a strain rate of 5 x 10^7 s^{-1}. Cavitation in the interlamellar region was found experimentally in the PE fiber deforming at room temperature as predicted by simulation with constant lateral dimensions at the higher strain rate. Melting, recrystallization, and removal of entanglements observed in the PE fiber deformation at 100 °C agree with the simulation results of a constant volume deformation at the slower strain rate. The ability to define the deformation behavior of

PE at room and at high temperatures through simulation offered unique opportunities to examine the effect of the interlamellar amorphous topology on PE deformation.

In Chapter 7, the morphological changes in uniaxially oriented fibers of HDPE and LLDPE resulting from the swelling in toluene was examined and quantified by SAXS, WAXD, and DSC. By analyzing WAXD and DSC data, no significant changes in crystalline unit cell structure and overall crystallinity after swelling of HDPE and LLDPE were found, suggesting that there was no solvent penetration into the crystalline phases of HDPE and LLDPE. An increase in long spacing, as measured by SAXS, was found in both HDPE and LLDPE. Using a two-phase stacking model to analyze SAXS data revealed a small increase, about 5%, in the crystallite thickness and a larger increase, about 7-8%, in the amorphous thickness. The slight increase in the crystallite thickness after swelling could arise from the solvent-induced crystalline-amorphous interfacial crystallization. Although LLDPE swelled up about 45% more toluene than HDPE as a result of its lower crystallinity, its normalized amorphous swelling with respect to its amorphous fraction was lower that the normalized amorphous swelling of HDPE. Additionally, its amorphous thickness increased by scattering was found to be equivalent to that of HDPE. This constrained swelling in LLDPE might be attributed to its higher tie chain and trapped entanglement concentrations in its amorphous phase. Two-dimensional correlation analysis also revealed the presence of small crystalline structures on the order of 10 nm in LLDPE that were not observed in HDPE, which was believed to be fringed micelles.

8.1 Future Work

One of the most important natural resources in the world is natural rubber. All commercially-available NR is harvested from *Hevea Brasiliensis*. NR is a vital raw material for industrial applications due to its superior physical properties, such as elasticity, heat dispersion, and resistance to wear and tear. With the increasing demands of Hevea NR, the global average annual NR production is about 11.5 million tons per year. However, there is a limitation to the supply of Hevea NR because it can only be grown in a few specific tropical regions around the world. Recently, there have been plant diseases and flu pandemics that caused a reduction in the production of Hevea NR[3], and therefore, the sole dependence on this plant species is risky. All Hevea NR fields have already been tapped, and therefore, there are no reserves[4]. The properties of all synthetic rubbers and other natural rubber substitutes are inferior to those of Hevea NR. Due to these reasons, the prices and demands for Hevea NR are at its all-time highs. The consumption is predicted to exceed 20 million tons by 2020, which is about double the current consumption[5]. The International Rubber Study Group predicted a 2-3 million tons per year shortage in the global rubber supply by 2020[6]. With limited supply, soaring prices, and increasing demands for Hevea NR, there needs to be an alternative source for rubber supply.

In recent years, guayule (also known as *Parthenium Argentatum*) has gain significant attention as an alternate source for NR because it can be more easily cultivated around the world and can be produced in larger quantities as compared to Hevea NR. In addition, guayule NR contains less than 2% of the overall proteins that are present in Hevea NR, including the absence of the allergenic proteins that Trigger Type 1 latex allergy symptoms in individuals[7-12]. This has a major advantage over Hevea NR for medical and surgical applications. However, the properties and performance of guayule NR is inferior to that of Hevea NR. Its current properties do not meet the standards for applications in materials, which can be attributed to differences in the chemical structure between the two. The weak tensile properties of pristine guayule NR is attributed to the absence of a pseudo-network, which leads to the absence of SIC even up to large strains of 600%. It is of particular interest to the industry to find a preparation method that can improve the properties and performance of guayule NR so that it can meet the requirements for the materials industry. This can overall reduce the global dependence on Hevea NR.

Finding preparation methods to increase the network density in guayule NR can significantly improve its properties. The interactions between the polymer and certain non-rubber constituents in NR that were uncovered in this thesis can help modify the structure of guayule NR to mimic the structure of Hevea NR. The combination of synchrotron X-ray scattering techniques and DQ NMR discussed in this work can characterize and provide a considerable amount of information regarding rubber network structure over a wide range of length scales. Synchrotron X-rays can analyze network structures at much larger length scales, whereas DQ NMR studies the fluctuations of molecules at more local length scales.

8.2 References

1. Ikeda, Y.; Yasuda, Y.; Hijikata, K.; Tosaka, M.; Kohjiya, S. *Macromolecules*, **2008**, *41*, 5876
2. Kroon, M. *Mechanics of Materials*, **2010**, *42*, 873
3. Davis, W. *Fortune* **1997**, 4
4. Feher, F. J.; Benko, D.; Sabo, T.; Wong, T.; Rodewald, S.; Whited, G.; Cervin, M.; McAuliff, J.; Calabria, A.; Miasnikov, A.; LaDuca, R.; Sandford, K. "*BioIsoprene Products as Renewable/Sustainable Alternatives to Natural Rubber.*" Tire Technology Expo 2011, Cologne, Germany, **2011**
5. McMahan, C. M.; Williams, J.; Cornish, K. "*Guayule Latex: Physical, Chemical, and Rheological Properties*."
6. International Rubber Study Group. "Statistical Summary of World Rubber Situations." **2013**
7. Kekwick, R. G. O. *Latex Protein Allergy*: *The Present Position*, Crain Commun, Rubber Consultants, Brickendonbury, Hertford, UK, **1993**, p. 21
8. Morales, C.; Bascomba, A.; Carrieira, J.;Sastre, A. *Clin. Exp.Allergy*, **1989**, *19*, 425
9. Ownby, D. R.; Ownby, H. E.; McCullough, J. A.; Shafer, A. W. *J. Allergy Clin. Immunol.*, **1994**, *93*, 282
10. Pailhories, G. *Clin. Rev. Allergy*, **1993**, *11*, 391
11. Slater, J. E. *New Engl. J. Med.* **1989**, *320*, 1126
12. Tomazic, V. J.; Withrow, T. J.; Fisher, B. R.; Dillard, S. F. *Clin. Immunol. Immunopathol.*, **1992**, *64*, 89

Bibliography

Chapter 1

1. Cornish, K. *Nat. Prod. Rep.* **2001**, *18*, 182
2. Cornish, K. "*Alternative Rubber Production*." Tire Technology Expo 2011, Cologne, Germany, **2011**
3. Smithers Rapra, Emerging Applications for Elastomers to 2017
4. Toki, S.; Sics, I.; Ran, S.; Liu, L.; Hsiao, B. S.; Murakami, S.; Senoo, K.; Kohjiya, S. *Polymer* **2003**, *44*, 6003
5. Amnuaypornsri, S.; Sakdapipanich, J.; Toki, S.; Hsiao, B. S.; Ichikawa, N.; Tanaka, Y. *Rubber Chem Technol.* **2008**, *81*, 753
6. Tanaka Y. *Rubber Chem Technol.* **2001**, *74*, 355
7. Encarta World English Dictionary, Bloomsbury Publishing Plc.: latex **2009**
8. Amnuaypornsri, S.; Sakdapipanich, J.; Tanaka, Y. *J. Appl. Polym Sci. Appl Polym.*, **2009**, *111*, 2127
9. Perrella, F. W.; Gaspari, A. A. *Methods*, **2002**, *27*, 77
10. Amnuaypornsri, S.; Toki, S.; Hsiao, B. S.; Sakdapipanich, J. *Polymer* **2012**, *53*, 3325
11. Diene Polymers, Polymer Sci, University of Southern Miss
12. L. Loan, Peroxide Crosslinking Reactions in Polymers, Bell Laboratories
13. Flory, P. J., *J. Chem. Phys.* **1947**, *15*, 397
14. Flory, P. J., Principles of Polymer Chemistry Cornell University Press, **1953**
15. Toki, S.; Che, J.; Rong, L.; Hsiao, B. S.; Amnuaypornsri, S.; Nimpaiboon, A.; Sakdapipanich, J. *Macromolecules*, **2013**, *46*, 5238-5248
16. Piringer, O. G.; Baner, A. L. *Plastic Packaging: Interactions with Food and Pharmaceuticals* **2008**, 2nd edition, Wiley-VCH
17. UL IDES, Polyethylene Plastic
18. Polymer Research Laboratory, Crystallizable Block Copolymers, 2010, Department of Chemical and Biological Engineering, The Trustees of Princeton University

19. Contreras, J. A. A. **2007**, *Micromechanical modelling of polyethylene* (Doctoral Dissertation), University of Waterloo, Waterloo, Ontario, Canada
20. Bunn, C. W. *Transactions of the Faraday Society*, **1944**, *40*, 23
21. Bunn, C. W. *Journal of Appl Phy*, **1954**, *25*, 820
22. National Research Council Canada. Properties and Behavior of Plastics, **2005**
23. O'Connell, P.A.; McKenna, G. B. *Yield and Crazing in Polymers*. Encyclopedia of Polymer Science and Technology (John Wiley & Sons, 2004)
24. Ward, I. M. *Mechanical Properties of Solid Polymers*, 2nd ed. (Wiley, New York, 1990)
25. Schultz, J. *Polymer Materials Science* (Prentice-Hall, Englewood Cliffs, 1974)
26. Uribe, A. R.; Manzur, A.; Olayo, R. *J. Mater. Res.*, **2012**, *27*, 1351
27. Essentials of Polymer Science & Engineering, Painter & Coleman, p.236
28. Treloar, L. R. G. "The Physics of Rubber Elasticity," Oxford University Press, London (1975)

Chapter 2

1. Toki, S.; Sics, I.; Ran, S.; Liu, L.; Hsiao, B. S.; Murakami, S.; Senoo, K.; Kohjiya, S. *Polymer* **2003**, *44*, 6003
2. Toki, S.; Sics, I.; Ran, S.; Liu, L.; Hsiao, B. S.; Murakami, S.; Senoo, K.; Kohjiya, S. *Macromolecules* **2002,** *35*, 6578
3. Keddie, J.; Routh, A. **"**Fundamentals of Latex Film Formation: Processes and Properties," *UK: Canopus Academic Publishing Limited* **2010**
4. Perrellaa, F.; Gaspari, A. *Methods* **2002**, *27*, 77
5. Amnuaypornsri, S.; Sakdapipanich, J.; Tanaka, Y. *Jour. Appl. Polym Sci. Appl Polym*. **2009**, *111*, 2127
6. Saalwachter, K. *Prog. Nucl. Magn. Reson. Spectrosc*. **2007**, *51*, 1
7. Valentin, J. L.; Posadas, P.; Fernandez-Torres, A.; Malmierca, M. A.; Gonzalez, L.; Chasse, W.; Saalwachter, K. *Macromolecules* **2010**, *43*, 4210
8. Chasse, W.; Valentin, J. L.; Genesky, G. D.; Cohen, C.; Saalwachter, K. *J. Chem. Phys* **2011**, *134*, 044907
9. Lewis, A. "Accelerator DPTT," *AkroChem Corporation* **2009**

10. Valentín, J. L.; López, D.; Hernández, R.; Mijangos, C.; Saalwächter, K. *Macromolecules* **2009**, *42*, 263
11. Vaca-Chavez, F.; Saalwachter, K. *Phys. Rev. Lett.* **2010,** *104***,** 198305
12. Vaca-Chavez, F.; Saalwachter, K. *Macromolecules* **2011**, *44***,** 1560
13. Saalwachter, K.; Gottlieb, M.; Liu, R.; Oppermann, W. *Macromolecules* **2007**, *40*, 1555
14. Posadas, P.; Fernández-Torres, A.; Valentin, J. L.; Rodríguez, A.; González, L.; *J Appl. Polym. Sci.* **2010**, *115*, 692
15. Lemayev, N. V.; Kurbatov, V. A.; Liakumovich, A. G. *Polymer Science URSS* **1981**, *23*, *419*
16. Amnuaypornsri, S.; Sakdapipanich, J.; Toki, S.; Hsiao, B. S.; Ichikawa, N.; Tanaka, Y. *Rubber Chemistry and Technology* **2008**, *81*, 753
17. Ikeda, Y.; Yasuda, Y.; Hijikata, K.; Tosaka, M.; Kohjiya, S. *Macromolecules* **2008**, *41*, 5876
18. Suzuki, T.; Osaka, N.; Endo, H.; Shibayama, M.; Ikeda, Y.; Asai, H.; Higashitani, N.; Kokubo, Y.; Kohjiya, S. *Macromolecules* **2010**, *43*, 1556
19. Dohi, H.; Horiuchi, S. *Polymer* **2007,** *48*, 2526
20. Ho, C.C.; Khew, M.C. *Langmuir* **2000**, *16*, 2436
21. Rault, J., Marchal, J., Judeinstein, P., Albouy, P. A., *Macromolecules* **2006**, *39*, 8356
22. Dupres, S., Long, D. R., Albouy, P. A., Sotta, P., *Macromolecules* **2009**, *42*, 2634
23. Kimura, H., Dohi, H., Kotani, M., Matsunaga, T., Yamauchi, K., Kaji, H., Kurosu, H., Asakura, T., *Polymer journal* **2010**,*42*, 25
24. Kameda, T., Asakura, T., *Polymer* **2003**, *44*, 7539

Chapter 3

1. Katz, J. R., (1925b), *Kolloid Zeitschrif.*, **1925,** *36*, 300
2. Treloar, L. R. G., The physics of rubber elasticity, 3rd ed., Oxfrd press, **1975**
3. Mark, J. E., Erman, B., Rubberlike elasticity. A molecular premier. Wiley-Interscience, New York, **1988**
4. Arruda, E. M., Boyce, M. C. *J. Mechanic. Physic. Solid*, **1993**, *41*, 389
5. Boyce, M. C., Arruda, E. M. *Rubber Chem. Technol.* **2000**, *73*, 504

6. Treloar L. R. G., *Trans. Faraday Society*, **1944**, *40*, 59
7. Treloar, L. R. G., *Trans. Faraday Society*, **1947**, *43*, 284
8. Doi, M and Edwards, S. F., The theory of polymer dynamics. Clerendon press, Oxford, London. **1986**
9. James, H. M., Guth, E., *J. Chem. Phys*. **1943**,*11*, 455
10. Fetters, L. J., Lohse, D. J., Richter, D., Witten, T. A., Zirkel, A. *Macromolecules* **1994**, *27*, 4639
11. Edwards, S. F., Vilgis, T. A., *Rep. Prog. Phys.*, **1988,** *51*, 243
12. Eyring, H., *Physi. Rev*. **1932,** *39*, 746
13. Oka, S. *Proc. Phys-Math. Soc. Japan*, **1942,** *24*, 657
14. deGennes, P. G. *J. Chem. Physi.* **1971**, *55*, 572
15. Doi, M. *J. Polym. Sci. part C : Polym. Letter*. **1981**, *19*, 265
16. Toki, S., Fujimaki, T., Okuyama, M. *Polymer* **2000**, *41*, 5423
17. Toki, S., Sics, I., Ran, S., Liu, L., Hsiao, B, Murakami, S., Tosaka, M.,Senoo, K., Kohjiya, S. *Macromolecules* **2002**, *35*, 6578
18. Murakami, S., Senoo, K., Toki, S., Kohjiya, S. *Polymer* **2002** *43*, 2117
19. Trabelsi S., Albouy. P. A., Rault, J. *Macromolecules* **2003**, *36*, 7624
20. Tosaka, M.; Murakami, S.; Poompradub, S.; Kohjiya, S.; Ikeda, Y.; Toki, S.; Sics, I.; Hsiao, B. S. *Macromolecules* **2004**, *37*, 3299
21. Flory, P. J., *J. Chem. Phys.* **1947**, *15*, 397
22. Flory, P. J., Principles of Polymer Chemistry Cornell University Press, **1953**
23. Toki S., Hsiao S. H., Amnuaypornsri S., Sakdapipanich J. *Polymer* **2009**, *50*, 2142
24. Toki S., Hsiao S. H., Amnuaypornsri S., Sakdapipanich J., Tanaka Y. *J. Polym. Sci. Polym. Phys*. **2008**, *46*, 2456
25. Amnuaypornsri, S.,Toki, S., Hsiao, B. S., Sakdapipanich, J. *Polymer* **2012**, *53*, 3325
26. Anthony. B. L., Caston, R. H., Guth, E. *J. Phys. Chem*., **1942**, *46*, 826
27. Toki, S., Sics, I., Liu, L., Hsiao, B. S., Murakami, S., Tosaka, M., Poompradub, S., Kohjiya, S., Ikeda, Y. *Macromolecules*, **2005**, *38*, 7064
28. Karino, T., Ikeda, Y., Yasuda, Y., Kohjiya, S., Shibayama, M. *Biomacromol.* **2007**; *8*, 693

29. Ikeda, Y; Higashitani, N; Hijikata, K; Kokubo, Y; Morita, Y; Shibayama, M; Osaka, N; Suzuki, T; Endo, H; Kohjiya, S. *Macromolecules* **2009**, *42*, 2741
30. Che, J.; Toki, S.; Valentin, J.; Brasero, J. Nimpaiboon, A.; Rong, L.; Hsiao, B. S. *Macromolecules* **(2012)** *45*, 6491-6503
31. Valentin, J. L., Posadas, P., Fernandez-Terres, A., Malmierca, M. A, Gonzalez, L., Chasse, W., Saalwachter, K. *Macromolecules* **2010**, *43*, 4210
32. Toki, S., Takagi, R., Ito, M., Hsiao B. S. *Polymer* **2011**, *52*, 2453
33. Che, J.; Burger, C.; Toki, S.; Rong, L.; Hsiao, B. S. *Macromolecules*, **(2013)** *46*, 4520-4528

Chapter 4

1. Katz, J. R. *Kolloid Zeitschrif.* **1925**, *36*, 300
2. Katz, J. R. *Kolloid Zeitshrif*. **1925**, *37*, 10
3. Mark, H.; von Susich, G. *Kolloid Zeits*. **1928**, *46*, 11
4. Morss Jr, H. A. *J. Amer. Chem. Soc.* **1938**, *60*, 237
5. Bunn, C. W. *Proc. R. Soc. London A* **1942**, *180*, 40
6. Nyburg, S. C. *Acta Crystal.* **1956**, *7*, 385
7. Natta, G.; Corradini, P. *Angew. Chem*. **1956**, *68*, 615
8. Takahasi, Y.; Kumano, T. *Macromolecules* **2004**, *37*, 4860
9. Immirzi, A.; Tedesco, C.; Monaco, G.; Tonelli, A. E. *Macromolecules* **2005**, *38*, 1223
10. Rajkumar, G.; Squire, J. M.; Arnott, S. *Macromolecules* **2006**, *39*, 7004
11. Gent, A. N. *Trans. Faraday Society*, **1954**, *50*, 521
12. Mitchell, G. R. *Polymer*, **1984**, *25*, 1563
13. Toki, S.; Sics, I.; Ran, S.; Liu, L.; Hsiao, B. S.; Murakami, S.; Senoo, K.; Kohjiya, S. *Macromolecules* **2002**, *35*, 6578
14. Trabelsi, S.; Albuoy, P. A.; Rault, J. *Macromolecules* **2003,** *36*, 7624
15. Tosaka, M.; Murakami, S.; Poompradub, S.; Kohjiya, S.; Ikeda, Y.; Toki, S.; Sics, I.; Hsiao, B. S. *Macromolecules* **2004**, *37*, 3299
16. Tosaka, M.; Senoo, K.; Sato, K.; Noda, M.; Ohta, N. *Polymer*, **2012**, *53*, 864
17. Flory, P. J. *J. Phys. Chem*., **1947**, *15*, 397

18. Mitchell, J. C.; Meier, D. J. *J. Polymer Science*, **1968**, *6*, 1689
19. Tosaka, M.; Kawakami, D.; Senoo, K.; Kohjiya, S. *Macromolecules* **2006**, *39*, 5100
20. Tanaka, Y. *Rubber Chem. Technol.* **2001**, *74*, 355
21. Karino, T.; Ikeda, Y.; Yasuda, Y.; Kohjiya, S.; Shibayama, M. *Biomacromolecules* **2007**, *8*, 693
22. Amnuaypornsri, S.; Toki, S.; Hsiao, B. S.; Sakdapipanich, J.; Tanaka, Y. *Rubber Chem. Technol.* **2008**, *81*, 753
23. Toki, S.; Burger, C.; Hsiao, B. S; Amnuaypornsri, S.; Sakdapipanich, J.; Tanaka Y. *J. Polym. Sci. Part B: Polym. Phys.* **2008**, *46*, 2456
24. Burger, C.; Hsiao, B. S.; Chu, B. *Polymer Reviews* **2010**, *50*, 91
25. Burger, C.; Zhou, H.; Sics, I.; Hsiao, B. S.; Chu, B.; Graham, L.; Glimcher, M. J. *J. Appl. Cryst*. **2008**, *41*, 252
26. Mao, Y.; Burger, C.; Zuo, F.; Hsiao, B. S.; Mehta, A.; Mitchell, C.; Tsou, A. H. *Macromolecules* **2011**, *44*, 558
27. Ruland, W. *Colloid Polym. Sci.* **1977**, *255*, 833
28. Guinier, A. X-Ray Diffraction: In Crystals, Imperfect Crystals, and Amorphous Bodies; W. H. Freeman: San Francisco, CA, and London, **1963**
29. Sears, V. F.; Shelley, S. A. *Acta Crystal.* **1991**, *47*, 441
30. Fraser, R. D. B.; Macrae, T. P.; Miller, A.; Rowlands, R. J. *J. Appl. Cryst*. **1976**, 9, 81
31. Toki, S.; Fujimaki, T.; Okuyama, M. *Polymer*, **2000** *41*, 5423
32. Toki, S.; Sics, I.; Ran, S.; Liu, L.; Hsiao, B. S.; Murakami, S.; Senoo, K.; Kohjiya, S. *Polymer* **2003**, *44*, 6003
33. Toki, S.; Sics, I.; Hsiao, B. S.; Murakami, S.; Tosaka, M.; Poompradub, S.; Kohjiya, S.; Ikeda, Y. *J. polym., Sci., B, Polym. Phys*. **2004**, *42*, 956

Chapter 5

1. Che, J.; Burger, C.; Toki, S.; Rong, L.; Hsiao, B. S.; Amnuaypornsri, S.; Sakdapipanich, J. *Macromolecules* **2013**, *46*, 4520
2. Kroon, M. *Mech of Materials* **2010**, *42*, 873

3. Toki, S.; Kohjiya, S.; Ikeda, Y. "Chapter 7: The effect of strain-induced crystallization on the physical properties of natural rubber." *Chemistry, Manufacture, and Applications of Natural Rubber*. Woodhead Publishing Ltd, **2013** (in print)
4. Flory, P. J. *J. Phys. Chem*. **1947**, *15*, 397
5. Yamamoto, M.; White, J. L. *J. Poly. Sci. A-2* **1971**, *9*, 1399
6. Tosaka, M. *Macromolecules* **2009**, *42*, 6166
7. Treolar, L. R. G. *The Physics of Rubber Elasticity*. New York: Oxford University Press, **2005**
8. Mitchell, J. C.; Meier, D. J. *J. Polymer Science, part A-2*, **1968**, *6*, 1689
9. Tosaka, M.; Senoo, K..; Sato, K.; Noda, M.; Ohta, N. *Polymer* **2012**, *53*, 864
10. Toki, S.; Fujimaki, T.; Okuyama, M. *Polymer* 2000, *41*, 5423
11. Andrews, E. H. *Proc. Roy. Soc.***1964**, *277*, 562
12. Luch, D.; Yeh, G. S. Y. *J. Appl. Phys*. **1972**, *43*, 4326
13. Luch, D.; Yeh, G. S. Y. J. *Macomol. Sci. Phys* .**1973**, *B7*, 121
14. Luch, D.; Yeh, G. S. Y. *J. Polym. Sci. Polymer Phys* **1973**, *11*, 467
15. Toki, S.; Che, J.; Rong, L.; Hsiao, B. S.; Amnuaypornsri, S.; Nimpaiboon, A.; Sakdapipanich, J. *Macromolecules* **2013**, *46*, 5238
16. Che, J.; Toki, S.; Valentin, J. L.; Brasero, J.; Nimpaiboon, A.; Rong, L.; Hsiao, B. S. *Macromolecules* **2012**, *45*, 6491
17. Amnuaypornsri, S.; Toki, S.; Hsiao, B. S.; Sakdapipanich, J. *Polymer* **2012**, *53*, 3325
18. Burger, C.; Hsiao, B. S.; Chu, B. *Polymer Reviews* **2010**, *50*, 91
19. Burger, C.; Zhou, H.; Sics, I.; Hsiao, B. S.; Chu, B.; Graham, L.; Glimcher, M. J. *J. Appl. Crystallogr.* **2008**, *41*, 252
20. Hermans, J. J. *Recl. Trav. Chim. Pays-Bas* **1944**, *63*, 211
21. Stribeck, N. *Macromolecules* **1996**, *29*, 7217
22. Ruland, W.; Smarsly B. *J. Appl. Crystallogr.* **2004**, *37*, 575
23. Burger, C.; Zhou, H.; Wang, H.; Sics, I.; Hsiao, B. S.; Chu, B.; Graham, L.; Glimcher, M. J. *Biophys. J.* **2008**, *95*, 1985
24. Fraser, R. D. B.; Macrae, T. P.; Miller, A.; Rowlands, R. J. *J. Appl. Cryst*. **1976**, 9, 81
25. Tosaka, M.; Senoo, K.; Kohjiya, S.; Ikeda, Y. *J. Appl. Phys*. **2007**, *101*, 084909

26. Gehman, S. D.; Field, J. E. *J. Appl. Phys*. **1939**, *10*, 564
27. Guinier, A. X-Ray Diffraction: In Crystals, Imperfect Crystals, and Amorphous Bodies; W. H. Freeman: San Francisco, CA, and London, **1963**
28. Sears, V. F.; Shelley, S. A. *Acta Crystal*. **1991**, *47*, 441
29. Bukhina, M. F. *Rubb Chem and Tech*. **1964**, *37*, 404
30. Rajkumar, G.; Squire, J. M.; Arnott, S. *Macromolecules* **2006**, *39*, 7004
31. Trabelsi, S.; Albouy, P. A.; Rault, J. *Macromolecules* **2003**, *36*, 7624

Chapter 6

1. Kolgjini, B.; Schoukens, G.; Kiekens, P. *Intern. J. Poly. Sci.* **2011**, 731708, 1-7.
2. Na, B.; Zhang, Q.; Fu, Q.; Men, Y.; Hong, K.; Strobl, G. *Macromolecules* **2006**, 39, 2584-2591.
3. Fu, Q.; Men, Y.; Strobl, G. *Polymer* **2003**, 44, 1927-1933.
4. Hobeika, S.; Men, Y.; Strobl, G. *Macromolecules* **2000**, 33, 1827-1833.
5. Stribeck, N.; Alamo, R. G.; Mandelkern, L.; Zachmann, H. G. *Macromolecules* **1995**, 28, 5029-5036.
6. Fu, Q.; Men, Y.; Strobl, G. *Polymer* **2003**, 44, 1941-1947.
7. Jiang, Z.; Tang, Y.; Men, Y.; Enderle, H.; Lilge, D.; Roth, S. V.; Gehrke, R.; Rieger, J. *Macromolecules* **2007**, 40, 7263-7269.
8. Tang, Y.; Jiang, Z.; Men, Y.; An, L.; Enderle, H.; Lilge, D.; Roth, S. V.; Gehrke, R.; Rieger, J. *Polymer* **2007**, 48, 5125-5132.
9. Uribe, A.; Manzur, A.; Olayo, R. *J. Mater. Res.* **2012**, 27, 1351-1359.
10. Bowden, P. B.; Young, R. J. *J. Mater. Sci* **1974**, 9, 2034-2051.
11. Goderis, B.; Reynaers, H.; Koch, M. H. J.; Mathot, V. B. F. *J. Poly. Sci: Part B: Poly. Phys.* **1999**, 37, 1715-1738.
12. Hiss, R.; Hobeika, S.; Lynn, C.; Strobl, G. *J. Macro Sci, Part B: Phys* **1999**, 38, 847-858.
13. Hiss, R.; Hobeika, S.; Lynn, C.; Strobl, G. *Macromolecules* **1999**, 32, 4390-4403.
14. Moysés S. C.; Machado, R. *Eur. Poly. Journ.* **2002**, 38, 2041-2044.
15. Hong, K.; Strobl, G. *Macromolecules* **2006**, 39, 268-273.
16. Lee, S.; Rutledge, G. C. *Macromolecules* **2011**, 44, 3096-3108.

17. Veld, P. in't; Rutledge, G. C. *Macromolecules* **2003**, 36, 7358-7365.
18. Humbert, S.; Lame, O.; Chenal, J.; Rochas, C.; Vigier, G. *J. Poly. Sci: Part B: Poly. Phys.* **2010**, 48, 1535-1542.
19. Z. Wilchinsky, *J. Appl. Phys.* **1960**, 31, 1969-1972.
20. Desper, C.; Stein, R. *J. Appl. Phys.* **1966**, 37, 3990-4002.
21. Hermans, J. J. *Rec. Trav. Chim. Pays-Bas.* **1944**, 63, 211-218.
22. Stribeck, N. *Macromolecules* **1996**, 29, 7217-7220.
23. Ruland, W.; Smarsly, B. *J. Appl. Crystal.* **2004**, 37, 575-584.
24. Burger, C.; Zhou, H.; Wang, H.; Sics, I.; Hsiao, B. S.; Chu, B.; Graham, L.; Glimcher, M. J. *Biophysical Journ.* **2008**, 95, 1985-1992.
25. Veld, P. in't; Hutter, M.; Rutledge, G. C. *Macromolecules* **2006**, 39, 439-447.
26. Eyring, H. *J. Chem. Phys.* **1936**, 4, 283-291.
27. Sweeney, J.; Shirataki, H.; Unwin, A. P.; Ward, I. M. *J. App. Poly. Sci.* **1999**, 74, 3331-3341.
28. Capaldi, F. M.; Boyce, M. C.; Rutledge, G. *Polymer* **2004**, 45, 1391-1399.
29. Hutter, M.; Veld, P. in't ; Rutledge, G. C. *Polymer* **2006**, 47, 5494-5504.

Chapter 7

1. McCall, D. W.; Anderson, E. W. *Journal of Polymer Science Part A: General Papers*, **1963**, *1*, 1175
2. Rogers, C. E.; Stannett, V.; Szwarc, M. *Journal of Polymer Science*, **1960**, *45*, 61
3. McCall, D.W. *Journal of Polymer Science*, **1957**, *26*, 151
4. Ng, H. C.; Leung, W. P.; Choy, C. L. *Journal of Polymer Science: Polymer Physics Edition*, **1985**, *23*, 973
5. Kwei, T. K.; Wang, T. T. *Macromolecules*, **1972**, *5*, 128
6. Kim, M. H.; Glinka, C. J. *Journal of Applied Crystallography*, **2005**, *38*, 734
7. Huang, Y. L.; Brown, N. *Journal of Polymer Science, Part B: Polymer Physics*, **1991**, *29*, 129
8. Seguela, R. *Journal of Polymer Science, Part B: Polymer Physics,* **2005**, *43*, 1729

9. Patel, R. M.; Sehanobish, K.; Jain, P.; Chum, S. P.; Knight, G. W. *J. Appl. Polym. Sci.*, **1996**, *60*, 749
10. Howard, R. N. *Macromolecules*, **1993**, *26*, 5860
11. Flory, P. J. *"Principle of Polymer Chemistry"*, **1953**, Cornell University Press, Ithaca, NY, Chapter 13, 577-584
12. Wunderlich, B.; Czornyj, G. *Macromolecules*, **1977**, *10*, 906
13. Cser, F. *Journal of Applied Polymer Science*, **2001**, *80*, 2300
14. Burger, C.; Zhou, H.; Wang, H.; Sics, I.; Hsiao, B. S.; Chu, B.; Graham, L.; Glimcher, M. J. *Biophysical Journal*, **2008**, *95*, 1985
15. Noda, I. *Applied Spectroscopy*, **1993**, 47, 1329
16. Noda, I., *Applied Spectroscopy*, **2000**, *54*, 994
17. Noda, I.; Ozaki, Y. *"Two-Dimensional Correlation Spectroscopy: Applications in Vibrational and Optical Spectroscopy"*, **2004**, England John Wiley & Sons Ltd
18. Mathew, A. P.; Packirisamy, S.; Kumaran, M. G.; Thomas, S. *Polymer*, **1995**, *36*, 4935
19. Igwe, I. O. *Journal of Applied Polymer Science*, **2007**, *104*, 3849
20. Chalykh, A. Y.;. Shreder, V. L ; Krivoshei, V. N. *Polymer Science U.S.S.R.*, **1989**, *31*, 976
21. Guo, L.; Spegazzini, N.; Sato, H.; Hashimoto, T.; Masunaga, H.; Sasaki, S.; Takata, M.; Ozaki, Y. *Macromolecules*, **2012**, *45*, 313
22. Smirnova, D. S.; Kornfield, J. A.; Lohse, D. J. *Macromolecules*, **2011**, *44*, 6836
23. Bensason, S. *Journal of Polymer Science: Part B: Polymer Physics*, **1996**, *34*, 1301
24. Crist, B.; Williams, D. N. *Journal of Macromolecular Science-Physics*, **2000**, *B39*, 1
25. Alizadeh, A. *Macromolecues*, **1999**, *32*, 6221
26. Ruland, W.; Smarsly, B. *J. Appl. Crystal.* **2004**, 37, 575-584
27. Hermans, J. J. *Rec. Trav. Chim. Pays-Bas.* **1944**, 63, 211-218
28. Stribeck, N. *Macromolecules* **1996**, 29, 7217-7220

Chapter 8

1. Ikeda, Y.; Yasuda, Y.; Hijikata, K.; Tosaka, M.; Kohjiya, S. *Macromolecules*, **2008**, *41*, 5876

2. Kroon, M. *Mechanics of Materials,* **2010**, *42*, 873
3. Davis, W. *Fortune* **1997**, 4
4. Feher, F. J.; Benko, D.; Sabo, T.; Wong, T.; Rodewald, S.; Whited, G.; Cervin, M.; McAuliff, J.; Calabria, A.; Miasnikov, A.; LaDuca, R.; Sandford, K. "*BioIsoprene Products as Renewable/Sustainable Alternatives to Natural Rubber.*" Tire Technology Expo 2011, Cologne, Germany, **2011**
5. McMahan, C. M.; Williams, J.; Cornish, K. "*Guayule Latex: Physical, Chemical, and Rheological Properties*."
6. International Rubber Study Group. "Statistical Summary of World Rubber Situations." **2013**
7. Kekwick, R. G. O. *Latex Protein Allergy*: *The Present Position*, Crain Commun, Rubber Consultants, Brickendonbury, Hertford, UK, **1993**, p. 21
8. Morales, C.; Bascomba, A.; Carrieira, J.;Sastre, A. *Clin. Exp.Allergy*, **1989**, *19*, 425
9. Ownby, D. R.; Ownby, H. E.; McCullough, J. A.; Shafer, A. W. *J. Allergy Clin. Immunol.*, **1994**, *93*, 282
10. Pailhories, G. *Clin. Rev. Allergy*, **1993**, *11*, 391
11. Slater, J. E. *New Engl. J. Med.* **1989**, *320*, 1126
12. Tomazic, V. J.; Withrow, T. J.; Fisher, B. R.; Dillard, S. F. *Clin. Immunol. Immunopathol.*, **1992**, *64*, 89